The Origin of the Initial Mass Function: The Role of Gravity, Turbulence, Jets, and Radiative Feedback

Sajay Sunny Mathew

A thesis submitted for the degree of

Doctor of Philosophy

The Australian National University

Research School of Astronomy & Astrophysics

November 2024

To the Creator and the beautiful creation I got to learn and marvel at

Disclaimer

I hereby declare that the work undertaken in this thesis has been conducted by me alone, except where indicated in the text. I conducted this work between May 2021 and November 2024, during which period I was a PhD student at the Australian National University. This thesis, in whole or any part of it, has not been submitted to this or any other university for a degree.

This thesis has been compiled as a Thesis by Compilation in accordance with relevant ANU policies. The four main chapters in this thesis (Chapters 2, 3, 4, and 5) have been published in peer-reviewed journals. I have made significant contribution to each of these journal articles and have written the text of the papers myself, except where indicated otherwise.

Sajay

Sajay Sunny Mathew

17 February 2025

Acknowledgements

My path to pursuing a PhD and completing the work outlined in this thesis is a testament to the love, care, and encouragement of many people. I would like to take this opportunity to convey my heartfelt thanks to these wonderful people. First of all, I would like to acknowledge the traditional custodians of the land where I got to carry out my PhD research - the Ngunnawal and Ngambri people.

This thesis would not have been possible without the exceptional guidance of my supervisors - Christoph Federrath as the chair of my supervisory panel and Amit Seta as my primary supervisor. From being the one to introduce me into astrophysics to the funding of my PhD, Christoph has provided continuous support to my growth in research. I am grateful to Christoph for training me to work efficiently, structure ideas effectively, and present science with clarity. I am constantly amazed by Christoph's attention to detail. I greatly appreciate Christoph's vital role in ensuring the quality of my publications, including the minor (but important) aspects such as presenting well the text in figures - especially considering my special talent for always picking super tiny font sizes for the figure and caption. It is hard to summarise all the roles Amit has played in my PhD journey. In addition to being an excellent mentor, Amit is a great advisor, motivator, and equally important a good friend. I deeply appreciate Amit's encouragement to see the broader perspective, the unwavering assistance in adapting my work to appeal to a wider audience, and the constructive feedback on my publications. I am indebted to Amit for always finding time for my impromptu meeting requests, whether it's troubleshooting a code or framing an important email. I thank Amit and Christoph for providing me with the freedom to pursue different ideas in my PhD and for all of their invaluable advice on future prospects.

I would like to thank my collaborators, Siyao Xu and Yue Hu, for their significant contributions to this thesis. I am grateful to them for helping me in expanding the scope of my research. I would also like to acknowledge the productive interactions with Andrew Hopkins, Patrick Hennebelle, Noé Brucy, Blakesley Burkhart, Mark Krumholz, and Pavel Kroupa. I wish to thank the Thesis Oversight Committee at RSAA for regularly checking in on us PhD students and making sure that we complete our milestones on time. I am thankful to the anonymous referees of my papers for their constructive criticism, which helped in improving the paper's clarity and impact. I also owe gratitude to my teachers from school to undergrad and postgrad, for providing the solid foundation for my research and personal growth.

I am grateful to Astrid Bardelang, Sam Slater, Mat Malzacher, Sindu Nair, Cate

Pickering, Michelle Cicolini, and all the admin staff at Mt Stromlo Observatory for the assistance they provided, in matters ranging from enrolling to ANU, relocating, scholarship approval, travel logistics, and handling the behind-the-scenes tasks, ensuring an easy and smooth experience. I am grateful to the IT Team for ensuring that all the necessary resources are available to us. I am thankful to the maintenance staff for developing an optimal and pleasant workspace.

Huge thanks to Samuel Lai, Simon Ho, Radhika Achikanath Chirakkara, Hayden Park, Hilay Shah, Neelesh Amrutha, Marcie Mun, Heran Xiong, and other fellow PhD students for making Mt Stromlo an exciting place to work at. Going down the mountain together to get a Pide, weekend meetups for movies or dinner, playing badminton, computer games or tennis, and long lunch break chats which at times extended into the evening coffee break, were all fun experiences. I would also like to thank the people of D.012 for being excellent office mates. I would like to express my gratitude to Amit and Nirali, and also Christoph and Daniela for hosting delightful get-togethers. Thanks to the Warden, Council, and fellow residents at the All Saints College for making it a pleasant and enjoyable place to live at - it was a pleasure to share and listen to each other's stories about what's going on in our lives during our BBQ Sundays and other social events. Special thanks to the choir at All Saints Church, for welcoming me into the group and bringing the warmth of music into my PhD journey. I am always in awe of their mastery, which inspires me to work more on keeping up with their exceptional talent in singing. I would like to thank John Kuruvilla, Molly John, and Edwin Thanavelil for being a family-like support system in Canberra. Their help in settling in Canberra was indispensable.

I cannot thank my parents enough for their love, care, and sacrifice, molding me into the person I am. They have always been my biggest supporters. I am forever moved by their humbleness and drive to help others. I am deeply grateful to my brother and sister-in-law, Sachu and Nannu, for their concern for my well-being, and for constantly checking in to show how much they care. Thanks to my nephew, little baby Ian, for bringing a lot of joy with his beautiful smiles - looking forward to seeing him in person when I get home. I would also like to thank my grandparents, who are among the most influential people in my life, for nurturing important values in me. Endless thanks to my girlfriend, Jaclyn Holland, for standing by me and listening to both my highs and lows. I greatly cherish exploring Canberra with you, the dance classes together, and all our adventures that brought so much joy to my life. Meeting you was the most precious part of doing a PhD in Canberra. Finally, I would like to thank all the amazing people I met in Canberra, who were very welcoming, friendly, and kind.

Abstract

Understanding the origin of stellar masses is one of the most compelling and important challenges in modern astrophysics. This is because the evolution and lifetime of a star, which are influenced by its mass, shape the structure and evolution of the interstellar medium of galaxies. Understanding the origin of the mass of a star is directly linked to understanding the mass distribution of stars since stars generally form in clusters. The stellar mass distribution is referred to as the initial mass function (IMF). The IMF is often thought to be relatively universal, and explaining the IMF characteristics like the existence of a peak mass and the power-law nature at the high mass end lies at the forefront of star formation research. In this thesis, I perform a comprehensive parameter study of the IMF using state-of-the-art star cluster formation simulations that incorporate physically important mechanisms such as gravity, turbulence, magnetic fields, jets, and radiative heating.

I show that the inclusion of outflow feedback in numerical simulations is essential to accurately model star formation and the IMF, as its effects significantly influence other key physical mechanisms such as turbulence and stellar radiative heating. I find that protostellar outflows shift the IMF to lower masses by roughly a factor of 2. Furthermore, I find that variations in the mode of turbulence driving play a significant role in shaping the form of the IMF, where a purely compressive (curl-free) turbulence driving produces a higher fraction of low-mass stars ($\lesssim 1\,\mathrm{M}_\odot$) as compared to a purely solenoidal (divergence-free) driving. Changing the turbulence driving mode in simulations from purely solenoidal to purely compressive decreases the median stellar mass by a factor of ~ 1.5. My study also reveals that the IMF exhibits a weak dependence on the cloud virial parameter, the ratio of twice the kinetic energy to gravitational energy, which is another crucial cloud property. My study suggests that the dominance of solenoidal turbulence driving modes and relatively high cloud virial parameter values detected in the vicinity of the Galactic centre can partly explain the top-heavy nature of the IMFs in the associated clouds, i.e., the presence of a higher fraction of stars with super-solar masses as compared to standard IMF models. I propose that the scatter in the IMF observed in different regions of the Milky Way is due to the difference in the environmental conditions.

I also use the results from my simulation suite to study the binary properties of stars, which are closely tied to understanding the IMF. I verify that my simulations reproduce the observed trends like the increase in the fraction of multiple systems with mass and the dependence of orbital eccentricity on binary separation. I find that the turbulence driving mode has a considerable influence on the binary eccentricity, with simulations having compressively driven turbulence producing a higher fraction of high-eccentricity binaries as compared to simulations with solenoidal or a mixture of driving modes. This implies that the universal eccentricity distribution often used as an initial condition in N-body simulations of stellar cluster dynamics needs revision and further shows the broad impact of my work.

I conclude that the IMF and the binary properties are controlled by the combined effect of gravity, magnetic fields, turbulence and protostellar feedback. The inferences from my studies can be used to calibrate sub-grid models used in large-scale simulations of galaxy formation and evolution, which often assume a universal IMF independent of the local physical conditions. This would enable more accurate modelling of energy output from star clusters, which are crucial drivers of galaxy evolution. My study advocates for future observational surveys to quantify the associated cloud conditions, such as the turbulence properties, together with measuring the IMF of star clusters. Creating distinct ensembles of observational IMFs for various cloud conditions would enable isolating the individual effects of different physical mechanisms and facilitate one-to-one comparisons with my theoretical work. Meticulous comparisons between observations and theory are quintessential to deepening our understanding of the IMF and star formation.

Contents

List of Figures

List of Tables

Chapter 1

Introduction

The formation of stars is one of the fundamental processes that shapes the nature of the cosmos. The birth of the first stars transformed the thermal and chemical composition of the Early Universe. The feedback from these stars triggered a sequence of new star formation events, building up star clusters and galaxies, and yielding the fabric of the Universe. Stars are a prominent source of radiation and are responsible for the formation of many of the heavy elements in the Universe. The present-day interstellar medium (ISM) is a consequence of the continuous recycling of gas and dust, driven by star and galaxy formation across cosmic time. The formation of planets, including our Earth, is also an outcome of star formation, initiated by the condensation of matter collected around stars when they form. Thus, star formation is an important element in all aspects of astrophysics and understanding star formation is a critical prerequisite for fully comprehending the workings of the Universe.

Stars form in the cold, dense and dusty molecular clouds (MCs) of the ISM, consisting primarily of molecular hydrogen (H_2) (Zuckerman & Evans 1974). Despite its abundance, H_2 cannot be directly used to trace MCs because of its weak emission signature. Much of the observations of MCs come from carbon monoxide (CO) emissions, dust emission at sub-millimeter wavelengths and absorption at near-infrared wavelengths (Krumholz 2011). Numerical and observational studies from the past several decades suggest that MCs have filamentary and clumpy morphology (Schneider & Elmegreen 1979; Elmegreen 1993a; Blitz 1993). The densest regions within these structures, called dense cores, are the direct progenitors of stars (Myers 1983; Klessen et al. 2005). The recent *Herschel* images revealed many filamentary regions of size $\sim 0.1\,\mathrm{pc}$ in nearby cloud complexes, harbouring overdense regions analogous to cores (e.g, André et al. 2010; Arzoumanian et al. 2011). The left panel of Fig. 1.1 shows an image of the B211/B213 filament in the Taurus molecular cloud and the right panel reveals three dense cores within the filament.

We have made tremendous progress in the past few decades towards star formation

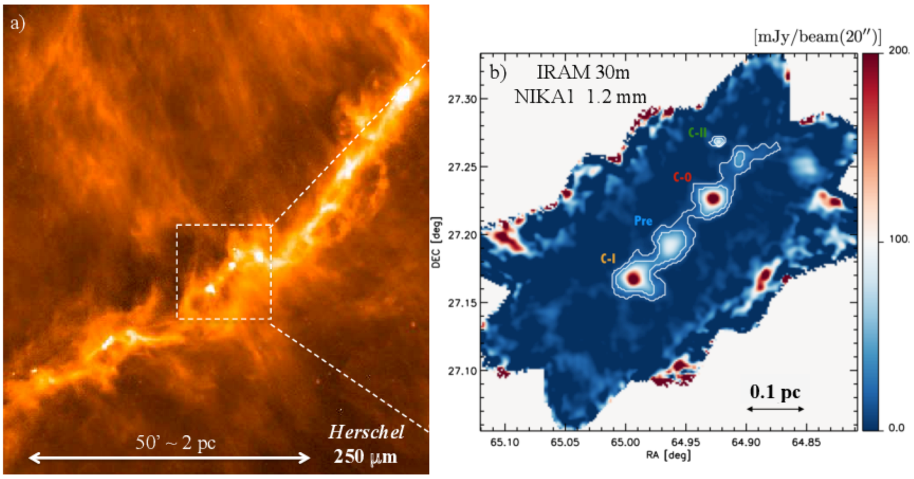

Figure 1.1: Left panel: Herschel/SPIRE 250 µm image of the Taurus B211/B213 filament in the Taurus molecular cloud (Palmeirim et al. 2013; Marsh et al. 2016). Right panel: IRAM/NIKA1 1.2 mm dust continuum map of a small area within the Herschel field on the left, indicating presence of dense cores (Bracco et al. 2017). *Adapted from Lee et al. (2020).*

research because of the advanced observations, rigorous theoretical analysis and ever-expanding numerical capabilities. But as a result of the associated complexity in the process, star formation is yet to be fully explained. Some of the outstanding problems are 1) Why is star formation very inefficient?, 2) What is the origin of the mass of a star?, and 3) What determines binary formation and the observed multiplicity properties? My thesis will primarily focus on the origin of stellar mass, in particular, the origin of the stellar mass distribution or the initial mass function (IMF), which is directly related to the origin of a star's mass, since stars typically form in clusters (Lada & Lada 2003). Comprehending the IMF, star formation efficiency (SFE), and the binary properties (three outstanding questions) are not mutually exclusive. The efficiency or the rate of star formation is governed by physical mechanisms like gravity, magnetic fields, turbulence, and protostellar feedback. The interplay between these mechanisms also significantly affects the fragmentation within the cloud, affecting both the IMF and binary statistics. By studying the role played by each of these mechanisms, my work will not only contribute to a better understanding of the IMF, but will also shed more light on the star formation rate (SFR) and binary properties.

In this Chapter, I outline our current understanding of the IMF from observations and theoretical works, and the potential role of different physical mechanisms in shaping the IMF. §1.1 discusses the IMF, introducing some of the empirical models of the IMF. §1.2 reviews the observational evidence of the IMF in detail. §1.3 addresses some of the important physical mechanisms involved in the star formation process that can affect the fragmentation within the cloud. §1.4 reflects on some of the theoretical models of the IMF. Finally, in §1.5, I summarise the motivation for my work and briefly outline the main chapters in this thesis.

1.1 Initial mass function (IMF)

The mass distribution of stars in a newly formed cluster is termed the initial mass function or the IMF. Observational surveys in the Galactic field and also in different nearby active star-forming regions suggest that the IMF is *relatively* universal (Bastian et al. 2010; Hopkins 2018). The IMFs obtained in the surveys exhibit similar features, with detected variations smaller than expected given the large differences in cloud properties across environments, and hence considered *relatively* universal (see also §1.2.3). The IMF is usually treated as a probability distribution function (PDF) of the masses of stars at their birth. A universal IMF has far-reaching implications since the initial mass of a star governs its further evolution. The IMF is used for measuring the chemical yield in stellar populations, quantifying the brightness and colour of galaxies, and determining the star formation history and total baryonic content (Kennicutt 1998). The IMF is also used as a subgrid or approximation model in cosmological simulations to quantify the influence of stellar populations on cosmological scales. Due to its extensive applications, the IMF is a prominent research topic. However, the extent of the universality is a matter of continuing debate (Dib 2014; Hennebelle & Grudić 2024).

Extracting the IMF directly is difficult, as measuring the stellar masses directly is not feasible. One of the most common techniques of determining the IMF is by measuring the luminosities or more specifically the luminosity function (LF), and converting the LF into the stellar mass function using mass-to-light ratio calculations. An indirect method of gauging the IMF is by inferring the ratio of Oxygen (formed primarily in core-collapse Type II supernovae) to Iron (formed in Type II and Type Ia supernovae) content (Thielemann et al. 1993; Wyse 1998). Since Type II supernovae typically result from high mass stars ($M \gtrsim 8\,\mathrm{M}_\odot$), a 'plateau' in the ratio of [O/Fe] implies that the chemical enrichment is mainly by Type II supernovae and points to a relatively high fraction of high-mass stars. On the other hand, a decline in the [O/Fe] ratio suggests a decrease in the fraction of high-mass to intermediate-mass stars. A detailed description of extracting the IMF based on chemical abundances can be found in Wyse (1998) and Hopkins (2018).

1.1.1 Challenges in IMF measurements

Measuring the stellar mass distribution in a young star-forming region or in the Galactic field involves multiple stages. The mass function we obtain by converting the LF measured in observational surveys using the mass-luminosity relation corresponds to the present-day mass function (PDMF). To convert the PDMF into the IMF, stellar evolution and star formation history models are used (Hopkins & Beacom 2006; Offner et al. 2014), requiring details of metallicities and ages (Elmegreen & Scalo 2006; Hopkins 2018). Dynamical models are also employed to account for the evaporation of low-mass stars and the mass segregation that may arise due to the cluster evolution (see reviews by Meyer et al. 2000; Lee et al. 2020). Further, stars generally form with at least one gravitationally bound pair and it is observationally challenging to resolve them as individual stars, especially when the binary separations are short. Therefore, the mass dependence of the multiplicity fraction and the mass ratio distribution of binaries should also be taken into account while determining the IMF (Bastian et al. 2010). All of these intermediate steps contribute to the overall uncertainty in constraining the IMF characteristics. Additionally, in the Solar Neighbourhood, where it is easiest to observationally measure the low-mass IMF, the fraction of high-mass stars is low. Furthermore, given the fact that high-mass stars are short-lived, most of the massive stars in old populations would have completed their main sequence phase (Elmegreen 2009a). Thus, to have a statistically significant sample of the high-mass end of the IMF, it is necessary to observe over a large volume and survey young massive clusters, where in contrast, identifying low-mass stars becomes difficult because of their low luminosities (Elmegreen 2009a). Thus, it is extremely challenging to measure the IMF over the full mass range. Meanwhile, in the case of IMF measurement based on chemical abundances, the technique is limited by the accuracy in the theoretical prediction of elemental yields for different supernova progenitor masses (Wyse & Gilmore 1992; Wyse 1998). Nevertheless, applying innovative approaches that surmount existing limitations, there have been many observational surveys over the past few decades assessing and constraining the IMF form.

1.1.2 Observational models of the IMF

Salpeter (1955) was the first to suggest a universality in the mass distribution of stellar populations. Salpeter (1955) expressed the number of stars $N(M)$ as a power-

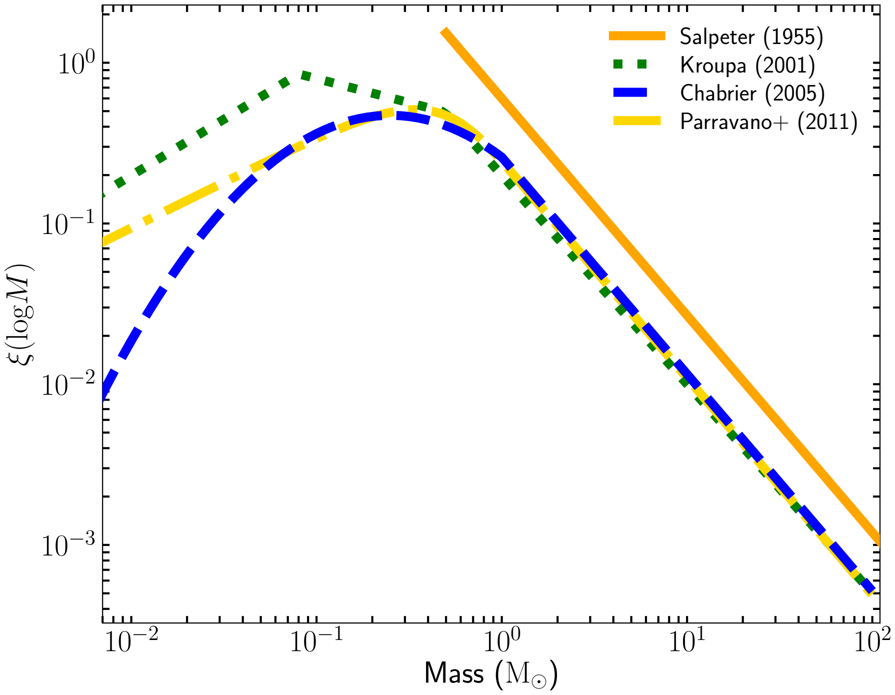

Figure 1.2: The IMF models by Kroupa (2001) (Eq. 1.1, dotted curve), Chabrier (2005) (Eq. 1.2, dashed curve), and Parravano et al. (2011) (Eq. 1.3, dash-dotted curve). The IMFs are normalised such that the respective area under the curve is unity. The solid line represents the IMF slope measured by Salpeter (1955).

law distribution of stellar mass $M(\mathrm{M}_\odot)$ represented by $dN \propto M^{-1.35}\, d\log M$. Later, Miller & Scalo (1979) and Scalo (1986) identified that the IMF flattens at sub-solar masses and proposed that the low-mass end can be described by a log-normal function with the possibility of a peak at around $0.3\,\mathrm{M}_\odot$. Kroupa (2001) proposes a series of power-laws to represent the IMF given by $\xi(M) \propto M^{-\alpha}$, where

$$\alpha = \begin{cases} 0.3 & \text{for } 0.01\,\mathrm{M}_\odot \leq M < 0.08\,\mathrm{M}_\odot, \\ 1.3 & \text{for } 0.08\,\mathrm{M}_\odot \leq M < 0.5\,\mathrm{M}_\odot, \\ 2.3 & \text{for } M \geq 0.5\,\mathrm{M}_\odot, \end{cases} \tag{1.1}$$

and $\xi(M)\,dM$ is the number of stars in the mass interval M to $M + dM$.

The recent study by Chabrier (2005) suggests a log-normal form for sub-solar masses, i.e., for masses less than $1\,\mathrm{M}_\odot$, and a power-law distribution similar to the one in Salpeter (1955) for the higher stellar masses. Their functional form is given by

$$\xi(\log M) \propto \begin{cases} \exp\left(-\frac{(\log M/M_0)^2}{2\sigma^2}\right) & \text{for } M < 1\,\mathrm{M}_\odot, \\ M^{-1.35\pm0.3} & \text{for } M \geq 1\,\mathrm{M}_\odot, \end{cases} \tag{1.2}$$

where the peak mass $M_0 = 0.2\,\mathrm{M}_\odot$ and the width of the log-normal function $\sigma = 0.55$.

There are also more parameterised models of the IMF. A commonly used representation is the Smoothed Two Power-Law model by Parravano et al. (2011) (see also Paresce & De Marchi 2000), defined as

$$\xi_{\mathrm{STPL}}(\log M) \propto M^{-\Gamma}\left(1 - \exp\left[-(M/M_0)^{\eta+\Gamma}\right]\right), \tag{1.3}$$

where $\Gamma = \alpha - 1$, M_0, and η are the high-mass slope, peak mass, and low-mass slope, respectively. The values of M_0 and η, are estimated utilising the observational constraints such as the fraction of M-dwarfs ($0.1\,\mathrm{M}_\odot \leq M < 0.6\,\mathrm{M}_\odot$) to K-dwarfs ($0.6\,\mathrm{M}_\odot \leq M < 0.8\,\mathrm{M}_\odot$), and ratio of sub-solar main sequence stars ($0.08\,\mathrm{M}_\odot \leq M < 1\,\mathrm{M}_\odot$) to brown dwarfs ($0.03\,\mathrm{M}_\odot \leq M < 0.08\,\mathrm{M}_\odot$) (Andersen et al. 2008; Parravano et al. 2011; Kroupa et al. 2013).

Fig. 1.2 depicts the IMF models derived from the studies mentioned above. The models appear to be in agreement in terms of the characteristic or peak mass of $0.2 - 0.3\,\mathrm{M}_\odot$ (Chabrier 2003; Elmegreen et al. 2008; Offner et al. 2014) and a high-mass slope of $\Gamma \sim 1.3$ (Bastian et al. 2010).

Next, I will discuss some of the observational works that measured the IMF in different regions within the Milky Way and beyond. This includes the studies that inspired the above empirical models and also the subsequent works that probed these models. It is important to note that this discussion provides an overview, but is not exhaustive. For a comprehensive perspective, please refer to the recent reviews and the references therein (Bastian et al. 2010; Offner et al. 2014; Hopkins 2018; Lee et al. 2020).

1.2 Observational measurements of the IMF

1.2.1 Galactic field

Low-mass regime ($< 1\,\mathrm{M}_\odot$)

Following the foundational work by Salpeter (1955), there have been numerous surveys examining the stellar mass distribution in the Galactic field (see the review by Bastian et al. 2010). Most of the early works were aimed at stellar populations in the Solar Neighbourhood, as they were reliable for accurate distance calculations, which are integral for precisely determining the stellar luminosity and subsequently the mass using the mass-luminosity relation. These studies were restricted to the samples within a distance of 5 – 8 pc from the Sun to obtain a complete sample, i.e., to detect even the fainter stars. Since the Solar Neighbourhood lacks a significant population of high-mass stars, the Galactic field measurements are mainly associated with the low-mass end of the IMF. Kroupa et al. (1993) illustrated that the stars within ≈ 5.2 pc of the Sun compiled using trigonometric-parallax based distance measurements and the sample of stars surveyed to distances of up to 100 pc using photographic surveys can be shown to be governed by the same underlying mass function if the age, metallicity distribution, binary properties, and the Galactic structure are taken into account. The study by Kroupa et al. (1993) expanded the scope of an invariant IMF out to larger distances from the Sun.

Building on their previous spectroscopic observations of M dwarfs (Reid et al. 1995; Hawley et al. 1996, 1997) and incorporating the *Hipparcos* Catalogue with astrometry information, Reid et al. (2002) compiled a volume-complete sample of the Solar Neighbourhood M dwarfs. They find that their derived IMF in the mass range $0.1\,\mathrm{M}_\odot < M < 0.7\,\mathrm{M}_\odot$ can be represented by a power-law with $\Gamma = 0.1 - 0.3$. Chabrier (2001, 2003) used the mass-luminosity relations from Baraffe et al. (1998) and Delfosse et al. (2000) to derive an IMF for the Galactic disc from the available LFs at that time. They find that the Galactic disc mass function for low-mass stars is best fitted by a log-normal function (see also Covey et al. 2008). Employing the Sloan Digital Sky Survey photometric survey, Bochanski et al. (2010) studied a large sample of low-mass stars in the mass range $0.1\,\mathrm{M}_\odot < M < 0.8\,\mathrm{M}_\odot$. Bochanski et al. (2010) show that their IMF matches with either a log-normal function having a peak mass of ~ 0.2 and $\sigma \sim 0.34$ or broken power-laws with $\Gamma \sim 0$ in the range $0.1\,\mathrm{M}_\odot < M < 0.32\,\mathrm{M}_\odot$ and $\Gamma \sim 1.7$ in the range $0.32\,\mathrm{M}_\odot < M < 0.8\,\mathrm{M}_\odot$. Most of the IMF studies focusing on the sub-solar regime ($0.075\,\mathrm{M}_\odot < M < 1\,\mathrm{M}_\odot$) are consistent with a peak mass around $0.2 - 0.5\,\mathrm{M}_\odot$, and therefore the sub-solar IMF is somewhat well constrained at least in the immediate Solar Neighbourhood (Bastian et al. 2010; Offner et al. 2014; Hopkins 2018).

The sub-stellar IMF ($M < 0.075\,\mathrm{M}_\odot$) on the other hand is insufficiently explored (Jeffries 2012). The studies that focus on the sub-stellar range generally suffer from a lack of statistical significance and limitations in observational techniques arising largely from the complexity associated with the age-dependence in the mass-luminosity relation of brown dwarfs (Pinfield et al. 2008; Allen et al. 2005). Chabrier (2002) generate a brown dwarf (BD) population of given mass, age and distance using Monte-Carlo simulations with different IMF forms (log-normal and power-laws with different slopes), considering the brown dwarf spatial distribution, formation rate, and binary fraction. They find that the extension of the log-normal IMF derived for the Galactic disc M dwarfs (Chabrier 2001) into the BD regime agrees well with the observational constraints on BDs such as the fraction of L dwarfs and T dwarfs within a fixed distance from the Sun (see also Reid et al. 1999). On the other hand, Kroupa et al. (2013) propose that the BDs and stars should be represented by separate mass functions to satisfy the known constraints on the BD binary properties.

High-mass regime ($> 1\,\mathrm{M}_\odot$)

The studies of the high-mass end of the IMF in the Galactic field is limited. Surveys of the high-mass field stars generally employ prescriptions for star formation history (Hopkins 2007) and star formation rate to account for the 'missing' high-mass stars and constrain the IMF shape (Offner et al. 2014). Through a detailed review of the different high-mass IMF measurements taken over kpc scales, Scalo (1986) conclude that the variation in the power-law slope Γ is less than ± 0.5. The majority of the studies find that the mass distribution of field high-mass stars can be fitted by a power-law (Rana & Basu 1992; Maciel & Rocha-Pinto 1998; Calamida et al. 2015). Nevertheless, the high-mass regime of the Galactic field IMF is slightly steeper than the Salpeter slope (Bastian et al. 2010; Offner et al. 2014; Hopkins 2018), which might be due to the overabundance of low-mass star clusters (Kroupa & Weidner 2003). The recent work by Mor et al. (2017) obtained a power-law IMF with $\Gamma \sim 2$ for super-solar stars in the Galactic thin disc population up to 2 kpc from the Sun. They again attribute the reason for the steeper value of Γ to the lower fraction of massive clusters compared to the low-mass clusters. Most of the IMF measurements in the high-mass end are derived from surveys in young clusters and extragalactic regions, which are discussed next.

1.2.2 Young clusters and extragalactic regions

Recently, young individual star clusters are being explored for probing the universality (or the absence thereof) of the IMF. While young clusters are difficult to detect since they are deeply embedded within the cloud of gas and dust, such clusters are still the best candidates for IMF measurements because the stars here are characterised by similar ages, distance, and are born in similar environments. Therefore, the modelling required to take into account the evolutionary effects is minimal. The nearby Orion Nebula Cluster (ONC) has been a focus of extensive IMF measurements over the past decades (Hillenbrand & Carpenter 2000; Luhman et al. 2000; Muench et al. 2002; Weights et al. 2009; Da Rio et al. 2012). The IMFs derived for ONC by different studies seem to be consistent with each other in terms of exhibiting a power-law nature at high-masses with a Salpeter-like slope and a flattening at sub-solar masses with a broad peak at around $0.2 - 0.3\,\mathrm{M}_{\odot}$ (Bastian et al. 2010). The Taurus molecular cloud is another active region of star formation that is in close proximity. It was first considered that Taurus had a deficit of BDs (Briceño et al. 2002; Luhman 2004). Later, the deficit was treated as marginal based on discoveries of new BDs (Slesnick et al. 2004; Guieu et al. 2006) and consideration of the high binary fraction in the Taurus cloud (Kroupa et al. 2013). However, there is evidence for a variation in the Taurus IMF relative to other star-forming regions, particularly the emergence of a peak at around twice the value of the typical peak of $\sim 0.3\,\mathrm{M}_{\odot}$ (Luhman et al. 2009; Bastian et al. 2010). Determination of the high-mass IMF in young massive clusters like the NGC 2264 and NGC 6231 yield $\Gamma = 1.7 \pm 0.1$ and $\Gamma = 1.1 \pm 0.1$, respectively. Hosek et al. (2019) find that the shape of the mass distribution of the Arches cluster, which is a young massive cluster in the central molecular zone, corresponds to a power-law (in the range $M > 1\,\mathrm{M}_{\odot}$) with a slope significantly shallower than the Salpeter slope (top-heavy IMF) or a power-law with a Salpeter-like slope but with a turnover mass at $\sim 5\,\mathrm{M}_{\odot}$ (bottom-light IMF). Other IMF studies focusing on the Galactic centre (Figer et al. 1999; Kim et al. 2006; Lu et al. 2013) also point to a top-heavy/bottom-light IMF, i.e., a higher fraction of high-mass stars as compared to the typical IMF models.

Brandl et al. (1996) find that the slope of the IMF for stars $> 5\,\mathrm{M}_{\odot}$ in R136, which is the inner region of the 30 Doradus in the Large Magellanic Cloud (LMC) is ~ 1.6 on average, with the slope becoming steeper at larger distances from the center, hinting at mass segregation. Later, Andersen et al. (2009) found that the low-mass end of the IMF in R136 agrees with a Chabrier (2005) IMF. Based on spectroscopic observations, Schneider et al. (2018a) derive $\Gamma = 0.90^{+0.37}_{-0.26}$ for the massive stars ($> 15\,\mathrm{M}_{\odot}$) in the 30 Doradus. The IMF determinations in the Small Magellanic Cloud (SMC) are found to be consistent with a Chabrier (2005) or Kroupa (2001) model within the uncertainty limits (e.g., Massey et al. 1989; Sirianni et al. 2002; Sabbi et al. 2008). Veltchev et al. (2004) investigates the IMF in 50 OB associations within M31 (Andromeda Galaxy) and obtain $\Gamma = 1.59 \pm 0.09$. Weisz et al. (2015) find $\Gamma = 1.45^{+0.03}_{-0.06}$ for stars $\geq 2\,\mathrm{M}_{\odot}$ over a sample of 85 young clusters in M31. Smith & Gallagher (2001) find that the luminosity-to-mass ratio they obtained for the super star cluster ‘F’ in the starburst galaxy M82 is higher than that predicted by a simple stellar population model with a standard Kroupa (2001) IMF by a factor of 5, implying a top-heavy IMF (see also McCrady et al. 2005).

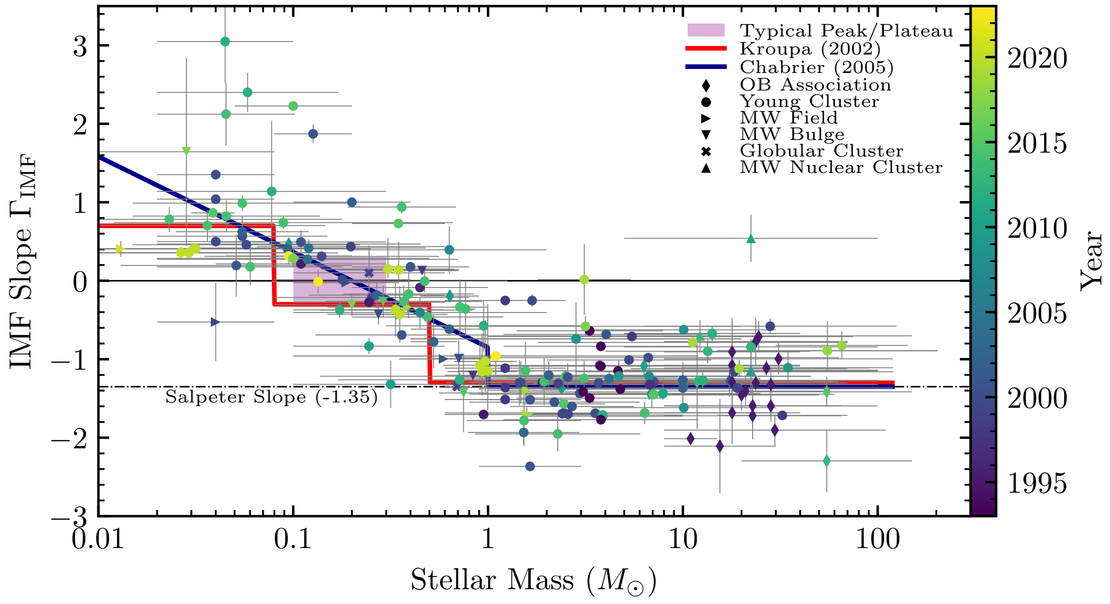

Figure 1.3: IMF slope as a function of the stellar mass from different studies. The horizontal bars represent the mass range in which the slope is measured and vertical bars correspond to the $1-\sigma$ uncertainty. The red line represents the slope expected for a Kroupa (2001, 2002) IMF and the blue line corresponds to that of a Chabrier (2005) IMF. *Adapted from Hennebelle & Grudić (2024).*

1.2.3 Extent of universality of the IMF

The IMF measurements by different observations for the Galactic field population moderately agree with each other in terms of a Salpeter-like slope and flattening at sub-solar masses, although the power-law slope on average is slightly steeper than the Salpeter slope (Bastian et al. 2010; Offner et al. 2014). However, the field population has undergone significant dynamical evolution and represents the amalgamation of stars from different clusters formed at different points in time (Scalo 1986). The IMF for an individual cluster need not be the same as the mass function measured across large volumes or a galaxy-wide IMF (Dib et al. 2017; Kroupa et al. 2024). It is clear from §1.2 that IMFs different from the standard IMF models have been indicated in numerous studies. However, the results are, at times, affected by observational biases and systematic errors or measurements of the same region by other studies produce contrasting results, diminishing the ability to reach definitive conclusions. At present, the Taurus molecular cloud, Galactic centre, and starburst regions are some of the most prominent candidates for non-typical IMFs.

With increasing capabilities of observations in obtaining complete samples, improvements in stellar evolution models, recent IMF measurements are able to significantly reduce the observational biases, systematic errors, and therefore lower uncertainties. The recent review by Hennebelle & Grudić (2024) presents a comprehensive data compilation of the IMF measurements from different surveys (see Fig. 1.3). It is evident from Fig. 1.3 that the values of the slope suggested by most observations in the high-mass regime ($> 1\,\mathrm{M}_\odot$) are relatively consistent with a Salpeter slope of $\Gamma = 1.35$. In addition, $\Gamma = 0$ (peak mass) emerges at $\sim 0.3\,\mathrm{M}_\odot$, in agreement with the empirical models (Kroupa 2001; Chabrier 2005; Parravano et al. 2011). However, the scatter in the data points in Fig. 1.3 is non-negligible in the power-law part, around the peak, and in the sub-stellar regime. In recent years, there has also been compelling evidence for the environment-dependence of the IMF (Dib 2023; Grudić et al. 2023; Kroupa et al. 2024). Thus, while assuming a universal IMF makes interpreting observables and calculating important astrophysical parameters simpler, the extent of validity of the universality approximation needs scrutiny.

There has been tremendous progress in constraining the origin of the IMF from analytical and numerical studies. A key challenge in obtaining a complete picture of the IMF lies in the complexity associated with the physical mechanisms involved in the star cluster formation process, which is discussed next.

1.3 Physical mechanisms in star formation

Star formation is a multi-scale and highly chaotic process. It involves different physical mechanisms like gravity, turbulence, magnetic fields, radiation and outflow feedback. Each of these mechanisms plays a fundamental role in the star formation process and in setting the mass of a star. This section summarises the impact of these mechanisms and introduces the important associated parameters. I note that this section will not be addressing the effect of cosmic rays and non-ideal magnetohydrodynamics (MHD) such as the ion-neutral drift and ambipolar diffusion, which are highly interesting and remain largely unexplored in relation to the IMF. I encourage the reader to see recent reviews and the references therein on these topics (e.g., Elmegreen & Scalo 2004; Lequeux 2005; Draine 2011; Hennebelle & Inutsuka 2019).

1.3.1 Turbulence

Turbulence is prevalent in the ISM and MCs are supersonically turbulent (Elmegreen & Scalo 2004). The lifetime of MCs is comparable to the crossing time of the turbulent gas within clouds (Hennebelle & Chabrier 2013; Chabrier & Dumond 2024). Recent studies advocate turbulence as a primary mechanism responsible for the low SFR observed in MCs (Krumholz & McKee 2005; Evans et al. 2009; Murray 2011; Federrath & Klessen 2012; Federrath 2015; Lee et al. 2016; Vutisalchavakul et al. 2016; Federrath et al. 2021). Numerical studies find that supersonic turbulence results in an approximately log-normal PDF of gas density (Vazquez-Semadeni 1994; Padoan et al. 1997a; Kritsuk et al. 2007; Federrath et al. 2008; Federrath 2013a; Hopkins 2013b; Federrath & Banerjee 2015; Seta & Federrath 2022). Further, the arrangement of supersonic turbulent energy on different scales follows a power-law given by $E(k) \propto k^{-2}$, where $E(k)$ is the velocity power spectrum and k is the wave number (Frisch 1995). The universality of the velocity power spectrum and the log-normal nature of the gas density PDF could provide insights into why different star-forming regions produce similar IMF forms (Nam et al. 2021; Hennebelle & Grudić 2024).

Turbulence plays a dual role in the star formation process (McKee & Ostriker 2007). On large scales, the kinetic energy associated with supersonic turbulent flows supports the clouds against a monolithic collapse, while on the small scales, it promotes star formation by generating turbulent shocks or local compressions, which can later become gravitationally unstable (Padoan et al. 2001; Hennebelle & Chabrier 2008). The cloud virial parameter, α_{vir}, which is the ratio of twice the turbulent kinetic energy to the gravitational energy, provides a measure of the turbulent support of the cloud. The sonic Mach number, $\mathcal{M}$, which is the ratio of the gas velocity dispersion to the sound speed, gives a measure of the strength of the shocks. Lowering α_{vir} or raising $\mathcal{M}$ enhances the fragmentation of the cloud and allows more low-mass stars to form (Padoan & Nordlund 2002; Hennebelle & Chabrier 2008; Hopkins 2012; Bertelli Motta et al. 2016). The type of turbulence in the ISM can be characterised by a mixture of compressive and solenoidal modes of driving (Padoan et al. 1997b; Brunt 2010; Price et al. 2011; Kainulainen et al. 2013; Ginsburg et al. 2013; Federrath et al. 2016; Menon et al. 2021; Sharda et al. 2022; Gerrard et al. 2023, 2024). Dynamical mechanisms (such as galactic shear and magneto-rotational instability) generate solenoidal models of turbulence driving while accretion, supernova explosions, and other stellar feedback mechanisms drive compressive modes of turbulence (Federrath et al. 2017a). The SFR in simulations that implement a purely compressive (curl-free) driving is an order of magnitude higher than that with a purely solenoidal (divergence-free) driving (Federrath & Klessen 2012, 2013; Padoan et al. 2014; Krumholz & Federrath 2019). While the impact of the turbulence driving mode on the SFR is well-studied, its effect on the IMF is not fully understood. Ultimately, the overall influence of turbulence on the star formation process depends on the specific combination of the cloud properties such as the sonic Mach number $\mathcal{M}$, cloud virial parameter α_{vir}, and the turbulence driving parameter b (Federrath

& Klessen 2012; Haugbølle et al. 2018a).

1.3.2 Magnetic fields

The ISM is strongly magnetised. The origin of strong magnetic fields is generally attributed to the amplification of seed fields by turbulence in the early Universe via a dynamo mechanism (Subramanian 1998; Brandenburg & Subramanian 2005; Sur et al. 2010; Schober et al. 2012, 2013; Federrath 2016; Seta & Federrath 2020; Achikanath Chirakkara et al. 2021). This highlights the inter-relationship between the turbulence and magnetic fields. The properties of magnetic fields are different in the cold phase of the ISM (relevant to the cloud scales) as compared to the warm phase (Mac Low et al. 1998; Krumholz & Federrath 2019; Seta & Federrath 2022). Magnetic fields have a considerable impact on the early stages of cloud evolution. The important parameters associated with magnetic fields are the mass-to-flux ratio μ_{B} (ratio of cloud mass to magnetic critical mass), Alfvén Mach number $\mathcal{M}_{\mathrm{A}}$ (ratio of the turbulent gas velocity dispersion to the Alfvén speed), and the plasma beta β (ratio of thermal-to-magnetic pressure) (Krumholz & Federrath 2019). Early works considered that MCs are subcritical ($\mu_{\mathrm{B}} \lesssim 1$), i.e., they can be supported against gravitational collapse by magnetic fields alone (Shu et al. 1987; Mouschovias 1995; Mouschovias & Ciolek 1999). Non-ideal MHD effects such as ambipolar diffusion were favoured to render the clouds supercritical ($\mu_{\mathrm{B}} \gtrsim 1$) (Mouschovias 1995; Tassis & Mouschovias 2004). However, the recent compilation of observational results, primarily based on Zeeman splitting measurements, suggest that MCs are inherently supercritical and the magnetic energy itself cannot avert the gravitational contraction of dense cores (McKee et al. 1993; Crutcher 2012; Krumholz & Federrath 2019). While they might not be the primary candidate for regulating star formation, numerical simulations find that magnetic fields lower the SFR by a factor of $2-3$ for trans-Alfvénic gas ($\mathcal{M}_{\mathrm{A}} \approx 1$) (Price & Bate 2009; Padoan & Nordlund 2011; Federrath & Klessen 2012; Federrath 2015; Krumholz & Federrath 2019).

The Alfvén Mach number $\mathcal{M}_{\mathrm{A}}$ governs how the magnetic field intensity B scales with the gas density ρ in star-forming regions and determines the nature of the collapse (Ostriker et al. 2001; Hennebelle et al. 2008; Burkhart et al. 2009; Crutcher et al. 2010; Beattie & Federrath 2020). The existing knowledge is that, when the flow is sub-Alfvénic ($\mathcal{M}_{\mathrm{A}} < 1$) in the collapsing regions, $B \propto \rho^{1/2}$ and the collapse is anisotropic with the magnetic field exhibiting an hour-glass structure (Mocz et al. 2017a; Tritsis et al. 2015; Hennebelle & Inutsuka 2019). When the flow is super-Alfvénic ($\mathcal{M}_{\mathrm{A}} > 1$), $B \propto \rho^{2/3}$ and the collapse is isotropic (Collins et al. 2012a; Mocz et al. 2017a). However, the B-to-ρ correlation is likely more complicated than these simple relationships, and more rigorous analysis is required to constrain the dependence. There have been a few studies on the effect of variations in β. Molina et al. (2012) find that the width of the log-normal gas density PDF is dependent on β for super-Alfvénic flows (see also Mocz & Burkhart 2018), although the extent of dependence is uncertain in sub-Alfvénic conditions (Krumholz & Federrath 2019).

The influence of magnetic fields on the scales of dense cores and accretion discs is widely studied (Wurster & Li 2018). Numerical studies find that magnetic fields suppress fragmentation on core-scales by providing additional magnetic-pressure support against the gravitational force (Price et al. 2008; Federrath 2015; Cunningham et al. 2018). Magnetic braking can partly explain the slow rotation rates of stars and they play a decisive part in transferring angular momentum from the discs, facilitating accretion onto the protostar (Gillis et al. 1974; Mouschovias & Paleologou 1979; Shu et al. 1987). They also decrease the occurrence of violent interactions between protostars and therefore reduce the number of low-mass stars by preventing the ejection of these objects (Price et al. 2008).

1.3.3 Stellar Feedback

Jets and Outflows

The highly energetic outflows from newly formed stars and the interaction of the outflowing gas with the parent cloud is an integral part of the cluster formation process (Shu et al. 1987; Richer et al. 2000; Woitas et al. 2002). The protostellar mechanical feedback entails two components—the fast and narrow gas stream called the jets and the broad-angled and low-speed molecular outflows. The outflow feedback is proposed to have emerged as a result of the pressure associated with the toroidal component of magnetic fields in accretion discs, although this theory has certain drawbacks and a consensus regarding the outflow mechanisms remains elusive (Shu et al. 1987; Ouyed & Pudritz 1997; Tomisaka 1998). However, the effect of the outflows in the star formation process is fairly well understood. The ejected matter from young stellar objects (YSOs) forms cavities by sweeping away the envelope of surrounding gas. They also drive turbulence within the cloud and modify the density contrasts, enhancing fragmentation (Li & Nakamura 2006; Nakamura & Li 2011; Federrath et al. 2014). The recent images of the Cosmic Cliffs in the Carina Nebula from the James Webb Space Telescope (JWST) reveal numerous jets and outflows at close proximities (see Fig. 1.4). The stars lose a significant fraction of their mass through the outflow feedback (Li et al. 2010; Krumholz et al. 2012b; Cunningham et al. 2018; Guszejnov et al. 2021; Rohde et al. 2021). The bipolar outflows

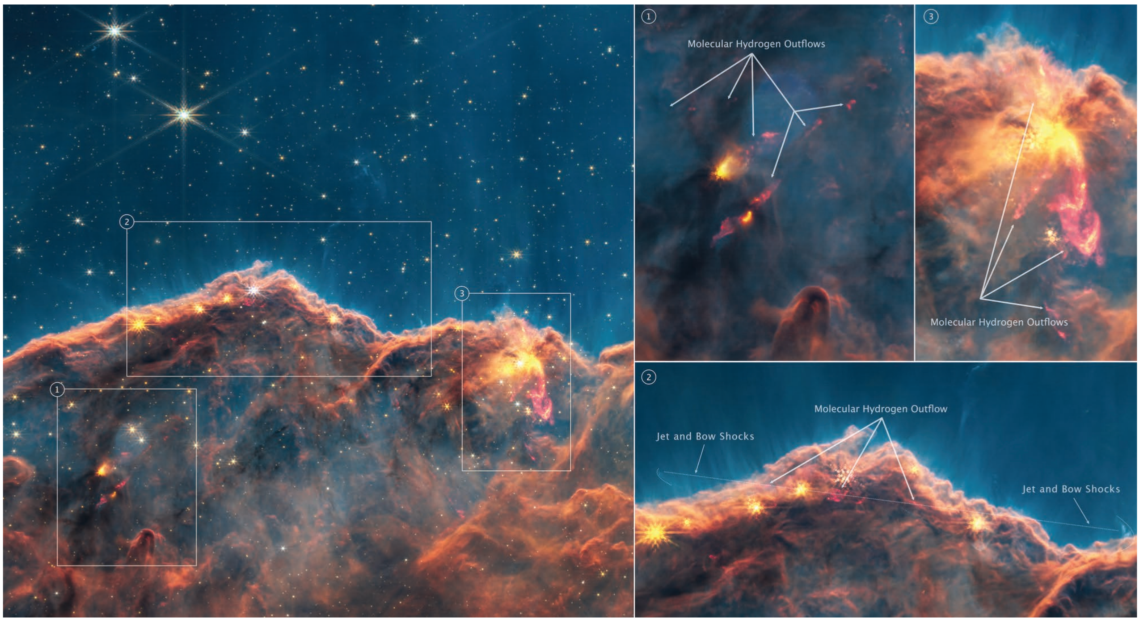

Figure 1.4: Jets and outflows captured in the Cosmic Cliffs (Carina Nebula) by the Near-Infrared Camera (NIRCam) of the James Webb Space Telescope (JWST). It is evident from the image that multiple jets/outflows are emerging within a small region, which can together perturb the gas distribution significantly and affect the formation of new stars. *Image credits: NASA, ESA, CSA, STScI.*

reduce the SFR and star formation efficiency (Krumholz et al. 2014; Padoan et al. 2014; Federrath 2015). Federrath et al. (2014) show that, in simulations including protostellar outflows, there is an increase in the number of stars and a reduction in the core-to-star accretion efficiency (Matzner & McKee 2000; Myers 2008; Federrath & Klessen 2012; Federrath et al. 2014; Offner & Arce 2014).

Radiative feedback

Stars in the young stages of formation have high luminosities, dominated by their accretion luminosity (Offner et al. 2009). The protostellar radiation field heats up the surrounding medium, raising the local temperature around the progenitor star. This radiative heating by stars suppresses the fragmentation of the immediate environment by providing additional pressure support, and therefore affects the number of stellar objects formed (Bate 2009b; Krumholz et al. 2011; Guszejnov et al. 2016; Federrath et al. 2017b; Mathew & Federrath 2020; Hennebelle et al. 2020b). In addition, the radiation from massive stars can exert a pressure force on the infalling material and potentially stop the accretion process, setting a limit on the final mass (Menon et al. 2023). These kinds of feedback mechanisms dissociate stellar clusters and allow the constituent stars to disperse (Dale & Bonnell 2011; Walch et al. 2012; Grudić et al. 2019). The extent of the influence of radiation pressure on the termination of gas accretion to stars, in particular its role in high-mass formation, is a largely debated topic. Factors like high optical depths of the accretion discs, low-density bipolar paths, and Rayleigh-Taylor instability of the radiation bubble have been proposed that can diminish the control of radiation pressure on the accretion flow (Yorke & Sonnhalter 2002; Krumholz et al. 2005; Kuiper et al. 2015). Recent works argue that photoionisation is also an important feedback mechanism in regulating star formation (Krumholz & Matzner 2009; Krumholz & Thompson 2012; Sales et al. 2014; Grudić et al. 2018a; Menon et al. 2021). Photoionisation refers to the ionisation and heating of gas atoms by the high-frequency light rays from young massive stars. The pressure difference between the resulting hot H II (i.e., ionised hydrogen) regions and the surrounding cold neutral medium leads to the expansion of these hot bubbles, pushing out the remaining gas in the core (Whitworth 1979). The dominance of radiation pressure over photoionisation or vice-versa as the primary radiative feedback mechanism is still open for debate (Matzner 2002; Kim et al. 2018). In contrast to halting star formation by dispersing the cloud, the radiative feedback can also trigger star formation by generating shocked regions of gas that can later collapse (Elmegreen & Lada 1977; Bertoldi 1989; Dale et al. 2007; Bisbas et al. 2011; Walch et al. 2012). Furthermore, supernova explosions in star clusters can blow away the clouds in which they formed, and also trigger star formation, but they commence towards the late stages of star formation at which the shape of the IMF is relatively established for the progenitor cluster (Guszejnov et al. 2022b).

1.4 Physical origin of the IMF

The early explanations for the shape of the IMF were based on the concept of hierarchical fragmentation (Hoyle 1953; Fowler & Hoyle 1963; Larson 1972; Bodenheimer 1978). Later, Larson (1973b) presented an IMF model by introducing stochasticity into the theory of hierarchical fragmentation (see also Marcus 1968; Silk 1978). Zinnecker (1984) employs the central limit theorem to arrive at a theoretical reasoning for the log-normal nature of the IMF in terms of random hierarchical cloud fragmentation process (see also Bonnell et al. 2003; Ballesteros-Paredes et al. 2007; Vázquez-Semadeni et al. 2017; Grudić et al. 2018b). Vázquez-Semadeni et al. (2019) propose that the high-mass end of the IMF can be explained by a global hierarchical collapse in giant molecular clouds, where an accretion process similar to the Bondi-Hoyle-Lyttleton scenario (Hoyle & Lyttleton 1939; Bondi 1952) on gravity-dominated scales (including scales of dense cores and protostars) results in a power-law mass distribution with $\Gamma \sim 1$ (see also Ballesteros-Paredes et al. 2015).

Some studies have linked the IMF peak to the Jeans mass at the density corresponding to the gas-dust thermal coupling, where the relationship between the temperature and density changes sharply, implying a characteristic density for fragmentation (Li et al. 2003; Larson 2005; Jappsen et al. 2005; Elmegreen et al. 2008; Grudić & Hopkins 2023). Lee & Hennebelle (2018b) and Hennebelle et al. (2019) find that the peak of the IMF is set by the development of the first hydrostatic core (Larson 1969, 1985). The thermodynamical evolution associated with the formation of the first hydrostatic core and the tidal shielding of its immediate surroundings results in an optimal stellar mass of around ten times the mass of the core (Hennebelle et al. 2019; Colman & Teyssier 2020). Further, the dependence of the IMF peak on the chemical composition of the gas such as its metallicity is a highly debated topic, which is especially relevant for galaxies at high redshifts (Sharda & Krumholz 2022; Bate 2023; Li et al. 2023; Yan et al. 2024; Tanvir & Krumholz 2024; Menon et al. 2024).

1.4.1 Theoretical models of the IMF

There exist a few theoretical models of the IMF that aim to explain the shape of the IMF over the full mass range motivated by our current understanding of the star formation process and the physical mechanisms involved. These models can be categorised into two classes based on how the stars fragment out of the clouds.

Gravo-turbulent fragmentation

The gravo-turbulent models of the IMF are built upon the interplay between gravity and turbulence (Mac Low & Klessen 2004). These models propose that stars accrete from a predefined mass reservoir and assume that the form of the IMF is similar or derived from the mass distribution of dense cores (core mass function or CMF) (Motte et al. 1998; Testi & Sargent 1998; Johnstone et al. 2000; Nutter & Ward-Thompson 2007; Alves et al. 2007). Padoan & Nordlund (2002) put forward a model for the CMF/IMF centered around the idea of the formation of dense cores in a turbulent shocked layer. They deduce the mass distribution of unstable cores leveraging the power-law nature of the power spectrum of turbulence, consistent with Larson's velocity dispersion–size relation (Larson 1981; Porter et al. 1992). Padoan & Nordlund (2002) assume that the size of a core scales with the thickness of the post-shock gas, and employ the isothermal shock jump conditions in a magnetised gas to express the mass of a dense core in terms of the scale L and the rms Mach number $\mathcal{M}$, which in turn is scale-dependent. They analytically derive the fraction of dense cores that are unstable by assuming a log-normal gas density PDF (Padoan et al. 1997a; Passot & Vázquez-Semadeni 1998; Ostriker et al. 2001) combined with the scale dependence of the mass and number ($\propto L^{-3}$) of dense cores.

Hennebelle & Chabrier (2008) determine the mass spectrum of cores by extending the Press-Schechter formalism (Press & Schechter 1974), originally used in the context of cosmological scenarios, into the star formation regime (Inutsuka 2001). By assuming a log-normal gas density PDF and a collapse-criterion based on the thermal Jeans mass and turbulent Jeans mass, they arrive at the mass function by statistically counting the masses that, when smoothed at a scale L, has a density higher than the critical density for collapse at that scale. The form of the CMF/IMF derived by Hennebelle & Chabrier (2008) is a result of the competition between the thermal-supported and turbulence-supported regimes of the cloud. According to the Hennebelle & Chabrier (2008) model, a higher Mach number on the cloud scales increases the number of low-mass stars due to the increase in the fraction of high-density contrasts, while a higher Mach number at the Jeans length (core scales) leads to a shallower slope at the high-mass end as a result of the suppression of fragmentation at those scales due to the increased turbulent support. Later, Hennebelle & Chabrier (2009) extended the model to non-isothermal conditions, and Hennebelle & Chabrier (2013) further improved the model by incorporating the effect of magnetic fields and the time-dependence of collapse (see also Padoan et al. 2020).

Hopkins (2012) argue that, while counting collapsing objects, it is important to take into account that a given region may be self-gravitating on different scales at the same time. Hopkins (2012) apply the Monte Carlo excursion set theory method (Bond et al. 1991) to deduce the mass distribution of self-gravitating structures on the largest scales (first crossing distribution) and on the smallest scales (last crossing distribution). Hopkins (2012) claim that the first crossing mass function represents the mass function of giant molecular clouds and the last crossing function corresponds to the core mass function (CMF). The model, like the above gravo-turbulent models (Padoan & Nordlund 2002; Hennebelle & Chabrier 2008), uses a log-normal function for the density field, but the variance of the field and collapse criterion is derived self-consistently from the properties of the Galactic disc. On small scales, the criterion for collapse reduces into the Jeans condition for the combination of thermal and turbulent support. The mass function of Hopkins (2012) is a power-law in the high-mass regime, which flattens at the turnover mass M_{sonic}. M_{sonic} is the mass associated with the sonic scale L_{sonic}, i.e., the scale at which the turbulent gas flow becomes subsonic (Federrath et al. 2021).

Competitive accretion and dynamical ejection

In contrast to the concept of gravo-turbulent models where the stars primarily accrete from their parent cores, Bonnell et al. (2001a) argue that the accretion is highly stochastic in nature and the mass of a star is primarily dependent on its relative position to the center of the cluster's gravitational potential and its interaction with other stars (see also Basu & Jones 2004; Dib et al. 2010; Myers 2011; Maschberger et al. 2014). According to the formation mechanism proposed by Bonnell et al. (2001a), all stellar/sub-stellar objects form with similar masses initially, set by the opacity limit of fragmentation (Larson 1972; Bate et al. 2003). Each of these objects then accrete (at a relatively constant rate) from the same mass reservoir competitively until dynamical interactions with other members of the cluster eject them from the parent cloud (Bonnell & Bate 2006). Bate & Bonnell (2005) develop a semi-analytical model for the IMF based on the principle of stochastic accretion and ejections. They derive a PDF for the mass of an object at time t, given by $\mathrm{f}(M,t)$, from the distribution of the accretion rates which is assumed to be a log-normal function. The PDF for an object to be ejected, $e(t)$, is obtained by treating ejections stochastically in terms of the half-life of the process (Bate & Bonnell 2005). The final mass of an object is then given by integrating $\mathrm{f}(M,t)\, e(t)$ over the time period of cloud evolution. According to the model (see Bate & Bonnell 2005, for more details), the slopes of the IMF in the high-mass and low-mass regimes are approximately defined by the standard deviation in the accretion rates. The IMF peak scales with the quantity $\overline{\dot{M}}_{\mathrm{acc}}\, t_{\mathrm{eject}}$, where $\overline{\dot{M}}_{\mathrm{acc}}$ is the mean accretion rate and t_{eject} is the characteristic ejection time-scale.

While the above theoretical models have improved our understanding of the IMF profoundly, they exhibit limitations in incorporating the confirmed effect of some of the physical mechanisms (such as protostellar feedback) or employ assumptions (such as a correlation between CMF and IMF or a log-normal PDF for the accretion rate) that need further investigation. Furthermore, a model of the IMF should also concur with the observed binary properties of stars. To accurately model the IMF, it is critical to fully understand the effect of each of the physical mechanisms involved in star formation and their inter-relationship. My thesis aims to contribute to a better understanding of the dependence of the IMF on cloud properties and stellar feedback by performing an extensive parameter study of the IMF as detailed below.

1.5 Thesis Outline

My thesis, focused on understanding the IMF, is numerical in nature and is achieved through performing MHD simulations of star cluster formation. The main factors that make numerical studies of the IMF challenging are

- *High-resolution requirements*: Star formation is a multi-scale process. The star-forming regions strongly interact with their surrounding gas. To model star cluster formation reasonably well, it is crucial to self-consistently follow the gas evolution in MCs from the evolution of the turbulent gas on large scales to the formation of shocked regions and dense fragmenting cores, down to the scales of individual accretion discs. This requires sufficiently resolving scales ranging over at least a few parsecs down to a few tens of AU.
- *Implementation of important physical mechanisms*: Star formation is a highly complex process and involves multiple physical mechanisms such as gravity, turbulence, magnetic fields, and protostellar feedback. The effects of these mechanisms are inter-related, and therefore they have to be implemented simultaneously in simulations to obtain conclusive results.
- *Statistical significance*: To constrain the IMF characteristics such as the IMF peak, turnover mass (transition between the log-normal and power-law parts), and the high-mass slope, numerical simulations need to produce a large sample of stars. This becomes increasingly difficult when the simulations are at a high level of resolution and incorporate multiple physical mechanisms.
- *Long run-time*: Star formation is highly inefficient and slow. Hence the associated numerical simulations that follow this regime necessarily have long run-times. Meanwhile, some numerical experiments are specifically configured to produce a large number of stars in a short time, but at the expense of unrealistically high SFRs. This means that such experiments deviate from the low-SFR scenario as indicated by observations. Such constraints on the setup also narrow down the cloud parameter space that can be explored in these simulations.

A primary feature of my work is that I thoroughly address the above elements that are critical for studying the origin of the IMF, making it unique and contributing significantly to the existing literature. We use the FLASH code with adaptive mesh refinement (AMR) to perform high-resolution star cluster formation simulations that include a wide range of physics and explore how different cloud properties and stellar processes affect star formation. For each of our studies, we perform multiple simulations with different turbulence realisations so that we have a statistically meaningful sample of stars, enabling us to comprehensively analyse the origin of the IMF.

In Chapter 2, we incorporate the outflow feedback developed by Federrath et al. (2014) into cloud-collapse simulations that employ mechanisms such as gravity, turbulence, magnetic fields and stellar radiative heating. We study the effect of protostellar outflows in setting the IMF by comparing the evolution of star cluster formation simulations in both the presence and absence of the feedback. With the inclusion of the outflow feedback, our simulations represent a relatively realistic model of star formation, and therefore we compare our simulation IMF with different observational and theoretical models of the IMF.

In Chapter 3, we study the role of the mode of turbulence driving in the star formation process. We carry out simulations with purely compressive (curl-free) turbulence driving and contrast it with simulations that employ purely solenoidal driving (divergence-free) in terms of the IMF variations. We also evaluate how the variations observed between the two sets relate to the expectations of the theoretical IMF models.

Chapter 4 investigates the impact of the cloud virial parameter on the IMF. We perform a suite of simulations with three different values of the cloud virial parameter and study how the different properties like the gas density PDF, IMF, and SFR vary between them.

Chapter 5 is an in-depth analysis of the orbital eccentricity properties of the binaries in our simulations, with a focus on probing the observational findings on the topic. Since the binary properties are linked to the IMF, studying the orbital eccentricity, the multiplicity fraction (Chapters 2, 3, 4), and the binary mass ratio (Chapter 3) enables us to draw strong connections between the IMF and binary formation, which is crucial for a complete comprehension of the star formation process.

Chapter 2

The IMF and multiplicity of stars from gravity, turbulence, magnetic fields, radiation and outflow feedback

Context and Contribution

This chapter has been previously published as 'The IMF and multiplicity of stars from gravity, turbulence, magnetic fields, radiation and outflow feedback', by Sajay Sunny Mathew, Christoph Federrath, 2021, MNRAS, 507, 2448. The research is presented here as it appears in the original publication, except for a few minor typographical changes. I have carried out the simulations described in this paper, and post-processed the data for further investigation. I have written the majority of the paper, with inputs and suggestions from the co-author.

Abstract

We perform a series of three-dimensional, magnetohydrodynamical (MHD) simulations of star cluster formation including gravity, turbulence, magnetic fields, stellar radiative heating and outflow feedback. We observe that the inclusion of protostellar outflows (1) reduces the star formation rate by a factor of ~ 2, (2) increases fragmentation, and (3) shifts the initial mass function (IMF) to lower masses by a factor of 2.0 ± 0.2, without significantly affecting the overall shape of the IMF. The form of the sink particle (protostellar objects) mass distribution obtained from our simulations matches the observational IMFs reasonably well. We also show that turbulence-based theoretical models of the IMF agree well with our simulation IMF in the high-mass and low-mass regime, but do not predict any brown dwarfs,

whereas our simulations produce a considerable number of sub-stellar objects, which are produced by dynamical interactions (ejections). We find that these dynamical interactions also play a key role for the binary separation distribution and stellar kinematics in general. Our numerical model of star cluster formation also reproduces the observed mass dependence of multiplicity. Our multiplicity fraction estimates generally concur with the observational estimates for different spectral types. We further calculate the specific angular momentum of all the sink particles and find that the average value of $1.5 \times 10^{19}\,\mathrm{cm^2\,s^{-1}}$ is consistent with observational data. The specific angular momentum of our sink particles lies in the range typical of protostellar envelopes and binaries. We conclude that the IMF is controlled by a combination of gravity, turbulence, magnetic fields, radiation and outflow feedback.

2.1 Introduction

Our understanding of the star formation process has improved remarkably in past few years by virtue of advanced, high-resolution observations, rigorous theoretical works and ever-expanding numerical techniques. However, we are far from having achieved a complete picture of star formation. Numerical simulations enable scrutiny of observations and provide a framework for theoretical analysis. However, performing large-scale simulations of the collapse of molecular clouds is challenging because it involves complex, interrelated physical mechanisms like gravity, magnetic fields, and stellar radiative and mechanical feedback (Federrath 2018; Krumholz & Federrath 2019). Moreover, the interstellar medium (ISM) is turbulent down to the scales of molecular clouds and star-forming sub-regions (Elmegreen & Scalo 2004). Numerical models of star formation strive to reproduce or explain, but not limited to, the observed initial mass function (IMF), star formation rate and efficiency, multiplicity and mass ratio in stellar systems, the slow rotation rates of zero-age main sequence stars (ZAMS), and how these properties are affected by different physical mechanisms (e.g., Jappsen & Klessen 2004; Hennebelle & Teyssier 2008; Offner et al. 2009; Federrath & Klessen 2012; Bate 2012; Krumholz et al. 2012b; Federrath & Klessen 2013; Myers et al. 2014; Cunningham et al. 2018; Guszejnov et al. 2020; Mathew & Federrath 2020; Rohde et al. 2021). Here we aim to determine the role of the combined effects of gravity, turbulence, magnetic fields, and feedback for the IMF.

The IMF represents the distribution of the mass of stars formed in a single cloud-collapse event and it is found to be surprisingly universal, not just in the solar neighbourhood, but also beyond (see the reviews by Bastian et al. 2010; Hopkins

2018; Lee et al. 2020). Salpeter (1955) proposed that the IMF can be described by a power-law of the form $dN \propto M^{-\Gamma}\, d\log M$, where N is the number of stars, M is the stellar mass and $\Gamma = 1.35$. Later it was realised that the mass spectrum flattens at masses less than $1\,\mathrm{M}_{\odot}$ and that the distribution of low-mass stars can be represented by a log-normal function (Miller & Scalo 1979). The most commonly referenced functional forms of the IMF include a log-normal function that transforms into a Salpeter-like power-law at high masses (Chabrier 2005), and a three-segment power-law (Kroupa 2001). The IMF has a peak or characteristic mass at around $0.2-0.3\,\mathrm{M}_{\odot}$ (Chabrier 2003; Elmegreen et al. 2008; Offner et al. 2014). It is intriguing that supersonic turbulence, which embodies the chaotic nature of star formation, is also considered primarily responsible for the observed universality of the initial mass function (IMF). The role of turbulence in the star formation process is two-fold. Turbulence is supersonic on the scales of molecular clouds, and the turbulent pressure supports the cloud against a monolithic collapse (Elmegreen 1993b; Padoan 1995; Klessen et al. 2000). On the other hand, it also seeds star formation by creating local density fluctuations or over-dense regions (analogous to the observed dense cores) (Mac Low & Klessen 2004; McKee & Ostriker 2007). Supersonic turbulence results in a probability density function (PDF) of the gas density that is approximately log-normal (Vazquez-Semadeni 1994; Padoan et al. 1997a; Kritsuk et al. 2007; Federrath et al. 2008; Federrath 2013a; Hopkins 2013b; Federrath & Banerjee 2015). It is on this premise that recent IMF theories are formulated (Padoan & Nordlund 2002; Hennebelle & Chabrier 2008, 2009; Hopkins 2012, 2013a). These gravo-turbulent IMF models are built upon the observed correlation between the core mass function (CMF) and the IMF. The CMF has a form similar to the IMF, but is shifted to higher masses by a factor of 2–4 (Motte et al. 1998; Testi & Sargent 1998; Johnstone et al. 2000; Alves et al. 2007; Stanke et al. 2006). The mass gap between the CMF and the IMF is thought to be the result of the mass loss of the protostellar object due to jets and outflows, which is generally parameterized by a mass-independent core-to-star efficiency $\epsilon \sim 0.25 - 0.5$ (Matzner & McKee 2000; Myers 2008; Federrath & Klessen 2012; Federrath et al. 2014; Offner & Arce 2014). Jets and outflows not only remove a fraction of accreting material from the protostars, but also drive small-scale turbulence by injecting turbulent kinetic energy into the cloud (Li & Nakamura 2006; Nakamura & Li 2011). They reduce the star formation rate significantly and aid the formation of new protostellar objects (Federrath et al. 2014). Previous numerical studies suggest that the mechanical feedback indeed play a fundamental role in bringing out the observed mass scale of the IMF (Li et al. 2010; Krumholz et al. 2012b; Cunningham et al. 2018; Guszejnov et al. 2021; Rohde et al. 2021). Thus, the incorporation of outflow feedback in numerical works is essential to produce conclusive results on the IMF.

The multiplicity of stars is a highly debated topic that is coupled to the IMF. Stars generally form in clusters (Lada & Lada 2003) and observations suggest that the multiplicity fraction is an increasing function of primary mass (Duchêne & Kraus 2013). Astronomers make use of the mass-dependence of multiplicity and the mass ratio in stellar systems to correct for the unresolved companions and extract the individual-star IMF from the system IMF. Core fragmentation due to the inherent rotation in dense cores is a viable mechanism for the formation of multiple systems. The angular momentum of the cores is acquired from the large-scale turbulent motions and the differential rotation of the galactic disc. The angular momentum transport is a long-standing problem in the field of astrophysics (Spitzer 1978). At least 5 to 6 orders of magnitude in specific angular momentum are lost between the evolution from a dense core to a typical star like the Sun (Bodenheimer 1995; Belloche 2013). The processes proposed for solving the angular momentum problem include magnetic braking (Mouschovias & Paleologou 1980), disc formation (Papaloizou & Lin 1995) and removal by jets and outflows (disc winds) (Blandford & Payne 1982). The multiplicity and angular momentum of stars are therefore key properties that can be used to probe theories of star formation.

The major aim of this paper is to investigate the impact of protostellar outflows on the star formation process, in particular on the IMF and the star formation rate. Our results are derived from multiple simulations to form a statistically significant sample of stars. We compare the mass distribution of stars formed in our simulations with observations and theoretical models of the IMF. We also study the multiplicity and angular momentum of the protostellar objects that form in our simulations and compare them with observational data.

In Section 2.2, we explain the simulation methodology, introduce the sub-grid models for stellar heating and outflow feedback, and define the initial configuration and simulation parameters. In Section 2.3, we study the effect of jets/outflows in the process of star cluster formation by comparing a model that includes the outflow feedback with a model with no protostellar outflows. For each of the two models, we investigate the column density and temperature morphology, evolution of dynamical quantities and the IMF of the stars formed in 10 cloud/cluster simulations. In Section 2.4, we compare our IMF with the observational and theoretical models of the IMF. In Section 2.5, we discuss the multiplicity and the specific angular momenta of the stars. Limitations are discussed in Section 2.6. Section 2.7 summarises the main results and presents our conclusions.

2.2 Methods

2.2.1 Magnetohydrodynamical equations

The cloud-collapse is modelled numerically by solving the magnetohydrodynamical (MHD) equations including gravity on an adaptive mesh refinement (AMR) (Berger & Colella 1989) grid using the PARAMESH library (MacNeice et al. 2000) in the FLASH4 code (Fryxell et al. 2000; Dubey et al. 2008),

$$\frac{\partial \rho}{\partial t} + \nabla \cdot (\rho \mathbf{v}) = 0, \tag{2.1}$$

$$\rho \left(\frac{\partial}{\partial t} + \mathbf{v} \cdot \nabla\right) \mathbf{v} = \frac{(\mathbf{B} \cdot \nabla)\mathbf{B}}{4\pi} - \nabla P_{\mathrm{tot}} + \rho(\mathbf{g} + \mathbf{F}_{\mathrm{stir}}), \tag{2.2}$$

$$\frac{\partial \mathbf{B}}{\partial t} = \nabla \times (\mathbf{v} \times \mathbf{B}), \quad \nabla \cdot \mathbf{B} = 0, \tag{2.3}$$

where $\rho, \mathbf{v}, \mathbf{B}, P_{\mathrm{tot}} = P + 1/(8\pi)|\mathbf{B}|^2$, and $\mathbf{F}_{\mathrm{stir}}$ denote the gas density, velocity, magnetic field, pressure (sum of thermal and magnetic) and turbulent acceleration field, respectively. Here $\mathbf{g}$ is the gravitational acceleration and is the aggregate of the self-gravity of the gas and the acceleration due to the presence of sink particles (see §2.2.3)

We utilize a multi-grid Poisson solver for computing the self-gravity of the gas (Ricker 2008). We use the 5-wave HLL5R approximate Riemann method to solve the MHD equations. The HLL5R solver has comparable accuracy to the standard FLASH-Roe solver, but it is more efficient and has a better stability (Waagan et al. 2011).

2.2.2 Turbulence

The kinetic energy of freely decaying turbulence dissipates on timescales shorter than a dynamical timescale (Gammie & Ostriker 1996; Mac Low et al. 1998; Stone et al. 1998). Stellar feedback, such as stellar winds and supernova explosions, inject turbulent kinetic energy and replenish the turbulence. Turbulence can also be induced by accretion and shear motions on galactic scales (Elmegreen 2009b; Federrath et al. 2017a). We use a stochastic Ornstein-Uhlenbeck process (Eswaran & Pope 1988; Schmidt et al. 2006; Federrath et al. 2010b) to construct an acceleration field $\mathbf{F}_{\mathrm{stir}}$ and continuously drive turbulent motions. $\mathbf{F}_{\mathrm{stir}}$ is added as a momentum and energy source term in the MHD equations (see Eq. 2.2). Our turbulence driving module inputs kinetic energy on the largest scales (wavenumbers $k = 1 \ldots 3$, where k is in units of $2\pi/L$ with the side length L of the computational domain), which cascades down to smaller scales, naturally producing the velocity power spectrum $\sim k^{-2}$ or equivalently a velocity dispersion – size relation of $\sigma_v \propto \ell^{1/2}$ (Larson 1981; Ossenkopf & Mac Low 2002; Heyer & Brunt 2004; Roman-Duval et al. 2011; Federrath 2013a; Federrath et al. 2021). We define the turbulence driving parameter $\zeta = 0.5$ (Schmidt et al. 2009; Federrath et al. 2010b) to obtain a natural mixture of forcing modes. Such a value produces a ratio of compressive forcing power to the total forcing power, of about 1/3, typical for clouds in the Milky Way disc (Federrath et al. 2016). A mixed turbulence driving represents a combination of compressive ($\nabla \times \mathbf{F}_{\mathrm{stir}} = 0$, $\zeta \sim 0$) and solenoidal ($\nabla \cdot \mathbf{F}_{\mathrm{stir}} = 0$, $\zeta \sim 1$) modes of driving (Federrath et al. 2008, 2010a; Molina et al. 2012; Nolan et al. 2015).

2.2.3 Sink particles and AMR

As the central gas density of a collapsing region increases, its internal structure becomes complex and the timescale decreases. Eventually, it becomes extremely difficult to follow the gas evolution numerically. Sink particles are sub-grid models that are used to represent the gravitationally bound, high-density regions in cloud-collapse simulations. Depending on the requirement or maximum resolution that can be achieved, sink particles are used to model the formation and accretion of individual protostellar cores or the disc + protostar systems that form later within these cores. In addition to requiring that the gas forming a sink particle be gravitationally bound, we perform a series of tests as described by Federrath et al. (2010c) before locally converting gas to sink particles to ensure that only truly bound and collapsing gas is turned into sink particles. The sink particles are introduced and centred at the computational cell that exceeds the threshold density defined by the Jeans length,

$$\rho_{\mathrm{sink}} = \frac{\pi\, c_s^2}{G\,\lambda_{\mathrm{J}}^2} = \frac{\pi\, c_s^2}{4\,G\,r_{\mathrm{sink}}^2}, \tag{2.4}$$

where c_s^2 is the sound speed, G is the gravitational constant, $\lambda_{\mathrm{J}} = [\pi c_s^2/(G\rho)]^{1/2}$ is the local Jeans length, and $r_{\mathrm{sink}} = \lambda_{\mathrm{J}}/2$ is the sink particle radius.

We define the size of the sink particle as $2r_{\mathrm{sink}} = 5\,\Delta x$, where Δx is the grid cell length on the highest level of refinement. This ensures that the Truelove et al. (1997) criterion is satisfied, avoiding artificial fragmentation. On all other AMR levels, λ_{J} is always resolved with at least 16 grid cell lengths to prevent underestimation of the turbulent energy and to resolve the local collapse reasonably well (Federrath et al. 2011c).

The conservation laws are exercised to update the mass, linear momentum and angular momentum of each sink particle in every accretion step. The new position of the sink particle after accretion is the centre of mass of the sink particle and the accreted material. In order to conserve total angular momentum, an intrinsic angular momentum (spin) is introduced for the sink particle, which stores the accreted angular momentum. The spin is then used to determine the rotational axis of the sink particle along which jets and outflows are launched (see Federrath et al. 2014); see details in Sec. 2.2.5.

All gravitational interactions of the sink particles with the gas and between each other are calculated by direct summation over all the sink particles and grid cells. A second-order leapfrog integrator is employed for advancing the sink particles in time.

2.2.4 Equation of state (EOS)

The thermodynamics of the gas in protostellar cores is determined by the competition between heating and cooling mechanisms, e.g., compressional heating, cosmic-ray heating, and cooling by dust grains (Larson 1973a; Masunaga et al. 1998). The early phase of the collapse of molecular cloud cores (birthplace of stars) is isothermal (Wolfire et al. 1995; Masunaga & Inutsuka 2000; Glover et al. 2010). The cores are optically thin initially, and the gravitational energy released is readily radiated away. However, cooling becomes inefficient and the compressional heating dominates when an opaque region forms in the centre, trapping the infrared radiation from dust grains. To accurately model the thermal evolution of the gas, the equation of energy conservation has to be solved simultaneously with the RT equation. Solving the RT equation, even on the small scales of cloud cores, is difficult because it involves tracing rays that get absorbed, emitted and scattered by the constituents of the dust and gas. Further, it requires knowledge of the dust chemistry. Since we follow the collapse of molecular clouds that contain $\sim$ 20–50 cores, and considering the fact that we perform multiple simulations for better statistics, solving the energy conservation and RT equations is impractical. Therefore, to close the system of MHD equations, we use a polytropic equation of state for the gas pressure $P = P_{\mathrm{EOS}}$, with

$$P_{\mathrm{EOS}} = c_s^2\,\rho^{\gamma}. \tag{2.5}$$

Using the ideal gas EOS, the respective temperature is given by

$$T_{\mathrm{EOS}} = \frac{\mu\, m_{\mathrm{H}}}{k_{\mathrm{B}}\,\rho}\,P_{\mathrm{EOS}} = \frac{\mu\, m_{\mathrm{H}}}{k_{\mathrm{B}}}\,c_s^2\,\rho^{\gamma-1}\,. \tag{2.6}$$

Here $c_s^2 = (0.2\,\mathrm{km/s})^2$ is the square of the sound speed in the isothermal regime ($\gamma = 1$) for solar-metallicity, molecular gas at $10\,\mathrm{K}$, and $\mu = 2.35$ is the mean molecular weight (in units of hydrogen atom mass $m_{\rm H}$). The polytropic exponent is then set differently depending on the density of the gas, as

$$\gamma = \begin{cases} 1 & \text{for} \quad \rho \leq \rho_1 \equiv 2.50 \times 10^{-16}\,\mathrm{g\,cm^{-3}}, \\ 1.1 & \text{for} \quad \rho_1 < \rho \leq \rho_2 \equiv 3.84 \times 10^{-13}\,\mathrm{g\,cm^{-3}}, \\ 1.4 & \text{for} \quad \rho_2 < \rho \leq \rho_3 \equiv 3.84 \times 10^{-8}\,\mathrm{g\,cm^{-3}}, \\ 1.1 & \text{for} \quad \rho_3 < \rho \leq \rho_4 \equiv 3.84 \times 10^{-3}\,\mathrm{g\,cm^{-3}}, \\ 5/3 & \text{for} \quad \rho > \rho_4. \end{cases} \tag{2.7}$$

The value of the polytropic exponent γ varies with the local density of the gas, and is based on previous detailed radiation-hydrodynamic simulations of protostar formation. It covers the phases of isothermal collapse, adiabatic heating during the formation of the first and second core and the impacts of H_2 dissociation in the second collapse (Larson 1969; Yorke et al. 1993; Masunaga & Inutsuka 2000; Offner et al. 2009). However, it does not account for the increase in thermal pressure due to protostellar heating, which we discuss next.

2.2.5 Stellar feedback

Radiative heating

Stellar heating feedback influences the number and mass distribution of stars formed in the collapse of molecular clouds (Bate 2009b; Krumholz et al. 2011; Guszejnov et al. 2016; Federrath et al. 2017b; Mathew & Federrath 2020; Hennebelle et al. 2020a). The high luminosities of young stars suppress fragmentation, allowing the stars to accrete more gas and grow in mass. Therefore, it is essential to account for the change in gas temperature due to the stellar radiative heating. But as mentioned above, solving the RT equation involving every point in space and for every timestep is computationally expensive, and therefore including it for parameter studies in large-scale simulations is often not possible. To include protostellar heating in our simulations, we use the polar stellar heating model implemented in Mathew & Federrath (2020). The model takes into account the existence of optically-thick accretion discs around the new-born stars and the resulting shielding of stellar radiation by dust. Based on the works of Pascucci et al. (2004) and Buntemeyer et al. (2016), it assumes a disc density distribution around each sink particle (protostar) that is dependent on the radial distance r and the angle θ subtended from the sink particle's angular momentum axis. The stellar radiant power is distributed on the grid cells surrounding the sink particle based on this dust/disc density distribution.

Dust particles absorb the radiation from the central star with the rate of energy absorption given by

$$Q(r,\theta) = \chi \, \frac{L_\star}{4\pi r^2} \, \exp\left(-\tau(r,\theta)\right), \tag{2.8}$$

where χ is the absorption coefficient. The star's luminosity ($L_\star$), which includes both the accretion and intrinsic luminosities, is calculated by employing the protostellar evolution model by Offner et al. (2009). The total optical depth (τ) in any direction given by θ is

$$\tau = \int \kappa \, \rho(r,\theta) \, \mathrm{d}r, \tag{2.9}$$

where κ is the grey opacity and $\rho(r,\theta)$ is the assumed dust/disc density distribution (see Mathew & Federrath 2020, for a description of the analytical model of the disc density distribution used here). The radiation is attenuated in the directions of the disc because of the absorption by dust grains, and therefore the main heating is confined to the polar directions.

At the equilibrium temperature, the amount of energy emitted by the dust grains will be equal to the amount they absorb, i.e., Q. Therefore we can write

$$\frac{\sigma_{\mathrm{SB}}}{\pi} \, \chi \, T_{\mathrm{heat}}^4 = \frac{Q}{4\pi}, \tag{2.10}$$

where σ_{SB} is the Stefan-Boltzmann constant and T_{heat} is the temperature due to stellar radiative heating. Here we have neglected the reprocessed radiation field.

To account for the change in thermal pressure due to stellar radiative feedback, we add the space-dependent pressure term obtained from the polar stellar heating module to the pressure computed from the polytropic equation of state (see Guszejnov et al. 2016, 2018a; Federrath et al. 2017b). Thus, the final gas pressure is

$$\begin{aligned} P &= \left[P_{\mathrm{EOS}}^4 + P_{\mathrm{heat}}^4\right]^{1/4} \\ &= \left[P_{\mathrm{EOS}}^4 + \left(\frac{k_B \, \rho}{\mu \, m_{\mathrm{H}}}\right)^4 T_{\mathrm{heat}}^4\right]^{1/4}, \end{aligned} \tag{2.11}$$

which is imposed in the MHD momentum equation, Eq. (2.2).

Jets/Outflows

The bipolar mechanical feedback from stars consists of two components — the highly collimated fast stream of gas, called jets, that drill through the cloud, and the wide-angle low-speed molecular outflows (Frank et al. 2014). We employ the subgrid-scale (SGS) outflow model of Federrath et al. (2014) for launching this jet/outflow combination in our simulations. It captures the fast jet component and includes angular momentum transfer.

The SGS module imparts momentum uniformly to the grid cells within a confined volume defined by two spherical sections (cones) around the sink particle. The cones open towards the opposite poles of the sink particle and are characterised by an opening angle $\theta_{\rm out} = 30^\circ$ measured from the angular momentum axis. We set the radial extent equal to $r_{\rm out} = 16\Delta x$ measured from the position of the sink particle (tip of the cone), where Δx is the cell size on the highest level of refinement, as tested and recommended in Federrath et al. (2014). The model uses radial and angular smoothing functions to prevent numerical artifacts at the interfaces. The momentum injected into each of the cones is

$$\mathbf{P}_{\rm out} = \pm(1/2)\, M_{\rm out}\, \mathbf{V}_{\rm out}, \tag{2.12}$$

where $M_{\rm out}$ is the ejected mass, which is equal to the fraction $f_{\rm m}$ of the mass accreted by the sink particle in a timestep Δt, i.e., $M_{\rm out} = f_{\rm m}\, \dot{M}_{\rm acc}\, \Delta t$. We use $f_{\rm m} = 0.3$ (Federrath et al. 2014), which is consistent with observations (Hartmann & Calvet 1995; Cabrit et al. 2007; Bacciotti et al. 2011), theoretical models of the outflow mechanism (Blandford & Payne 1982; Shu et al. 1988; Pudritz et al. 2007) and the values derived from previous numerical simulations (Hennebelle & Fromang 2008; Seifried et al. 2012; Fendt & Sheikhnezami 2013)

$\mathbf{V}_{\rm out}$ is set to the Kepler speed near the surface of the protostar, such that

$$|\mathbf{V}_{\rm out}| = 100\,{\rm km\,s^{-1}} \left(\frac{M_{\rm sink}}{0.5\,{\rm M_\odot}}\right)^{1/2}, \tag{2.13}$$

where $M_{\rm sink}$ is the mass of the sink particle and $100\,{\rm km\,s^{-1}}$ is the typical jet speed (and Kepler speed) for a protostar of mass $M = 0.5\,{\rm M_\odot}$ at a radius of $R = 10\,{\rm R_\odot}$. $\mathbf{V}_{\rm out}$ consists of a slow component with a speed of $0.25\,|\mathbf{V}_{\rm out}|$ and a fast component with speed of $0.75\,|\mathbf{V}_{\rm out}|$. The high-speed component contributes to the momentum injection in the cones only within an opening angle of 5°. By using such a velocity profile, the model distinguishes the faster jet and the slower molecular outflow components. A fraction $f_{\rm a}$ of the accreted angular momentum is removed from the sink particle and re-introduced to the two outflow/jet components. We use the default value of $f_{\rm a} = 0.9$ in the SGS model, which is based on the observations in Bacciotti et al. (2002) and numerical works, e.g., Banerjee & Pudritz (2006) and Hennebelle & Fromang (2008).

The inserted momentum into the two cones is effectively carried away to larger scales by the MHD code. The SGS outflow model reproduces converged large-scale outflow properties for the mass, linear momentum, angular momentum and the outflow speed, almost independent of the resolution. We refer the reader to Federrath et al. (2014) and references therein for a detailed description of the SGS model and justification of the parameter choices.

2.2.6 Initial conditions and simulation parameters

The computational domain of the simulations is a three-dimensional triple-periodic box with side length $L = 2\,\mathrm{pc}$. The maximum refinement level provides a maximum effective grid resolution of $N^3_{\mathrm{eff,\,res}} = 4096^3$ cells or a minimum cell size of $\Delta x_{\mathrm{cell}} = 100\,\mathrm{AU}$. The initial gas density is uniform with $\rho_\circ = 6.56 \times 10^{-21}\,\mathrm{g\,cm^{-3}}$, which gives a total cloud mass of $M_{\mathrm{cl}} = 775\,\mathrm{M_\odot}$ and a mean free-fall time of $t_{\mathrm{ff}} = 0.82\,\mathrm{Myr}$. The turbulence driving module stirs the gas in the box initially in the absence of self-gravity. The induced turbulence creates cloud-typical structures and density contrasts in the form of filaments and clumps. The high-density regions within these structures are potential sites of star formation (Arzoumanian et al. 2011; Schneider et al. 2013; André et al. 2014). The amplitude of the turbulence driving is set by the velocity dispersion $\sigma_v = 1.0\,\mathrm{km\,s^{-1}}$ and the initially isothermal sound speed $c_s = 0.2\,\mathrm{km\,s^{-1}}$, which gives a steady-state sonic Mach number of $\mathcal{M} = \sigma_v/c_s = 5.0$. The magnetic field, which is uniform initially with $B = 10^{-5}\,\mathrm{G}$ along the z-axis of the computational box, is later modified due to the compression, tangling and folding by the turbulence, approximating the morphology of magnetic fields in real molecular clouds (Federrath 2016). The initial virial parameter $\alpha_{\mathrm{vir}} = 2E_{\mathrm{kin}}/E_{\mathrm{grav}} = 0.5$ is in the range of observed values (Falgarone et al. 1992; Kauffmann et al. 2013; Hernandez & Tan 2015). After two turbulent crossing times, $2t_{\mathrm{turb}} = L/(\mathcal{M}c_s) = 2\,\mathrm{Myr}$, a fully-developed turbulent state is reached, which is when we turn on self-gravity and allow for sink particle creation, which is the typical procedure for this type of cluster-formation experiments. We study the temporal evolution of different dynamical quantities and statistical properties of the forming star clusters from this point in time, which we define as $t = 0$, i.e., when self-gravity is activated. This method is similar to that used in earlier works (e.g., Federrath & Klessen 2012; Krumholz et al. 2012b; Padoan et al. 2016; Guszejnov et al. 2018b).

2.3 Results

We run 10 simulations of star cluster formation with different turbulence realisations (T1–T10), incorporating gravity, turbulence, magnetic fields, stellar heating and

Table 2.1: Key simulation results.

Model (1)	$t_{5\%}[t_{\rm ff}]$ (2)	$\overline{\rm SFR}_{\rm ff}[\%]$ (3)	$N_{\rm Total\,sinks}$ (4)	$\overline{M}_{\rm median}\,[{\rm M}_\odot]$ (5)	$\overline{M}_{\rm avg}\,[{\rm M}_\odot]$ (6)	Γ (7)	SSF (8)	$j_{\rm mean}\,[{\rm cm^2\,s^{-1}}]$ (9)
1. NOWIND	0.68 ± 0.15	15 ± 3	212	1.0 ± 0.3	1.9 ± 0.3	1.3 ± 0.2	0.65	1.2×10^{20}
2. OUTFLOW	0.89 ± 0.20	7 ± 2	449	0.5 ± 0.1	0.9 ± 0.1	1.5 ± 0.3	0.66	1.5×10^{19}

Notes. Ten simulations with different turbulence realisations (T1–T10) are run for both the NOWIND and OUTFLOW models. In the table, $t_{5\%}$ is the average time taken (in units of the free-fall time) by the simulations to reach SFE $= 5\%$ and is measured from the moment self-gravity is turned on. The value of $\overline{\rm SFR}_{\rm ff}$ quoted in the table is time averaged, while all the other quantities are calculated at SFE $= 5\%$. The resolution level, cloud properties and turbulence setup are the same in both models and the only difference is that protostellar outflows are absent in the NOWIND simulations. Main simulation parameters: computational box size: $L = 2\,{\rm pc}$, maximum effective grid resolution: $N^3_{\rm eff,\,res} = 4096^3$ cells, minimum cell size: $\Delta x_{\rm cell} = 100\,{\rm AU}$, sink particle threshold density: $\rho_{\rm sink} = 3.8 \times 10^{-16}\,{\rm g\ cm^{-3}}$, uniform initial gas density: $\rho_\circ = 6.56 \times 10^{-21}\,{\rm g\,cm^{-3}}$, total cloud mass: $M_{\rm cl} = 775\,{\rm M}_\odot$, uniform initial magnetic field: $B = 10^{-5}\,{\rm G}$ (along the z-axis), turbulence driving parameter: $\zeta = 0.5$, velocity dispersion on the driving scale of the turbulence: $\sigma_v = 1.0\,{\rm km\,s^{-1}}$.

outflow feedback (Model OUTFLOW). We evolve the simulations until 5% of the total mass of the cloud has formed stars, i.e., the star formation efficiency SFE = 5%. The objective of performing multiple simulations is to produce a sufficient number of stars to obtain statistically conclusive results. Since we include a set of physical mechanisms (gravity, turbulence, magnetic fields, and both mechanical and radiation feedback) governing the star formation process, we are in a good position to compare the statistical properties like the IMF and multiplicity with observations and theory. We begin by examining how the evolution of the cloud is influenced by the outflow feedback.

We investigate the impact of jets/outflows on the number and distribution of the stars formed and the star formation rate (SFR) by comparing the simulations of the OUTFLOW model with another set of 10 simulations with no outflow feedback (Model NOWIND). The simulation setup and turbulence seeds used in the NOWIND simulations are the same as in the OUTFLOW simulations. Fig. 2.1 shows the mass-weighted column density (integral of the number density weighted by mass along the line-of-sight) of both the models for one particular turbulence realisation (simulation T1). The NOWIND and OUTFLOW models form 21 and 48 sink particles, respectively. The NOWIND simulation reaches an SFE = 5% in 0.58 Myr, while the OUTFLOW simulation takes 0.70 Myr to reach the same SFE. It is evident from the temperature maps (bottom panel in Fig. 2.1) that the gas temperature around the sink particles in the NOWIND model is higher than that in the OUTFLOW simulation.

The OUTFLOW model generates a higher number of stars as compared to the NOWIND model at the same SFE of 5% because (1) the molecular cloud in the OUTFLOW model has evolved further in time, and therefore some stars that form independent of the presence of the outflow feedback have not yet emerged in the NOWIND case, (2) the outflows from protostellar objects can inject enough momentum into the cloud to drive small-scale turbulence and perturb the accretion flow, allowing the formation of more stars (Wang et al. 2010; Federrath et al. 2014), and (3) they indirectly lower the efficiency of stellar heating. The ejection of the accreted material from the star+disc system and the sweeping away of a part of the surrounding envelope by disc and/or stellar winds reduce the mass of the stars and therefore their luminosity (Hansen et al. 2012; Krumholz et al. 2012b). Thus,

---

[1] We define the mass-weighted projection of the gas number density as $\int \rho^2\, dz \,/\, \int \rho dz$ and the mass-weighted projection of the temperature as $\int \rho T dz \,/\, \int \rho dz$, where the projection is taken along the z-direction. All figures in this paper showing density and temperature maps are mass-weighted. The aim of the mass-weighting is to enable better visualisation of the morphological features, i.e., to bring out the densest structures. A version of Fig. 2.2 without mass-weighting is shown in Fig. 2.17.

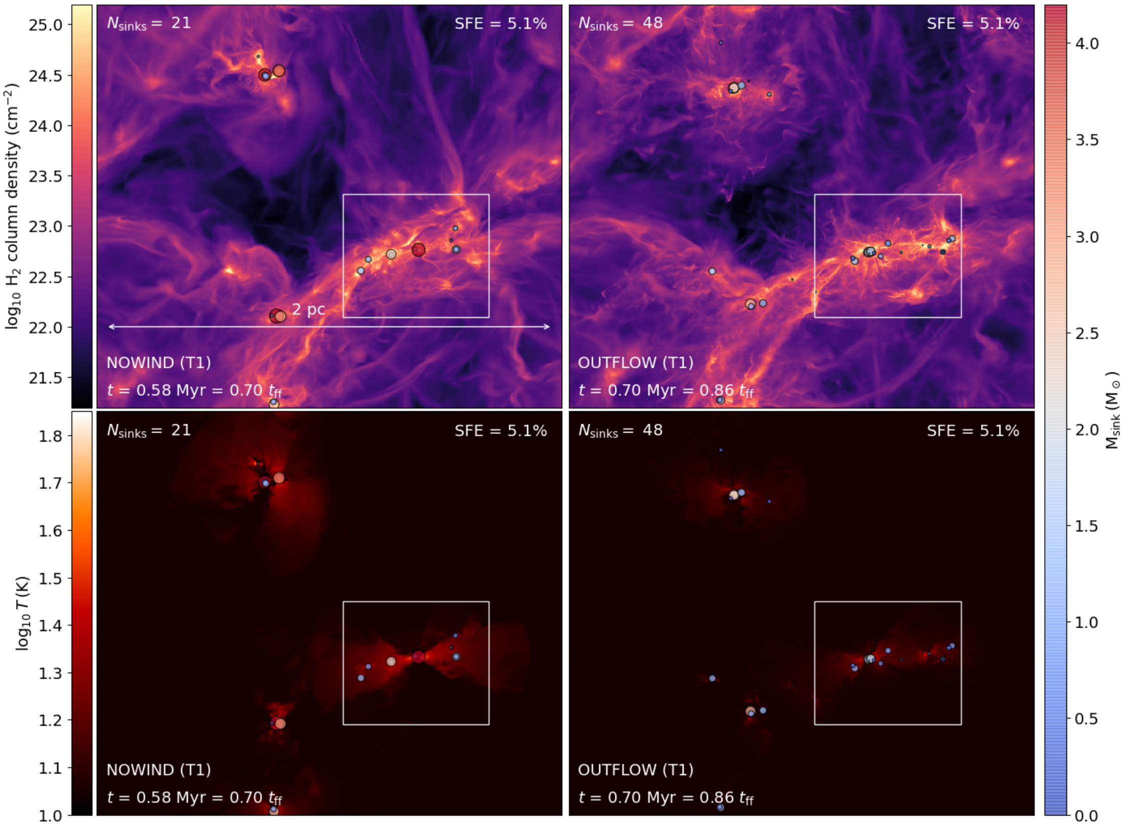

Figure 2.1: The first column presents the mass-weighted[1] projection maps of the gas number density (top) and temperature (bottom) of the NOWIND model and the second column shows the same for the OUTFLOW model at SFE = 5%. The circular markers in each panel represent the position of the sink particles formed in the simulations. The colour and size of the markers are scaled by the mass of the sink particles (see right-hand colour scale). The size of the markers should not be confused with the numerical size of the sink particles, which is constant with a radius of $r_{\rm sink} = 250\,\rm AU$. The OUTFLOW model produces 48 sinks compared with 21 sinks in the NOWIND model. The SFR during the main star formation stages is reduced by a factor ~ 2 in the OUTFLOW model compared to the NOWIND case (see Tab. 2.1), and there is less heating in the OUTFLOW model (compare the bottom panels).

the ability of the stellar heating feedback to suppress fragmentation is significantly reduced when jet/outflow feedback is included.

The influence of the outflows in promoting star formation by redirecting accretion flows and in reducing the stellar heating efficiency can be inferred from Fig. 2.2. The figure shows the gas density structure and the temperature distribution of the region within the marked squares in Fig. 2.1 for each of the models at the same simulation time. At the time the OUTFLOW model has reached SFE = 5%, the NOWIND model has already reached SFE = 11%. Even in this small region of size 0.6 pc, the OUTFLOW model has almost double the number of stars. Since the considered region of both the models are now viewed at the same simulation time $t = 0.69\,\mathrm{Myr}$, we can say with confidence that the increase in the number of sinks with the inclusion of outflows is not just because of the slow star formation rate, i.e., the OUTFLOW model being more evolved than the NOWIND model when considered at the same SFE (see also panel (c) in Fig. 2.4). The stars in the OUTFLOW model are relatively lower in mass, and also the main filament in which most of the stars form in this region breaks into several sub-fragments due to the action of the jets/outflows. By contrast, the NOWIND model preserves the main filament structure with significantly less fragmentation, and the matter within the main filament is accreted by the existing stars. Clearly, the stellar heating is more efficient in the NOWIND model. The gas temperature in the immediate regions around the high-mass stars in the NOWIND simulation reach a few hundred Kelvin, which leads to suppression of fragmentation.

Fig. 2.3 presents the time evolution of a 0.4 pc sub-region in the cloud of NOWIND and OUTFLOW simulations with turbulence realisation T2. At $t = 0.25\,\mathrm{Myr} = 0.31\,t_{\mathrm{ff}}$ (first panel), there are four over-dense regions close to the already formed sink particle, marked as o1, o2, o3 and o4. The sink particle in the OUTFLOW case is lower in mass than the one in the NOWIND case because of the mass loss through jet/outflows. The outflow axis of the sink is parallel to the filament, which can be inferred from the velocity field lines and the orientation of the heating zones around the sink particle. The radiative flux is primarily in the directions of the disc/outflow axis, because of the extinction by dust particles in the disc. It can be observed from the snapshots that the sink particles that formed in o2 and o1 in the OUTFLOW model at $t = 0.28\,\mathrm{Myr}$ and $t = 0.32\,\mathrm{Myr}$, respectively, only form much later in the NOWIND case. This suggests that protostellar outflows can trigger local star formation in nearby cores. Core o4 harbours a binary in both models, for which both components of the binary formed around the same time. In the NOWIND simulation, o3 does not form a star and all the gas is completely accreted

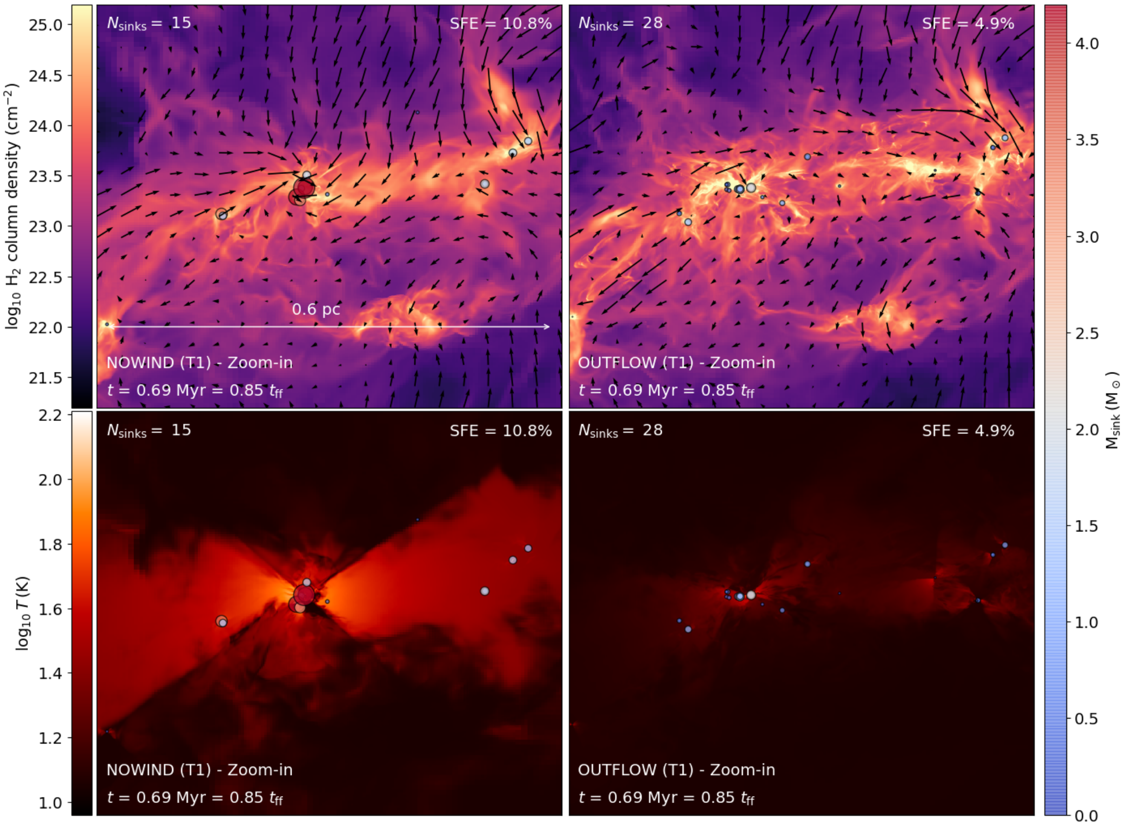

Figure 2.2: Zoom-in images of the region within the squares in Fig. 2.1 showing the contrast in the morphology and temperature structure between the NOWIND (left) and OUTFLOW (right) models at the same simulation time. The arrows represent the velocity field lines of the gas.

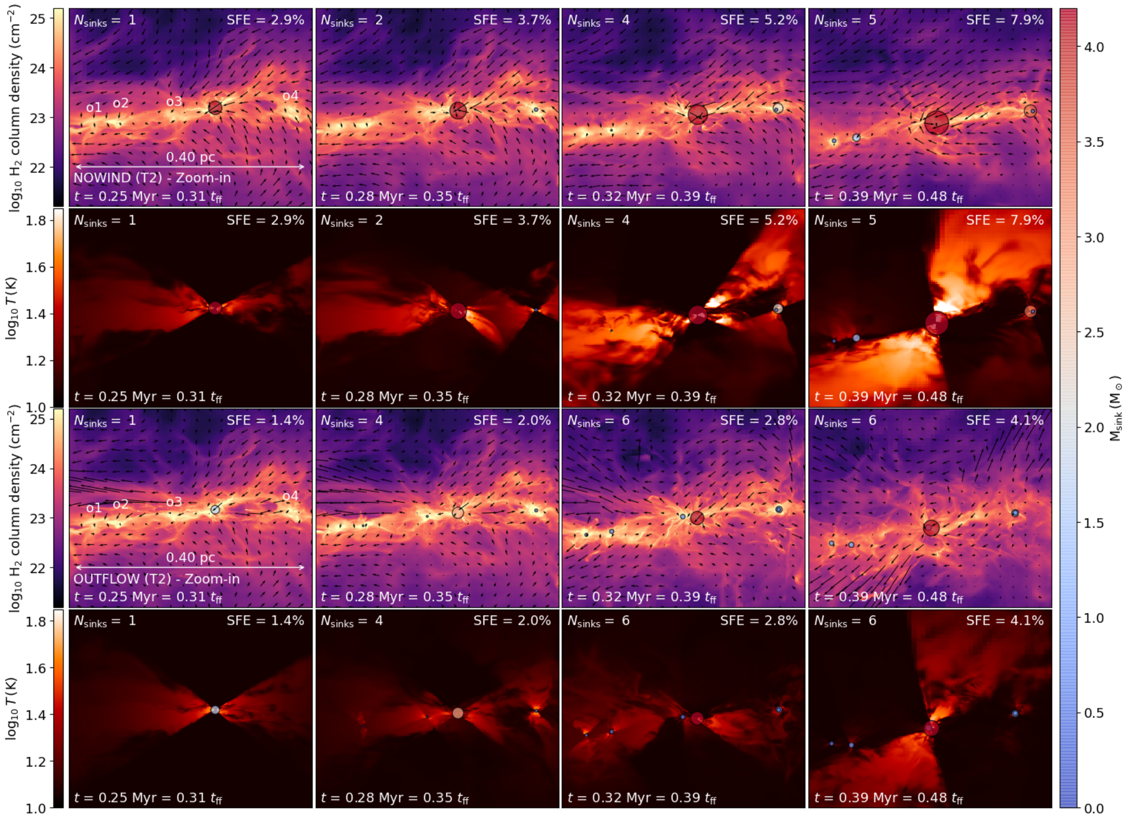

Figure 2.3: Zoom-in time snapshots of a filament in the T2 simulation of the NOWIND (rows 1 and 2) and the OUTFLOW (rows 3 and 4) models showing the evolution of overdensities within the filament and comparing the evolution of the formation (or absence thereof) of stars in locations o1, o2, o3, and o4, as labelled in the first panel of each simulation set.

by the high-mass sink particle. The higher gas temperature in o3 due to the higher luminosity of the massive sink particle in the NOWIND model has likely prevented the collapse of o3. However, in the OUTFLOW case, a sink particle does form in o3, which later goes into a close binary orbit with the massive sink particle.

We plot the evolution of the average number of sink particles and the average stellar mass with SFE and time in Fig. 2.4. We find that, at the same SFE, the ratio of the number of sinks formed in the OUTFLOW model to that in the NOWIND model is 2.1 ± 0.1 averaged over the SFE range 1–5%. Li et al. (2010) also find that their simulation including outflow feedback has twice as many stars as their simulation with no outflows when compared at the same SFE. When compared at the same time, the number of sink particles in the OUTFLOW model is higher by a factor of 1.3 ± 0.1 in the range $0.1 < t_{\rm elap}/t_{\rm ff} < 0.3$. The momentum injection by the outflows and the reduced heating effect are responsible for the difference in the number of sink particles between the models when compared at the same time.

Federrath et al. (2014) detect that the inclusion of outflow feedback in simulations increases the number of stars by a factor of ~ 1.5 compared to simulations with no outflows at the same time. The simulation model in Federrath et al. (2014) does not include the stellar radiative heating and therefore the momentum injection by the outflows is solely responsible for the increase in the number of stars in their study. This, along with the fact that they also observe an increase by a similar factor as in our case, suggests that, although the reduced heating effect is important, the momentum injection by outflows plays a more significant role in increasing fragmentation. The average sink particle mass ($\overline{M}_{\mathrm{avg}}$) in the NOWIND case increases with the evolution of the cloud, while it is relatively constant with a value of $0.7 \pm 0.1\,\mathrm{M}_{\odot}$ in the OUTFLOW case. Here the measurement is made by taking the average of $\overline{M}_{\mathrm{avg}}$ over the SFE range 1–5% with the error bars corresponding to the standard deviation over this SFE range. The overbar in $\overline{M}_{\mathrm{avg}}$ denotes the average over the 10 simulations. At the same SFE, $\overline{M}_{\mathrm{avg}}$ in the OUTFLOW simulations is lower than in the NOWIND simulations by a factor of 2.2 ± 0.2, reflecting the fact that the number of stars increased by a similar factor at the same SFE. When compared at the same time, $\overline{M}_{\mathrm{avg}}$ in the OUTFLOW simulations is lower by a factor of 2.6 ± 0.2. Fig. 2.5 presents the average SFE and average star formation rate per free-fall time ($\mathrm{SFR}_{\mathrm{ff}}$ in %) (Krumholz & McKee 2005; Federrath & Klessen 2012) as functions of time. We observe that the star formation rate per free-fall time averaged over 10 simulations, $\overline{\mathrm{SFR}}_{\mathrm{ff}}$ (%), increases with time, but the progression is slower in the OUTFLOW model, because of self-regulation by the outflows. $\overline{\mathrm{SFR}}_{\mathrm{ff}}$ in the NOWIND and OUTFLOW simulations are $15 \pm 3\%$ and $7 \pm 2\%$, respectively, in the range $0.05 < t_{\mathrm{elap}}/t_{\mathrm{ff}} < 0.25\,t_{\mathrm{ff}}$ (see Tab. 2.1). Therefore, the stellar outflows reduce the SFR by a factor of ~ 2. Our results are consistent with Federrath et al. (2014) who also observed a reduction in the SFR by the same factor with the inclusion of outflow feedback. As mentioned above, one major difference between our model and that of Federrath et al. (2014) is that stellar heating was missing in the latter. However, the SFR is relatively insensitive to radiative feedback (Mathew & Federrath 2020). Although our value of $\mathrm{SFR}_{\mathrm{ff}}$ (OUTFLOW case) is higher than the average value in the Milky Way ($\sim$ 1–2% per free-fall time) (Krumholz & Tan 2007; Khullar et al. 2019), it is still within the dispersion of $\mathrm{SFR}_{\mathrm{ff}}$ obtained in observational surveys and from theoretical predictions (e.g., Krumholz & McKee 2005; Evans et al. 2009; Hennebelle & Chabrier 2011; Murray 2011; Federrath & Klessen 2012; Vutisalchavakul et al. 2016; Lee et al. 2016).

Finally, we mention that the properties of the turbulence can significantly affect the SFR (Federrath & Klessen 2012) and the IMF (Schmidt et al. 2010; Nam et al. 2021). For example, the effect of the turbulence driving and Mach number on the

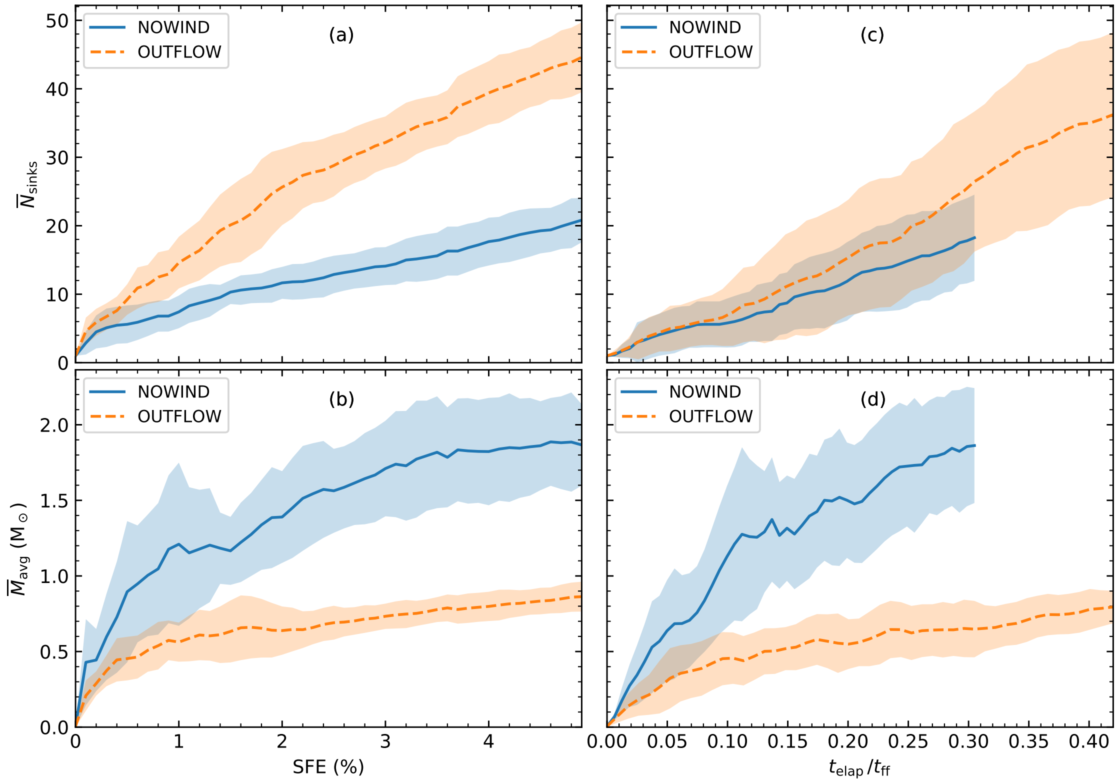

Figure 2.4: The left panels show (a) the average number of sink particles formed and (b) the average stellar mass as a function of the star formation efficiency (SFE in %). The right panels (c) and (d) indicate the average number of sink particles formed and the average stellar mass, respectively, as a function of time. All quantities shown here for both the models correspond to the average values obtained from 10 simulations (T0–T10), and the coloured bands represent the standard deviation over the set of these 10 simulations. Here $t_{\rm elap}/t_{\rm ff}$ is the elapsed time from the formation of the first sink particle in units of the free-fall time and is distinguished from the time t in the above column density maps, which is the time measured from the moment self-gravity was turned on.

SFR and IMF with the physics included here will be the main focus of a follow-up study.

2.3.1 Sink particle mass distributions

The mass distribution of stars formed in the 10 simulations of each model is presented in Fig. 2.6. With the introduction of the outflow feedback, the sink mass distribution (SMD) shifts to lower masses, with the median and average masses reduced by factors of 2.0 and 2.1, respectively. However, putting aside the shift in mass, the OUTFLOW SMD has almost the same shape as that of the NOWIND SMD. This means that outflows do not seem to significantly change the basic shape (or functional form) of the IMF, and thus, the same basic mechanism(s) that set

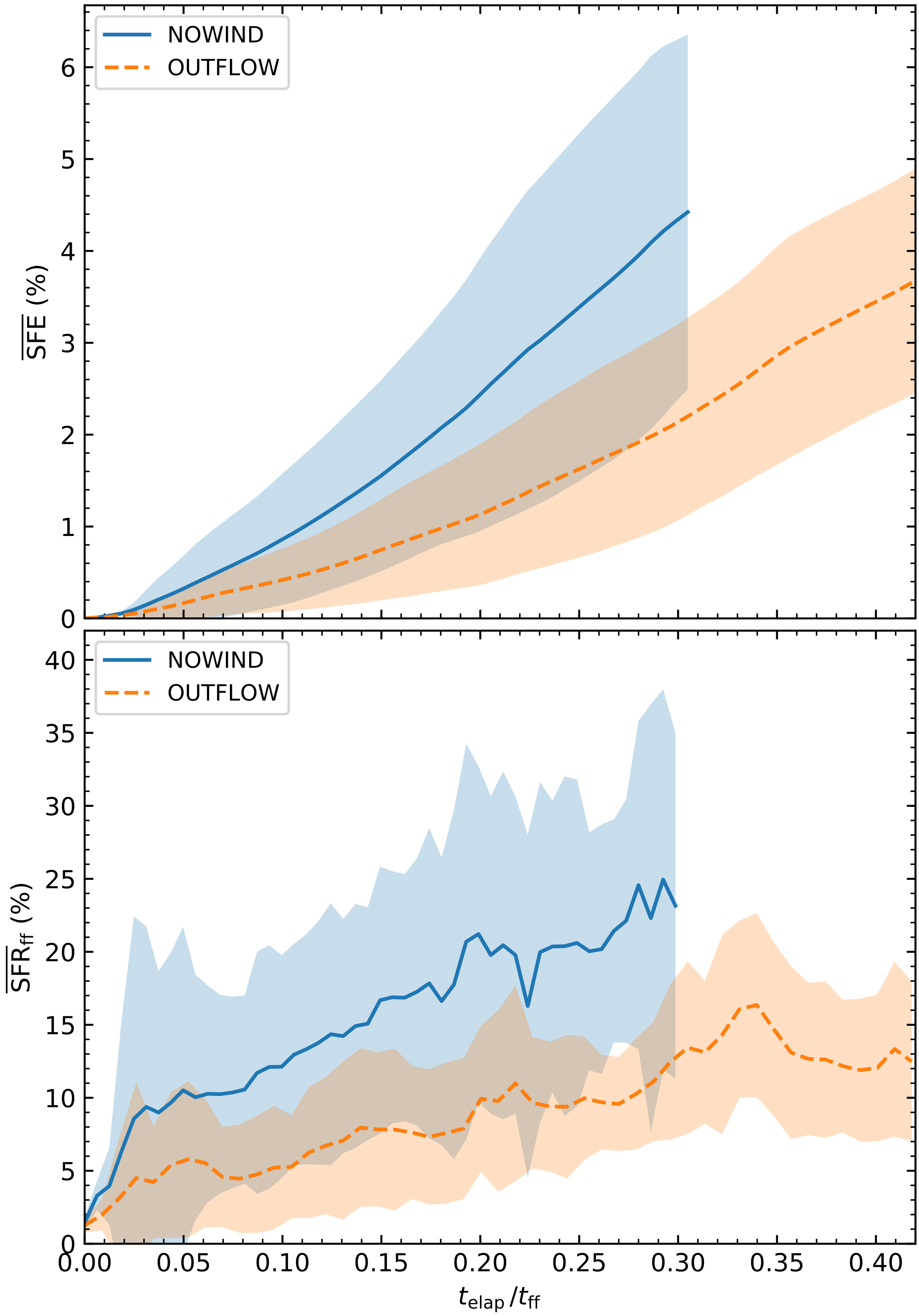

Figure 2.5: The top and bottom panels show the time evolution of the average SFE and average star formation rate per free-fall time ($\mathrm{SFR}_{\mathrm{ff}}$ in %), respectively.

the high-mass slope of the IMF and a turnover at intermediate masses seem to be at play regardless of whether jet/outflow feedback is included or not. A log-normal function with a standard deviation for the Chabrier IMF fits both models well at the low-mass end, with a peak at $1.0\,\mathrm{M}_{\odot}$ for the NOWIND distribution and $0.5\,\mathrm{M}_{\odot}$ for the OUTFLOW SMD. While the power-law fit to the high-mass end of the OUTFLOW SMD ($\Gamma = 1.5 \pm 0.3$) is slightly steeper than the fit to the NOWIND SMD ($\Gamma = 1.3 \pm 0.2$), they are statistically identical within the 1-sigma uncertainties.

The parallelism between the two distributions resembles the observed correlation between the observed core mass function (CMF) and the stellar IMF. The existence of a correspondence between the CMF and the IMF implies that a star's mass is decided at the core level. The recognition of dense cores as the direct progenitors of stellar objects allows us to explain why the overall form of the distribution did not change with the inclusion of mechanical feedback. Supersonic turbulence creates density enhancements of varying sizes, but not all of these over-densities form stars. Only the ones that exceed the threshold mass for collapse will form stars. Outflows do not create new density enhancements; instead, they increase the chance that a star forms in an over-density generated by gravo-turbulent fragmentation. This can be seen in Fig. 2.3, where the extra sink particle forms in an over-density that pre-existed (see Fig. 2.18 of Appendix A for another example). It should then naturally follow that the mass distribution of extra sinks in the OUTFLOW SMD also reflects the distribution of over-density masses, i.e., the typical mass of the extra sinks should conform to the typical over-density mass with an efficiency factor decided by the mass loss via winds and entrainment of the envelope material by jets.

Observational surveys of dense cores find high-mass CMF slopes of Γ between 1.0 and 1.6 (Motte et al. 1998; Testi & Sargent 1998; Johnstone et al. 2000; Nutter & Ward-Thompson 2007; Alves et al. 2007), similar to the Salpeter slope of the IMF, but the range of CMF slopes does not impose strong constraints on the similarity of the CMF and the IMF. Nevertheless, we find that the introduction of the outflow feedback shifts the IMF to lower masses, but virtually sustaining its overall shape. Within the limit of these arguments, the present set of simulations suggests that jet/outflow feedback can be responsible for the observed correlation and shift between the CMF and the IMF (Alves et al. 2007; Clark et al. 2007; Smith et al. 2008).

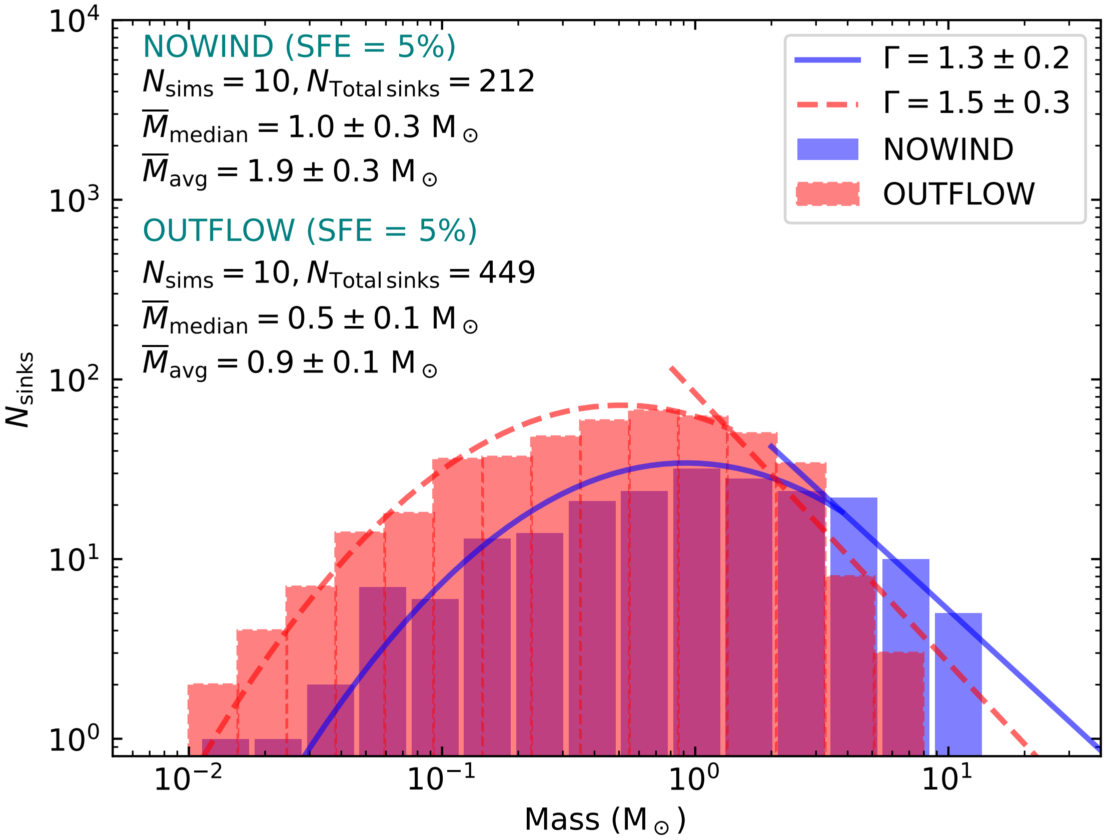

Figure 2.6: Comparison between the sink mass distribution of the NOWIND (no outflow feedback) and OUTFLOW models at SFE = 5%. The data compilation in each model is acquired from 10 simulations. The histogram with solid edges and the solid curves correspond to the NOWIND model, while the histogram with dashed edges and the dashed curves correspond to the OUTFLOW model. The standard deviation of the lognormal curves are equal to that of the Chabrier (2005) IMF ($\sigma = 0.55$), but the peaks are located at around the median (mean) mass of the respective SMDs, i.e., at 1.0 (1.9) M$_\odot$ for NOWIND and 0.5 (0.9) M$_\odot$ for OUTFLOW. $\overline{M}_{\rm median}$ and $\overline{M}_{\rm avg}$ are the median and average sink masses averaged over the 10 simulations at SFE = 5%, where the error bars represent the standard deviation (see Tab. 2.1).

2.4 Comparison with observational data and theoretical IMF models

2.4.1 Comparisons with observed IMFs

Fig. 2.7 compares the distribution of the sink masses formed in the 10 simulations of each model with various fits to the observed IMF studied in the literature since Salpeter (1955) (dash-dotted line). We compare the SMDs with the system IMFs rather than the individual-star IMFs, because we do not resolve all the low-order multiple systems. The Chabrier (2005) system IMF is represented by a short-dotted curve. The Parravano et al. (2011) IMF (long-dotted line) is an analytical model defined by multiple parameters based on observational constraints, e.g., the slope of the high-mass end of the IMF and the ratio of the number of brown dwarfs (BDs) to the number of stars (see also Paresce & De Marchi 2000). This function predicts a higher fraction of BDs below $0.03\,\mathrm{M}_\odot$ than the Chabrier (2005) IMF. Da Rio et al. (2012) (solid line) measured the IMF in the Orion Nebula Cluster (ONC) and observed a steep decline in the brown dwarf regime. Their census was focused on the low-mass range and they successfully fit a log-normal function to the obtained mass distribution. We use the best-fit parameters, namely the characteristic mass m_c and the standard deviation $\sigma\,(\log m)$, from table 3 of Da Rio et al. (2012) to reproduce the log-normal fit to the mass distribution they derived by assuming a Baraffe et al. (1998) evolutionary model. We then combine it with a Salpeter-like power-law tail, similar to what was done in Krumholz et al. (2012b). Kroupa et al. (2013) argue that stars and brown dwarfs (BDs) must be represented by separate mass functions because the hypothesis that BDs form in the same manner as stars contradicts the observed binary properties of BDs. The Kroupa et al. (2013) stellar system IMF (taken from Fig. 25 in Kroupa et al. 2013) and BD IMF (short-dashed and long-dashed lines) result from random pairing of companions out of the canonical IMF (Kroupa 2001) by assuming initial binary fractions of 100% and 0%, respectively. Damian et al. (2021) (dash-dot-dotted line) studied the role of environmental conditions on the form of the IMF by analysing the mass distribution of nine young clusters that differ in terms of the stellar density, number of massive stars and the Galactocentric distance. They observe no significant disparity between the mass distributions and find that the low-mass end of the IMF can be fitted by a log-normal distribution peaked at 0.32 ± 0.02 and $\sigma = 0.47 \pm 0.02$ (in logarithmic scale).

The NOWIND SMD (top panel in Fig. 2.7) peaks at around $1\,\mathrm{M}_\odot$ while the the system IMFs of Chabrier (2005) (dotted line) and Da Rio et al. (2012) (solid line)

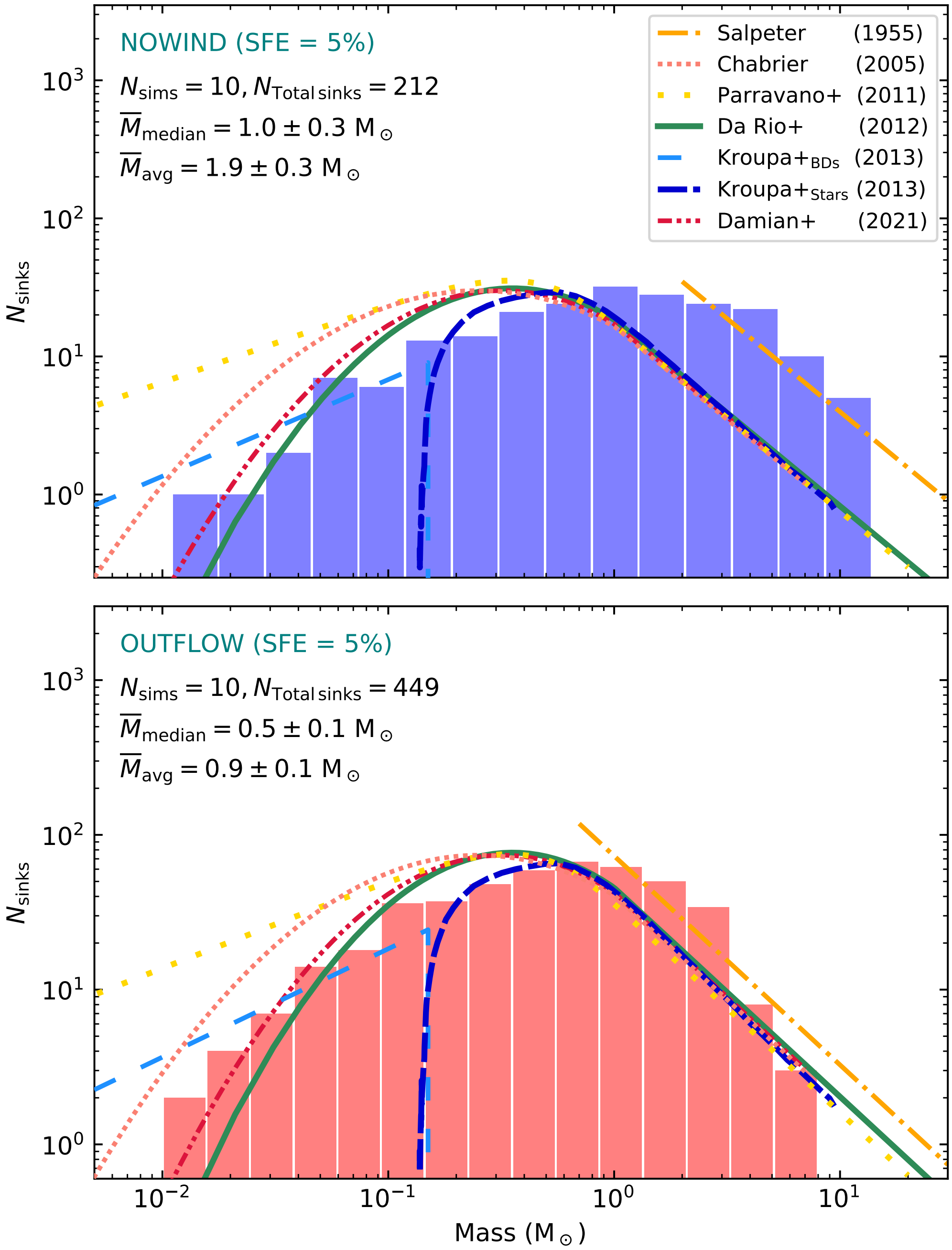

Figure 2.7: Top panel: Comparison between the sink mass distribution of the NOWIND model at SFE = 5% with various observational IMFs. Bottom panel: Same as the top panel, but for the OUTFLOW data. The plotted curves are the system IMF models, based on observations, by Salpeter (1955) (dash-dotted), Chabrier (2005) (short-dotted), Parravano et al. (2011) (long-dotted), Da Rio et al. (2012) (solid), Kroupa et al. (2013) for brown dwarfs (long-dashed) and stars (short-dashed), and Damian et al. (2021) (dash-dot-dotted).

have peak masses of $\sim 0.25\,\mathrm{M}_\odot$ and $0.35\,\mathrm{M}_\odot$, respectively. In contrast, the broad peak of our OUTFLOW SMD (bottom panel in Fig. 2.7) is located at around 0.4–$0.6\,\mathrm{M}_\odot$. Clearly, the introduction of the outflow feedback has resulted in a mass scale of the sink particles comparable to that of the observational models, although the peak mass is still higher by a factor of ~ 2. The slope of the power-law fit to the high-mass end of our SMD (OUTFLOW; $\Gamma = 1.5 \pm 0.3$) is slightly steeper than the Salpeter slope ($\Gamma = 1.35$), but is well within the 1σ uncertainties, both from our fit and from observational estimates (Weisz et al. 2013; Offner et al. 2014). The median stellar mass of our SMD is $0.5 \pm 0.1\,\mathrm{M}_\odot$ and the average mass is $0.9 \pm 0.1\,\mathrm{M}_\odot$ (at SFE = 5%). We also calculate M_{50} which is, as defined in Krumholz et al. (2012b), the 50th percentile mass associated with a cumulative mass distribution, i.e., the sum of all the stellar masses lower than M_{50} is half the total mass of the distribution. We find $M_{50} = 1.5\,\mathrm{M}_\odot$ which is close to the value of $\sim 2\,\mathrm{M}_\odot$ for the observed IMFs. The ratio of the number of sink particles with sub-stellar masses ($M_{\mathrm{sink}} \leq 0.08\,\mathrm{M}_\odot$) to that of the sink particles with stellar masses ($0.15 < M_{\mathrm{sink}} \leq 1.0\,\mathrm{M}_\odot$) is $43/225 = 0.19$, which is consistent with observations (where close binaries are unresolved) that approximately one BD is formed per every five late-type (sub-solar) stars (Andersen et al. 2006, 2008; Thies & Kroupa 2007; Parravano et al. 2011; Kroupa et al. 2013).

2.4.2 Comparisons with gravo-turbulent theoretical models of the IMF

In Fig. 2.8, we compare the NOWIND (top panel) and OUTFLOW (bottom panel) SMDs with the mass function (MF) predicted by different theoretical models of the CMF/IMF for parameters relevant to our simulation setup, e.g., the Mach number $\mathcal{M} = 5$ and the turbulence driving parameter $\zeta = 0.5$. The resulting functions from the gravo-turbulent theories (Padoan & Nordlund 2002; Hennebelle & Chabrier 2008; Hopkins 2012) are analogous to the mass distribution of cores (CMF) and the models are generally multiplied by a core-to-star efficiency factor ϵ (primarily to account for the impact of outflows) to facilitate comparison with the observational IMFs or the MF obtained in numerical studies. Therefore the comparison between the NOWIND SMD and the theoretical MFs is almost equivalent to a comparison between the OUTFLOW SMD and the theoretical MFs multiplied by an efficiency factor ($\epsilon \sim 0.5$ in our study).

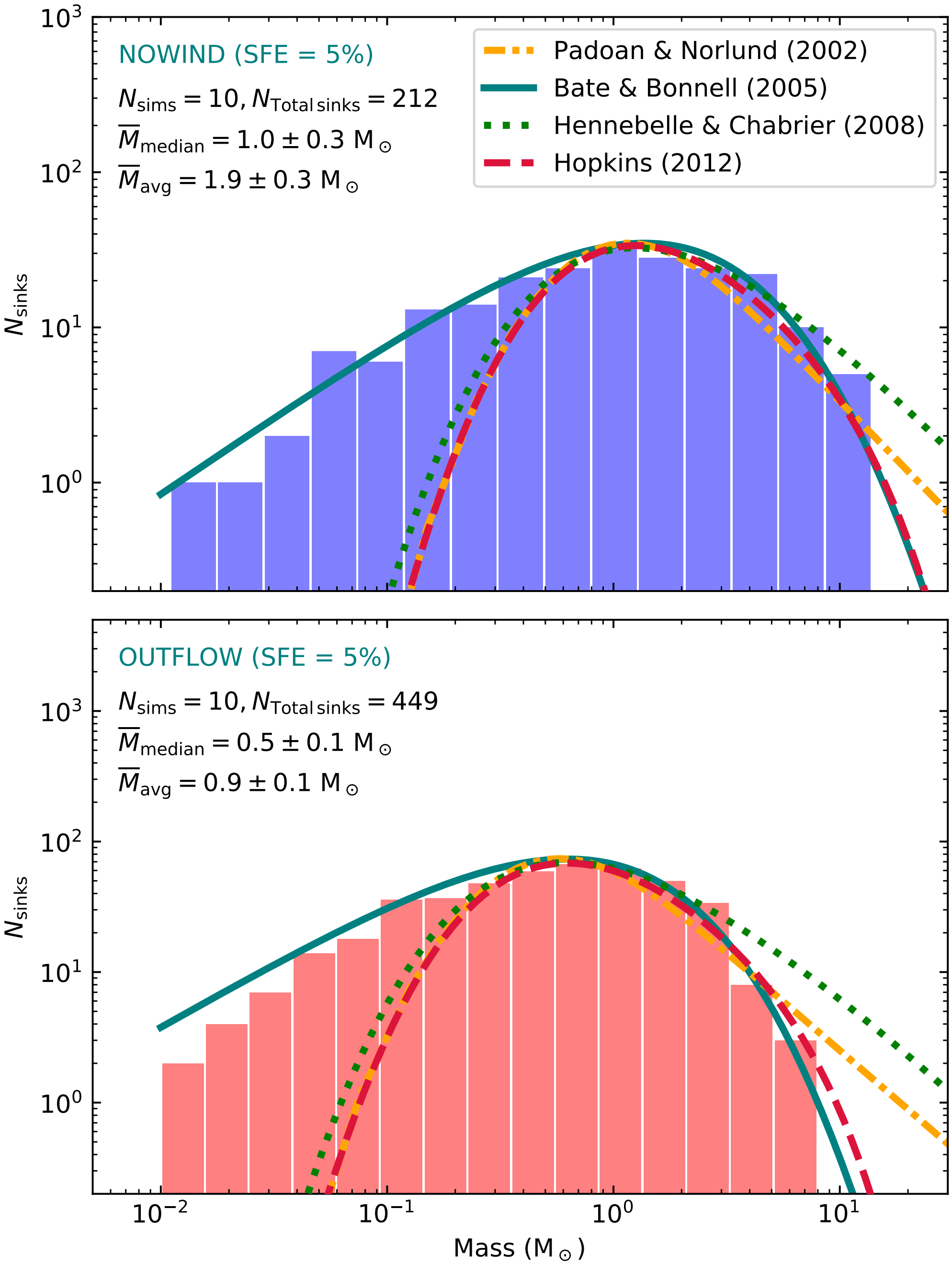

Figure 2.8: Top panel: Comparison between the sink mass distribution of the NOWIND model at SFE = 5% with various theoretical models of the CMF/IMFs ($\mathcal{M} = 5$, $\zeta = 0.5$, $\beta = 2$, $M_{\rm J,0} \approx 2$). The curves correspond to Padoan & Nordlund (2002) (dash-dotted), Bate & Bonnell (2005) (solid), Hennebelle & Chabrier (2008) (dotted), and Hopkins (2012) (dashed) CMF/IMFs. The Hopkins (2012) model has been shifted to lower masses by a factor of 2 such that the position of their peak coincides with the peak mass bin of the SMD. Bottom panel: Same as the top panel, but for the OUTFLOW simulations. Here the gravo-turbulent theoretical models (Padoan & Nordlund 2002; Hennebelle & Chabrier 2008; Hopkins 2012) have been shifted to lower masses by a factor of 2 from their positions in the top panel in order to account for the effect of outflows (core-to-star efficiency $\epsilon = 0.5$).

The Padoan & Nordlund (2002) model

According to the Padoan & Nordlund (2002) model, star-forming cores are the densest regions in the shocked layers of gas formed by supersonic turbulence. The model approximates the size of cores as the thickness of post-shock gas which in turn depends on the Mach number through the isothermal shock jump conditions. The scale dependence of Mach number (Larson 1981) and the connection between the Larson relation and the velocity power spectrum result in a distribution of core masses for which the slope of the high-mass tail can be calculated from the velocity power spectral index β in $P(k) \propto k^{-\beta}$ (Nam et al. 2021). The mass distribution of unstable cores is given by

$$N(M)\,d\log M \propto M^{-\Gamma}\left[\int_0^M p(M_\mathrm{J})\,\mathrm{d}M_\mathrm{J}\right] d\log M, \tag{2.14}$$

where $p(M_\mathrm{J})\,\mathrm{d}M_\mathrm{J}$ is the distribution of the Jeans mass and the integral gives the fraction of cores of mass M that are Jeans unstable. For $\beta = 2$, which is the typical one-dimensional power spectral index found for molecular clouds in observations and simulations (Ossenkopf & Mac Low 2002; Heyer & Brunt 2004; Roman-Duval et al. 2011; Federrath 2013a; Federrath et al. 2021), the high-mass slope of the IMF based on the MHD shock jump conditions is predicted to be (Padoan & Nordlund 2002)

$$\Gamma = 3/(4-\beta) = 1.5. \tag{2.15}$$

The mass distribution at low masses is decided by the Jeans mass distribution, which in turn is determined by the probability density function (PDF) of the turbulent gas, which is approximately log-normal with a standard deviation defined by $\sigma_\mathrm{s}^2 = \ln(1 + b^2\mathcal{M}^2)$ (see Padoan et al. 1997a; Federrath et al. 2008). The peak of the distribution is influenced by the scale of the mean thermal Jeans mass $M_{\mathrm{J},0}$, which is ~ 2–$3\,\mathrm{M}_\odot$ in our simulations.

The Padoan & Nordlund (2002) model is represented by dash-dotted curves in both the top and bottom panels of Fig. 2.8. The mass distribution has been reproduced by using $\mathcal{M} = 5$, $b = 0.4$, $\beta = 2$ and $M_{\mathrm{J},0} = 2$ as the input parameters for their model. In the bottom panel, the theoretical models have been shifted to lower masses by a factor of 2 from their positions in the top panel in order to account for the impact of the outflow feedback.

The Hennebelle & Chabrier (2008) model

Hennebelle & Chabrier (2008) apply the Press-Schechter formalism (Press &

Schechter 1974) to study condensations in molecular clouds. In this context, the over-densities or density contrasts are created by supersonic turbulent motions. The spectrum of collapsing cores is obtained by statistically calculating the mass fraction of self-gravitating regions assuming a Gaussian field of density fluctuations. These regions are identified based on whether their mass exceeds the Jeans mass, also taking into account the support by turbulent pressure. The derived analytical function for the CMF/IMF consists of a log-normal component and a power-law component. The mass distribution has a power-law nature in the high-mass regime, but gradually flattens and then declines sharply at $M \ll (1+b^2\mathcal{M}^2)^{-3/2}\, M_{\mathrm{J},0}$. Using their expression for the slope of the power-law mass spectrum based on the turbulence power spectral index $\beta = 2$, the prediction for the high-mass slope of the IMF is (Hennebelle & Chabrier 2008)

$$\Gamma \approx (\beta+3)/2\beta = 1.25. \tag{2.16}$$

We mention that, according to Hennebelle & Chabrier (2013), the high-mass slope becomes slightly steeper if the time-dependence is taken into account in the derivation of the IMF. We plot the Hennebelle & Chabrier (2008) CMF/IMF by using Eq. 44 in Hennebelle & Chabrier (2008) with input parameters as $\mathcal{M} = 5$, $b = 0.4$, $\beta = 2$, $M_{\mathrm{J},0} = 2$ and $\mathcal{M}_* = 1.4$, which approximately represent our simulation configuration. The effective Mach number $\mathcal{M}_*$ corresponds to the velocity dispersion on the scale of the mean Jeans length. The model is depicted by dotted curves in Fig. 2.8.

The Hopkins (2012) model

Hopkins (2012) employ the excursion set theory (Bond et al. 1991) based on the principle of random walks to obtain the mass spectrum of cores (last crossing distribution) and giant molecular clouds (first crossing distribution). An important signature of the model is that, for a Gaussian distribution of density contrasts, the density variance at any given scale is not assumed but is inferred from the ISM properties. The form of the MF strongly depends on the Mach number at the injection scale of turbulent energy, characterised by the Mach number $\mathcal{M}_h$ on the galactic scale-height. Further, the theory resolves the ‘cloud-in-cloud’problem, i.e., the over-counting associated with a structure embedded in another structure of a larger scale. The MF transitions from a power law to a log-normal behaviour at the turnover mass M_{sonic}, which is defined by the sonic scale R_{sonic}, i.e., the scale at which the turbulent flow becomes subsonic (Federrath et al. 2021). We use the Python code developed by Nam et al. (2021) to reproduce the Hopkins (2012) mass function (dashed line in Fig. 2.8). We point out that here we define $\mathcal{M}_h = 5$, which is the Mach number corresponding to the velocity dispersion on the driving scale of the turbulence ($L/2$) in the simulations. Our simulations do not have a characteristic scale height because of the periodic boundary conditions. Nam et al. (2021) show that such an ambiguity in the choice of $\mathcal{M}_h$ can significantly affect the results, particularly, the shape of the IMF as predicted in the Hopkins (2012) model.

The mass functions of the above three theoretical models matches considerably well with our IMF in the high-mass regime and down to the low-mass range, but falls off exponentially towards the very low-mass range, faster than our SMD, i.e., the models do not predict any brown dwarfs based on the input parameters relevant to our simulations.

2.4.3 Formation of sub-stellar objects

For the cloud properties adopted in our simulations, i.e., $\mathcal{M} = 5$, $\zeta = 0.5$, $T = 10\,\mathrm{K}$, $n = \rho_\circ/(2.35\, m_\mathrm{H}) = 1.7 \times 10^3\,\mathrm{cm}^{-3}$, the three theoretical models of the IMF introduced above predict very few dense cores small enough to produce BDs (Padoan & Nordlund 2004; Hennebelle & Chabrier 2008, 2009). In fact, we rarely observe sub-stellar objects forming in such small, marginally isolated over-densities in our simulations. Some of our very low-mass (VLM) sink particles ($< 0.1\,\mathrm{M}_\odot$) were the ones that were ejected from high-order systems, which truncates their accretion (Reipurth & Clarke 2001; Bate et al. 2002a), and some formed as companions to other sinks that are slightly higher in mass. Most of the VLM objects in our simulations emerged in small clumps where a cluster of stars is formed. Fig. 2.9 presents an example of the formation of VLM objects in a clump. The first snapshot shows sink particles forming at different locations of the clump. With time, they grow in mass and move towards the bottom of the potential well. When the stars are in close proximity to each other, multiple new objects are formed. These objects are likely to have formed due to fragmentation of the extended discs (Bate et al. 2002a; Goodwin & Whitworth 2007; Stamatellos et al. 2007, 2011; Rogers & Wadsley 2012; Thies et al. 2015) of some of the initial sink particles, encouraged by dynamical interactions, e.g., star-disc or disc-disc collisions (Boffin et al. 1998; Watkins et al. 1998; Shen et al. 2010). Thies et al. (2010) find that BDs can form by tidally induced fragmentation in extended discs due to close encounters with another star. Towards the end of the simulation, the cluster is dispersed because of gas removal from the clump. It is evident from the last time snapshot that in the process of clustering and eventual dispersal, at least 8 VLM objects were formed.

It is in the clustered regions, similar to the above example, that the influence of

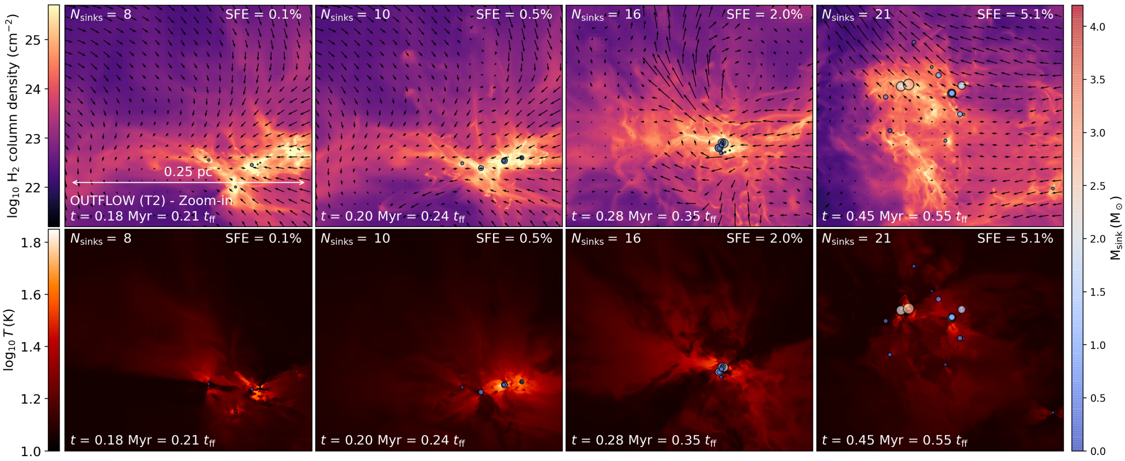

Figure 2.9: Time evolution (panels from left to right) of a clump in the T2 simulation (same simulation as the one considered in Fig. 2.3, but a different region of the cloud is studied here) of the OUTFLOW model illustrating the formation of sub-stellar objects.

Table 2.2: Calculated parameter values for the Bate & Bonnell (2005) IMF model.

Model (1)	$\overline{\dot{M}}_{\rm acc}$ [$\mathrm{M_\odot\,yr^{-1}}$] (2)	$\sigma_{\rm acc}(\log M)$ (3)	$t_{\rm eject}$ [yr] (4)	$\mathrm{T_p}$ [yr] (5)
1. NOWIND	1.6×10^{-5}	0.29	1.05×10^{5}	3.08×10^{5}
2. OUTFLOW	5.5×10^{-6}	0.26	1.33×10^{5}	4.32×10^{5}

Notes. The values listed here are averages of the parameter values derived from the 10 simulations (realisations of the turbulence) for each simulation set, NOWIND and OUTFLOW. The Bate & Bonnell (2005) IMF fits (solid curves in Fig. 2.8) have been obtained by using these parameter values.

stellar luminosity (including that due to accretion) is paramount. Despite the fact that the heating of the disc by the central source is significantly reduced due to the shielding by dust particles, the disc is within the radius of influence of all the other stars because of the crowding. The increase in temperature due to the overlap of heating zones of all the stars would be enough to reduce the degree of fragmentation (Mathew & Federrath 2020). Although outflows weaken the overall influence of stellar radiative heating feedback, the gas temperature would still be high enough to limit fragmentation, because of the contribution from multiple stars (see more examples of BD formation in Fig. 2.19 and Fig. 2.20 of Appendix A).

Since our results suggest that dynamical interactions are important for the formation of very low-mass objects, we also compare our simulation IMFs with the semi-analytical Bate & Bonnell (2005) IMF model, which proposes that the IMF is controlled by the combination of accretion (Bonnell et al. 1997, 2001a) and stochastic dynamical ejection (Reipurth & Clarke 2001; Bate et al. 2002a).

The Bate & Bonnell (2005) model

Bate & Bonnell (2005) IMF model assumes that all stellar and sub-stellar objects form with similar masses defined by the opacity limit for fragmentation. These objects then grow in mass at a constant rate until their accretion is terminated by dynamical ejection from dense gas region they formed in. The distribution of the accretion rate among the objects is assumed to be log-normal and the probability that an object is ejected at time t is proportional to $\exp(-t/t_{\rm eject})$, where $t_{\rm eject}$ is the characteristic ejection time-scale. The Bate & Bonnell (2005) fits to our simulation IMFs can be obtained by calculating the following parameters: the mean accretion rate $\overline{\dot{M}}_{\rm acc}$, the standard deviation in the accretion rates $\sigma_{\rm acc}(\log M)$, the characteristic ejection time $t_{\rm eject}$, the minimum stellar mass $M_{\rm min}$, and the time period of the cluster formation $\mathrm{T_p}$. The quantity $\overline{\dot{M}}_{\rm acc}\, t_{\rm eject}$ gives approximately the peak mass of the IMF in the model. The dispersion in the accretion rates $\sigma_{\rm acc}(\log M)$ defines the high-mass and low-mass slopes, and the minimum stellar mass $M_{\rm min}$ sets the low-mass cut-off of the IMF. The time period $\mathrm{T_p}$ is the time elapsed between the formation of the first star and the end of the simulation. The calculated parameter values for each of the models are shown in Tab. 2.2, which correspond to the averages of the parameter values obtained in the 10 simulations for each set (NOWIND and OUTFLOW). We set $M_{\rm min} = 0.01\,\mathrm{M_\odot}$ as the low-mass cut-off of the IMF fit for both the simulation models and substitute the above parameter values into equations 10–12 of Bate & Bonnell (2005) to reproduce their fits for our simulation IMFs. The Bate & Bonnell (2005) model is represented by solid curves in Fig. 2.8. The model matches well with our simulation IMFs, especially in the very low-mass regime, which was underestimated by the models based on turbulent fragmentation. This shows that stochastic dynamical ejections play an important role in determining the low-mass end of the IMF (see also Basu & Jones 2004; Dib et al. 2010; Myers 2011; Maschberger et al. 2014).

2.4.4 Stellar kinematics

Fig. 2.10 shows the sink particle velocity $|\mathbf{V}_{\rm sink}|$ immediately after creation (top panel) and $|\mathbf{V}_{\rm sink}|$ at the end of the simulations, i.e., at SFE = 5% (bottom panel) as functions of the their final mass (mass at SFE = 5%) in the OUTFLOW model. The top panel seems to exhibit a trend of low-mass objects having a higher velocity than the high-mass objects, i.e., the velocity at the birth of the objects correlates (negatively) with their final mass to some extent, which is consistent with the findings of Bonnell et al. (2008). However, there is no clear correlation between the velocity of the objects at the end of the simulation and their final mass. The apparent

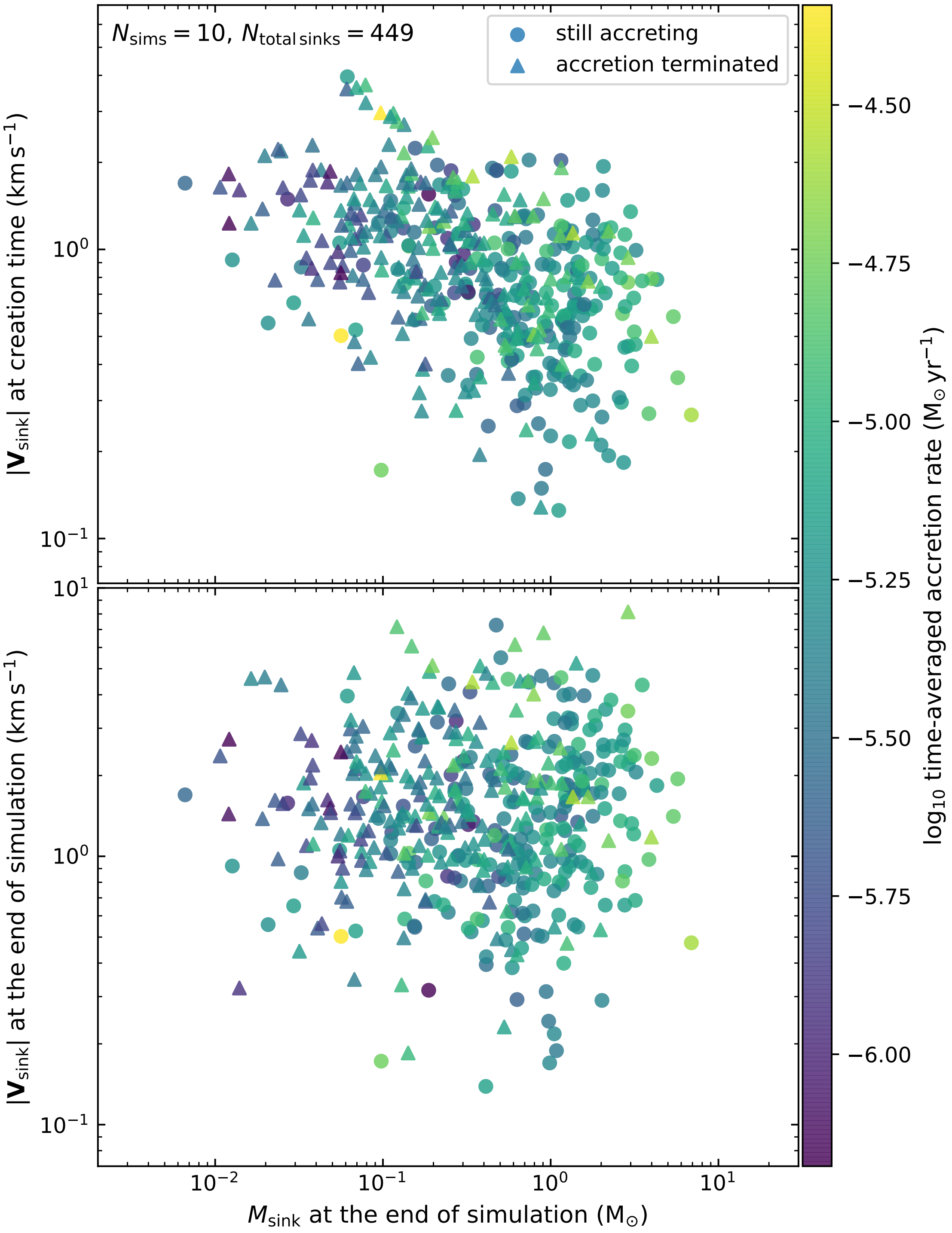

Figure 2.10: Top panel: velocity of the sink particles immediately after formation, as a function of their mass at SFE = 5%. The circular markers represent the sink particles that are still accreting and the triangular markers represent the sinks that have stopped accreting when SFE = 5% is reached. Each of the markers are colour-coded based on the time-averaged accretion rate of the sink particle (see right-hand colour scale). The data compilation is obtained from the ten OUTFLOW simulations. Bottom panel: same as top panel, but for the sink particle velocities at SFE = 5%.

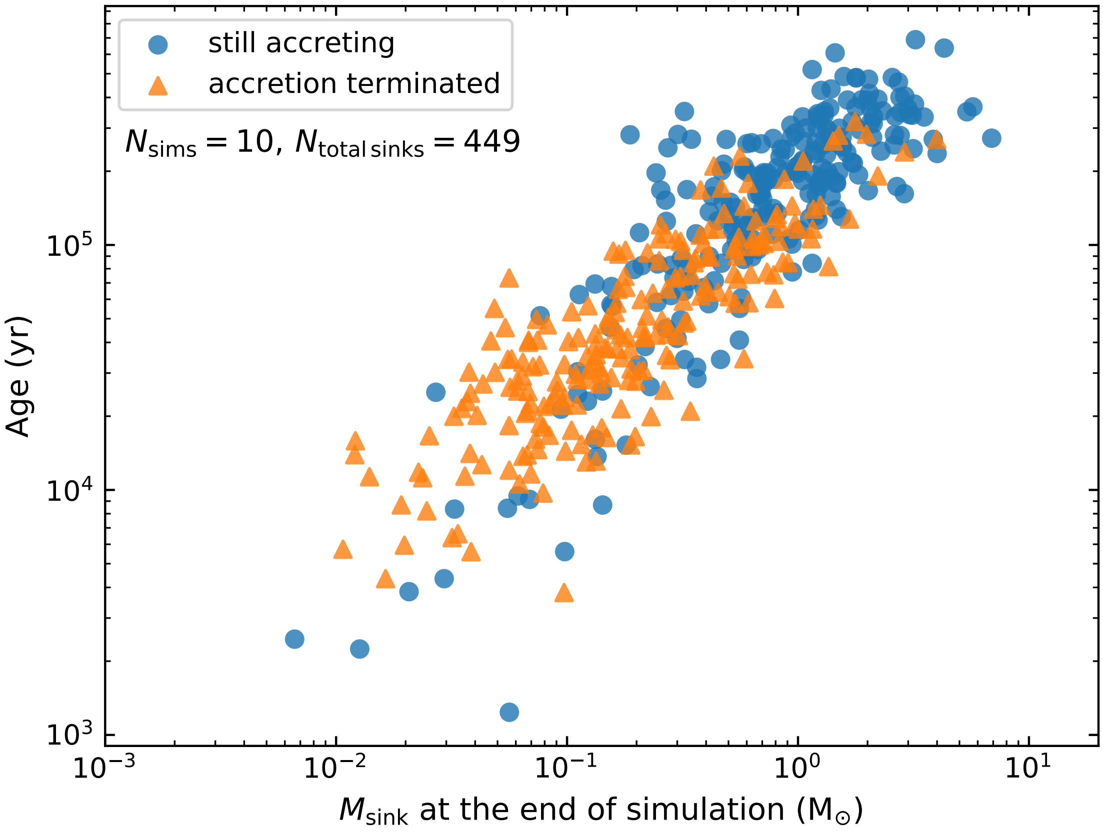

Figure 2.11: Age of the sink particles at the end of the corresponding simulation (SFE = 5%) in the OUTFLOW model. The circular markers represent the sink particles that are still accreting and the triangular markers represent the sinks that have stopped accreting at SFE = 5%. The age of the sink particles follows a roughly linear dependence on their final mass, similar to the simulations by Bate (2012).

uncorrelated behaviour in the bottom panel is because of the dynamical evolution of the objects (clustering and eventual dispersal as discussed above), which rearrange the velocities such that some of the more massive objects ($> 0.5\,\mathrm{M}_{\odot}$) attain higher velocities at later times, and therefore, the trend of the formation $|\mathbf{V}_{\mathrm{sink}}|$ with mass seen in the top panel, is lost at later times.

Fig. 2.11 shows the age of all the sink particles in our simulations, i.e., the time between their formation and the end of the simulation as a function of their final mass. The age of the sink particles follows a linear relationship with the final mass. The sink particles with masses in the BD regime are the youngest and the high-mass sink particles are the oldest. Bate (2012) also observed such a linear trend in their simulations.

Figs. 2.10 and 2.11 show that (1) the sink particles that reach high masses are the first to form in the simulations and have low velocities at the time of formation. Their velocities are modified due to the subsequent interaction with the gas and other sink particles. (2) A large number of the very low-mass objects form towards the end of the simulations, which have high velocities at the time of formation.

We find that the 1D velocity dispersion of the sink particles (at SFE = 5%) varies between the simulations and they lie in the range 0.65–$1.74\,\mathrm{km\,s^{-1}}$ with a mean value of $1.1 \pm 0.3\,\mathrm{km\,s^{-1}}$. The velocity dispersion measured by observational surveys in the ONC is around $2\,\mathrm{km\,s^{-1}}$ (Jones & Walker 1988; Tobin et al. 2009; Kim et al. 2019; Theissen et al. 2021). In the inner core region of the ONC, Theissen et al. (2021) derived a slightly higher 1D velocity dispersion of $\sim 2.5\,\mathrm{km\,s^{-1}}$. Kuhn et al. (2019) measured 1D velocity dispersions in the range 0.8–$2.8\,\mathrm{km\,s^{-1}}$ for a sample of different young stellar clusters and associations.

2.5 Multiplicity and angular momentum

2.5.1 Multiplicity fraction

We identify the multiple systems in our simulations by following the algorithm used in Bate (2009a). In the list of individual sink particles formed in a simulation, or equivalently a list of single objects, we find the closest pair of objects that are gravitationally bound to each other. These two objects are replaced by a binary object having the mass, position and velocity equal to the system mass, centre-of-mass position and velocity, respectively. In the resulting list, we again find the closest pair of bound objects. In case the pair consists of a binary object and a single object, then the new object will be a triple. The process of removing the closest bound pair and replacing it with a higher-order object is repeated until none of the objects in the list are bound to one another or the only possible gravitationally bound pair selection will result in a quintuple. We do not consider systems of order higher than quadruples, because most high-order multiple systems are dynamically unstable and are expected to decay with further evolution of the cloud.

The algorithm effectively converts a list of individual sink particles into a list of single, binary, triple and quadruple systems or objects, with none being a subset of a higher-order system. For example, none of the objects characterised as binaries is a part of a triple or quadruple object. The multiplicity fraction in any mass range can be obtained by calculating the ratio of the number of multiple systems to the total number of systems whose primary sink particle lie within the given mass range. The multiplicity fraction (mf) is defined as

$$mf = \frac{B+T+Q}{S+B+T+Q} \tag{2.17}$$

where S, B, T and Q represent the number of singles, binaries, triples and quadruples, respectively, whose primary sink's mass is within the range in which mf is to be calculated.

Fig. 2.12 depicts the multiplicity fraction in different primary mass intervals (also done in Bate 2012; Krumholz et al. 2012b; Cunningham et al. 2018; Sharda et al. 2020) at SFE = 5% in the case of the OUTFLOW model, which is the more realistic model. The mass ranges are selected similar to those chosen in the observational studies so as to allow for a direct comparison. We can immediately notice that the multiplicity fraction evolves as an increasing function of the primary mass, which is the general understanding. Our mf values also compare well with those of the observations, except that we are underestimating the value in the very low-mass star (VLMS) and BD regime.

Since our highest attainable spatial resolution is 100 AU, we do not resolve all of the low-order multiple systems. Therefore, some of the sink particles may be representing binaries by themselves, or rarely, triple systems. However, the multiplicity fraction is very robust numerically. Even if a sink particle can be further fragmented into a binary or a triple stellar system, mf increases only if the sink particle is a single. The value remains unchanged if the sink particle is part of a multiple system, i.e., a member of a binary, triple or quadruple object. For example, if one of the sinks belonging to a triple object is a binary by itself, then T and Q become $T-1$ and $Q+1$, respectively, which leaves mf unchanged. Further, considering the fact that the frequency of singles decreases and the average separation of binaries increases with increasing primary mass (Konopacky et al. 2007; Kraus & Hillenbrand 2007; Luhman 2012), the mass range that will be mainly affected is the low-mass end, which explains the underestimation of mf in the sub-solar regime. If a few of the sink particles in the mass range 0.01–0.1 $\mathrm{M}_{\odot}$ were actually binaries if we had higher numerical resolution, then the increase in the multiplicity fraction would balance the underestimation in the VLMS or BD regime, which would bring the simulations closer to the observations in the sub-solar mass regime.

Fig. 2.13 shows the fraction of singles, binaries, triples and quadruples at SFE = 5%. The fraction of singles is 0.66 and is the highest, i.e., most of the sink particles that formed in our simulations are not part of a higher-order multiple system (the fraction of single objects for the NOWIND model is quoted in Tab. 2.1 for reference). Rohde et al. (2021) also find that the fraction of singles is around 0.6 in their simulations of turbulent dense cores. Adopting the multiplicity fraction derived by Delfosse et al. (2004) for M-dwarfs and that by Duquennoy & Mayor (1991) for stars earlier than M-dwarfs, Lada (2006) estimated the single-star fraction (SSF) to be 0.66 by assuming a Muench et al. (2002) form of the IMF and 0.67 for a Miller & Scalo (1979) IMF. Our value of the fraction of single objects agrees with their estimates, but the exact match between the values is coincidental. Observational investigations do not well constrain the IMF or the multiplicity fraction of different spectral types. Therefore, the SSF estimate of Lada (2006) would vary depending on the study they choose to derive the multiplicity fraction and the number fraction of M-dwarfs. Further, Lada (2006) only considered stars of spectral type M and earlier, whereas we also include the very low-mass stars and brown dwarfs. The actual value of SSF could be slightly lower than what we calculated because of the possibility of unresolved binaries in our simulations. It is also plausible that we are somewhat underestimating the fraction because, with further evolution of the cloud, some of the higher-order systems may decay and lead to an increase in the number of single stars.

2.5.2 Companion separation distribution

The binary separation distribution of solar-type main-sequence stars resembles a Gaussian function with a peak at ~ 45 AU and a standard deviation of 1.5 in the logarithm of the separations according to the observational survey by Raghavan et al. (2010) (see also Duquennoy & Mayor 1991). Winters et al. (2019) fit a Gaussian to their projected separation distribution of M-dwarfs with a peak at 20 AU and a value of 1.16 for the standard deviation of the log-separation. However, the separation distribution of younger systems are shown to differ from the separation distribution

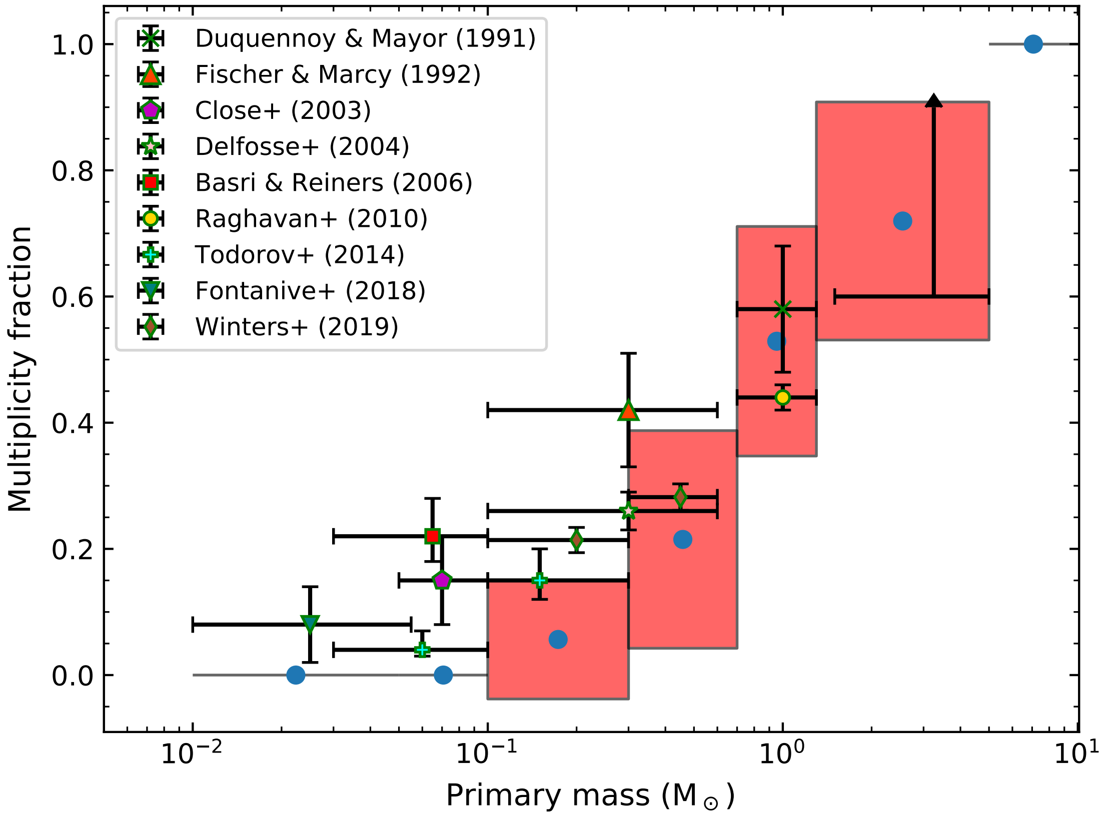

Figure 2.12: Multiplicity fraction (mf) as a function of primary mass. The circular markers represent the average mf, obtained from all our 10 simulations, in the mass interval represented by the width of the patch enclosing the marker. The height of the patch shows the standard deviation of mf across the 10 simulations. The centre of the crosses represent the value of mf obtained in different observational surveys, with the horizontal and vertical error bars corresponding to the mass range of study and the uncertainties, respectively. The observational data are (from left to right), from Fontanive et al. (2018), Todorov et al. (2014), Basri & Reiners (2006), Close et al. (2003), Todorov et al. (2014), Winters et al. (2019) (not corrected for undetected companions), Delfosse et al. (2004), Fischer & Marcy (1992), Raghavan et al. (2010) and Duquennoy & Mayor (1991). The multiplicity fraction of high-mass stars is relatively poorly understood. The lower limit of mf in the mass range of 1.5–5 $M_\odot$ is $\sim$ 0.5–0.6 (Chini et al. 2012; Duchêne & Kraus 2013). Massive stars are expected to have $mf \sim 1$ (Mason et al. 2009; Sana & Evans 2011; Sana et al. 2017; Lee et al. 2020).

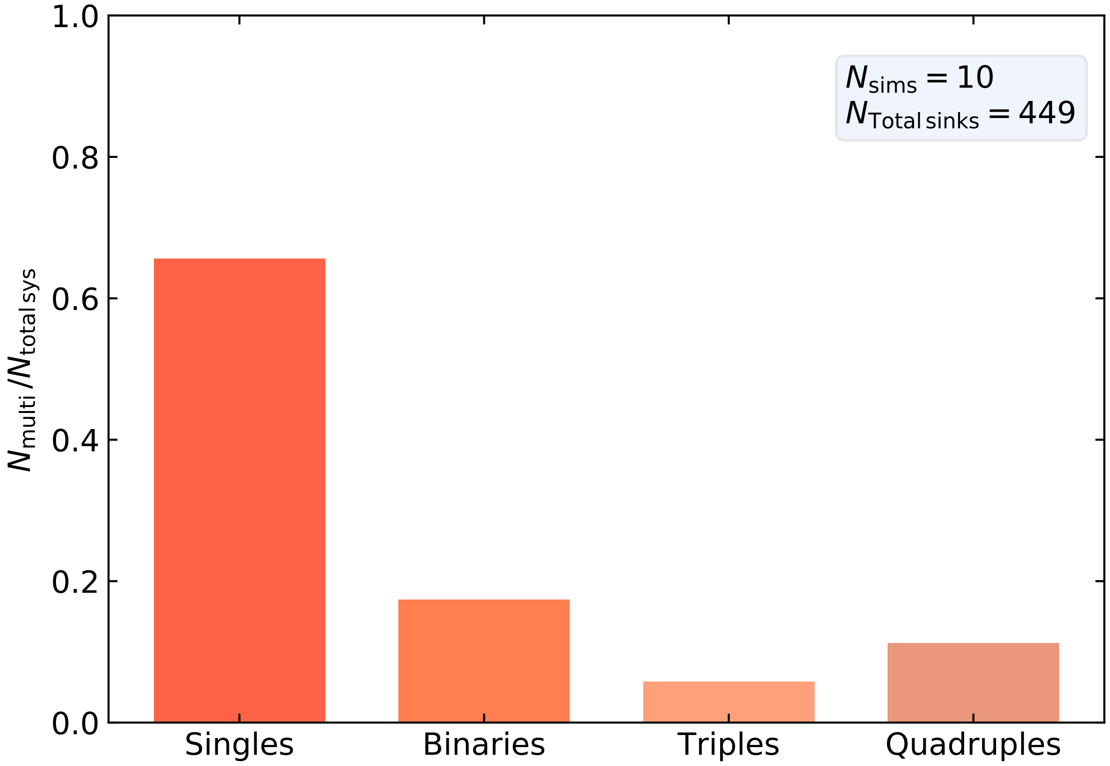

Figure 2.13: Fraction of single stars and multiple systems (binaries, triples, and quadruples), using the same data as for Fig. 2.12. The fraction of single objects is 0.6–0.7 in our simulations, which agrees well with the estimates of the single-star fraction of observed stars by Lada (2006).

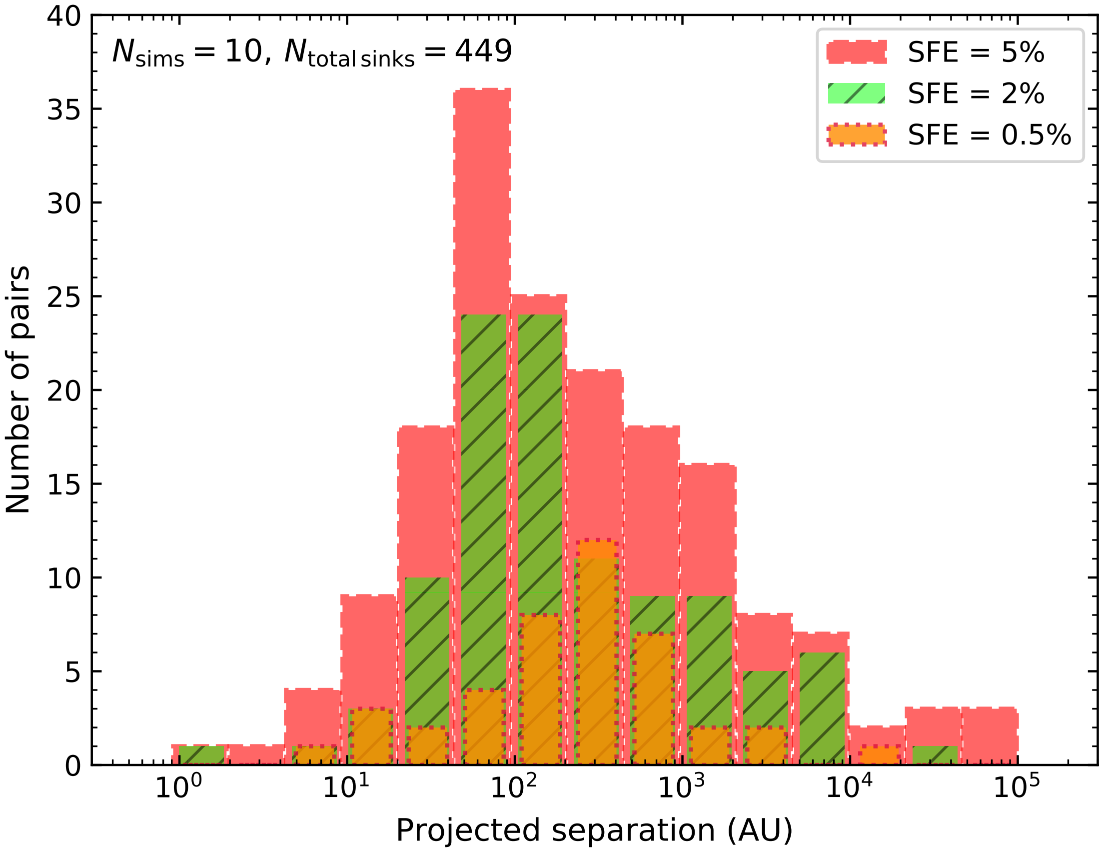

Figure 2.14: The projected separation distribution of the multiple systems in the ten OUTFLOW simulations at SFE = 0.5% (orange histogram with dotted edges), 2% (green hatched histogram) and 5% (red histogram with dashed edges). The projected distance presented here is the average of the projections of the separation in the three Cartesian planes. All distances are measured from the primary object. A binary provides a single separation, a triple provides two, and a quadruple contributes three separations.

of the field stars (Patience et al. 2002; Duchêne et al. 2004; Connelley et al. 2008; Chen et al. 2013; Tobin et al. 2016). The VANDAM survey (Tobin et al. 2016) studied a sample of Class 0 and Class I protostars in the Perseus molecular cloud and obtained a double-peaked distribution with a peak at $\sim$75 AU and a secondary peak at wide separations ($>$ 1000 AU), although the secondary peak was absent for their sample of only Class I protostars. There have been numerous numerical works in the past that study the formation of multiple systems and analyse their separation distribution (e.g., Bate 2009a; Offner et al. 2010; Bate 2012; Lee et al. 2019).

The Class 0 lifetime of approximately 10^4–10^5 yr and Class I lifetime of a few 10^5yr (Froebrich et al. 2006; Dunham et al. 2014) are relatable to the age of our sink particles (see Fig. 2.11). Fig. 2.14 shows the projected separation distribution of the multiple systems in our OUTFLOW simulations. In each of the systems, the separation distances are measured from the primary star. For example, a triple system will contribute two separation pairs to the distribution and a quadruple system contributes three pairs. The separation distribution at SFE = 0.5%, 2% and 5% are shown by the orange (dotted edges), green (hatched), and red (dashed edges) histogram, respectively. The peak of the distribution at SFE = 0.5% lies at around 300–400 AU. The statistical significance of the distribution at SFE = 0.5% is low since the number of sink particles that form within that time is small compared to the total number at SFE = 5%. The peak of the distribution shifts to shorter separations by the time SFE = 2% is reached and the peak is at an even shorter separation at SFE = 5%, indicating an evolution of systems to closer separations due to dynamical interactions (Reipurth & Clarke 2001; Bate et al. 2002b; Goodwin & Kroupa 2005; Offner et al. 2010). By the end of the simulations (at SFE = 5%), there is an appreciable number of wide separations ($> 1000\,\mathrm{AU}$), even though separation distances of less than 500 AU are more common. For the distribution at SFE = 5%, the standard deviation of the logarithm of the projected separations is 0.9, i.e., the dispersion is close to an order of magnitude. The number of short separations is only a lower limit since fragmentation on small scales (at $\lesssim 200\,\mathrm{AU}$) does not occur in our simulations. Our sink particle formation criterion does not allow the formation of new sink particles within the accretion radius (250 AU) of an existing sink particle. All the pairs in the distribution with separation less than 250 AU correspond to the pairs that formed at a greater separation initially, and moved closer to one another at later times. At SFE = 5%, the separation range 40–100 AU has the highest frequency of pairs. The comparison of the peak of our distribution with the observational results should be done with caution, because the gas dynamics on very small scales is poorly modelled in our simulations due to the limited resolution, and also the gravitational potential is softened within the accretion radius. Therefore, a resolution study would be required to find the converged location of the peak of the separation distribution.

2.5.3 Specific angular momentum of dense cores and stars

Previous studies estimate the specific angular momentum (j) of dense molecular cloud cores (diameter $\sim 0.1\,\mathrm{pc}$) to be greater than $10^{21}\,\mathrm{cm}^2\,\mathrm{s}^{-1}$ (Goodman et al. 1993; Burkert & Bodenheimer 2000; Caselli et al. 2002). The range of j value of class 0/I envelopes and binary systems is 10^{17}–$10^{21}\,\mathrm{cm}^2\,\mathrm{s}^{-1}$ (Simon 1992; Ohashi et al. 1997; Yen et al. 2015a), whereas that of T-Tauri stars is 10^{16}–$10^{17}\,\mathrm{cm}^2\,\mathrm{s}^{-1}$

(Hartmann et al. 1986). The angular momentum of the sink particles (spin) in our simulations (see §2.2.3) can be directly obtained from the simulation output. We plot the specific angular momentum distribution of all the sink particles that formed in the 10 simulations of the OUTFLOW model in Fig. 2.15. The range of specific angular momentum of the sinks ($\sim 10^{17}$–$10^{20}\,\mathrm{cm^2\,s^{-1}}$) spans the regime of protostellar envelopes and binaries, with a few sinks having j values typical of T-Tauri stars. The average specific angular momentum of all the sinks is $j_{\mathrm{mean}} = 1.5 \times 10^{19}\,\mathrm{cm^2\,s^{-1}}$. Yen et al. (2015b) report the j value of the class 0 protostar B335 to be $1.3 \times 10^{19}\,\mathrm{cm^2\,s^{-1}}$ at a scale of ~ 180 AU, which agrees well with the j_{mean} from the sink particles in our simulations (having an accretion radius of 250 AU). Gaudel et al. (2020) infer that the j value of class 0 protostellar envelopes is relatively constant, at around $10^{20}\,\mathrm{cm^2\,s^{-1}}$, from a scale of ~ 1600 AU to 50 AU. Jappsen & Klessen (2004) performed hydrodynamic simulations of the collapse of supersonic turbulent clouds and calculated $j_{\mathrm{mean}} = 8 \times 10^{19}\,\mathrm{cm^2\,s^{-1}}$ for their sink particles with a radius of 560 AU. We note that $j_{\mathrm{mean}} = 1.2 \times 10^{20}\,\mathrm{cm^2\,s^{-1}}$ for the NOWIND model, which is almost an order of magnitude higher than that for the OUTFLOW model. This is because, based on observational and numerical works, our SGS outflow module removes 90% of the accreted angular momentum from the sink particles and re-distributes it to the jet/outflow components (see §2.2.5).

Fig. 2.16 presents the distribution of the ratio of rotational to gravitational energy $E_{\mathrm{rot}}/E_{\mathrm{grav}}$ of the sink particles. We calculate $E_{\mathrm{rot}}/E_{\mathrm{grav}}$ by assuming solid-body rotation of a uniform density sphere,

$$\frac{E_{\mathrm{rot}}}{E_{\mathrm{grav}}} = \frac{(1/2) I \omega^2}{(3/5) G M_{\mathrm{sink}}^2 / r_{\mathrm{sink}}}, \tag{2.18}$$

where $I = (2/5) M_{\mathrm{sink}} r_{\mathrm{sink}}^2$ is the moment of inertia, $\omega = j M_{\mathrm{sink}}/I$ is the angular velocity, and G is the gravitational constant.

We can roughly estimate the number of sink particles that represent unresolved binaries by looking at their $E_{\mathrm{rot}}/E_{\mathrm{grav}}$ values. The sink particles with $E_{\mathrm{rot}}/E_{\mathrm{grav}} < 0.01$ tend to be stable against fragmentation while those with $E_{\mathrm{rot}}/E_{\mathrm{grav}} > 0.01$ are likely to fragment into binaries (Boss 1999; Jappsen & Klessen 2004). We observe that, out of the total 449 sink particles from the 10 simulations, 92 sinks have $E_{\mathrm{rot}}/E_{\mathrm{grav}} > 0.01$. However, the multiplicity fraction would only be affected by the fragmentation of the stellar objects that are not already a part of a higher-order system (i.e., single sink particles). For example, out of the 449 total, there are only 7 sink particles with masses less than $0.1\,\mathrm{M}_{\odot}$ that are simultaneously single and have $E_{\mathrm{rot}}/E_{\mathrm{grav}} > 0.01$. Since the number of singles decreases with increasing primary

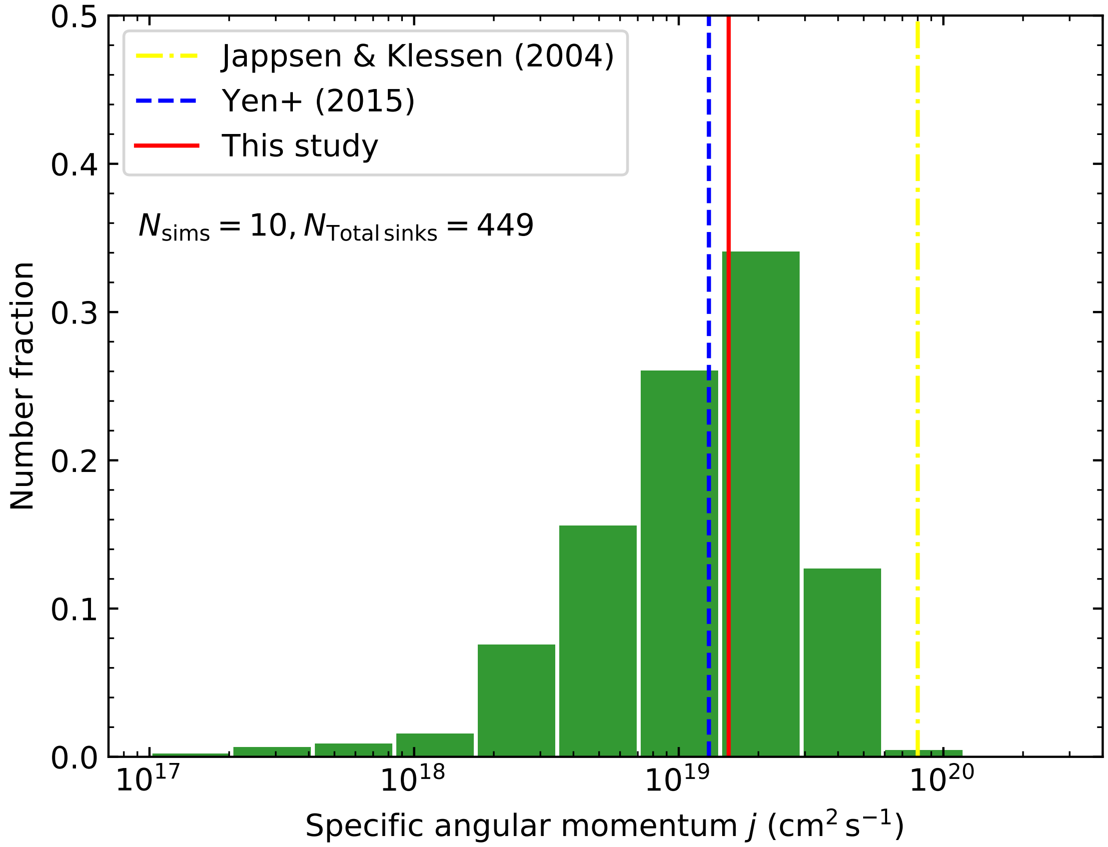

Figure 2.15: Specific angular momentum j of the sink particles ($r_\mathrm{sink} = 250\,\mathrm{AU}$) from the OUTFLOW simulations (green histogram), with the solid line marking the mean value of j. The dashed line shows the j value measured for the class 0 protostar B335 at $\sim$180 AU by Yen et al. (2015b), and the dash-dotted line denotes the mean value of j obtained in the numerical simulations of Jappsen & Klessen (2004) with a sink particle radius of 560 AU.

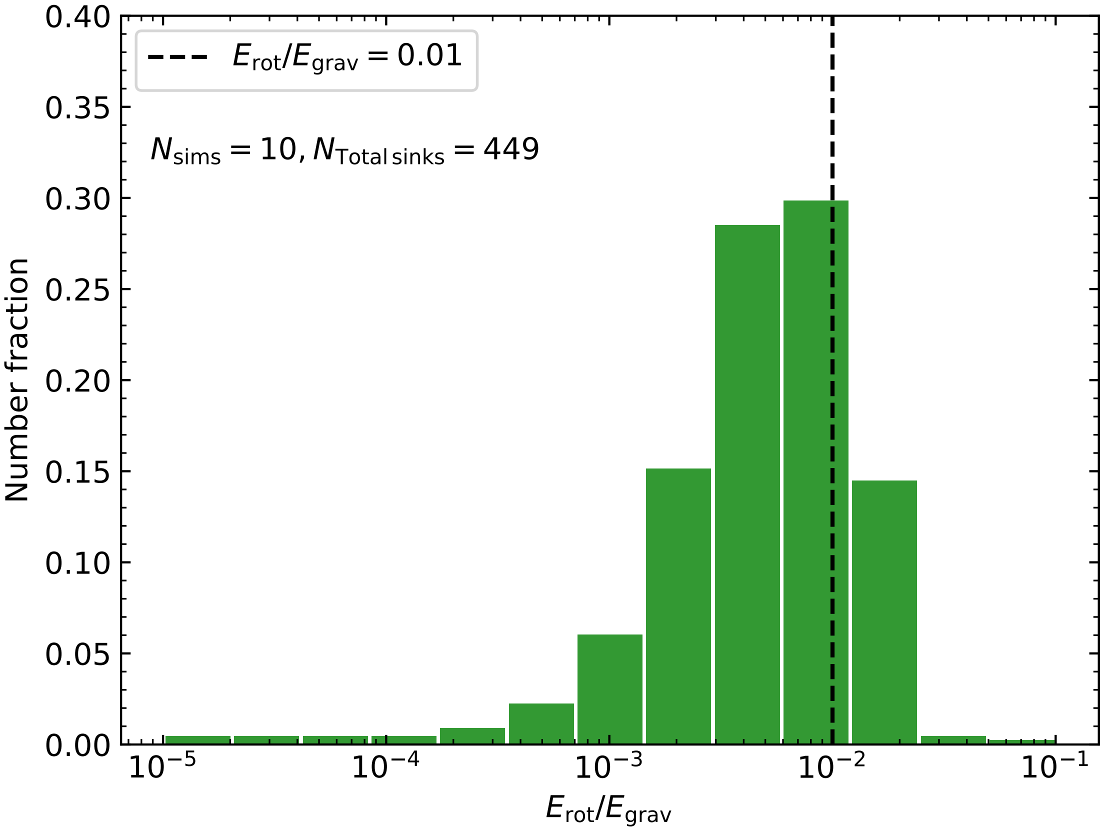

Figure 2.16: The distribution of the ratio of rotational to gravitational energy ($E_{\rm rot}/E_{\rm grav}$) of the sink particles formed in our simulations. The black dashed line marks $E_{\rm rot}/E_{\rm grav} = 0.01$, above which fragmentation into binaries is likely (Boss 1999; Jappsen & Klessen 2004). Thus, only a relatively small fraction of our sink particles ($92/449 = 20\%$) would have likely fragmented further, if we had higher numerical resolution.

mass, we expect that the mf estimates discussed above would not deviate much from the current value in the higher-mass range.

2.6 Caveats

2.6.1 Numerical resolution

Our sink mass distribution matches well with the form of the observed system IMFs. Despite the overall good agreement, higher numerical resolution might lead to a slight increase in fragmentation (c.f. Fig. 2.16), and thus, may result in a mass distribution that matches the individual-star IMF or may produce the observed IMF peak mass better (currently overestimated by factor ~ 2; c.f. Fig. 2.7). Here our sink particles have radii of $r_{\mathrm{sink}} = 250\,\mathrm{AU}$, and the high computational cost of these simulations currently prevents us from going higher in numerical resolution, because at the same time, we want to produce a statistically converged sample of stars (here built up from 10 independent simulations with different random seeds of the turbulence). Recent studies by Hennebelle et al. (2019) and Colman & Teyssier (2020) suggest that the origin of the peak of the IMF may lie in the tidal screening of the first hydrostatic core or the Larson core. The characteristic mass of the IMF would then be determined by the typical mass within the radius in which the tidal force by the Larson core prevents formation of any fragments, in which case a resolution of $\sim$10–20 AU would be necessary to obtain the peak mass. The multiplicity of stars can also be affected by the limitation in resolution. The current simulations do not resolve all the stars, particularly, the close binaries, which is why we somewhat underestimate the mf in the sub-solar range (c.f. Fig. 2.12). Very low-mass binaries generally have separations of $< 20\,\mathrm{AU}$, and therefore, sufficiently high-resolution simulations would be required to resolve such binaries. Nevertheless, we believe that the multiplicity fraction estimates in the mass range $> 0.1\,\mathrm{M}_{\odot}$ are relatively robust as discussed above. It is reassuring that state-of-the-art simulations are now being developed that can simultaneously follow the collapse from the scales of GMCs down to the disc scales and also include all the primary mechanisms involved in star cluster formation (Grudić et al. 2021).

2.6.2 Use of sub-grid models

The sub-grid models that we use for incorporating the effects of jets and outflows (Federrath et al. 2014) and stellar radiative heating (Mathew & Federrath 2020) have been calibrated and well tested. However, they are dependent on parameters that are based on previous observational and numerical studies. Guszejnov et al. (2021) find that the characteristic mass of the IMF somewhat depends on the choice of the parameter that decides the amount of momentum injection by their outflow model. Therefore, variations in the mass-loss factor f_m or the normalisation jet speed ($100\,\mathrm{km\,s^{-1}}$) used to define the outflow velocity profile might cause the peak of our sink mass distribution to deviate from the current position. In addition, the fact that the polar heating model we use calculates the extinction of stellar radiation by assuming a fixed dust/disc density distribution can cause discrepancies. In order to accurately model jets or the extinction of stellar radiation by dust, the inner regions of the accretion disc have to be resolved. Achieving such high resolution generally comes at the expense of statistical significance because only one or a few simulations can be performed or the outer scale of the simulation box has to be reduced (smaller cloud size) to reduce the computational cost. Therefore, employing sub-grid models is necessary to obtain statistically conclusive and quantitatively accurate results in a cost-efficient way.

2.7 Conclusions

We carry out an array of simulations of the collapse of turbulent, magnetized molecular clouds including stellar heating and mechanical feedback. We investigate the impact of jets/outflows on the IMF and the evolution of different dynamical quantities by comparing 10 simulations with different turbulence seeds incorporating outflow feedback with another set of 10 simulations in the absence of the outflow feedback. We observe that the outflow feedback reduces the star formation rate by a factor of ~ 2 and increases the number of stars formed (see details in Tab. 2.1). Jets/Outflows disturb the direct accretion flow onto a star and lower the efficiency of stellar heating (as a result of the mass loss) in suppressing fragmentation, and thereby promote star formation in nearby over-dense regions. We find that including outflow feedback does not generally affect the overall shape of the IMF, but results in a shift of the IMF to lower masses by a factor of 2.0 ± 0.2.

We find that the IMF obtained from our simulations broadly agrees with different functional forms of the observational IMF, although the peak mass is higher by a factor of ~ 2 (see discussion in Sec. 2.6). We also show that three different theoretical models of the IMF based on turbulent fragmentation (Padoan & Nordlund 2002; Hennebelle & Chabrier 2008; Hopkins 2012) broadly predict the shape of our IMF in the high-mass and low-mass range, but underestimate the number of very low-mass objects ($< 0.1\,\mathrm{M_\odot}$). Indeed, the fraction of sub-stellar objects produced in our simulations agrees well with the observed fraction. Therefore, our current set of simulations suggests that some modification of the gravo-turbulent theoretical models is required to account for the population of very low-mass stars (see also Thies et al. 2015).

We also compare our simulation IMF with the Bate & Bonnell (2005) model, which is based on accretion and dynamical ejections, and see that it matches well with our simulation IMF. Further, the Bate & Bonnell (2005) model reflects our very low-mass range better than the gravo-turbulent models, indicating the importance of dynamical ejections in the formation of sub-stellar objects. It is interesting to see that the IMF can be reproduced directly on the basis of the accretion and ejection history of the young stars. The Bate & Bonnell (2005) model only uses information about the stars and their evolution inside the cluster. On the other hand, the gravo-turbulent models only use the gas properties of the cloud to derive an IMF, not taking into account any information about the dynamical evolution of the stars when they have already formed. Therefore, the nature of the two classes of model (relying primarily on stellar versus gas properties) is fundamentally different. For example, Nam et al. (2021) find that the high-mass tail of the IMF is significantly influenced by the velocity power spectrum of the turbulence in the parent molecular cloud. Therefore, we suggest that both turbulent gas properties and the accretion and ejection history of the young stars play key roles in controlling the IMF, with a tendency of the high-mass end being controlled by turbulent gas properties, and the low-mass end being controlled by dynamical ejections and radiation feedback.

In our simulations, the velocity of the protostars at their birth correlates with their final mass, such that the objects with masses in the very low-mass regime have high velocities and the high-mass stars have low velocities at the time of their formation, consistent with the simulations of Bonnell et al. (2008). However, dynamical interactions during their lifetime modify the velocities such that no correlation remains by the end of the simulations. The 1D velocity dispersion of the protostars at the end of the simulations is $1.1 \pm 0.3\,\mathrm{km\,s^{-1}}$.

We find that the multiplicity fraction of the stellar systems in our simulations is an increasing function of the primary mass, consistent with other numerical studies and with observational surveys. Our multiplicity fractions compare well with observational estimates for different spectral types, although we are slightly underestimating the multiplicity fraction in the very low-mass range. This underestimation is mainly because our simulations do not fully resolve very close binaries. We see that, as more of the cloud gas gets converted into stars and the stellar density increases with time, the peak of the companion separation distribution of the multiple systems shifts to shorter separations, implying an orbital decay (hardening) of the systems (Reipurth & Clarke 2001; Bate et al. 2002b; Goodwin & Kroupa 2005; Offner et al. 2010), and therefore highlighting again the importance of dynamical interactions of the young stars.

The range of the specific angular momentum (j) of our sink particles can be directly compared to the j values in protostellar envelopes and binaries. We find that the average specific angular momentum of the sink particles, $j_{\mathrm{mean}} = 1.5 \times 10^{19}\,\mathrm{cm}^2\,\mathrm{s}^{-1}$, matches the value of specific angular momentum from observational measurements at a scale similar to the size of our sink particles.

Acknowledgements

We thank the anonymous reviewer for their comments and valuable suggestions, which helped to improve the paper. We thank Pavel Kroupa for valuable discussions regarding the system IMF. We further thank Piyush Sharda for helpful comments on the multiplicity algorithm and Donghee Nam for assistance with the python code for reproducing the Hopkins IMF. C.F. acknowledges funding provided by the Australian Research Council (Future Fellowship FT180100495), and the Australia-Germany Joint Research Cooperation Scheme (UA-DAAD). We further acknowledge high-performance computing resources provided by the Leibniz Rechenzentrum and the Gauss Centre for Supercomputing (grants pr32lo, pr48pi and GCS Large-scale project 10391), the Australian National Computational Infrastructure (grant ek9) in the framework of the National Computational Merit Allocation Scheme and the ANU Merit Allocation Scheme. The simulation software FLASH was in part developed by the DOE-supported Flash Center for Computational Science at the University of Chicago.

Appendix A: Column density and temperature maps of simulations with different random seeds for the turbulence

Fig. 2.17 is a non-weighted version of the column density and temperature maps in Fig. 2.2. It is evident from comparing both figures that the contrast between the densest regions and the surrounding medium is lower in Fig. 2.17.

Fig. 2.18 is similar to Fig. 2.3, but for the T1 simulations. This further demonstrates that the additional sink particles in the OUTFLOW simulations form in

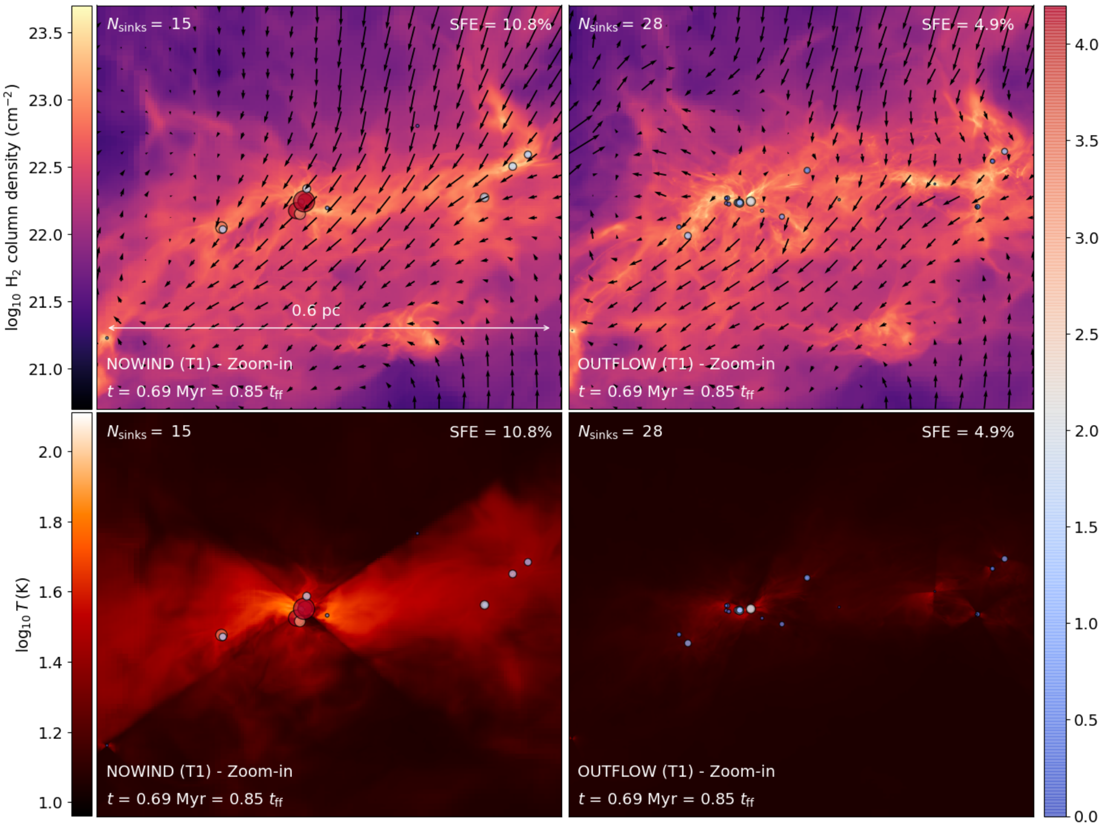

Figure 2.17: Same as Fig. 2.2, but without mass-weighting.

over-densities created by turbulent flows, which do not collapse in the NOWIND simulations. The figure shows that at $t = 0.40$ Myr (first snapshot), there are two sink particles in both NOWIND and OUTFLOW. Near the sink particle on the left in the OUTFLOW model, a new sink particle forms at $t = 0.42$ Myr (second snapshot) and another one forms at $t = 0.55$ Myr (last snapshot). The particular over-densities in which these two sinks form also exist in the NOWIND simulation, but there, they do not collapse to form stars.

Fig. 2.19 and Fig. 2.20 present the evolution of a clump and the formation of VLM objects in the T3 and T4 simulations, respectively.

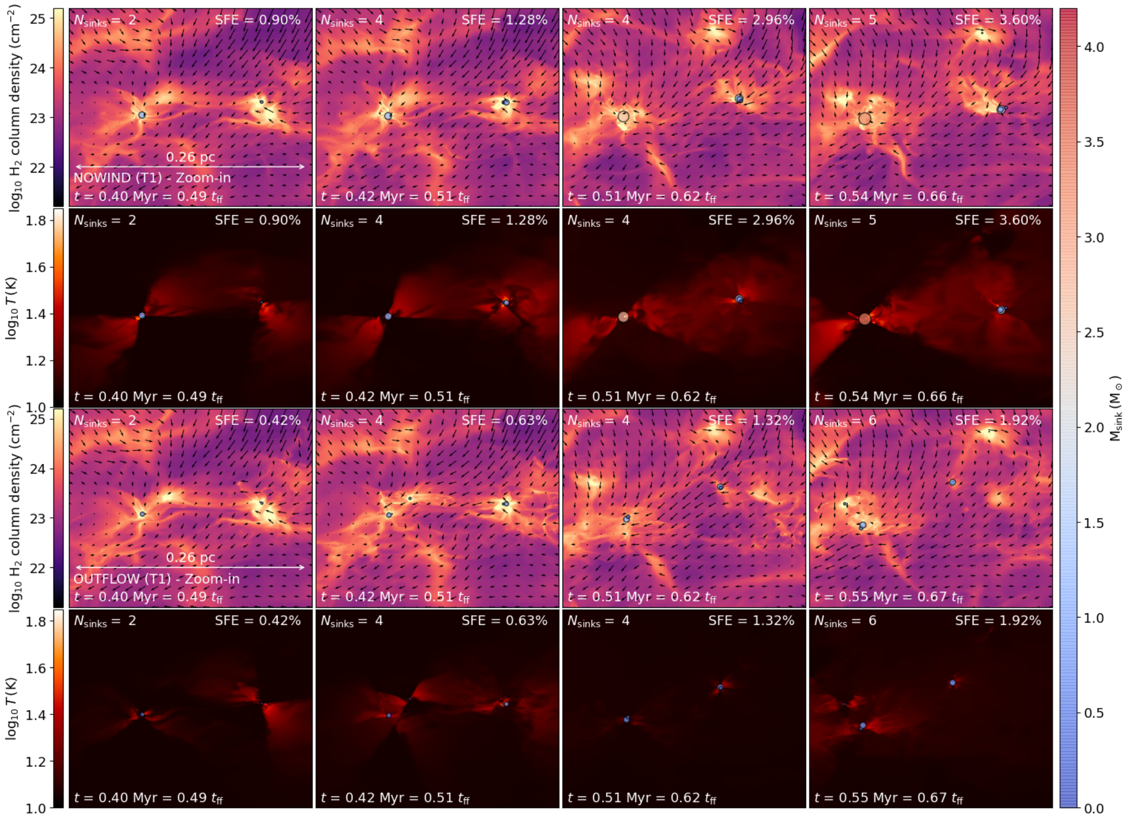

Figure 2.18: Same as Fig. 2.3, but for the T1 simulation.

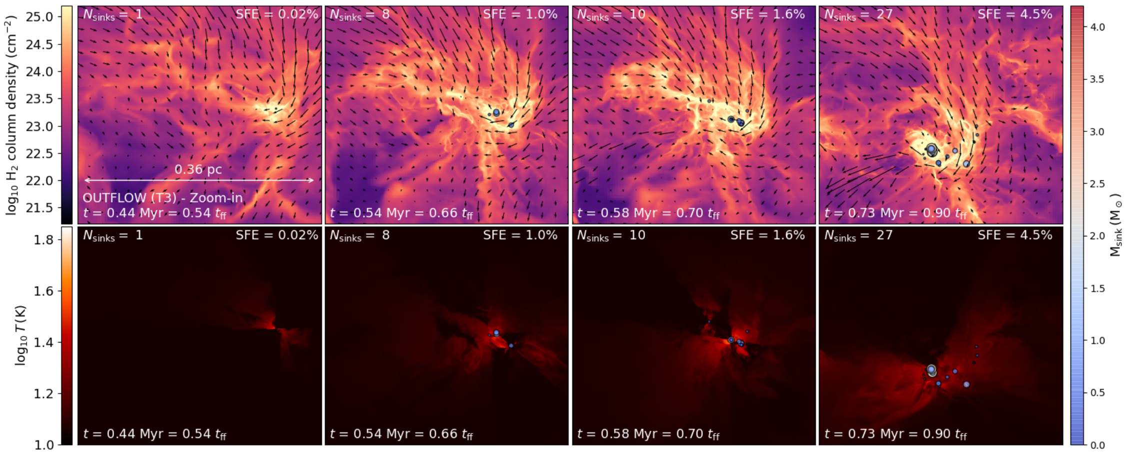

Figure 2.19: Same as Fig. 2.9, but for the T3 simulation, showing the formation of substellar objects.

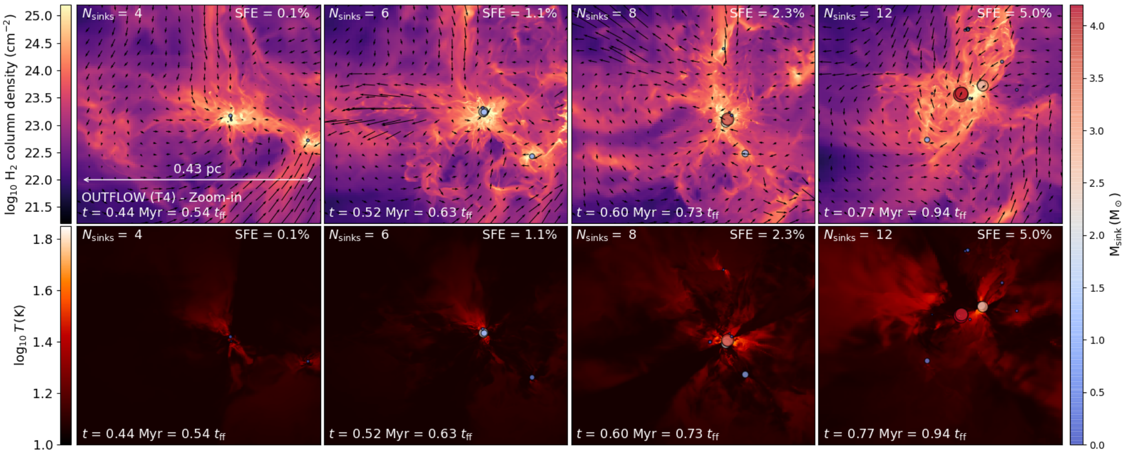

Figure 2.20: Same as Fig. 2.9, but for the T4 simulation.

Chapter 3

The role of the turbulence driving mode for the Initial Mass Function

Context and Contribution

This chapter has been previously published as 'The role of the turbulence driving mode for the Initial Mass Function', by Sajay Sunny Mathew, Christoph Federrath, Amit Seta, 2023, MNRAS, 518, 5190. The research is presented here as it appears in the original publication, except for a few typographical changes. I have carried out the simulations described in this paper, and post-processed the data for further investigation. I have written the majority of the paper, with inputs and suggestions from the two co-authors.

Abstract

Turbulence is a critical ingredient for star formation, yet its role for the initial mass function (IMF) is not fully understood. Here we perform magnetohydrodynamical (MHD) simulations of star cluster formation including gravity, turbulence, magnetic fields, stellar heating and outflow feedback to study the influence of the mode of turbulence driving on IMF. We find that simulations that employ purely compressive turbulence driving (COMP) produce a higher fraction of low-mass stars as compared to simulations that use purely solenoidal driving (SOL). The characteristic (median) mass of the sink particle (protostellar) distribution for COMP is shifted to lower masses by a factor of ~ 1.5 compared to SOL. Our simulation IMFs capture the important features of the observed IMF form. We find that turbulence-regulated theories of the IMF match our simulation IMFs reasonably well in the high-mass and low-mass range, but underestimate the number of very low-mass stars, which form towards the later stages of our simulations and stop accreting due to dynamical interactions. Our simulations show that for both COMP and SOL, the multiplicity fraction is an increasing function of the primary mass, although the multiplicity

fraction in COMP is higher than that of SOL for any primary mass range. We find that binary mass ratio distribution is independent of the turbulence driving mode. The average specific angular momentum of the sink particles in SOL is a factor of 2 higher than that for COMP. Overall, we conclude that the turbulence driving mode plays a significant role in shaping the IMF.

3.1 Introduction

Supersonic turbulence pervades the interstellar medium (ISM) and it is a critical ingredient for star formation in molecular clouds (MC). Turbulence, by moving the gas around randomly, counteracts a monolithic collapse of the cloud driven by gravity and serves as a primary agent for the low star formation rate observed in the Milky Way and nearby galaxies (Krumholz & McKee 2005; Evans et al. 2009; Murray 2011; Federrath & Klessen 2012; Federrath 2015; Vutisalchavakul et al. 2016; Lee et al. 2016). On the other hand, it also creates localised compressions within the clouds, enhancing the growth of high-density regions, which are potential sites of star formation. Thus, turbulence plays a fundamental role in regulating star formation. Numerical studies establish that the gas density probability distribution function (PDF) of supersonic turbulence is approximately log-normal (Vazquez-Semadeni 1994; Padoan et al. 1997a; Kritsuk et al. 2007; Federrath et al. 2008; Federrath 2013a; Hopkins 2013b; Federrath & Banerjee 2015; Seta & Federrath 2022). The density statistics of turbulence, particularly the log-normal nature of the gas density PDF, along with the velocity statistics have been used to explain the observed star formation efficiency (Federrath & Klessen 2013), star formation rate (Krumholz & McKee 2005; Krumholz et al. 2009; Hennebelle & Chabrier 2011; Federrath & Klessen 2012; Federrath 2015) and the initial mass function (IMF) (Padoan & Nordlund 2002; Hennebelle & Chabrier 2008, 2009; Hopkins 2012, 2013a).

The IMF refers to the mass distribution of young stars, e.g., in young star clusters, and it serves as the PDF for the mass of a star when it reaches the main sequence phase. The form of the IMF is found to be remarkably similar in different star-forming regions in the local neighbourhood and beyond, i.e., it is thought to be relatively universal (see the reviews by Bastian et al. 2010; Offner et al. 2014; Hopkins 2018; Lee et al. 2020), although there are studies that suggest that the IMF might also differ (e.g., Dib 2014; Dib et al. 2017). The IMF is a power law at high masses and the number of stars $N(M)$ can be defined via the relation, $dN \propto M^{-1.35}\, d\log M\, (M > 1\,\mathrm{M}_{\odot})$ (Salpeter 1955). The IMF flattens at lower masses and the mass distribution of the sub-solar range can be represented by a segmented power law (Kroupa 2001) or a log-normal function (Chabrier 2005). The peak mass or the characteristic mass of the IMF is located at around 0.2–0.3 $\mathrm{M}_\odot$ (Chabrier 2003; Elmegreen et al. 2008; Offner et al. 2014).

The standard deviation of the turbulent gas density PDF (σ_ρ) is proportional to the rms Mach number of the gas flow ($\mathcal{M}$) and is given by $\sigma_\rho/\langle\rho\rangle = b\mathcal{M}$, where $\langle\rho\rangle$ is the mean density. The value of the proportionality constant b is dependent on the mode of turbulence driving (Padoan et al. 1997a; Passot & Vázquez-Semadeni 1998; Federrath et al. 2008). Purely compressive (curl-free) driving corresponds to $b \sim 1$ and purely solenoidal (divergence-free) driving corresponds to a value of $b \sim 1/3$ (Federrath et al. 2008, 2010b). Values between 1 and 1/3 represent a mixture of compressive and solenoidal modes. Hence, the width of the gas density PDF is a function of the relative importance of the two driving modes. Dynamical mechanisms (such as galactic spiral shocks, and accretion) as well as supernova explosions and other stellar feedback mechanisms like radiation-pressure-driven shells tend to induce more compressive (curl-free) modes of turbulence in MCs, whereas shear and magneto-rotational instability excite more solenoidal (divergence-free) modes (Federrath et al. 2017a). The prospective influence on the IMF as a result of the dependence of the gas density PDF on the turbulence driving mode has been studied in a few numerical works (Schmidt et al. 2010; Girichidis et al. 2011; Lomax et al. 2015; Liptai et al. 2017), although a continuous turbulence driving was not employed in most of these studies, which is crucial to establish fully-developed turbulence statistics.

Here we investigate the effect of the mode of turbulence driving in setting the IMF. In addition to gravity and turbulence, we also include other important physics for the IMF: magnetic fields, protostellar heating and outflow feedback (Mathew & Federrath 2020, 2021). We perform multiple simulations with different turbulence realisations, such that we have a statistically meaningful sample to study the IMF. We also study how the stellar multiplicity properties are influenced by the mode of turbulence driving.

In Section 3.2, we describe the numerical methodology and turbulence setup, in particular the turbulence driving method that allows us to control the relative fraction of solenoidal and compressive modes in the driving field. We also explain the subgrid models for stellar radiative heating and jets/outflows, and provide the initial conditions for the simulations. In Section 3.3, we study the influence of the turbulence driving mode in the star cluster formation process by comparing the results of simulations that employ a purely compressive mode of driving with simulations characterised by a purely solenoidal mode of driving. For each of the two models, we investigate the column density and temperature structure, evolution of dynamical quantities, and the mass distribution of the stars formed in our simulations. In Section 3.4, we compare the protostellar mass distribution from our simulations with the IMF derived from observations and theoretical models. We examine the multiplicity and the stellar angular momentum in Section 3.5. In Section 3.6, we discuss some of the previous numerical works on the influence of turbulence on the IMF. The primary results and conclusions are discussed in Section 3.7.

3.2 Methods

3.2.1 Basic numerical methods and magnetohydrodynamics

To perform the numerical modelling of star cluster formation, we solve the magnetohydrodynamical (MHD) equations with gravity on an adaptive mesh refinement (AMR) (Berger & Colella 1989) grid, using the PARAMESH library (MacNeice et al. 2000) in a significantly modified version of the FLASH (version 4) code (Fryxell et al. 2000; Dubey et al. 2008),

$$\frac{\partial \rho}{\partial t} + \nabla \cdot (\rho \mathbf{v}) = 0, \tag{3.1}$$

$$\left(\frac{\partial}{\partial t} + \mathbf{v} \cdot \nabla\right) \mathbf{v} = \frac{(\mathbf{B} \cdot \nabla)\mathbf{B}}{4\pi\rho} - \frac{\nabla P_{\mathrm{tot}}}{\rho} + \mathbf{g} + \mathbf{F}_{\mathrm{stir}}, \tag{3.2}$$

$$\frac{\partial \mathbf{B}}{\partial t} = \nabla \times (\mathbf{v} \times \mathbf{B}), \quad \nabla \cdot \mathbf{B} = 0, \tag{3.3}$$

where $\rho, \mathbf{v}, \mathbf{B}, P_{\mathrm{tot}} = P + 1/(8\pi)|\mathbf{B}|^2$, and $\mathbf{F}_{\mathrm{stir}}$ correspond to the gas density, velocity, magnetic field, pressure (sum of thermal and magnetic pressures), and turbulent acceleration field, respectively. Here $\mathbf{g}$ is the gravitational acceleration and is the sum of the self-gravity of the gas and the acceleration as a result of the mass of sink (star) particles (see §3.2.3). We utilise the 5-wave HLL5R approximate Riemann method to solve the MHD equations (Waagan et al. 2011). The self-gravity of the gas is evaluated using a multi-grid Poisson solver (Ricker 2008).

3.2.2 Turbulence driving

We drive turbulent motions in our simulations through the specific forcing term $\mathbf{F}_{\mathrm{stir}}$ in the MHD equations (see Eq. 3.2). The acceleration field $\mathbf{F}_{\mathrm{stir}}$ is modelled using a stochastic Ornstein-Uhlenbeck (OU) process (Eswaran & Pope 1988; Schmidt et al. 2006; Federrath et al. 2010b). The OU process enables us to continuously drive turbulence with an $\mathbf{F}_{\mathrm{stir}}$ field that varies smoothly in space and time. If no Helmholtz decomposition is carried out, the output of such a process is a natural mixture of stirring modes, i.e., a 2:1 mixture of solenoidal ($\nabla \cdot \mathbf{F}_{\mathrm{stir}} = 0$) to compressive ($\nabla \times \mathbf{F}_{\mathrm{stir}} = 0$) modes. Using the respective projection in Fourier (k) space, we can decompose the acceleration field obtained from the OU process into purely solenoidal and purely compressive components, and depending on the requirement, we can choose to drive turbulence with any one of these components or with a mixture of the two. The projection operator in k-space is given by (Federrath et al. 2008)

$$\mathcal{P}_{ij}^{\zeta}(\mathbf{k}) = \zeta \mathcal{P}_{ij}^{\perp}(\mathbf{k}) + (1-\zeta)\mathcal{P}_{ij}^{\parallel}(\mathbf{k}) = \zeta\delta_{ij} + (1-2\zeta)\frac{k_i k_j}{|k|^2}. \tag{3.4}$$

The value of ζ controls the relative strength of solenoidal and compressive modes. By setting $\zeta = 1$, we can obtain the solenoidal component of the acceleration field, while $\zeta = 0$ gives the compressive component. We refer the reader to Federrath et al. (2008, 2010b) for a more detailed description of the OU process associated with the turbulence driving method used here.

Our forcing module is configured to inject kinetic energy only on the largest scales (wave numbers $k = 1 \ldots 3$, where k is in units of $2\pi/L$ with the side length L of the box) by using a parabolic function for the amplitude with the peak at $|\mathbf{k}| = 2$ and zero amplitude at $|\mathbf{k}| = 1, 3$. Such a treatment allows the injected kinetic energy to naturally cascade down to smaller scales, resulting in a velocity power spectrum $\sim k^{-2}$ or equivalently a velocity dispersion – size relation of $\sigma_v \propto \ell^{1/2}$, as we set the overall amplitude such that the turbulence has a sonic Mach number of $\mathcal{M} = 5$, a typical configuration for molecular clouds (Larson 1981; Ossenkopf & Mac Low 2002; Heyer & Brunt 2004; Roman-Duval et al. 2011; Federrath 2013a; Federrath et al. 2021). The turbulence driving module used here is publicly available (Federrath et al. 2022).

3.2.3 Star formation (sink particles) and AMR

Sink particles are used for modelling the collapsing, high-density regions of a cloud. When the density of the central part of a collapsing core becomes too high to resolve and the associated time-scale becomes too small to follow with AMR, the gravitational bound gas in the inner regions is replaced by a sink particle. To prevent artificial sink particle formation, in addition to the requirement that the gas constituting a sink particle be gravitationally bound, we carry out a suite of tests as implemented by Federrath et al. (2010c) before transforming gas to sink particles locally. The sink particles are introduced in a spherical control volume described by a given radius (here equal to the accretion radius of the sink particle) and centred at the cell at which the density is higher than the threshold density which in turn is decided by the Jeans length,

$$\rho_{\mathrm{sink}} = \frac{\pi\, c_{\mathrm{s}}^2}{G\, \lambda_{\mathrm{J}}^2} = \frac{\pi\, c_{\mathrm{s}}^2}{4\, G\, r_{\mathrm{sink}}^2}, \tag{3.5}$$

where c_{s} is the sound speed, G is the gravitational constant, $\lambda_{\mathrm{J}} = [\pi c_s^2/(G\rho)]^{1/2}$ is the local Jeans length, and $r_{\mathrm{sink}} = \lambda_{\mathrm{J}}/2$ is the sink particle radius.

In order to be conforming with the Truelove et al. (1997) criterion to avoid fragmentation artificially, the radius r_{sink} of the sink particle is set such that $2r_{\mathrm{sink}} = 5\,\Delta x$, where Δx is the size of the grid cell on the highest level of refinement. On all lower AMR levels, λ_{J} is always resolved with a minimum of 16 grid cell lengths to ensure that the turbulent flow is reasonably well resolved on the scales of a Jeans length (Federrath et al. 2011c).

At every accretion step, the mass, linear momentum and angular momentum of each sink particle are updated by following the conservation laws. The new position of the sink particle after accretion is determined by the centre of mass of the sink particle and the accreted material. An intrinsic angular momentum (spin) is assigned to the sink particle, which stores the accreted angular momentum, ensuring the conservation of the total angular momentum. The rotational axis of the sink particle along which jets and outflows are launched is determined by the spin (Federrath et al. 2014); see further details in Sec. 3.2.5.

All gravitational interactions of the sink particles between each other and with the gas are computed by direct summation over all the sink particles and grid cells (Federrath et al. 2011b). A second-order leapfrog integrator is utilised to advance the sink particles in time.

3.2.4 Equation of state (EOS)

The temperature structure of the gas in dense cores is controlled by a combination of different thermodynamical mechanisms including cosmic-ray heating, compressional heating, and cooling by dust grains (Larson 1973a; Masunaga et al. 1998). The initial phase of the collapse is approximately isothermal while the cores are still optically thin (Wolfire et al. 1995; Masunaga & Inutsuka 2000; Glover et al. 2010). However, as the density in the central regions increases, the gravitational energy is not readily radiated away and the temperature of the core starts to increase due to compressional heating. Thus, the collapse transitions from an isothermal to an adiabatic process. To accurately model the thermal evolution of the gas, the equation of energy conservation has to be solved simultaneously with the radiation transfer (RT) equation. Solving the RT equation involving every grid cell and for every timestep is computationally demanding (Menon et al. 2022), and thus incorporating it in these large-scale simulations is a challenging task. In order to enable a large statistical study, instead of solving the RT equations, we use an approximation, by closing the system of MHD equations with a polytropic equation of state for the gas pressure $P = P_{\mathrm{EOS}}$, given by

$$P_{\mathrm{EOS}} = c_{\mathrm{s}}^2\, \rho^{\gamma}. \tag{3.6}$$

Utilising the ideal gas EOS, the corresponding temperature is derived as

$$T_{\mathrm{EOS}} = \frac{\mu\, m_{\mathrm{H}}}{k_{\mathrm{B}}\, \rho}\, P_{\mathrm{EOS}} = \frac{\mu\, m_{\mathrm{H}}}{k_{\mathrm{B}}}\, c_{\mathrm{s}}^2\, \rho^{\gamma-1}\,. \tag{3.7}$$

Here $c_{\mathrm{s}}^2 = (0.2\,\mathrm{km/s})^2$ is the square of the sound speed in the isothermal range ($\gamma = 1$) for solar metallicity, molecular gas at $10\,\mathrm{K}$, and $\mu = 2.35$ is the mean molecular weight (in units of the atomic mass of hydrogen, m_{H}). The polytropic exponent is then adjusted based on the local density of the gas, as

$$\gamma = \begin{cases} 1 & \text{for} \quad \rho \le \rho_1 \equiv 2.50\times10^{-16}\,\mathrm{g\,cm^{-3}}, \\ 1.1 & \text{for} \quad \rho_1 < \rho \le \rho_2 \equiv 3.84\times10^{-13}\,\mathrm{g\,cm^{-3}}, \\ 1.4 & \text{for} \quad \rho_2 < \rho \le \rho_3 \equiv 3.84\times10^{-8}\,\mathrm{g\,cm^{-3}}, \\ 1.1 & \text{for} \quad \rho_3 < \rho \le \rho_4 \equiv 3.84\times10^{-3}\,\mathrm{g\,cm^{-3}}, \\ 5/3 & \text{for} \quad \rho > \rho_4. \end{cases} \tag{3.8}$$

The value of the polytropic exponent γ changes with the local gas density, and is based on previous detailed radiation-hydrodynamic simulations of the formation of protostars. It covers the isothermal phase during the initial collapse, adiabatic heating during the formation of the first and second core, and the influence of H_2 dissociation during the second collapse (Larson 1969; Yorke et al. 1993; Masunaga & Inutsuka 2000; Offner et al. 2009). However, it does not consider the increase in thermal gas pressure due to the stellar radiative heating (feedback), which is discussed next.

3.2.5 Stellar feedback

Radiative heating

Stars in their early stages of formation have high accretion luminosities, which can suppress fragmentation, enabling the existing stars to reach high masses by continued accretion (Bate 2009b; Krumholz et al. 2011; Guszejnov et al. 2016; Federrath et al. 2017b; Mathew & Federrath 2020; Hennebelle et al. 2020a). Thus, it is crucial to take into consideration the temperature variation due to the stellar heating feedback. To precisely model the stellar heating, the RT equation has to be solved together with the energy conservation equation, as mentioned in Sec. 3.2.4, which involves tracing the rays emitted from the protostars and the rays absorbed or scattered by dust grains. Solving the RT equation in large-scale simulations is extremely challenging because of the computational expense (Buntemeyer et al. 2016; Menon et al. 2022). As an alternative, we will employ the polar heating model developed by Mathew & Federrath (2020) to model the direct stellar heating. The polar heating model is based on the heating model in Federrath et al. (2017b) and takes into account the shielding of the radiation field by the dust particles in the accretion disc. Following the works of Pascucci et al. (2004) and Buntemeyer et al. (2016), our model assumes a disc density distribution around each sink particle (protostar) that is determined by the radial distance r and the angle θ subtended from the angular momentum axis of the sink particle. The stellar radiant power is distributed over the grid cells surrounding the sink particle based on this dust/disc density distribution.

The radiation from the central star is absorbed by the dust particles with the rate of energy absorption given by

$$Q(r,\theta) = \chi \, \frac{L_\star}{4\pi r^2} \, \exp\left(-\tau(r,\theta)\right), \tag{3.9}$$

where χ is the absorption coefficient. The star's luminosity ($L_\star$), which consists of both the accretion and intrinsic luminosities, is estimated by employing the protostellar evolution model by Offner et al. (2009). The total optical depth (τ) in any direction given by θ is

$$\tau = \int \kappa \, \rho(r,\theta) \, \mathrm{d}r, \tag{3.10}$$

where κ is the grey opacity (a constant here) and $\rho(r,\theta)$ corresponds to the dust/disc density distribution assumed (see Mathew & Federrath 2020, for a detailed discussion of the analytical model of the disc density distribution employed here). The dust grains in the disc can absorb the radiation and therefore the field will be diminished in the directions of the disc, and the primary heating will be restricted to the polar directions.

The dust grains will achieve an equilibrium temperature when they emit the same amount of energy they absorb. Thus, we can write

$$\frac{\sigma_{\mathrm{SB}}}{\pi}\,\chi\,T_{\mathrm{heat}}^4 = \frac{Q}{4\pi}, \tag{3.11}$$

where σ_{SB} is the Stefan-Boltzmann constant and T_{heat} is the temperature due to stellar heating. We note that the model ignores the reprocessed radiation field, but the change in temperature due to the presence of the reprocessed field is minimal and would barely affect the IMF.

The space-dependent pressure term derived from the polar stellar heating module is added to the pressure calculated from the polytropic equation of state to accomodate the change in temperature or equivalently the change in thermal pressure due to the stellar radiative heating (see Guszejnov et al. 2016, 2018a; Federrath et al. 2017b). Thus, the final gas pressure is

$$\begin{aligned} P &= \left[P_{\mathrm{EOS}}^4 + P_{\mathrm{heat}}^4\right]^{1/4} \\ &= \left[P_{\mathrm{EOS}}^4 + \left(\frac{k_{\mathrm{B}}\,\rho}{\mu\,m_{\mathrm{H}}}\right)^4 T_{\mathrm{heat}}^4\right]^{1/4}, \end{aligned} \tag{3.12}$$

which is used in the MHD momentum equation, Eq. (3.2).

Jets/Outflows

The bipolar mechanical feedback from protostars consists of jets which are highly collimated fast streams of gas that penetrate through the accreting envelope, and the wide-angle low-speed molecular outflows (Frank et al. 2014). All young stars lose part of their mass through jets and mass outflows (Richer et al. 2000; Woitas et al. 2002). The material ejected from stars or young stellar objects (YSOs) also disperses the gas envelope surrounding the protostar, creating cavities. The gap in the mass scale between the core mass function (CMF) and the IMF is generally considered to be caused by the mass loss in protostars as a result of jets and outflows, which is often parameterized by a mass-independent core-to-star efficiency $\epsilon \sim 0.25-0.5$ (Matzner & McKee 2000; Myers 2008; Federrath & Klessen 2012; Federrath et al. 2014; Offner & Arce 2014). Two primary effects of the inclusion of jets/outflows in simulations are the reduction in the star formation rate and the increase in the number of protostellar objects formed (Federrath et al. 2014; Guszejnov et al. 2021; Mathew & Federrath 2021). Thus, the incorporation of outflow feedback in numerical works is essential to produce conclusive results on the IMF.

We include jet/outflow feedback in our simulations by using the subgrid-scale (SGS) outflow model developed by Federrath et al. (2014). It captures both the low-speed molecular outflows and the fast jet components and includes angular momentum transfer. The SGS module redistributes momentum among the grid cells enclosed within a control volume determined by two conical sections about the sink particle. The conical sections open towards the opposite poles of the sink particle and are defined by an opening angle $\theta_{\mathrm{out}} = 30^\circ$ (Blandford & Payne 1982) measured from the angular momentum axis. We fix the radial extent (height of the cone) equal to $r_{\mathrm{out}} = 16\Delta x$ measured from the sink particle's position (tip of the cone), where Δx is the cell size on the highest AMR level, as done in Federrath et al. (2014), to ensure convergence. Radial and angular smoothing kernels are used to attain smooth transition at the interface. The momentum injected into each of the cones is

$$\mathbf{P}_{\mathrm{out}} = \pm(1/2)\, M_{\mathrm{out}}\, \mathbf{V}_{\mathrm{out}}, \tag{3.13}$$

where M_{out} corresponds to the mass ejected, which is equivalent to the fraction f_{m} of the mass accreted by the sink particle in a timestep Δt, i.e., $M_{\mathrm{out}} = f_{\mathrm{m}}\, \dot{M}_{\mathrm{acc}}\, \Delta t$. We define $f_{\mathrm{m}} = 0.3$ (Federrath et al. 2014), which agrees with observational surveys (Hartmann & Calvet 1995; Cabrit et al. 2007; Bacciotti et al. 2011), theoretical models of the outflow feedback (Blandford & Payne 1982; Shu et al. 1988; Pudritz et al. 2007), and the estimates from other numerical simulations (Hennebelle & Fromang 2008; Seifried et al. 2012; Fendt & Sheikhnezami 2013).

$\mathbf{V}_{\mathrm{out}}$ is set to the Kepler speed close to the protostellar surface, such that

$$|\mathbf{V}_{\mathrm{out}}| = 100\,\mathrm{km\,s^{-1}} \left(\frac{M_{\mathrm{sink}}}{0.5\,\mathrm{M}_\odot}\right)^{1/2}, \tag{3.14}$$

where M_{sink} is the sink particle mass and $100\,\mathrm{km\,s^{-1}}$ is the typical jet speed (and Kepler speed) for a protostar of mass $M \sim 0.5\,\mathrm{M}_\odot$ at a radius of $R \sim 10\,\mathrm{R}_\odot$. $\mathbf{V}_{\mathrm{out}}$ consists of a slow component with a speed of $0.25\,|\mathbf{V}_{\mathrm{out}}|$ and a high-speed component with a speed of $0.75\,|\mathbf{V}_{\mathrm{out}}|$. The momentum injection in the cones associated with the fast component is limited to an opening angle of 5°. Utilising such a velocity profile ensures that the faster jet and the slower molecular outflow components are distinguished.

The model removes a fraction f_{a} of the angular momentum accreted by the sink particle and re-introduces it to the jet and outflow components. We employ the default value of $f_{\mathrm{a}} = 0.9$ in the SGS model, which is based on the observations in Bacciotti et al. (2002) and previous numerical studies (e.g. Banerjee & Pudritz 2006; Hennebelle & Fromang 2008).

The MHD code self-consistently carries away the momentum inserted into the two cones to larger distances. Through a series of rigorous tests, Federrath et al. (2014) have shown that the large-scale outflow features, that is, the mass, linear momentum, angular momentum, and outflow speed, converge independent of the resolution with the SGS outflow model. We refer the reader to Federrath et al. (2014) and references therein for more details of the SGS model and justification of the parameter choices.

3.2.6 Initial conditions and simulation parameters

The simulations are performed in a three-dimensional triple-periodic computational box with side length $L = 2\,\mathrm{pc}$. At the highest level of refinement, we allow for a maximum effective grid resolution of $N^3_{\mathrm{eff,\,res}} = 4096^3$ cells or a minimum cell size of $\Delta x_{\mathrm{cell}} = 100\,\mathrm{AU}$. The initial gas density is uniform with $\rho_\circ = 6.56 \times 10^{-21}\,\mathrm{g\,cm^{-3}}$, which yields a total cloud mass of $M_{\mathrm{cl}} = 775\,\mathrm{M_\odot}$ and a mean free-fall time of $t_{\mathrm{ff}} = 0.82\,\mathrm{Myr}$. Initially, the turbulence driving module stirs the gas in the computational domain in the absence of self-gravity. To ensure that a fully-developed turbulent state is reached, self-gravity is activated only after two turbulent crossing times, $2t_{\mathrm{turb}} = L/(\mathcal{M}c_{\mathrm{s}}) = 2\,\mathrm{Myr}$ (Federrath et al. 2010b). The induced turbulence creates cloud-typical morphology and over-densities in the form of clumps and filaments. The high-density regions within these structures are potential sites of star formation (Arzoumanian et al. 2011; Schneider et al. 2013; André et al. 2014). The velocity dispersion on the scale of turbulence driving is assigned as $\sigma_v = c_{\mathrm{s}}\,\mathcal{M} = 1.0\,\mathrm{km\,s^{-1}}$ such that the steady-state sonic Mach number $\mathcal{M} = 5.0$.

The magnetic field is uniform initially with $B = 10^{-5}\,\mathrm{G}$ along the z-axis of the computational domain, but is later altered due to the tangling, stretching, and compression of magnetic field lines by the turbulence (Seta & Federrath 2021), producing a magnetic field structure similar to that observed in real MCs (Federrath 2016). The initial virial parameter is set as $\alpha_{\mathrm{vir}} = 2E_{\mathrm{kin}}/E_{\mathrm{grav}} = 0.5$ which is consistent with the observed values (Falgarone et al. 1992; Kauffmann et al. 2013; Hernandez & Tan 2015). We analyse the statistical properties like the IMF and time evolution of different dynamical quantities of the formed stellar clusters from this point in time, which we set as $t = 0$, i.e., when self-gravity is turned on. Such a technique is analogous to that employed in previous studies (e.g., Federrath & Klessen 2012; Krumholz et al. 2012b; Padoan et al. 2016; Guszejnov et al. 2018b; Mathew & Federrath 2020, 2021).

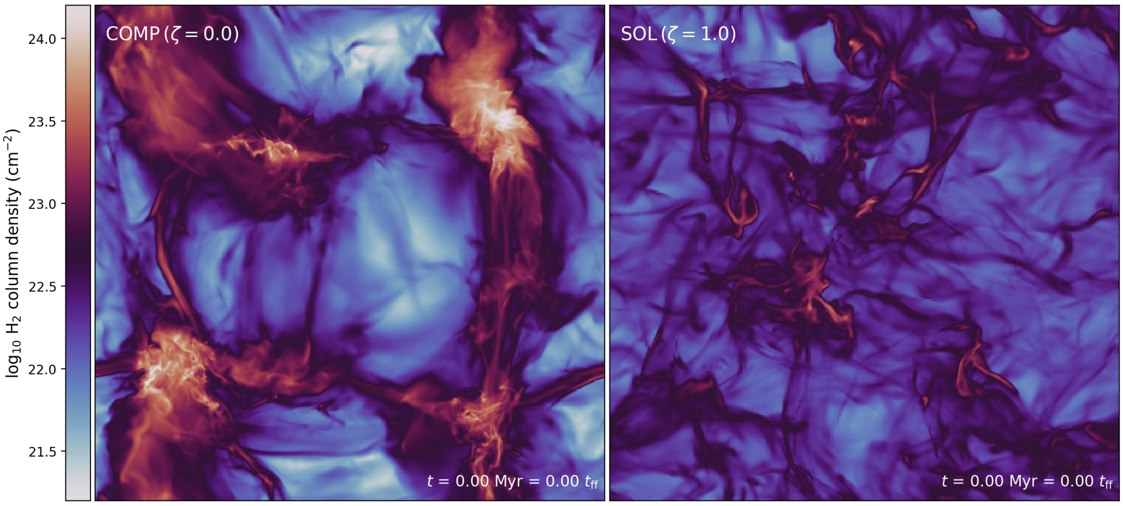

Figure 3.1: Left panel: The mass-weighted column density map of one of the simulations with a purely compressive driving (COMP) at the moment self-gravity is turned on, i.e., at $t = 0$. Right panel: The mass-weighted column density map of a purely solenoidal driving (SOL) simulation with the same turbulence seed and at the same time.

3.3 Results

We investigate the impact of the mode of turbulence driving by comparing MHD cloud-collapse simulations that use a purely compressive turbulence driving with simulations that are driven by purely solenoidal modes. To enhance the statistical significance, we carry out multiple simulations for each of the models with the same initial setup as prescribed in §3.2.6, but with different realisations of the turbulent flow. For the purely compressive model (COMP), we perform 7 simulations with different turbulence realisations, and for the purely solenoidal model (SOL), we run a total of 11 simulations with different turbulence realisations, to ensure that the total number of sink particles (protostars) formed is comparable in both the COMP and SOL models. The left panel in Fig. 3.1 shows the mass-weighted column density[1] of one of the COMP simulations and the right panel shows the same for the SOL simulation with the same turbulence realisation at the moment self-gravity is turned on. It can be clearly seen that the over-dense regions produced by turbulent shocks in the COMP model are comparatively larger in size and have a higher density on average than the over-dense structures in the SOL model. Therefore, as soon as self-gravity is turned on, star formation commences aggressively in COMP, while it

---

[1] We define the mass-weighted projection of the gas number density as $\int \rho^2 \, dz \, / \int \rho \, dz$ and the mass-weighted projection of the temperature as $\int \rho T \, dz \, / \int \rho \, dz$, where the projection is taken along the z-direction. All figures in this paper depicting density and temperature maps are mass-weighted. The objective of the mass-weighting is to allow better visualisation of the morphological features, i.e., to highlight the densest structures.

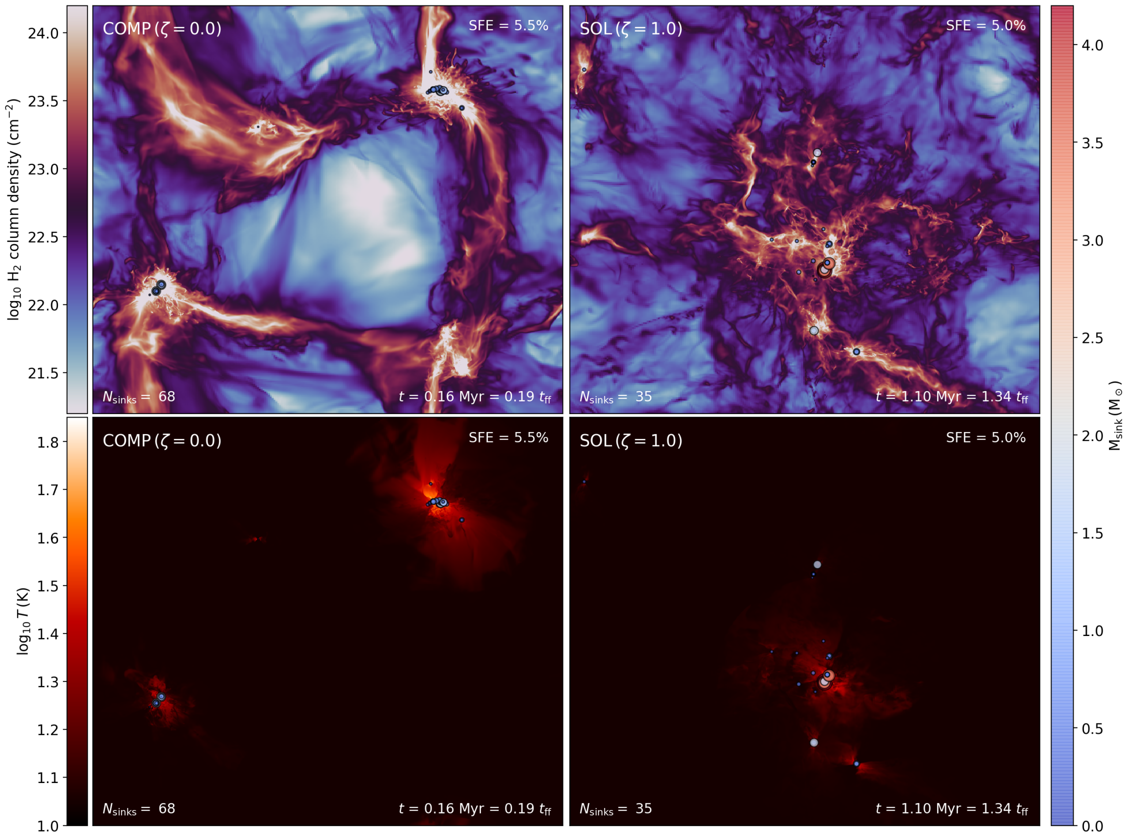

Figure 3.2: Left panel: Column density map (mass-weighted) of the COMP simulation shown in Fig. 3.1 at a star formation efficiency (SFE) of 5%. Right panel: The mass-weighted column density map of the SOL simulation shown in Fig. 3.1 at SFE = 5%. The circular markers correspond to the sink particle (star+disc system) positions and the colour bar on the right represents the mass of the sink particles. The size of the markers is scaled by the mass of the sink particles.

Table 3.1: Key simulation parameters and results.

Model (1)	$N_{\rm sims}$ (2)	$N_{\rm Total\,sinks}$ (3)	$\overline{M}_{\rm median}$ [M$_\odot$] (4)	$\overline{M}_{\rm avg}$ [M$_\odot$] (5)	SSF (6)
COMP	7	468	0.4 ± 0.1	0.6 ± 0.2	0.59 ± 0.08
SOL	11	445	0.6 ± 0.2	1.0 ± 0.2	0.64 ± 0.09

Notes. Multiple simulations with different turbulence realisations are run for the compressive turbulence driving (COMP) and solenoidal turbulence driving (SOL) models. All values quoted in the table are calculated at SFE = 5%. The resolution level and cloud properties are the same in both models, and the only difference is the mode of turbulence driving imposed. Main simulation parameters: computational box size: $L = 2\,\rm pc$, uniform initial gas density: $\rho_\circ = 6.56 \times 10^{-21}\,\rm g\,cm^{-3}$, total cloud mass: $M_{\rm cl} = 775\,\rm M_\odot$, uniform initial magnetic field: $B = 10^{-5}\,\rm G$ (along the z-axis), velocity dispersion on the driving scale of the turbulence: $\sigma_v = 1.0\,\rm km\,s^{-1}$, maximum effective grid resolution: $N^3_{\rm eff,\,res} = 4096^3$ cells, minimum cell size: $\Delta x_{\rm cell} = 100\,\rm AU$, and sink particle threshold density: $\rho_{\rm sink} = 3.8 \times 10^{-16}\,\rm g\ cm^{-3}$.

is much slower in the SOL run. Fig. 3.2 shows the mass-weighted column density (top row) and temperature structure (bottom row) of COMP (left column) and SOL (right column) simulations shown in Fig. 3.1, but at a star formation efficiency (SFE) of 5%. In the initial stages of the SOL simulation, a few stars form in some of the dense structures, but a substantial fraction of the stars form only much later when some of these structures merge under the action of self-gravity or due to the large-scale turbulent motions.

3.3.1 Evolution of dynamical quantities

Fig. 3.3 presents the evolution of the median sink mass $\overline{M}_{\rm median}$ (panel a) and average sink mass $\overline{M}_{\rm avg}$ (panel b) as a function of SFE (%). The overbar in the plotted quantities denotes that the respective values are averaged over multiple simulations. We find that, for both the COMP and SOL models, $\overline{M}_{\rm median}$ and $\overline{M}_{\rm avg}$ are nearly constant beyond an SFE of $\sim 1.5\%$. It is evident that the $\overline{M}_{\rm median}$ and $\overline{M}_{\rm avg}$ of the SOL simulations are relatively higher. On taking the average over the SFE range 1.5–5%, in the case of the COMP model, the median and average sink particle mass are $0.31 \pm 0.04\,\rm M_\odot$ and $0.53 \pm 0.06\,\rm M_\odot$, respectively, while they are $0.55 \pm 0.03\,\rm M_\odot$ and $0.87 \pm 0.05\,\rm M_\odot$, respectively, for the SOL model. The right panels in Fig. 3.3 depict the evolution of the star formation efficiency $\overline{\rm SFE}$ (panel c) and star formation rate per free-fall time $\overline{\rm SFR}_{\rm ff}$ (panel d) with time. The star formation rate is around an order of magnitude higher in the COMP simulations, as seen in previous simulations (e.g., Federrath & Klessen 2012; Liptai et al. 2017). The $\overline{\rm SFR}_{\rm ff}$ in the SOL simulations is between 1–3% for the most part of the cloud evolution, but increases towards the end. The acceleration in the $\overline{\rm SFR}_{\rm ff}$ in the later stages is due to the increased efficiency of gravity in the cluster-forming regions in bringing the gas together and increasing the local density, allowing more stars to form (see also Ballesteros-Paredes et al. 2011b; Burkhart et al. 2015; Lee & Hennebelle 2018a; Khullar et al. 2021). The average star formation rate in the Milky Way is estimated to be $\sim$ 1–2% per free-fall time (Krumholz & Tan 2007; Heiderman et al. 2010; Krumholz et al. 2012a; Federrath 2013b; Lada et al. 2013; Salim et al. 2015; Vutisalchavakul et al. 2016; Krumholz & Federrath 2019; Khullar et al. 2019), although the spread about the average value can be large (Heiderman et al. 2010; Lee et al. 2016; Vutisalchavakul et al. 2016; Heyer et al. 2016; Ochsendorf et al. 2017). Lee et al. (2016) measured the star formation rates per free-fall time in 191 star-forming giant molecular cloud complexes in the Milky Way and find that the dispersion in the rates is $\sim 0.9\,\mathrm{dex}$ with values as low as 0.01% to as high as 100% per free-fall time (see top left panel in Fig. 4 of Lee et al. 2016).[2] Therefore, both the high star formation rates seen in the COMP model and the low star formation rates seen in the SOL model are consistent with the star formation rates measured in Milky Way clouds, depending on the specific cloud or cloud region selected.

3.3.2 Sink mass distribution

Fig. 3.4 is a comparison between the sink mass distributions (SMDs) obtained for the COMP and SOL models at SFE = 5%. The mass distributions represent data collected from multiple simulations with different turbulent realisations. We see that a change in the mode of turbulence driving affects the IMF considerably. The SOL SMD has a higher fraction of high-mass stars ($M_{\mathrm{sink}} > 1\,\mathrm{M}_{\odot}$) and has a slightly higher turnover (peak) mass. The median stellar mass of our COMP SMD is $0.4 \pm 0.1\,\mathrm{M}_{\odot}$ (at SFE = 5%), while the same for the SOL SMD is $0.6 \pm 0.2\,\mathrm{M}_{\odot}$ (see Tab. 3.1). We performed a KS test and obtained a p-value of the order of 10^{-8}, meaning that we can neglect the hypothesis that the two distributions are identical.

To quantitatively confirm that the apparent difference between the shape of the COMP and SOL SMDs is not a consequence of the binning choice, we fit a modified version of the Chabrier (2005) IMF to our SMD data using the Markov Chain Monte-Carlo (MCMC) sampler emcee of Foreman-Mackey et al. (2013) (see also Nam et al. 2021). As opposed to other common model fitting methods, the MCMC sampling technique does not require binning of data. In order to account for the finite mass

---

[2] Note that star formation rates per free-fall time exceeding 100% are possible, if a particular cloud region undergoes local compression due to dynamical effects, such as shocks, which leads to a star formation rate that exceeds the purely gravitational free-fall rate (Federrath & Klessen 2012).

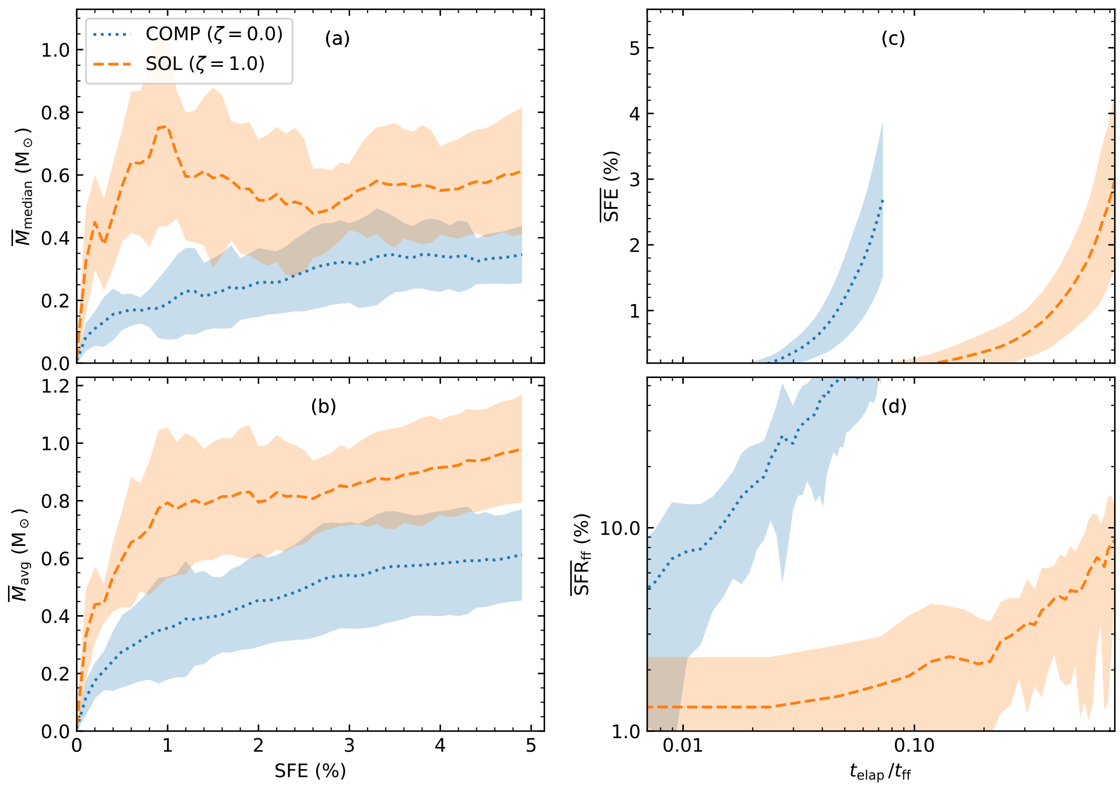

Figure 3.3: The left panels show (a) the median stellar mass and (b) the average stellar mass as a function of the star formation efficiency (SFE in %) for the COMP (dotted curve) and SOL (dashed curve) simulations. The right panels (c) and (d) indicate the star formation efficiency and star formation rate per free-fall time, respectively, as a function of time. For both COMP and SOL models, all quantities shown here represent the average values obtained from multiple simulations, and the coloured bands correspond to the standard deviation over the set of these simulations. Here $t_{\rm elap}/t_{\rm ff}$ is the elapsed time from the formation of the first sink particle in units of the free-fall time and is distinguished from the time t in the above column density projections, which is the time measured from the instant self-gravity was turned on.

Table 3.2: Parameter values from the MCMC fit.

	Model (1)	M_0 [M$_\odot$] (2)	σ (3)	$M_{\rm T}$ [M$_\odot$] (4)	Γ (5)	$M_{\rm cut}$ [M$_\odot$] (6)	p (7)
Free $M_{\rm T}$	COMP	$0.53^{+0.12}_{-0.12}$	$0.68^{+0.05}_{-0.05}$	$0.77^{+0.19}_{-0.11}$	$1.2^{+0.2}_{-0.2}$	$5.7^{+0.9}_{-0.7}$	4
	SOL	$0.76^{+0.21}_{-0.12}$	$0.64^{+0.06}_{-0.05}$	$2.07^{+0.85}_{-0.54}$	$1.5^{+0.7}_{-0.5}$	$6.7^{+0.9}_{-0.7}$	4
Fixed $M_{\rm T}$	COMP	$0.47^{+0.12}_{-0.07}$	$0.67^{+0.06}_{-0.05}$	1	$1.4^{+0.2}_{-0.2}$	$6.2^{+1.1}_{-0.9}$	4
	SOL	$0.85^{+0.10}_{-0.13}$	$0.65^{+0.04}_{-0.04}$	1	$0.8^{+0.1}_{-0.2}$	$6.2^{+0.8}_{-0.6}$	4

Notes. The values presented here correspond to the 50th percentile of each of the parameters, with the 16th and 84th percentiles denoting the uncertainty.

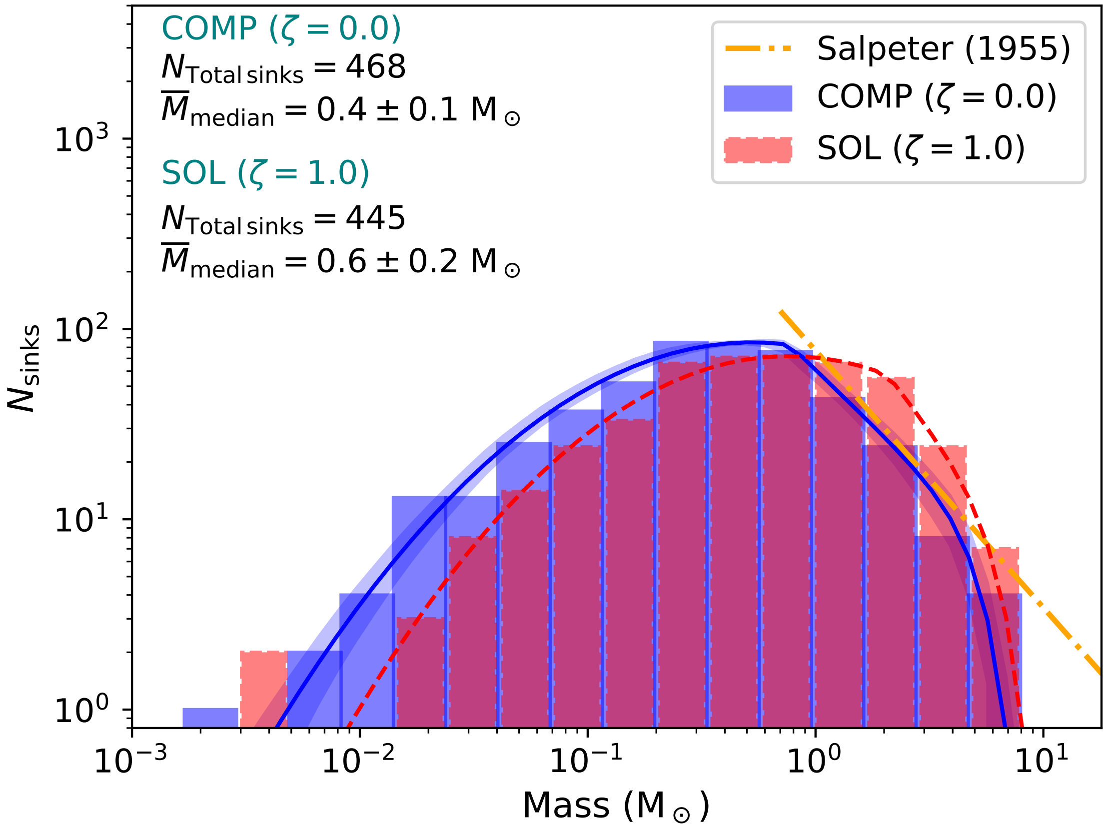

Figure 3.4: Comparison of the sink mass distribution (SMD) obtained for the COMP (histogram with solid edges) and SOL (histogram with dashed edges) turbulence driving models at SFE=5%. The solid (COMP) and dashed (SOL) curves fitted (the 16th to 84th percentile confidence interval shown as the shaded region), are Chabrier (2005)-type IMFs, but modified to take into account the finite mass of the simulated cloud (high-mass cutoff). The values of the IMF fit parameters (peak, standard deviation, transition mass and power-law slope) are derived using MCMC sampling (see §3.3.2). The dash-dotted line is the Salpeter (1955) IMF.

in our computational box, we include an exponential term that acts as a smooth cutoff at high masses in the power law part of the Chabrier (2005) IMF,

$$dN/d\log M = \begin{cases} k_1 \exp\left(-\frac{(\log M - \log M_0)^2}{2\,\sigma^2}\right) & \text{for } M < M_{\rm T}, \\ k_2\, M^{-\Gamma} \exp\left(-(M/M_{\rm cut})^p\right) & \text{for } M \geq M_{\rm T}. \end{cases} \tag{3.15}$$

with five free parameters $\theta = (\log M_0, \sigma, \log M_{\rm T}, \Gamma, \log M_{\rm cut})$ where $M_0, \sigma, M_{\rm T}$ and Γ are the peak mass, standard deviation of the log-normal part, mass at which the IMF transitions from a log-normal to a power-law form, and slope of the power-law part, respectively. k_1 and k_2 are normalisation constants, set to ensure continuity at $M_{\rm T}$. Due to the presence of the exponential term in the power-law part, the IMF will be cut-off at high masses. The mass at which the exponential term starts to dominate is characterised by $M_{\rm cut}$ and p defines how sharply the IMF drops around $M_{\rm cut}$.

The posterior probability $P(\theta|\{M_{\rm sink}\})$, i.e., the probability of θ given the list of sink particle masses $\{M_{\rm sink}\}$ can be calculated using the Bayes' theorem and is given by

$$P(\theta|\{M_{\rm sink}\}) = \frac{P(\theta)\, P(\{M_{\rm sink}\}|\theta)}{\int P(\theta')\, P(\{M_{\rm sink}\}|\theta')\, d\theta'}, \tag{3.16}$$

where $P(\theta)$ represents the prior distribution and $P(\{M_{\rm sink}\}|\theta)$ is the likelihood function, i.e., probability of $\{M_{\rm sink}\}$ given the IMF form defined by Eq. (3.15) with a particular parameter combination θ. The likelihood function is given by (Nam et al. 2021)

$$P(\{\mathrm{M}_{\rm sink}\}|\theta) = \prod_{M_{\rm i}\epsilon\{M_{\rm sink}\}} \frac{dN}{dM}(M_{\rm i}, \theta). \tag{3.17}$$

We employ uniform priors on $\log M_0, \sigma, \log M_{\rm T}$ and Γ. We set $p = 4$ since we want the cut-off to be sufficiently sharp. We note that changing p in the range from 1 to 10 does not affect the fit of the relevant physical quantities, most importantly, $\log M_0, \sigma, \log M_{\rm T}$, and Γ. In the case of the parameter $\log M_{\rm cut}$, we need to be cautious while defining the prior. Due to the low statistics in the high-mass end of our SMDs, the error in estimating $\log M_{\rm cut}$ can be large. Therefore, we need to have a rough estimate of where $\log M_{\rm cut}$ is located. Accordingly, instead of a uniform prior, we use a Gaussian prior on $\log M_{\rm cut}$ with the mean of the Gaussian defined by the maximum sink particle mass $M_{\rm max}$ in our simulations. For deriving $M_{\rm max}$, first the MCMC fit is derived as discussed above, except with a uniform prior on $\log M_{\rm cut}$. The fit thus obtained for each of the driving models correspond to the mass distribution of sink particles obtained from multiple simulations. The fit is then rescaled to correspond to a single simulation by dividing by the total number of simulations. M_{max} will be the mass at which the number of stars is less than 1 in the rescaled fit obtained with uniform priors. Finally, the MCMC fitting is performed again using a Gaussian prior for $\log M_{\mathrm{cut}}$ with a mean of $\log M_{\mathrm{max}}$. Using this method, we find a stable value for $\log M_{\mathrm{cut}}$ automatically, without having to impose any prior knowledge of its final value. Most importantly, while the cutoff allows us to account for the fact that our simulated clouds have a finite mass, $\log M_{\mathrm{cut}}$ is sufficiently high that none of the main physical parameters are affected by its details, namely $\log M_0, \sigma, \log M_{\mathrm{T}}$ and Γ.

The corner plot showing the posterior probability distribution of the parameters is presented in the Appendix section 3.7. Tab. 3.2 lists the 50th percentile value of the parameters obtained using the MCMC technique. The error bars denote the 16th and 84th percentiles. The parameter set obtained for the COMP and SOL SMDs are clearly different. The COMP model has a lower M_0 and also a slightly higher σ, which indicates the presence of a higher fraction of low-mass stars as compared to the SOL model. In addition, the combination of M_0 and M_{T}, which controls how the IMF turns over from a log-normal form to a power law, varies between the two models. While $M_0 = 0.5\,\mathrm{M}_{\odot}$ and $M_{\mathrm{T}} = 0.8\,\mathrm{M}_{\odot}$ in the case of the COMP model, they are located at $0.8\,\mathrm{M}_{\odot}$ and $2.1\,\mathrm{M}_{\odot}$, respectively, for the SOL model. The solid curve in Fig. 3.4 corresponds to the fit derived for the COMP SMD using the 50th percentiles of each of the parameters, with the spread bracketed by the 16th and 84th percentiles. The dashed curve represents the same for the SOL SMD. The curves compare very well with the corresponding histograms, justifying our binning choice and confirming that the SMDs produced with the two driving modes are different.

Our simulations do not produce very high-mass stars and the cut-off mass M_{cut} occurs well before $10\,M_{\odot}$ in both the models (see Tab. 3.2). As a consequence of the narrow high-mass range, it is difficult to have an accurate estimate of the power-law slope, which is why the error bars on Γ are large, particularly for the SOL model. In such a situation, small variations in the location of the transition mass M_{T} can significantly affect the value of the power-law slope. To understand the uncertainties that this introduces, we also produce another set of fits for our SMDs using MCMC sampling in the same manner as discussed above, but with M_{T} fixed at the transition mass for a Chabrier (2005) IMF, i.e., at $1\,\mathrm{M}_{\odot}$. The corresponding parameter values are shown in Tab. 3.2. We see that on fixing $M_{\mathrm{T}} = 1\,\mathrm{M}_{\odot}$, there is no significant change in the parameter values that define the log-normal part of the IMF fit, namely, M_0 and σ. However, we find that for the COMP fit, Γ becomes slightly steeper compared to its value when M_{T} was a free parameter (although not statistically significant, i.e., a change from $\Gamma = 1.2$ to 1.4, which is within the 1-sigma uncertainty), but for the SOL case, Γ becomes significantly shallower (from 1.5 to 0.8, just outside a 1-sigma overlap, considering the uncertainties of both fits). When M_{T} was a free parameter, the value of M_{T} derived for the COMP fit was lower than $1\,\mathrm{M}_{\odot}$, while it was higher than $1\,\mathrm{M}_{\odot}$ for the SOL fit. Therefore, on fixing M_{T} at $1\,\mathrm{M}_{\odot}$, M_{T} moves further away from the peak M_0 in the case of the COMP fit, while it moves closer to M_0 in the case of the SOL fit. This explains why Γ becomes steeper for the COMP fit and shallower in the case of the SOL fit. The combination of M_{T} and Γ obtained when M_{T} is a free parameter and those obtained when M_{T} is fixed both qualitatively agree on the fact that the SOL SMD has a higher fraction of high-mass stars. The IMF fits obtained with the parameter values for the fixed M_{T} case shown in Tab. 3.2 (see Fig. 3.14) and the associated parameter correlation (corner) plots (see Fig. 3.15 and Fig. 3.16) are presented in the Appendix section 3.7.

The plots shown in Fig. 3.5 present the sink mass distribution at SFE = 5%, but only of the sink particles that formed before the time at which a particular SFE is reached. For example, the top left panel shows the mass distribution of sink particles that formed before an SFE of 1% is reached, while the bottom right panel shows the mass distribution of the sinks that formed before an SFE of 4% is reached. We note that Fig. 3.5 does not represent the time evolution of the SMD, i.e., the distribution of stellar masses at different SFEs, rather it shows the distribution of final stellar masses (mass at the simulation end time, i.e., at SFE = 5%) of all the sink particles that were created before an SFE of 1%, 2%, 3% and 4% (from top left to bottom right panel in Fig. 3.5) is reached. We see that the peak of the distribution shifts to lower masses as we progressively include stars that form at later times. This is readily seen for SOL, where the peak is at around $2 - 3\,\mathrm{M}_{\odot}$ when only sinks that form before SFE=1% are included, while it is $\sim 0.5 - 1.0\,\mathrm{M}_{\odot}$ in the mass distribution when all the sink particles are included, i.e., sink particles that form before SFE = 5% (see Fig. 3.4). There is also a shift in the peak of the COMP model, although relatively minor, from $\sim 0.7 - 0.9\,\mathrm{M}_{\odot}$ to $\sim 0.3 - 0.5\,\mathrm{M}_{\odot}$. The shift to lower masses implies that the formation of comparatively lower-mass stars is more favourable at later times, which is also indicated by the decrease in the median and average mass as we include more younger stars in the distribution.

It is clear that the COMP and SOL distributions differ the most in the top left panel of Fig. 3.5, where only the sink particles that form in the early stages are considered. This is because these sink particles form before self-gravity modifies the gas density PDF substantially and begins to dominate in promoting fragmentation. Therefore,

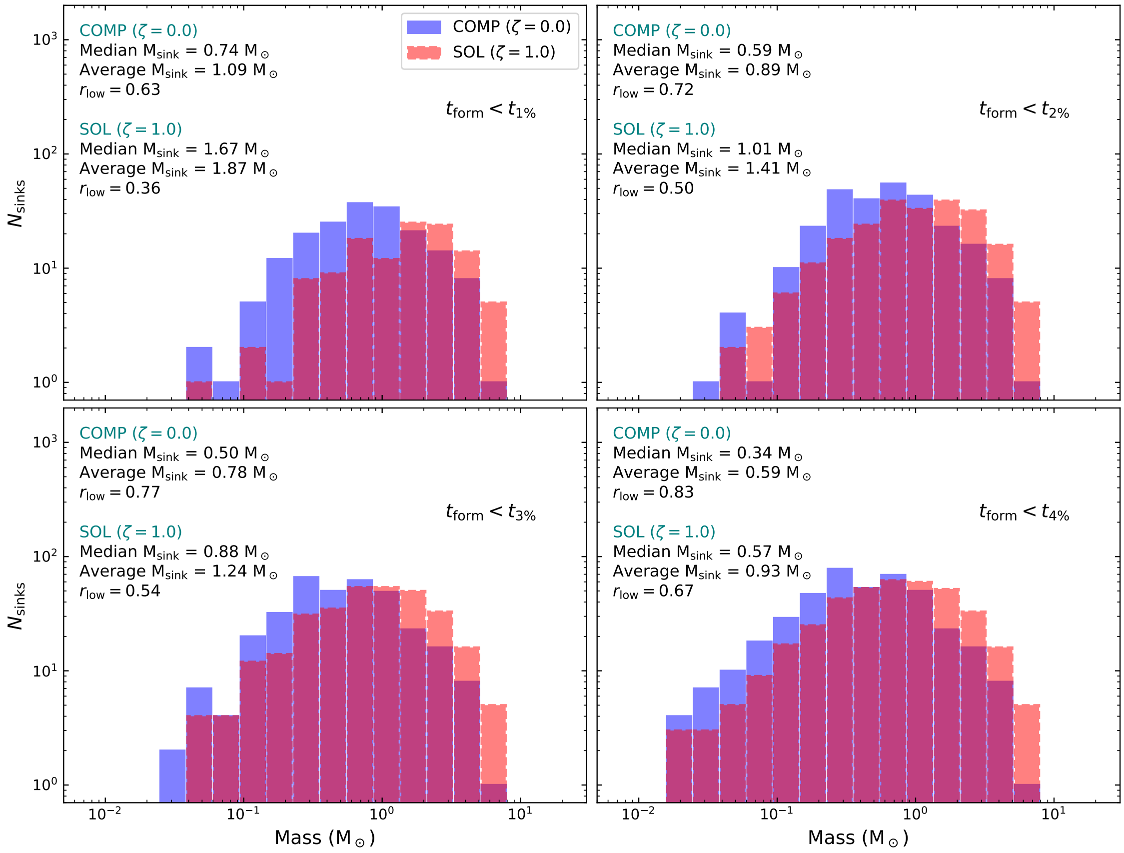

Figure 3.5: Distribution of stellar masses (mass at the end of the simulation, i.e., at SFE=5%) of all the sink particles that formed before an SFE of (from top left to bottom right) 1%, 2%, 3% and 4% is reached. The histogram with solid edges represents the COMP distribution and the histogram with dashed edges corresponds to the SOL distribution. We point out that for calculating the median and average sink masses shown in the plots here, the sink particle masses at SFE = 5% are used, but only of the sink particles that formed before a particular SFE. On the other hand, $\overline{M}_{\mathrm{median}}$ in Fig. 3.4 represents the median value for the sink particle masses at SFE = 5%, where all sink particles are considered, irrespective of when they formed.

the effect of the turbulence driving in setting the mass would be more pronounced for stars that form relatively early in the evolution of the cloud. For SOL, $r_{\rm low}$, the fraction of low-mass stars ($\mathrm{M} < 1\,\mathrm{M}_{\odot}$) that form early in the simulation is substantially smaller compared to that in COMP, and the shape of the SOL SMD is not established when only the sink particles that form before SFE=1% are included. The low-mass part of the SOL IMF becomes fully developed only when we include the younger sink particles, i.e., the sink particles that form in the later stages of the cloud evolution. The formation of many low-mass stars and the increase in the $\overline{\mathrm{SFR}_{\rm ff}}$ (see panel d in Fig. 3.3) towards the end of the simulations are inter-related. At later stages, the average density of the gas in the star-forming regions (where a cluster of stars forms) increases as a result of the increased influence of self-gravity on fragmentation. Previous studies have shown that, mathematically, this corresponds to the development of a power-law tail in the gas density PDF (e.g., Kritsuk et al. 2011; Ballesteros-Paredes et al. 2011b; Federrath & Klessen 2013; Burkhart et al. 2015; Lee & Hennebelle 2018a; Khullar et al. 2021). Therefore, gravitationally induced fragmentation (Lee & Hennebelle 2018a) begins to play a more important role in setting the mass of the sink particles that form during the later stages. Further, as more stars form, the stellar density increases. As a result, the frequency of dynamical encounters rises and thus the sink particles that form in the later stages are prone to the termination of accretion early on via dynamical ejections (Reipurth & Clarke 2001; Bate et al. 2002a). The fragmentation induced by self-gravity and dynamical effects allow more low-mass stars to form.

IMF in the Galactic centre

The above discussion implies that clouds that are primarily driven by solenoidal modes will produce only a small fraction of low-mass stars (i.e., low fragmentation) if star formation in later stages is suppressed. Low fragmentation would automatically lead to the existing stars reaching high masses. Such a scenario is a possibility in the case of star-forming regions near the Galactic centre. The clusters within the Central Molecular Zone (CMZ), particularly near the Galactic centre, are found to have top-heavy IMFs, i.e., a higher fraction of high-mass stars compared to the typical IMF (Figer et al. 1999; Kim et al. 2006; Lu et al. 2013; Hosek et al. 2019). The turbulence driving in the CMZ is expected to be dominated by solenoidal modes as a result of the enhanced shear (Federrath et al. 2016; Rani et al. 2022a) in the CMZ environment. Thus, if the turbulence driving is primarily solenoidal, the deviation from the average density is small (relatively narrow gas density PDF), and therefore the formation of stellar masses lower than the mean Jeans mass is also expected to be small. This means that only few low-mass stars can form in the early stages of star formation in CMZ clouds. Since the average temperature in the CMZ is significantly higher than that in typical clouds located in the Galactic disc (Ginsburg et al. 2016), the mean Jeans mass will also be high, which again suppresses the formation of low-mass stars (Bonnell et al. 2006; Klessen et al. 2007). As shown above, low mass stars can form only later in solenoidally-driven star-forming regions when the local density increases as a result of the increase in the gravitational influence. However, by that time, the existing stars will have already grown to high masses, because of the high Jeans mass. The radiative heating by these highly luminous stars prevents further fragmentation, and thus the fraction of high-mass stars in CMZ clouds would be relatively higher than that in typical Milky way clouds. Thus, the predominately solenoidal turbulence driving in CMZ clouds may (at least in part) explain observations of a top-heavy IMF in the CMZ.

3.4 Comparison of the SMDs with observational data and theoretical models

3.4.1 Comparisons with observed IMFs

In Fig. 3.6, we compare the SMD of each driving model with IMF fits obtained in different observational surveys since Salpeter (1955) (dash-dotted line). We compare the SMDs with the system IMFs instead of the canonical or the individual-star IMFs, because fragmentation on very small scales is not well resolved in our simulations, and therefore we cannot identify all the low-order multiple systems. The short-dotted curve in Fig. 3.6 represents the Chabrier (2005) system IMF. Parravano et al. (2011) propose an analytical model of the IMF (long-dotted line) described by various parameters based on observational constraints, e.g., the ratio of the number of brown dwarfs (BDs) to the number of stars and the slope of the high-mass regime of the IMF (see also Paresce & De Marchi 2000). This function predicts a higher fraction of BDs below $0.03\,\mathrm{M}_\odot$ than the Chabrier (2005) IMF. Da Rio et al. (2012) (solid line) fit a log-normal function for the mass distribution of low-mass stars in the Orion Nebula Cluster (ONC). However, the standard deviation of their fit is smaller compared to that in Chabrier (2005), i.e, they find a lower fraction of brown dwarfs as compared to that found in the Galactic disc. We adopt the best-fit parameters, namely the characteristic mass m_c and the standard deviation $\sigma\,(\log m)$, from table 3 of Da Rio et al. (2012) to reproduce their log-normal fit to the mass distribution they derived by considering a Baraffe et al. (1998) evolutionary model. We then extend

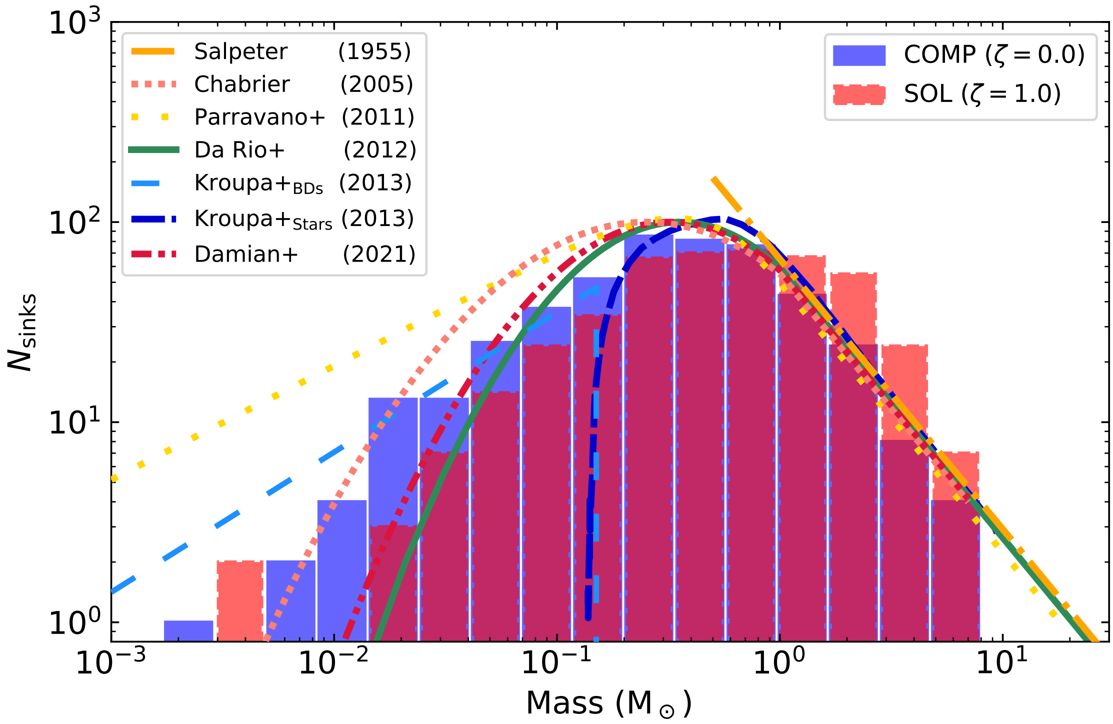

Figure 3.6: Comparison of various observational IMFs with the SMD (at SFE = 5%) obtained in the COMP (histogram with solid edges) and SOL (histogram with dashed edges) simulation models. The curves are the system IMF models, based on observational surveys, by Salpeter (1955) (dash-dotted), Chabrier (2005) (short-dotted), Parravano et al. (2011) (long-dotted), Da Rio et al. (2012) (solid), Kroupa et al. (2013) for brown dwarfs (long-dashed) and stars (short-dashed), and Damian et al. (2021) (dash-dot-dotted).

the fit to higher masses by combining it with a Salpeter-like power-law function, similar to what was done in Krumholz et al. (2012b). The Kroupa et al. (2013) system IMF has separate mass functions for stars and BDs based on the argument that if BDs form in the same manner as stars, then it contradicts the observed binary properties of BDs. The Kroupa et al. (2013) stellar system IMF (taken from Fig. 25 in Kroupa et al. 2013) and BD IMF (short-dashed and long-dashed lines) are obtained by random pairing of companions out of the canonical IMF (Kroupa 2001), where initial binary fractions of 100% and 0%, respectively, are assumed. Damian et al. (2021) (dash-dot-dotted line) compared the stellar mass distribution of nine young clusters with different environmental conditions with respect to the number of massive stars, stellar density and the Galacto-centric distance. They found that the functional form of the distributions are relatively similar and that they can be fitted by a log-normal distribution with a peak at 0.32 ± 0.02 and $\sigma = 0.47 \pm 0.02$ (in logarithmic scale).

The peak of the COMP SMD is at around $0.3 - 0.5\,\mathrm{M}_{\odot}$, while the peak of the

SOL SMD lies between $0.5 - 1.0\,\mathrm{M}_\odot$. The Chabrier (2005) (dotted line) and Da Rio et al. (2012) (solid line) system IMFs have peak masses of $\sim 0.25\,\mathrm{M}_\odot$ and $0.35\,\mathrm{M}_\odot$, respectively. The peak of the COMP SMD is comparable with the peak of the IMF derived from different observational surveys, which is located at around $\sim 0.3\,\mathrm{M}_\odot$ (Bastian et al. 2010; Offner et al. 2014). However, the peak of the SOL SMD is too high even when considering the scatter in the observational estimates. Observational surveys (where close binaries are unresolved) find that approximately one BD is formed per every five late-type (sub-solar) stars (Andersen et al. 2006, 2008; Thies & Kroupa 2007; Parravano et al. 2011; Kroupa et al. 2013). The ratio of the number of sink particles with sub-stellar masses ($M_{\mathrm{sink}} \leq 0.08\,\mathrm{M}_\odot$) to that of the sink particles with stellar masses ($0.15\,\mathrm{M}_\odot < M_{\mathrm{sink}} \leq 1.0\,\mathrm{M}_\odot$) are $67/278 = 0.24$ and $30/235 = 0.13$ for the COMP and SOL models, respectively. Our results imply that variations in the IMF, e.g., the discrepancy in the width of the low-mass end between the different observational IMF models, may be explained by different mixtures of turbulence driving modes in the ISM.

3.4.2 Comparisons with theoretical models of the IMF

The Padoan & Nordlund (2002) (PN02) model

Padoan & Nordlund (2002) proposed that the size of cores that form in shocked regions of clouds created by supersonic turbulence is comparable to the thickness of the shocked layers. Assuming the isothermal shock jump conditions, the mass of a dense core is found to be inversely proportional to the square of the Mach number, which in turn is scale-dependent, following the Larson relation (Larson 1981). Taking into consideration the scale dependence of the Mach number, or equivalently, the power-law nature of the velocity power spectrum $P(k) \propto k^{-\beta}$ (Federrath et al. 2021), Padoan & Nordlund (2002) arrive at the mass distribution of dense cores given by

$$N(M)\,\mathrm{d}\log M \propto M^{-3/(4-\beta)}\mathrm{d}\log M. \tag{3.18}$$

They argue that the distribution of collapsing cores is given by

$$N(M)\,\mathrm{d}\log M \propto M^{-3/(4-\beta)} \left(\int_0^M p(M_\mathrm{J})\,\mathrm{d}M_\mathrm{J} \right) \mathrm{d}\log M, \tag{3.19}$$

where $p(M_\mathrm{J})\,\mathrm{d}M_\mathrm{J}$ is the distribution of Jeans masses, and the integral over it yields the fraction of cores of mass M that are Jeans unstable. Padoan & Nordlund (2002) suggest that the Jeans mass distribution is linked to the turbulent gas density PDF,

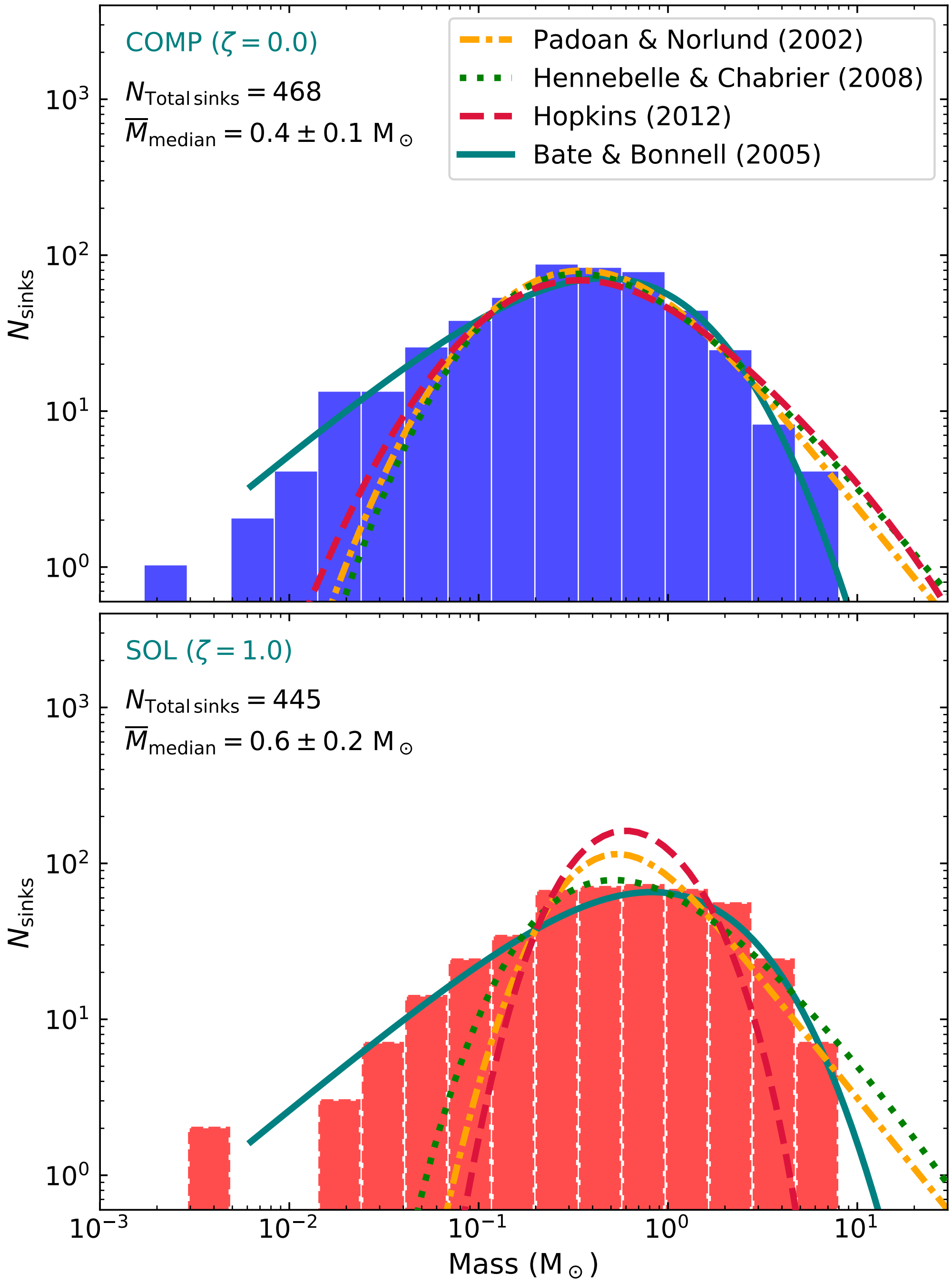

Figure 3.7: Top panel: Comparison between the sink mass distribution of the COMP model at SFE = 5% with different theoretical models of the CMF/IMFs. The plotted curves correspond to Padoan & Nordlund (2002) (dash-dotted), Bate & Bonnell (2005) (solid), Hennebelle & Chabrier (2008) (dotted), and Hopkins (2012) (dashed) CMF/IMFs. Both the Padoan & Nordlund (2002) and Hopkins (2012) CMF/IMFs have been shifted to lower masses by a factor of 1.3 and the Hennebelle & Chabrier (2008) CMF/IMF has been shifted to higher masses by a factor of 2, so as to fit the SMD. Bottom panel: Same as the top panel, but for the SOL simulations. Here the Padoan & Nordlund (2002), Hennebelle & Chabrier (2008), and Hopkins (2012) CMF/IMFs have been shifted to lower masses by a factor of 2.5, 1.7 and 8.7, respectively.

which is approximately log-normal with a standard deviation given by (see Padoan et al. 1997a; Federrath et al. 2008),

$$\sigma_{\mathrm{s}}^2 = \ln(1 + b^2 \mathcal{M}^2), \tag{3.20}$$

and therefore, the distribution of Jeans masses is given by (Padoan et al. 1997a; Padoan & Nordlund 2002),

$$P(M_{\mathrm{J}})\, d\ln M = \frac{1}{\sqrt{2\pi}\sigma_{\mathrm{s}}/2} \left(\frac{M_{\mathrm{J}}}{M_{\mathrm{J,0}}}\right)^{-2} \exp\left[-\frac{1}{2}\left(\frac{\ln M_{\mathrm{J}} - A}{\sigma_{\mathrm{s}}/2}\right)^2\right] d\ln M, \tag{3.21}$$

where $A = \ln M_{\mathrm{J,0}}^2 + \sigma_{\mathrm{s}}^2/2$ and $M_{\mathrm{J,0}}$ is the mean Jeans mass. For $\beta = 2$, which is the typical one-dimensional power spectral index derived for MCs through observations and numerical experiments (Ossenkopf & Mac Low 2002; Heyer & Brunt 2004; Roman-Duval et al. 2011; Federrath 2013a; Federrath et al. 2021), the high-mass slope of the IMF based on the Padoan & Nordlund (2002) model is

$$\Gamma = 3/(4 - \beta) = 1.5. \tag{3.22}$$

The peak of the distribution is then controlled by the scale of the mean thermal Jeans mass $M_{\mathrm{J,0}}$, which is ~ 2–$3\,\mathrm{M}_{\odot}$ in our simulations.

The Padoan & Nordlund (2002) model corresponds to the dash-dotted curves in both the top and bottom panels of Fig. 3.7 and is shown for the simulation input parameters: $\mathcal{M} = 5$, $\beta = 2$, $M_{\mathrm{J,0}} = 2$, and $b = 1$ (COMP) or $b = 1/3$ (SOL).

The Hennebelle & Chabrier (2008) (HC08) model

To derive an analytical model for the CMF/IMF, Hennebelle & Chabrier (2008) build upon the framework of the Press-Schechter formalism, which is originally employed in the context of cosmology. Based on the log-normal nature of the gas density PDF for supersonic turbulence, the model associates the self-gravitating structures (analogous to dense cores) with the over-densities in the density distribution that satisfy a collapse criterion. The collapse criterion is defined by the Jeans mass, where the turbulent support is also taken into account. The shape of the derived analytical CMF/IMF is determined by a combination of power-law and log-normal terms. At very small and very large masses, the log-normal term dominates and introduces an exponential cut-off, while the power-law term dominates in the intermediate mass range. The mass scales (both small and large) at which the transition from the power-law to the log-normal form occurs, is determined by the standard deviation of the density PDF ($\sigma_{\rm s}$), which in turn is dependent on the Mach number and the driving of the turbulence (see Eq. 3.20). Hennebelle & Chabrier (2008) argue that the power-law slope is steeper if the non-thermal support against collapse, e.g., the turbulent pressure, is not taken into account. Utilising their expression for the slope of the power-law contribution, which is defined by the turbulence power spectral index $\beta = 2$ (Federrath et al. 2021, as also assumed in the Padoan & Nordlund model above), Hennebelle & Chabrier (2008) find

$$\Gamma \approx (\beta + 3)/2\beta = 1.25. \tag{3.23}$$

We remark that Hennebelle & Chabrier (2013) later incorporated the time dependence of the gas density PDF in their derivation of the CMF/IMF, and found that as a consequence, the power-law slope steepens slightly. We plot the Hennebelle & Chabrier (2008) CMF/IMF by using Eq. 44 in Hennebelle & Chabrier (2008), again with the simulation input parameters: $\mathcal{M} = 5$, $\beta = 2$, $M_{\rm J,0} = 2\,{\rm M}_{\odot}$, $\mathcal{M}_* = 1.4$, and $b = 1$ (COMP) or $b = 1/3$ (SOL). We note that $\mathcal{M}_*$ is the effective sonic Mach number on the scale of the mean Jeans length. The dotted curves in the top and bottom panels of Fig. 3.7 depict the Hennebelle & Chabrier (2008) model.

The Hopkins (2012) (H12) model

Hopkins (2012) suggest that in order to accurately derive the mass spectrum of dense cores and subsequently the IMF, the 'cloud-in-cloud' problem has to be resolved, i.e., the over-counting arising due to a self-gravitating region being contained in another self-gravitating structure of larger size. Extending the excursion-set formalism to the case of log-normal gas density fluctuations in the ISM, they propose that the mass function of self-gravitating objects on the largest scales (first crossing distribution) represent the mass distribution of giant molecular clouds, while the mass spectrum of self-gravitating objects on the smallest scales (last crossing distribution) corresponds to the CMF/IMF. The absolute mass scale and the dispersion in the gas density PDF are calculated by taking into the account the effects of gas properties on all scales up to the scale of a galactic disc. The relation defining the mass required for collapse at different scales reduces to a Jeans criterion on very small scales and to a Toomre criterion on galactic-disc scales. The Mach number at the driving scale of turbulence or equivalently the Mach number $\mathcal{M}_h$ on the galactic scale height significantly influences the shape of the mass function. The Hopkins (2012) mass function has a power-law form in the high-mass regime, which flattens at the turnover mass $M_{\rm sonic}$, characterised by the sonic scale $R_{\rm sonic}$, i.e., the scale at which the gas flow becomes subsonic (Federrath et al. 2021). We employ the Python code developed by Nam et al. (2021) to reproduce the Hopkins (2012) mass function (dashed line in Fig. 3.7). We mention that here we define $\mathcal{M}_h = 5$, which is the Mach number representing the velocity dispersion on the driving scale of the turbulence ($L/2$) in the simulations. Due to the periodic nature of the computational domain, our simulations do not have a characteristic scale height. Nam et al. (2021) find that such an uncertainty in the distinction of $\mathcal{M}_h$ can significantly affect the shape of the IMF as predicted in the Hopkins (2012) model.

Comparison of the PN02, HC08, and H12 models

Our SMDs qualitatively agree with the above three theoretical models on the fact that an increase in the relative strength of compressive modes of the turbulence driving results in an increase in the number of low-mass stars formed. In all three turbulence-regulated theories of the IMF, this is because a purely compressive turbulence driving results in a larger standard deviation of the gas density PDF (Federrath et al. 2008), i.e., a higher fraction of high-density gas, which corresponds to a relatively lower Jeans mass.

In the case of COMP (top panel in Fig. 3.7), the forms of the three gravo-turbulent models agree with each other and compare reasonably well with our SMD, although they slightly underestimate the very low-mass range. In the case of SOL (bottom panel in Fig. 3.7), the HC08 model, compared to the PN02 and H12 models, matches marginally better with our SMD in the high-mass and low-mass regime. The underestimation of the very low-mass range is more apparent in the case of the SOL model where all the three theoretical models drop off exponentially as they approach the very low-mass regime, sharper than our SMD. Mathew & Federrath (2021) also found that these gravo-turbulent models underestimate the very low-mass regime of the simulation SMDs (in that study a natural mixture of turbulence driving modes, $b \sim 0.4$, was used). This suggests that the theoretical IMF models principally based on fragmentation promoted by turbulence underestimate the BD population.

We stress that the gravo-turbulent models discussed here essentially derive the mass distribution of unstable dense cores, analogous to the CMF. Although some observational studies suggest that the shape of the IMF is arguably similar to that of the CMF, the associated mass scales are different (Motte et al. 1998; Testi & Sargent 1998; Johnstone et al. 2000; Nutter & Ward-Thompson 2007; Alves et al. 2007). Further, the theoretical models here are compared based on their match with the IMF produced by our simulations, which have limitations in the maximum achievable resolution (see Sec. 3.6.3). The agreement of these theoretical models with the individual-star IMF from observations is a different question which is out of the

Table 3.3: Comparison of the median and peak masses (at SFE = 5%) obtained for the simulation SMDs with that of the CMF/IMFs predicted by different theoretical models for the input parameters relevant to our simulations.

Model	Median mass [$M_\odot$]				
	Sim	PN02	HC08	H12	BB05
(1)	(2)	(3)	(4)	(5)	(6)
COMP	0.37	0.47	0.19	0.47	0.35
SOL	0.62	1.54	1.02	5.11	0.61

Model	Peak mass [$M_\odot$]				
	Sim	PN02	HC08	H12	BB05
(1)	(2)	(3)	(4)	(5)	(6)
COMP	0.53	0.44	0.17	0.42	0.47
SOL	0.76	1.39	0.87	5.11	0.82

Notes. The median mass of the simulation SMDs presented here corresponds to the median sink particle mass and the peak mass presented here for the simulation SMDs corresponds to the peak of the fit to the SMDs obtained using MCMC sampling.

scope of the present study. The three gravo-turbulent models in Fig. 3.7 have been shifted along the mass-axis so as to fit our SMDs and enable a comparison between their shapes. The median mass and the position of the peak of the three theoretical CMF/IMFs before the mass-shift are compared with the same for the simulation SMDs in Tab. 3.3. While the peak mass of the COMP SMD is lower than that of the SOL SMD by a factor of ~ 1.4, the peak of the PN02, HC08, and H12 models shifts to lower masses by a factor of 3, 5 and 12, respectively, on changing the input parameter b from 1/3 (SOL) to 1 (COMP).

A direct comparison of the models with our SMDs is rational only if a one-to-one mapping between the CMF and IMF can be fully established. It is possible that the IMF may deviate from the CMF due to further fragmentation of the cores, the influence of protostellar outflows, and due to dynamical encounters between the stars, which can terminate accretion. On the other hand, the Bate & Bonnell (2005) model represents a different class where the IMF emerges as a result of stars accreting competitively from a common reservoir of gas, until they are dynamically ejected. This is fundamentally distinct from the gravo-turbulent models where the mass of a star is predetermined at the (gas) core level. The Bate & Bonnell (2005) model on the other hand derives the IMF from the stellar properties, e.g., the mean accretion rate, and therefore is more directly related to our SMDs (discussed next).

The Bate & Bonnell (2005) (BB05) model

According to the Bate & Bonnell (2005) IMF model, the final mass of a star is controlled by the interplay between accretion and stochastic ejections. All objects, whether stellar or sub-stellar, form with the same mass set by the opacity limit of fragmentation. The objects continue accreting at a constant rate and grow in mass until they are dynamically ejected from the parent cloud, which terminates their accretion. A log-normal function is assumed for the distribution of accretion rates ($P(\dot{M}_{\mathrm{acc}})$), and the probability of an object to be ejected at any given time $e(t)$ is proportional to $\exp(-t/t_{\mathrm{eject}})$, where t_{eject} is the characteristic ejection timescale. Given the mass of an object $M = M_{\mathrm{min}} + \dot{M}_{\mathrm{acc}} t$ at time t, where M_{min} is the minimum stellar mass set by the opacity limit of fragmentation and $\dot{M}_{\mathrm{acc}}$ is the time-averaged accretion rate, the probability distribution for the mass of an object is (Bate & Bonnell 2005),

$$f(M,t) = \frac{1}{\sqrt{2\pi}\sigma_{\mathrm{acc}}(M - M_{\mathrm{min}})} \exp\left\{ - \frac{\left[\log\left(\frac{M-M_{\mathrm{min}}}{t}\right) - \log\overline{\dot{M}}_{\mathrm{acc}}\right]^2}{2\sigma_{\mathrm{acc}}^2} \right\}. \tag{3.24}$$

When the termination of accretion via ejection is taken into account, the mass function becomes (Bate & Bonnell 2005),

$$f(M) = \int_0^{t_{\mathrm{p}}} f(M,t)\, e(t)\, dt, \tag{3.25}$$

where the time period t_{p} corresponds to the time elapsed between the formation of the first star and the end of the simulation. We fit the Bate & Bonnell (2005) IMF to our sink mass distribution for the SOL and COMP turbulence driving models by evaluating the following parameters: the mean accretion rate $\overline{\dot{M}}_{\mathrm{acc}}$, the standard deviation in the accretion rates (in logarithmic units) σ_{acc}, the characteristic ejection time t_{eject}, the minimum stellar mass M_{min}, and the time period of the cluster formation t_{p}. The turnover mass and the width of the IMF are characterised by the quantity $\overline{\dot{M}}_{\mathrm{acc}}\, t_{\mathrm{eject}}$ and the standard deviation in the accretion rates, respectively. The minimum stellar mass M_{min} defines the low-mass cut-off of the fit. The parameter values calculated for the SOL and COMP models are listed in Tab. 3.4, which represent the averages of the parameter values derived in the two sets (COMP and SOL). The solid curves in the top and bottom panels of Fig. 3.7 show the Bate & Bonnell (2005) IMF model. The median mass and peak of the Bate & Bonnell (2005) IMF for the COMP and SOL models are shown in Tab. 3.3. The peak of the Bate & Bonnell (2005) IMF for the COMP case is lower than that for the SOL case by a factor of 1.7.

We see that the Bate & Bonnell (2005) model provides a very good fit to both the COMP and SOL SMDs, especially in the sub-stellar regime, which was underes-

Table 3.4: Calculated parameter values for the Bate & Bonnell (2005) IMF model.

Model (1)	$\overline{\dot{M}}_{\rm acc}$ [M$_\odot$ yr^{-1}] (2)	$\sigma_{\rm acc}$ [dex] (3)	$t_{\rm eject}$ [yr] (4)	$t_{\rm p}$ [yr] (5)
COMP	1.6×10^{-5}	0.32	3.7×10^{4}	9.7×10^{4}
SOL	4.9×10^{-6}	0.26	1.9×10^{5}	7.8×10^{5}

Notes. The values presented here are averages of the parameter values obtained from the multiple simulations (realisations of the turbulence) for each simulation model, COMP and SOL. The Bate & Bonnell (2005) IMF fits (solid curves in Fig. 3.7) have been derived by substituting these parameter values into Eqs. 3.24–3.25 and setting $M_{\rm min} = 0.01\,{\rm M}_\odot$ as the low-mass cut-off of the fit for both the simulation sets.

timated by the gravo-turbulent fragmentation models (PN02, HC08, H12). This suggests that it is essential to take into account the dynamical ejections to fully explain the IMF (see also Basu & Jones 2004; Dib et al. 2010; Myers 2011; Maschberger et al. 2014). The reason why the COMP SMD compares reasonably well with the turbulent fragmentation models in contrast to the SOL SMD is because the COMP simulations have not undergone much time evolution, and therefore the effects of competitive accretion and dynamical ejections that are central to the Bate & Bonnell (2005) model, are comparatively low. In fact, in the case of the SOL model, if we consider only the stars that form in the early stages, i.e., those that form in an environment reflecting the initial conditions, then the number of low-mass stars is very small and matches the predictions of the gravo-turbulent models very well (see top left panel in Fig. 3.5).

Thus, we find that elements of both classes of IMF theoretical models, namely the gravo-turbulent and the competitive accretion/ejection models, are relevant for a comprehensive understanding of the IMF.

3.5 Stellar multiplicity and angular momentum

3.5.1 Multiplicity fraction

We follow the algorithm used in Bate (2009a) to identify the multiple stellar systems in our simulations. We find the closest gravitationally-bound pair (binary) in the list of N individual sink particles that form in a simulation. The closest bound pair is recorded as binary, and then replaced by a single object having the mass, centre-of-mass position and velocity equal to the original bound pair. Now the list consists of $N-2$ single objects and 1 binary object. In the new list, we search again for the closest pair of bound objects. In case the pair comprises of a binary object and a single object, then they are replaced by a triple. This procedure of replacing the closest bound pair with an object of higher order is carried out repetitively until none of the objects existing in the list are bound to one another or a quintuple is the only feasible outcome of the new pairing. We reject quintuples and systems of higher order, because most high-order multiple systems are dynamically unstable and will most likely decay to lower-order systems with further evolution of the cloud.

This iterative process transforms a list of individual sink particles into a list of single, binary, triple and quadruple systems, with none being a subset of a system of higher order. For example, none of the objects identified as binaries by the algorithm is a part of a triple or quadruple system. The multiplicity fraction in different mass ranges can be obtained by calculating the ratio of the number of multiple systems to the total number of systems whose primary star lies within the given mass range. Thus, the multiplicity fraction (mf) is defined as

$$mf = \frac{B+T+Q}{S+B+T+Q}, \tag{3.26}$$

where S, B, T, and Q denote the number of singles, binaries, triples, and quadruples, respectively, whose primary star mass is within the range for which mf is to be evaluated.

Fig. 3.8 presents the multiplicity fraction as a function of primary mass (also done in Bate 2012; Krumholz et al. 2012b; Cunningham et al. 2018; Sharda et al. 2020; Mathew & Federrath 2021) at SFE = 5% for the COMP and SOL models. The mass ranges are selected similar to those chosen in the observational studies so as to allow for a direct comparison. We immediately notice that the multiplicity fraction is an increasing function of the primary mass, for both COMP and SOL, consistent with observational surveys (see the reviews by Duchêne & Kraus 2013; Offner et al. 2022). However, the multiplicity fraction in each primary mass interval is higher in COMP compared to SOL (see Fig. 3.9 and the associated text for an explanation).

Our mf values also agree well with observations, except that we are underestimating the multiplicity in the very low-mass stellar (VLMS) and BD ranges. We mention that we do not resolve all of the low-order multiple systems, since the numerical cell width at the highest level of AMR is 100 AU. Therefore, some of the sink particles may actually represent binaries by themselves or triple systems (rarely). However, the numerical resolution effect is expected to be nominal because of the robust nature of the multiplicity fraction definition. The mf value will differ only if a sink particle identified as a single can be further fragmented into multiple individual stars. The value remains unaffected if the sink belongs to a multiple system, i.e., a part of a

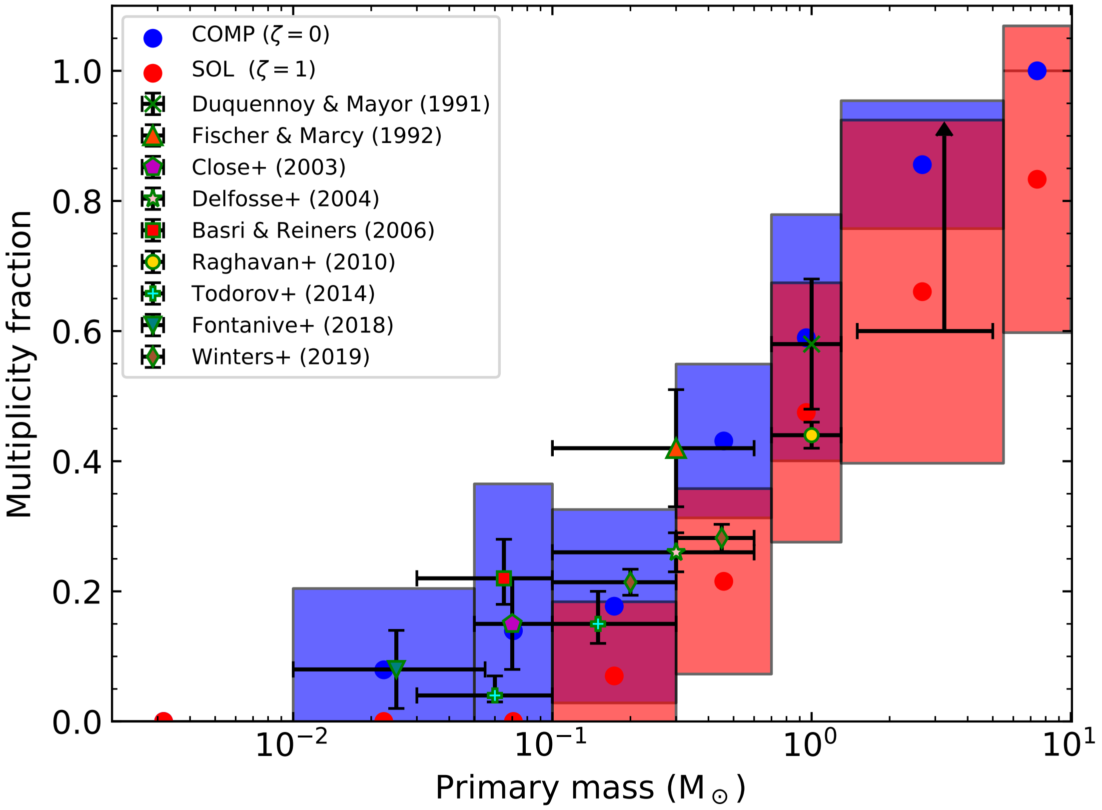

Figure 3.8: Multiplicity fraction (mf) computed via Eq. (3.26) in different primary mass intervals for the COMP (blue circular markers and boxes) and SOL (red circular markers and boxes) models. The circular markers denote the average mf, obtained across multiple simulations, in the mass interval represented by the width of the patch enclosing the marker. The height of the patch depicts the standard deviation of mf obtained from all the simulations. The centre of the crosses represents the value of mf obtained in different observational studies, with the horizontal and vertical error bars representing the mass range considered in the survey and the uncertainties, respectively. The observational data are (from low to high primary mass), from Fontanive et al. (2018), Todorov et al. (2014), Basri & Reiners (2006), Close et al. (2003), Todorov et al. (2014), Winters et al. (2019) (not corrected for undetected companions), Delfosse et al. (2004), Fischer & Marcy (1992), Raghavan et al. (2010) and Duquennoy & Mayor (1991). The multiplicity fraction of high-mass stars is relatively poorly understood. The lower limit of mf in the mass range of 1.5–5 $M_\odot$ is ~ 0.5–0.6 (Chini et al. 2012; Duchêne & Kraus 2013). Massive stars are expected to have $mf \sim 1$ (Mason et al. 2009; Sana & Evans 2011; Sana et al. 2017; Lee et al. 2020).

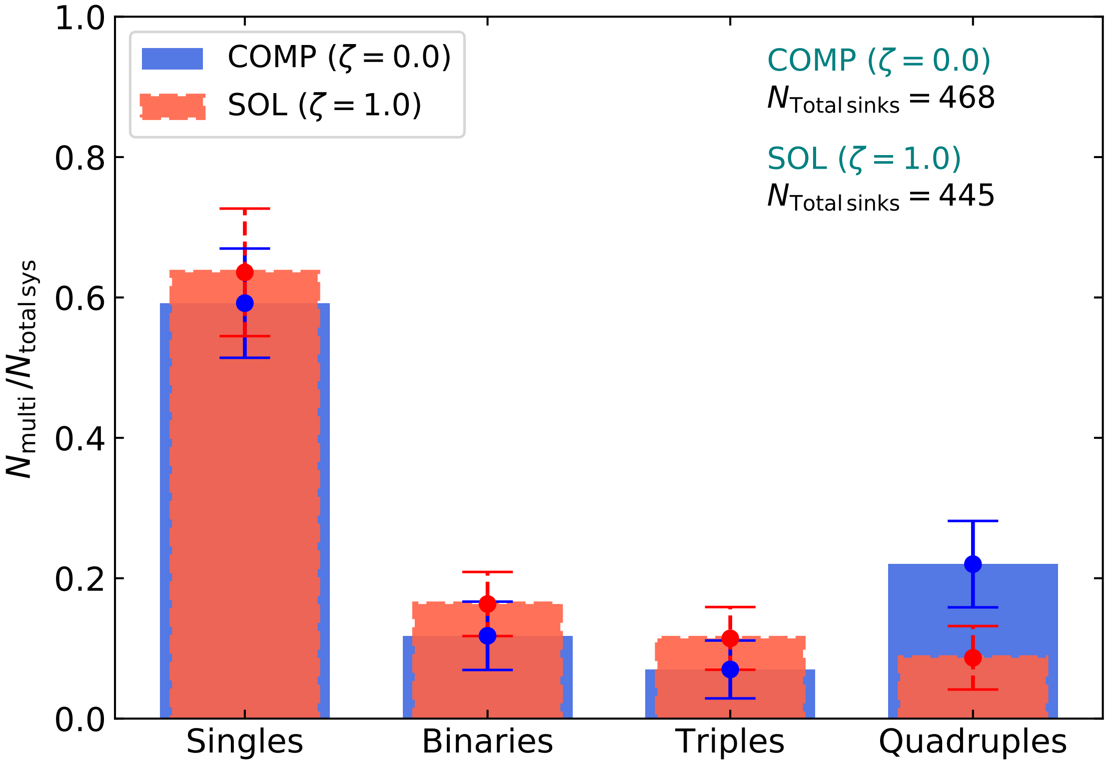

Figure 3.9: Fraction of single stars and multiple systems (binaries, triples, and quadruples), using the same data as for Fig. 3.8. The bars with solid edges correspond to the fractions derived for the COMP model and the bars with dashed edges correspond to the SOL model. The solid and dashed error bars represent the associated standard deviation in the set of simulations for the COMP and SOL models, respectively.

binary, triple or quadruple object. For example, if a member of a triple system is a binary by itself, then T and Q changes to $T - 1$ and $Q + 1$, respectively, which leaves mf unaltered. Based on the observational evidence that the average separation of binaries increases and the frequency of singles decreases with increasing primary mass (Konopacky et al. 2007; Kraus & Hillenbrand 2007; Luhman 2012), the mass range that is likely to be affected by the limitation in resolution is the low-mass end, particularly the BD regime. Therefore, the mf values in the sub-solar range (mainly in the regime of M-dwarfs and later types) are expected to be higher than what we obtained for COMP and SOL simulations.

Fig. 3.9 shows the fraction of singles, binaries, triples and quadruples at SFE = 5%. The fraction of single stars is highest for both SOL and COMP models, i.e., a large fraction of the sink particles that formed in our simulations are not members of a higher-order multiple system. For the COMP model, the single star fraction (SSF) is 0.59 ± 0.08, while the SSF is 0.64 ± 0.09 for the SOL model (see Tab. 3.1). While 150 of the 468 sink particles formed in the 7 COMP simulations are singles, 177 of the 445 sink particles formed in the 11 SOL simulations are singles. Further, the COMP simulations have a substantially higher fraction of quadruples. The total number of quadruples in the COMP simulations is 52, while there are only 22 quadruples in the SOL simulations in total. The COMP case is efficient in creating shocked regions of gas that have sufficient mass and high density on average to promote fragmentation into high-order systems, and therefore star formation in these regions is extremely clustered (see Fig. 3.2). In addition, the average time period of the COMP simulations is much smaller than that of the SOL simulations (see Tab. 3.4). As a result, the occurrence of dynamic encounters and therefore decay to lower-order systems is low in COMP compared to SOL. This explains the trend of high mf values for the COMP simulations as seen in Fig. 3.8. The value of mf is more sensitive to the number of high-order systems. When the number of quadruples increases, the total number of systems (denominator in the mf definition) decreases significantly, leading to high mf values.

3.5.2 Mass ratio distribution

Fig. 3.10 shows the mass ratio distribution of binaries for three different primary mass intervals, where the mass ratio is given by $q = M_2/M_1$ and $M_2 < M_1$. For selecting the pairs in each multiple system to be included in the mass-ratio distribution, we use two approaches: 1) the closest pairs (binaries) from each multiple system are selected—every binary, triple, and quadruple system contributes one mass-ratio value, except a quadruple consisting of two binaries orbiting each other which then contributes two mass-ratio values (similar to what is done in Bate 2009a); 2) the two most massive components from each multiple system are included—every binary, triple and quadruple system contributes only one mass-ratio value, including quadruples consisting of two binaries orbiting each other (similar to what is done in Guszejnov et al. 2017).

The left, middle and right panels in the top row of Fig. 3.10 present the binary mass ratio distributions obtained for the systems whose primary star is in the mass interval $M_{\rm prim} < 0.1\,{\rm M}_\odot$, $0.1 \leq M_{\rm prim} < 0.5\,{\rm M}_\odot$, and $M_{\rm prim} \geq 0.5\,{\rm M}_\odot$, respectively, using the approach similar to that in Bate (2009a). The bottom row shows the same, but the approach similar to that in Guszejnov et al. (2017) is used to obtain the distribution here. In the left panels, there is no mass-ratio distribution for the SOL model because no multiple systems were derived in the primary mass range $M_{\rm prim} < 0.1\,{\rm M}_\odot$ in the case of the purely solenoidal simulations. The mass-ratio distributions obtained using the two approaches seem to be somewhat different,

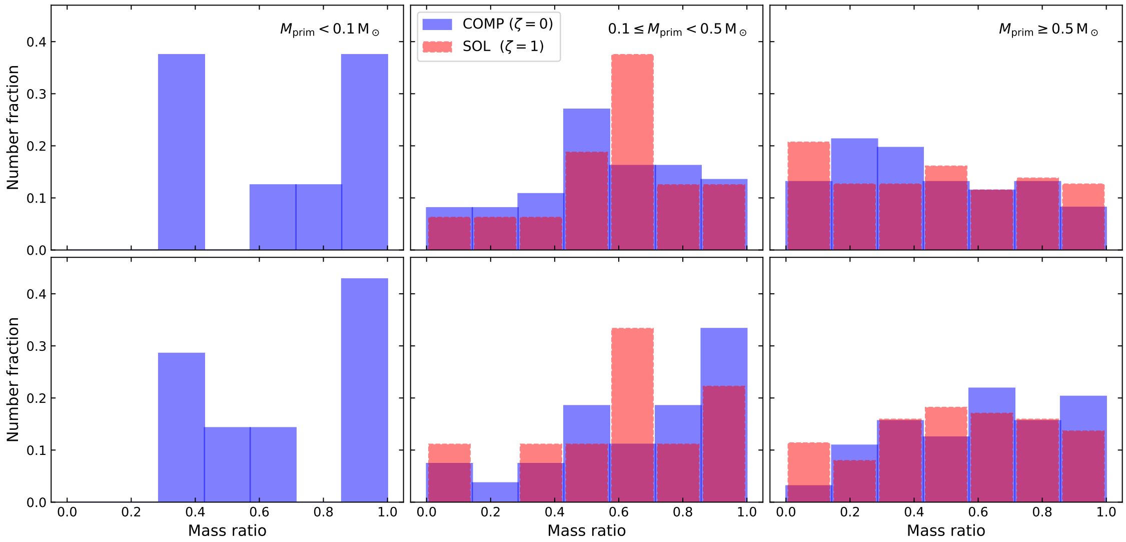

Figure 3.10: Top panels: Mass ratio distribution of binaries in the multiple systems whose primary mass lies in the range (from left to right) $M_{\rm prim} < 0.1\,{\rm M}_\odot$, $0.1 \leq M_{\rm prim} < 0.5\,{\rm M}_\odot$, and $M_{\rm prim} \geq 0.5\,{\rm M}_\odot$. From each system, the closest binaries are selected for the distribution. The histogram with solid edges represents the distribution for the COMP model and the histogram with dashed edges corresponds to the SOL models. Bottom panels: Similar to the respective panels on the top row, but here, instead of the closest pair, the most massive two members are selected from each system.

especially in the primary mass range $M_{\rm prim} \geq 0.5\,{\rm M}_\odot$ (right panels). For the primary mass range $M_{\rm prim} \geq 0.5\,{\rm M}_\odot$, the top panel has a slightly higher fraction of pairs with $q < 0.5$ while the bottom has a marginally higher fraction of pairs with $q > 0.5$. Stars with masses in the solar range and higher are generally members of high-order systems, i.e., triples and quadruples. Therefore, the choice in the approach used for selecting the binary pairs for the mass-ratio distribution is expected to affect the distribution.

Overall, irrespective of the turbulence driving mode or the method used for selecting the binaries, the mass ratio distribution for the mass range $M_{\rm prim} \geq 0.5\,{\rm M}_\odot$ is relatively flat, while the distributions for the mass ranges $0.1 \leq M_{\rm prim} < 0.5\,{\rm M}_\odot$ and $M_{\rm prim} < 0.1\,{\rm M}_\odot$ clearly have higher fractions of pairs with $q > 0.5$, which is consistent with the mass-ratio distributions derived from observations in the solar, M-dwarf and VLM regimes, respectively (see reviews by Raghavan et al. 2010; Offner et al. 2022). We note that observational surveys find that the mass-ratio distribution is also dependent on the orbital period or separation of the binary (e.g., Reid & Gizis 1997; Tokovinin 2011; Dieterich et al. 2012; Ward-Duong et al. 2015; Moe & Di Stefano 2017). Here, we do not make such a distinction while producing the mass-ratio distributions.

3.5.3 Specific angular momentum of dense cores and stars

The evolution of angular momentum from the early stages of the collapse of a dense core to the formation of a main sequence star is a highly debated topic. The specific angular momentum (j) of dense molecular cloud cores (diameter $\sim 0.1\,\mathrm{pc}$) is found to be greater than $10^{21}\,\mathrm{cm^2\,s^{-1}}$ (Goodman et al. 1993; Burkert & Bodenheimer 2000; Caselli et al. 2002). The specific angular momentum regime of class 0/I envelopes and binary systems is 10^{17}–$10^{21}\,\mathrm{cm^2\,s^{-1}}$ (Simon 1992; Ohashi et al. 1997; Yen et al. 2015a), while that of T-Tauri stars is 10^{16}–$10^{17}\,\mathrm{cm^2\,s^{-1}}$ (Hartmann et al. 1986). Gaudel et al. (2020) find that the j value of class 0 protostellar envelopes is virtually constant, at around $10^{20}\,\mathrm{cm^2\,s^{-1}}$, from a scale of ~ 1600 AU to 50 AU.

Jappsen & Klessen (2004) carried out hydrodynamic simulations of the collapse of supersonic turbulent clouds and determined $j_{\mathrm{mean}} = 8 \times 10^{19}\,\mathrm{cm^2\,s^{-1}}$ for their sink particles, which have an accretion radius of 560 AU. The specific angular momentum distribution of every sink particle that formed in the simulations of the COMP and SOL models, respectively, is shown in Fig. 3.11. The range of specific angular momentum of the sinks (having an accretion radius of 250 AU) in both the simulations ($\sim 10^{17}$–$10^{20}\,\mathrm{cm^2\,s^{-1}}$) spans the regime of protostellar envelopes and binaries, although a small fraction of the sink particles have j values typical of T-Tauri stars. The average specific angular momentum in the COMP model is $j_{\mathrm{mean}} = 8.4 \times 10^{18}\,\mathrm{cm^2\,s^{-1}}$, while that in the SOL model is $j_{\mathrm{mean}} = 1.8 \times 10^{19}\,\mathrm{cm^2\,s^{-1}}$, i.e., about a factor of 2 higher in SOL vs. COMP. This is most likely because the sink particles in SOL form from gas with ~ 2 times higher fraction of solenoidal (rotational) modes compared to COMP (see the bottom panel of Fig. 3 in Federrath et al. 2011a, for $\mathcal{M} = 5$). The j value inferred by Yen et al. (2015b) of the class 0 protostar B335 ($1.3 \times 10^{19}\,\mathrm{cm^2\,s^{-1}}$) measured at a scale of ~ 180 AU, lies between the average values of the COMP and SOL simulations.

3.6 Discussion

3.6.1 The mode of turbulence driving

Schmidt et al. (2010) studied the effect of turbulence driving on the mass distribution of dense cores in simulations where the cores were identified using a clump-finding algorithm. They find that a purely compressive turbulence driving results in a higher fraction of low-mass cores compared to purely solenoidal driving, which qualitatively agrees with our conclusions. Self-gravity is absent in the simulations of Schmidt et al.

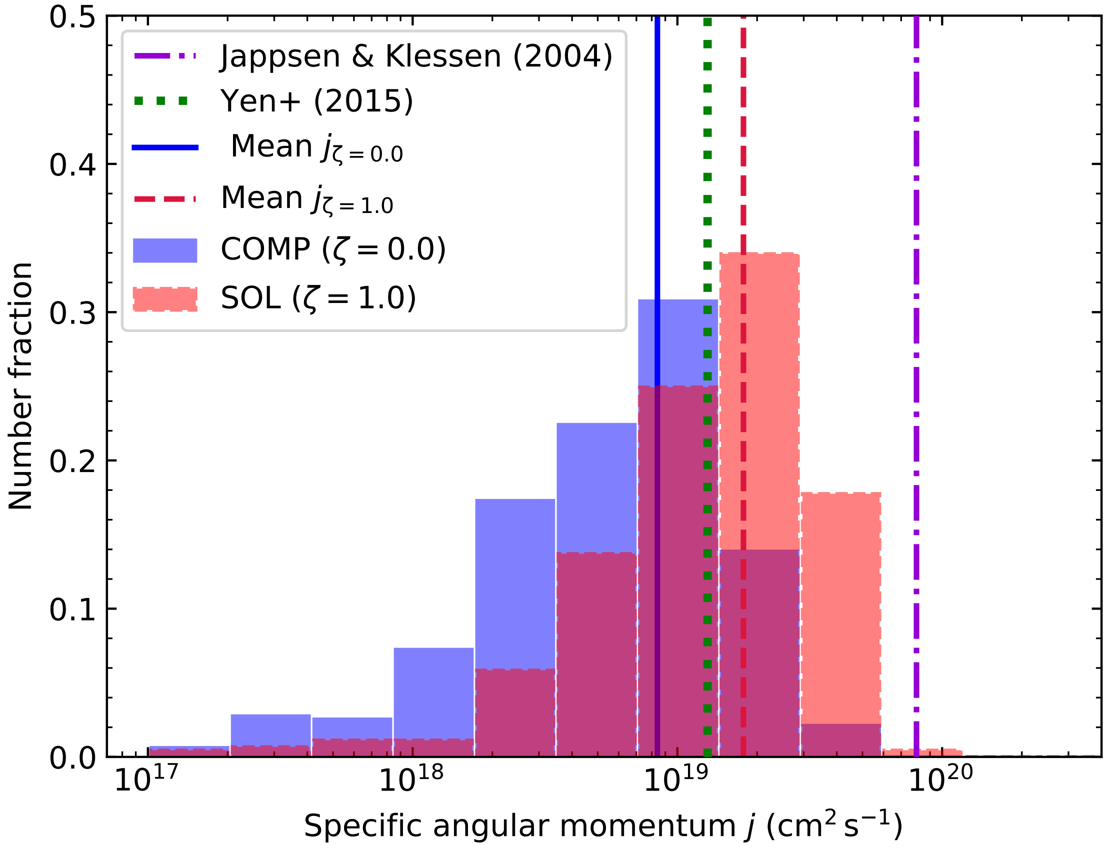

Figure 3.11: Specific angular momentum j of the sink particles ($r_{\rm sink} = 250\,$AU) from the COMP (histogram with solid edges) and SOL (histogram with dashed edges) simulations. The solid and dashed lines correspond to the mean j value of the COMP and SOL models. The dotted line presents the j value measured for the class 0 protostar B335 at $\sim$180 AU by Yen et al. (2015b), and the dash-dotted line represents the mean value of j obtained in the hydrodynamic simulations of Jappsen & Klessen (2004) where the sink particle radius is 560 AU.

(2010). Consequently, some of the dense cores identified may not be gravitationally bound, and also conversely, some regions that are not identified as bound might become (or have become) gravitationally bound if gravity had been included in their simulations. Moreover, the study assumes that the obtained CMF can be directly mapped to the IMF, which might not be the case in reality (Smith et al. 2009).

Lomax et al. (2015) carried out multiple simulations of cloud-collapse on the scales of prestellar cores with different turbulence realisations (no driving though) and analysed the dependence of the stellar mass on the variation of the fraction of solenoidal turbulent energy δ_{sol}. They find that the median stellar mass decreases with increasing δ_{sol}, contrary to our findings. Lomax et al. (2015) mention that in their simulations with high δ_{sol}, disc fragmentation dominates over filament fragmentation. Since discs are more prone to multiple fragmentation, the mean stellar mass would be lower in their simulations with high δ_{sol}, which generate sufficient angular momentum to form discs. However, it is difficult to directly compare their results with that of our relatively large-scale simulations, because, although the large-scale driving is purely solenoidal in our SOL simulations, it is not necessary that the solenoidal modes would always dominate on the scales where stars form, i.e., on the scales of prestellar cores.

Our results also tend to disagree with Liptai et al. (2017) who observed that the simulation IMF obtained from a purely compressive inital velocity field was indistinguishable from the one obtained with a purely solenoidal initial velocity field. However, as in Lomax et al. (2015), the turbulence was not continuously driven. In such a setup, the turbulence decays rapidly, and therefore the differences between solenoidal and compressive modes is relatively small once the stars begin to form. Another problem with that type of setup is that the initial density field (usually chosen to be uniform or of some radial power-law form, Girichidis et al. 2011) is inconsistent with the initial turbulent velocity field; that is, it takes about 2 turbulent cloud crossing times for the turbulence to become fully developed and the density and velocity field to establish reasonable turbulent statistics (Federrath et al. 2009; Kitsionas et al. 2009; Price & Federrath 2010b), a time by which the star formation experiments in Lomax et al. (2015) and Liptai et al. (2017) are already completed, and therefore, the turbulence in their simulations is never actually fully developed. This can only be achieved with continuous driving (Stone et al. 1998; Mac Low et al. 1998).

3.6.2 The velocity power spectrum

Bate (2009c) examined the dependence of the IMF on the kinetic power spectrum of the turbulent gas by comparing cloud-collapse simulations that are initialised with a power spectrum given by $P(k) = k^{-4}$ with those that start with a power spectrum consistent with the Larson scaling relations, i.e., $P(k) = k^{-2}$. They find that the IMFs produced by the two models are nearly indistinguishable. On the other hand, Nam et al. (2021) performed a set of simulations driven with a power spectrum given by $P(k) = k^{-2}$ and another set of simulations with the same initial conditions, except that they change the power spectrum of driving to $P(k) = k^{-1}$. They show that the shallower power spectrum results in a shallower high-mass slope in the IMF. The differences in how the turbulence was injected is likely the reason why the results of Bate (2009c) and Nam et al. (2021) are contradictory to each other—only an initial turbulent velocity field was imposed in the simulations of Bate (2009c), while the turbulence in the Nam et al. (2021) simulations was driven continuously (see also Guszejnov et al. 2022a).

It is clear that the conclusions of the above studies vary in terms of the effect of turbulence on the IMF. This is mainly due to the differences in the numerical setup chosen to conduct the experiment, particularly how turbulent motions are introduced in the simulations, e.g., impulsive initial velocity field versus continuous driving, with the former having only limited predictive power (c.f., discussion in the preceding subsection).

3.6.3 Numerical resolution and physics included

Another important aspect is the maximum numerical resolution that can be attained in simulations of star formation. Numerical studies like Bate (2009c) and Liptai et al. (2017) can resolve down to very small scales. However, with the increase in resolution, it also becomes important to include more physical mechanisms, such as magnetic fields, stellar heating and mechanical feedback (jets/outflows), which we do. While our simulations cannot capture fragmentation on the smallest scales ($\lesssim 100\,\mathrm{AU}$), the resolution is sufficient to compare our simulation SMDs with the system IMFs (unresolved close binaries) from observations. While the limitations in numerical resolution only allow us to compare system IMFs, the inclusion of the aforementioned physics in our simulations is crucial for a comprehensive understanding of the IMF.

3.7 Conclusions

We carried out a series of simulations of star cluster formation in molecular clouds incorporating gravity, turbulence, magnetic fields, stellar radiative heating and protostellar outflows to study the influence of the turbulence driving mode on the IMF. We find that the IMF derived for simulations driven by purely compressive modes has a higher fraction of low-mass stars and has a lower characteristic mass (median) as compared to the IMF obtained for simulations driven by purely solenoidal modes. We performed a Kolomogrov-Smirnov test to dismiss the possibility that the differences in the distributions are insignificant. In addition, to quantitatively confirm that the shape of the two distributions differs, we fit a modified version (to account for the finite mass in our numerical domain) of the Chabrier (2005) IMF, where the parameters including the peak mass, the standard deviation of the log-normal part, the transition mass and the slope of the power-law part of the IMF, are estimated using Markov Chain Monte-Carlo sampling. We find that the IMF parameter sets obtained for purely compressive and purely solenoidal driving primarily differ in the median (characteristic) mass of the IMF, i.e., the IMF from compressive driving is shifted to lower masses by a factor of ~ 1.5 compared to solenoidal driving.

We find that our simulation SMDs generally agree with the functional form of the IMF derived from different observational studies, i.e., the existence of a power-law tail at high masses and flattening at sub-solar masses. We see that, while the peak of the SMD produced by simulations with purely compressive driving ($\sim 0.3 - 0.5\,\mathrm{M}_\odot$) is comparable to the peak of the observed IMF ($\sim 0.3\,\mathrm{M}_\odot$), the peak of the SMD corresponding to the purely solenoidally driven simulations is too high ($\sim 0.6 - 1.0\,\mathrm{M}_\odot$). We also compare our IMFs with various theoretical models of the IMF based on gravo-turbulent fragmentation. We find that the gravo-turbulent models of the IMF (Padoan & Nordlund 2002; Hennebelle & Chabrier 2008; Hopkins 2012) successfully predict a decrease in the fraction of low-mass stars on switching from a purely compressive to purely solenoidal turbulence driving, as observed in our simulations. However, the gravo-turbulent models underestimate the number of low-mass stars formed in the purely solenoidal driving simulations, especially in the very low-mass regime. While many stars in the mass range of M dwarfs and later types form in the early stages of the purely compressive driving simulations, the number of such stars that form early is significantly lower in the case of the purely solenoidal driving simulations. A substantial fraction of the low-mass stars in the solenoidal simulations form towards the later stages of the cloud evolution. This explains why the models based on turbulent fragmentation underestimate the low-mass stars in the solenoidal simulations—these models are based on the cloud properties characteristic of a cloud in the early stages of the evolution. The gravo-turbulent models do not consider the time evolution of the parent cloud and stars while they are forming, such as changes in the gas density PDF, fragmentation of discs, and ejections via encounters (Bate et al. 2002a; Goodwin & Whitworth 2007; Stamatellos et al. 2007, 2011; Ballesteros-Paredes et al. 2011b; Rogers & Wadsley 2012; Thies et al. 2015; Burkhart et al. 2015; Lee & Hennebelle 2018a; Khullar et al. 2021).

We find that our simulation SMDs compare well with the Bate & Bonnell (2005) IMF model, which is based on accretion and stochastic ejections of stars. The agreement is most significant in the very low-mass range of the IMF compared with the gravo-turbulent models, emphasising the relevance of dynamical ejections during the formation of sub-stellar objects. However, the Bate & Bonnell (2005) IMF model is based on stellar properties, i.e., the mean and dispersion of the accretion rate, and the ejection timescale, as opposed to the gravo-turbulent models, which rely only on gas properties. The Bate & Bonnell (2005) model does not address how the IMF depends on stellar feedback and/or the properties of the MHD turbulence in the parental gas cloud, i.e., it cannot explain why our array of simulations shows that feedback and MHD turbulence, specifically the mode of driving, plays an important role in setting the characteristic stellar mass and the power-law slope (see also Nam et al. 2021). On the other hand, the gravo-turbulent models attempt to predict the shape of the IMF based on the turbulent gas properties only, without taking into the account the important dynamical evolution of the young stars when they interact in dense multiple systems. Therefore, our results and discussion here suggests that the theoretical models of the IMF need further revision, such that both the gas properties of the parental cloud and the dynamical interaction of young stars are self-consistently taken into account.

Our results further suggest that the top-heavy nature of the IMF observed in clouds near the Galactic centre (in the Central Molecular Zone, CMZ) may be (at least partly) a consequence of the turbulence driving properties in those regions—turbulent motions in the CMZ are likely driven by solenoidal modes, as a result of enhanced shear (Federrath et al. 2016; Rani et al. 2022a). As our simulations show, solenoidally-driving turbulence leads to less fragmentation and produces a higher median mass of stars than compressive driving. Therefore, in addition to the increased temperature, a predominately solenoidal driving mode of turbulence in the CMZ may explain the increased Jeans mass and consequently the observed top-heavy IMF in clouds near the Galactic centre (see also Klessen et al. 2007). The stars that are able to form in these conditions can grow to relatively higher masses, and as a consequence, the increased radiative heating by these stars hinders fragmentation in the later stages of the cloud collapse. Thus, the end result would be a higher fraction of high-mass stars in the CMZ compared to solar-neighbourhood clouds.

Finally, we compare the multiplicity properties of stars formed in purely compressive and purely solenoidal driving simulations. We find that purely compressive driving produces a higher fraction of multiple systems compared to solenoidal driving. For both driving modes, we observe that the multiplicity fraction is a monotonically increasing function of the primary mass, which is consistent with observations. However, compressive driving leads to a relatively higher multiplicity fraction for any primary mass. We find that the mass-ratio distribution of binaries in our simulations agree with observations, and this distribution does not seem to be influenced by the turbulence driving mode. The specific angular momentum j of the sink particles (having an accretion radius of 250 AU) for both solenoidal and compressive driving compares well with the j value obtained for protostellar envelopes and binaries in observational surveys. The mean j value for solenoidal driving is about twice as large as that for compressive driving, as a consequence of the factor ~ 2 higher solenoidal kinetic energy fraction for solenoidal driving compared to compressive driving.

Acknowledgements

We thank the anonymous reviewer for their comments, which helped to improve the paper. C.F. acknowledges funding provided by the Australian Research Council (Future Fellowship FT180100495), and the Australia-Germany Joint Research Cooperation Scheme (UA-DAAD). We further acknowledge high-performance computing resources provided by the Leibniz Rechenzentrum and the Gauss Centre for Supercomputing (grants pr32lo, pr48pi and GCS Large-scale project 10391), the Australian National Computational Infrastructure (grant ek9) in the framework of the National Computational Merit Allocation Scheme and the ANU Merit Allocation Scheme. The simulation software FLASH was in part developed by the DOE-supported Flash Center for Computational Science at the University of Chicago.

Appendix A: IMF fit using MCMC sampling

Fig. 3.12 depicts the corner plots showing the one-dimensional and two-dimensional posterior probability distributions for the different parameters of the IMF fit derived using the MCMC sampling method (free M_{T} case in Tab. 3.2) in the case of the COMP model, and Fig. 3.13 shows the same for the SOL model. Fig. 3.14 presents the fits obtained for the COMP and SOL SMDs using the values from the fixed M_{T} case in Tab. 3.2. The corresponding corner plots are shown in Fig. 3.15 (COMP) and Fig. 3.16 (SOL), respectively. We note that we have added the additional constraint that $M_0 < M_{\mathrm{T}}$, which is the reason for the abrupt cut-off in the posterior distribution of M_0 in Fig. 3.16. We can see that on fixing $M_{\mathrm{T}} = 1$, the value of Γ changes significantly between SOL and COMP. However, the important feature is that the parameter set associated with the COMP and SOL SMDs are still different.

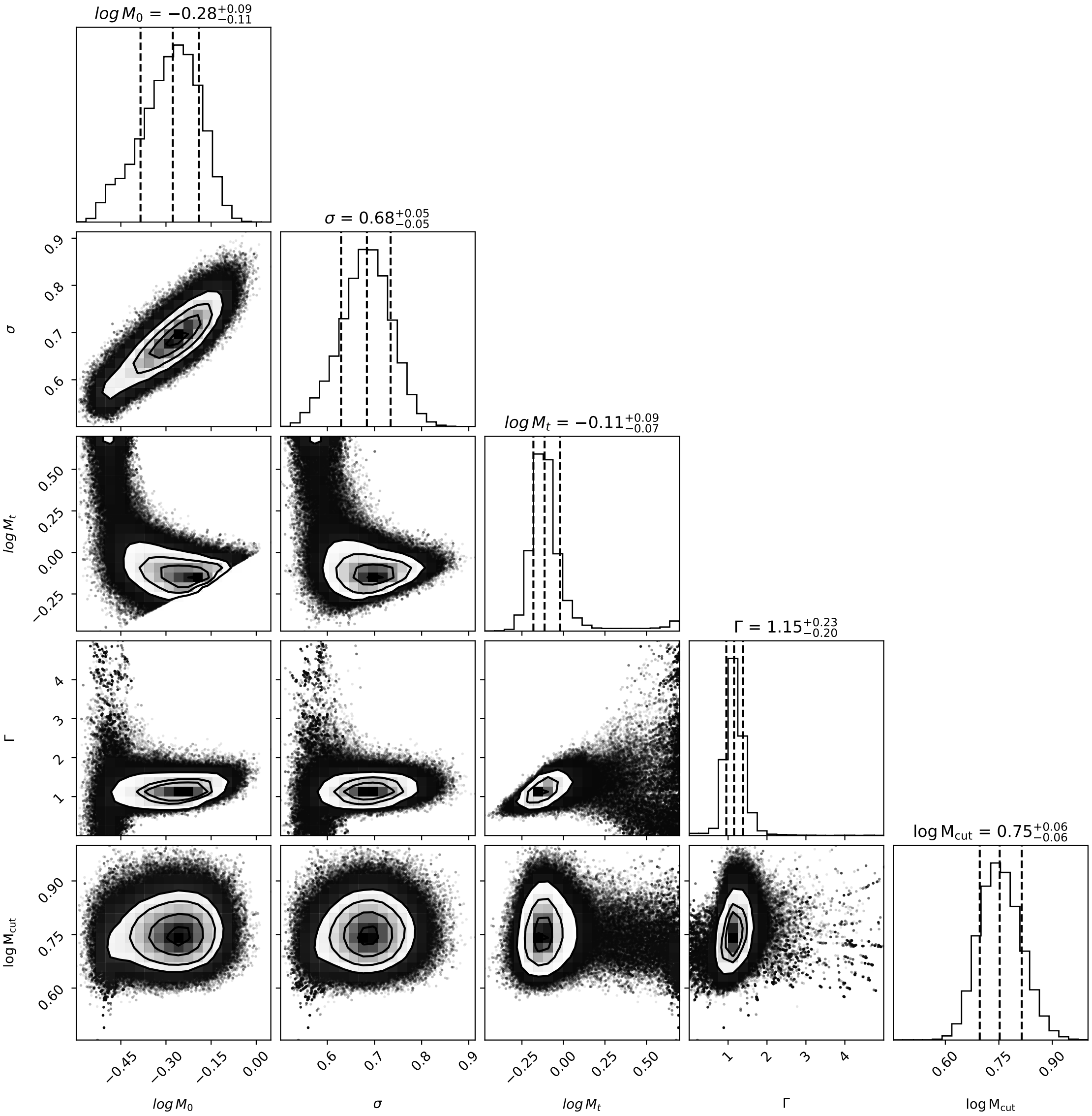

Figure 3.12: Posterior probability distribution of the parameters corresponding to the IMF fit for the COMP model obtained using MCMC sampling.

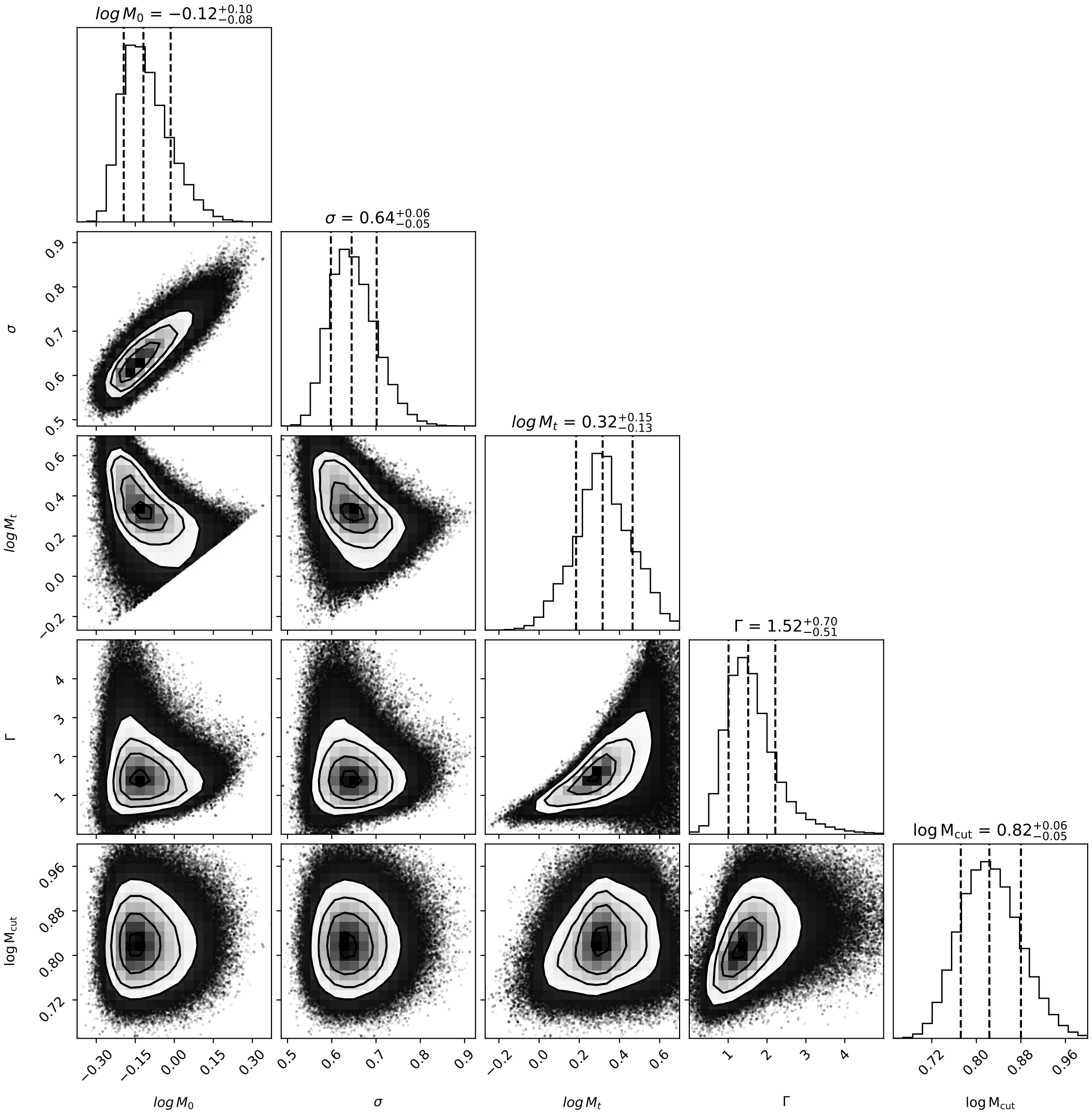

Figure 3.13: Same as Fig. 3.12, but for the SOL model.

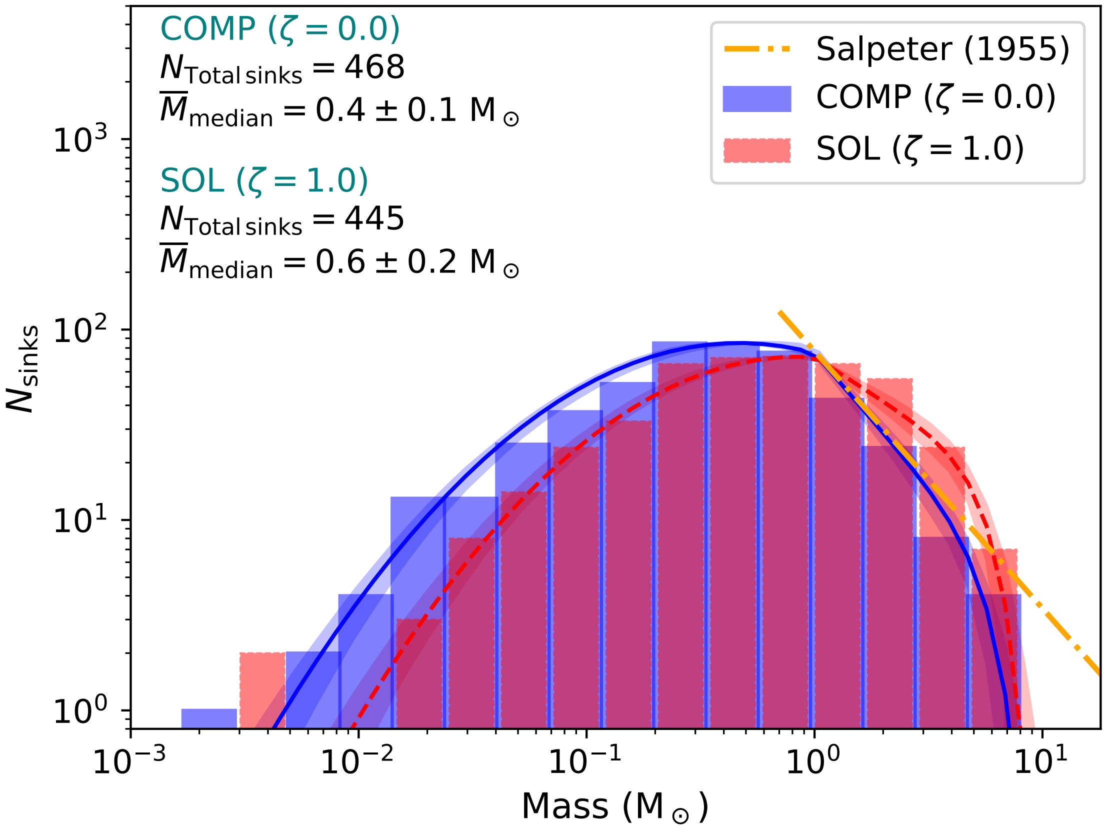

Figure 3.14: Same as Fig. 3.4, but the fitted curves (solid and dashed) are based on the parameter values for the fixed M_{T} case in Tab. 3.2.

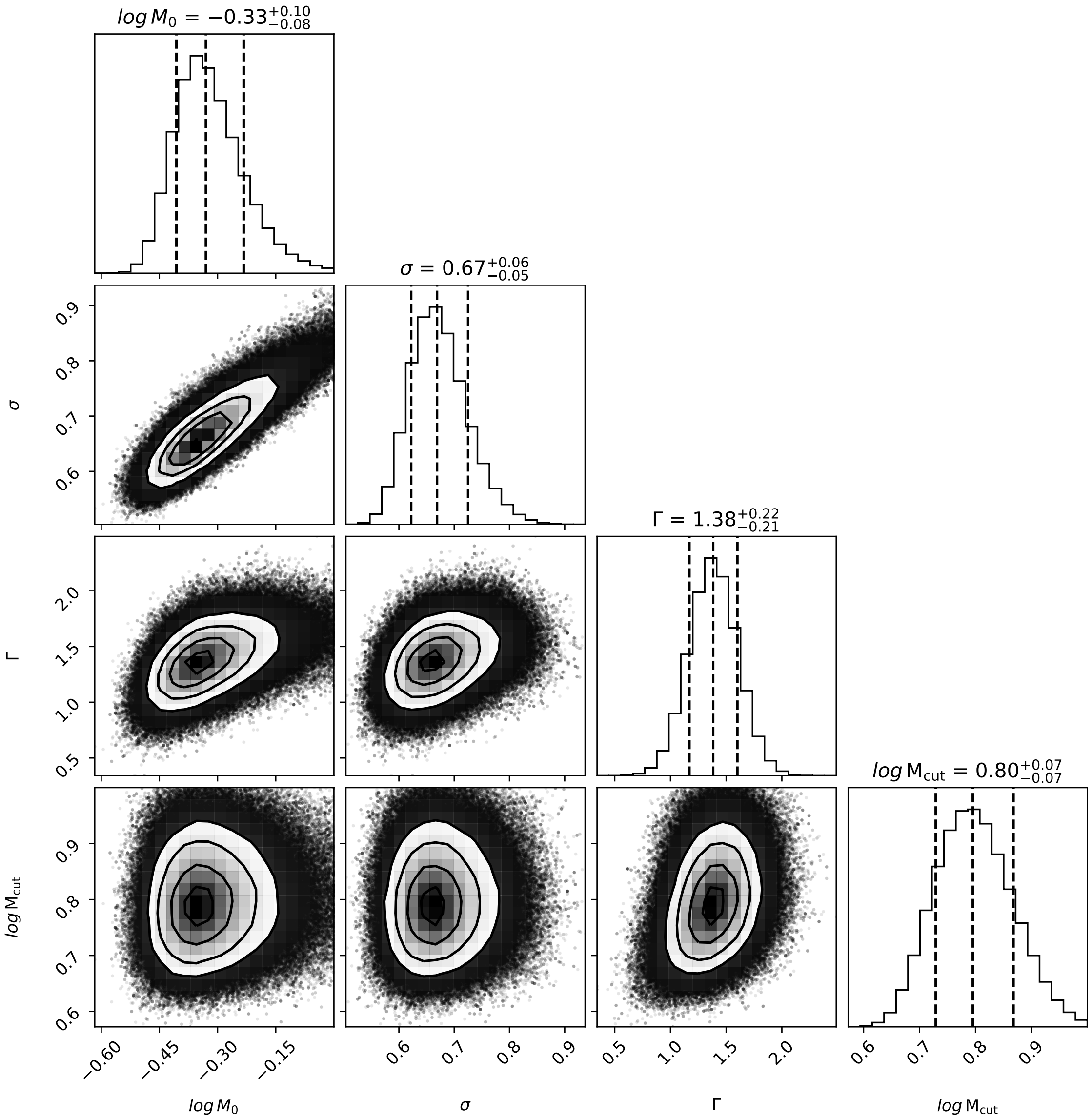

Figure 3.15: Same as Fig. 3.12, but where M_{T} is fixed.

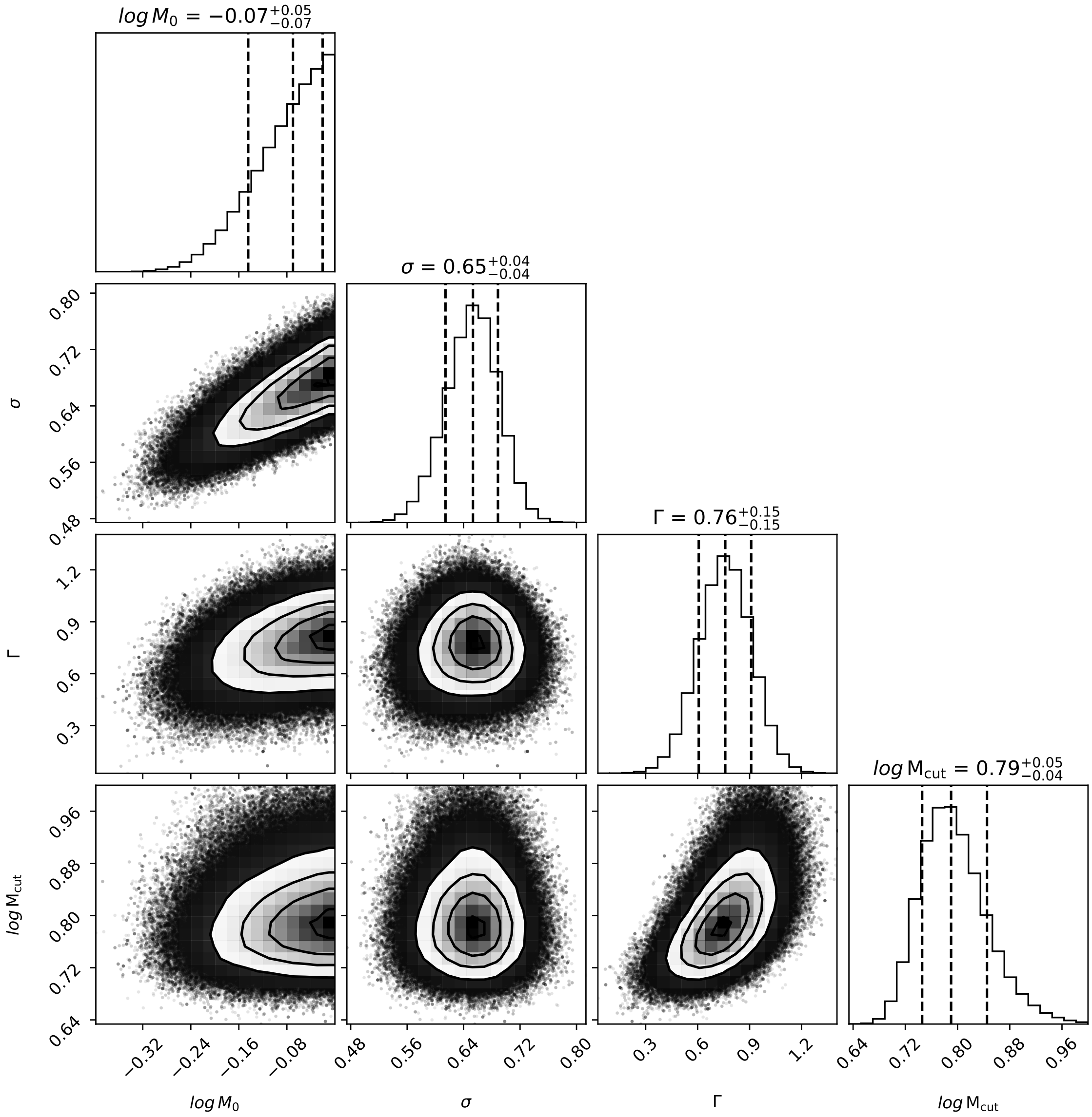

Figure 3.16: Same as Fig. 3.13, but where M_{T} is fixed.

Chapter 4

The influence of the cloud virial parameter on the initial mass function

Context and Contribution

This chapter has been previously published as 'The influence of the cloud virial parameter on the initial mass function', by Sajay Sunny Mathew, Christoph Federrath, Amit Seta, 2025, MNRAS, 536, 1932. The research is presented here as it appears in the original publication, except for a few minor typographical changes. I have carried out the simulations described in this paper, and post-processed the data for further investigation. I have written the majority of the paper, with inputs and suggestions from the two co-authors.

Abstract

Crucial for star formation is the interplay between gravity and turbulence. The observed cloud virial parameter, $\alpha_{\rm vir}$, which is the ratio of twice the turbulent kinetic energy to the gravitational energy, is found to vary significantly in different environments, where the scatter among individual star-forming clouds can exceed an order of magnitude. Therefore, a strong dependence of the initial mass function (IMF) on $\alpha_{\rm vir}$ may challenge the notion of a universal IMF. To determine the role of $\alpha_{\rm vir}$ on the IMF, we compare the star-particle mass functions obtained in high-resolution magnetohydrodynamical simulations including jet and heating feedback, with $\alpha_{\rm vir} = 0.0625$, 0.125, and 0.5. We find that varying $\alpha_{\rm vir}$ from $\alpha_{\rm vir} \sim 0.5$ to $\alpha_{\rm vir} < 0.1$ shifts the peak of the IMF to lower masses by a factor of ~ 2 and increases the star formation rate by a similar factor. The dependence of the IMF and star formation rate on $\alpha_{\rm vir}$ is non-linear, with the dependence subsiding at $\alpha_{\rm vir} < 0.1$.

Our study shows a systematic dependence of the IMF on $\alpha_{\rm vir}$. Yet, it may not be measurable easily in observations, considering the uncertainties, and the relatively weak dependence found in this study.

4.1 Introduction

One of the fundamental questions in star formation is the initial mass function (IMF), which is the stellar mass distribution in a newly formed cluster. The IMF is considered nearly universal based on observations (see reviews by Bastian et al. 2010; Kroupa et al. 2013; Krumholz 2014; Offner et al. 2014; Hopkins 2018; Lee et al. 2020; Hennebelle & Grudić 2024). Despite some variations in the functional form, most observational IMF models identify the existence of a peak at around $0.3\,{\rm M}_\odot$ and a power-law tail at high masses given by $dN \propto M^{-\Gamma}\, d\log M$, where N is the number of stars and M is the stellar mass (Salpeter 1955; Miller & Scalo 1979; Kroupa 2001; Chabrier 2005; Parravano et al. 2011). The slope (power-law on a logarithmic scale) of the high-mass end measured in the Milk Way and nearby galaxies is generally consistent with the Salpeter (1955) slope (Kroupa 2002; Bastian et al. 2010; Hopkins 2018; Kroupa et al. 2013), although cluster-to-cluster variations exist (Dib 2014; Dib et al. 2017; Schneider et al. 2018b; Hennebelle & Grudić 2024; Kroupa et al. 2024).

Recent observations challenge the notion of a universal IMF. There is compelling evidence for a top-heavy IMF near the Galactic center, i.e, having a higher fraction of high-mass stars compared to the IMF in the solar neighbourhood (e.g., Figer et al. 1999; Kim et al. 2006; Lu et al. 2013; Hosek et al. 2019). On the other hand, massive elliptical early-type galaxies (ETGs) are discovered to have a bottom-heavy IMF, i.e, a higher fraction of low-mass stars (e.g., Cenarro et al. 2003; van Dokkum & Conroy 2010; Treu et al. 2010; Cappellari et al. 2012; Conroy et al. 2013). Further, the slope of the IMF seems to be dependent on the star formation rate (SFR) of the galaxy, where the power-law slope becomes shallower with the increase in SFR (Gunawardhana et al. 2011). In addition, Kroupa et al. (2013) suggest that the underlying formation mechanism of brown dwarfs (BDs) and stars are likely different based on the observed BD binary statistics and propose separate mass functions for BDs and stellar objects. The need to treat the mass functions for BDs and stars separately would put further constraints on the modelling of the IMF parameters and interpreting the IMF shape in the sub-solar range. An accurate theoretical model of the IMF must reproduce the typical IMF characteristics such as the presence of a peak in the low-mass end, the existence of a power-law tail at super-solar masses with a slope close to the Salpeter (1955) estimate, and at the same time address the observed outlier IMFs, apparent SFR dependence, and the BD-star issue discussed above. A prerequisite to achieving such a model is understanding the dependence of the IMF on environmental conditions.

There have been significant contributions from theoretical and numerical works towards understanding the IMF. Some of the proposed candidates responsible for setting the peak mass include the Jeans mass at the density of the thermal coupling of gas to the dust (Li et al. 2003; Larson 2005; Jappsen et al. 2005; Elmegreen et al. 2008; Grudić & Hopkins 2023), the Jeans mass associated with protostellar heating (Bate 2009b; Krumholz et al. 2011; Guszejnov et al. 2016; Federrath et al. 2017b; Mathew & Federrath 2020; Hennebelle et al. 2020a), and the formation of the first hydrostatic core and tidal screening of the gas in the immediate environment by the core (Hennebelle et al. 2019; Colman & Teyssier 2020). Another important mechanism extensively studied in the context of the IMF is the role of magnetic fields, which is found to reduce fragmentation by providing additional pressure support (Price et al. 2008; Federrath 2015), although the extent of influence is debatable in the presence of protostellar feedback (Myers et al. 2014; Krumholz & Federrath 2019). Protostellar jets/outflows, which are driven by magnetic fields, induce fragmentation and reduce the median mass by a factor of ~ 2–3 (Li & Nakamura 2006; Wang et al. 2010; Federrath et al. 2014; Frank et al. 2014; Offner & Chaban 2017; Mathew & Federrath 2021; Guszejnov et al. 2021; Lebreuilly et al. 2024). Further, the impact of magnetic fields may differ for super-Alfvénic and trans-Alfvénic conditions, and also in a multi-phase medium (Mac Low et al. 1998; Krumholz & Federrath 2019; Beattie et al. 2021; Seta & Federrath 2022). Assuming a correlation between the core mass function (CMF) and the IMF, supported by some observations (Motte et al. 1998; Testi & Sargent 1998; Johnstone et al. 2000; Stanke et al. 2006; Alves et al. 2007; Könyves et al. 2015), analytical theories of the CMF/IMF (Padoan & Nordlund 2002; Hennebelle & Chabrier 2008; Hopkins 2012) based on gravo-turbulent fragmentation suggest that the IMF is sensitive to the turbulent properties of the cloud, such as the Mach number and the mode of turbulence driving. Meanwhile, star formation and IMF theories based on a global hierarchical collapse (e.g., Ballesteros-Paredes et al. 2007; Vázquez-Semadeni et al. 2017, 2019) and stochastic, competitive accretion are also prominent (e.g., Zinnecker 1982; Bonnell et al. 2001b; Bate & Bonnell 2005; Basu et al. 2015). Recently, there have been numerous studies on the IMF in the early universe, with a focus on the influence of varying metallicities (e.g., Sharda & Krumholz 2022; Bate 2023; Li et al. 2023; Yan et al. 2024; Tanvir & Krumholz 2024; Menon et al. 2024).

While the above findings put crucial constraints, we are yet to reach a clear consensus on the origin of the IMF. A primary reason why it is difficult to isolate the mechanism(s) responsible for the observed IMF characteristics is because the effects of the mechanisms involved in star formation are inter-related. Thus, it is important to include all these mechanisms simultaneously and analyse the impact of the relative parameters associated with the cloud. The current analytical theories of the CMF/IMF are fundamentally based on the interaction between gravity and turbulence (Mac Low & Klessen 2004). The principal quantity that defines the relative importance of gravity vs. turbulence is the cloud virial parameter α_{vir}, defined as twice the ratio of turbulent kinetic to gravitational energy. It is typically found to be around unity, but the scatter in the measurements is large and the difference in α_{vir} between individual clouds can be more than an order of magnitude (Kauffmann et al. 2013; Polzin et al. 2024). A strong dependence of the IMF on α_{vir} would place the concept of IMF universality under scrutiny. Therefore, we carry out a comprehensive study of the influence of the virial parameter on the star formation process, in particular the IMF, using simulations of star cluster formation. The simulations include gravity, turbulence, magnetic fields, protostellar heating and mechanical feedback in the form of jets and outflows.

In Section 4.2, we outline the numerical methodology and the initial conditions of the simulations. In Section 4.3, we study the impact of the cloud virial parameter on the SFR and the IMF. We also compare the IMF and the multiplicity associated with simulations of different virial parameters with observations. In Section 4.4, we discuss some of the previous numerical studies on the effect of the cloud virial parameter on the IMF. The main conclusions are presented in Section 4.5.

4.2 Methodology

4.2.1 Numerical setup

Here we provide a brief summary of the numerical methods used in this study, which build upon the simulation framework in Mathew & Federrath (2021). A more detailed description of the general setup can be found in §2 of Mathew & Federrath (2021). We model star cluster formation by solving the magnetohydrodynamical (MHD) equations in the presence of gravity utilising the FLASH (version 4) code (Fryxell et al. 2000; Dubey et al. 2008) with in-house modifications (Waagan et al. 2011). In addition to gravity and magnetic fields, which are taken into account through the MHD equations, we also implement other important mechanisms such as turbulence, protostellar heating and jets/outflows in our simulations.

Turbulence driving

We employ a stochastic Ornstein-Uhlenbeck (OU) process (Eswaran & Pope 1988) to drive turbulence in the simulations, which generates an acceleration field that is included as a source term in the momentum equation of MHD (Federrath et al. 2010b, 2022). The turbulent energy is injected only on the largest scales, but it cascades down to smaller scales, producing a velocity power spectrum $\sim k^{-2}$ or equivalently a velocity dispersion – size relation of $\sigma_v \propto \ell^{1/2}$ (Larson 1981; Ossenkopf & Mac Low 2002; Heyer & Brunt 2004; Roman-Duval et al. 2011; Federrath 2013a; Federrath et al. 2021). In this study, we use a natural mixture of turbulence driving modes, i.e., equal power in compressive and solenoidal modes, which corresponds to a turbulence driving parameter of $b \sim 0.4$ (see Federrath et al. 2008, 2010b, 2022, for details on the turbulence driving method adopted here).

Sink particles and protostellar feedback

We use sink particles to replace the gas within the innermost parts of the collapsing regions in the simulations, which is a common practice in numerical works (Bate et al. 1995; Krumholz et al. 2004; Federrath et al. 2010c). The introduction of sink particles is to prevent the simulations from reaching extremely small time steps and stalling as a consequence of the rapid increase in the density within the bound regions. We set the sink particle radius $r_{\text{sink}} = 250\,\text{AU}$, i.e., sink particles will replace spherical volumes of gas with radius $r_{\text{sink}} = 250\,\text{AU}$ that satisfy several gravitational collapse and sink particle formation criteria (Federrath et al. 2010c), to avoid spurious formation of star particles. The sink particles inherit the position, linear momentum, and angular momentum of the gas enclosed within the respective spherical volume. The sink particles in our simulations therefore represent star+disc systems. To model protostellar heating and outflow feedback, we use sub-resolution models, which are approximations based on previous theoretical, numerical and observational studies. We encourage the reader to refer to Federrath et al. (2014) and Mathew & Federrath (2020, 2021) for the full description of the outflow and heating feedback models, respectively.

Limitations

We note that the minimum attainable grid cell size in our simulations is 100 AU (see §4.2.2) and the sink particles correspond to star-disc systems as mentioned above. While fragmentation in the extended discs (Bate et al. 2002a; Goodwin & Whitworth 2007; Stamatellos et al. 2007, 2011; Rogers & Wadsley 2012; Thies et al. 2015) can occur in our simulations, fragmentation on typical disc scales (see reviews by Kratter & Lodato 2016; Lee et al. 2020, and the references therein) is not fully resolved. However, we aim to analyse the relative differences in the IMFs on changing the virial parameter, which does not require resolving fragmentation entirely on all scales. Moreover, our comparison analysis with observations is aimed at the system IMFs (unresolved close binaries) rather than the canonical (individual star IMF).

4.2.2 Initial conditions

The computational domain of the simulations is a three-dimensional box with side length $L = 2\,\mathrm{pc}$ and periodic boundary conditions. The grid structure embodies an adaptive mesh refinement (AMR) framework with a maximum effective resolution of 4096^3 cells or equivalently a minimum cell size of 100 AU. The initial gas density ρ_0 and the magnetic field strength B_0 in the simulations are uniform. The magnetic field is directed only along the z-axis initially. The initial cloud temperature is isothermal at 10 K, but we employ a polytropic equation of state (EOS) such that the gas pressure (and the temperature via the ideal gas equation) is dependent on the local density (see Mathew & Federrath 2021, for a detailed description of the polytropic EOS implemented here). The polytropic EOS is based on previous radiation-hydrodynamical simulations and theoretical works (Larson 1969; Yorke et al. 1993; Masunaga & Inutsuka 2000; Offner et al. 2009). The steady state sonic Mach number is set as $\mathcal{M} = \sigma_\mathrm{v}/c_\mathrm{s} = 5$, where $\sigma_\mathrm{v} = 1.0\,\mathrm{km\,s^{-1}}$ is the velocity dispersion on the driving scale and $c_\mathrm{s} = 0.2\,\mathrm{km\,s^{-1}}$ is the isothermal sound speed. Once turbulence driving starts, filamentary and clump-like over-dense regions start to emerge via turbulent shocks. The stirring of the gas also makes the magnetic field morphology inhomogeneous due to the tangling, compression, and elongation of magnetic field lines by the turbulent flow (Seta et al. 2020; Seta & Federrath 2021), producing a field structure comparable to that in actual molecular clouds (Federrath 2016).

To allow turbulence to fully develop and reach a steady state, we drive turbulence in the simulations without self-gravity for two turbulent crossing times, $2\,t_\mathrm{turb} = L/(\mathcal{M} c_\mathrm{s}) = 2\,\mathrm{Myr}$ (Federrath et al. 2010b; Price & Federrath 2010b). Once a steady state of turbulence is reached, we turn on self-gravity, which we define as time $t = 0$. We allow the simulations to progress until a star formation efficiency (SFE) of 5% is reached, i.e., when 5% of the total cloud mass has been converted into stars, during which the turbulence driving is also sustained (Mac Low 1999). Throughout this phase of evolution, the over-dense regions (analogous to dense cores) in the shocked gas become unstable and form stellar clusters.

With the numerical setup and initial conditions discussed above, we carry out three sets of simulations with different initial cloud virial parameters. For a homogeneous spherical cloud of radius R_{cl}, total mass M, and 3D turbulent velocity dispersion σ_v, the cloud virial parameter is given by

$$\alpha_{\mathrm{vir}} = \frac{2E_{\mathrm{turb}}}{|E_{\mathrm{grav}}|} = \frac{5\sigma_v^2 R_{\mathrm{cl}}}{3GM} = \frac{5\mathcal{M}^2 c_{\mathrm{s}}^2}{6G\rho_0 L^2}, \tag{4.1}$$

where $E_{\mathrm{turb}} = M\sigma_v^2/2$ and $E_{\mathrm{grav}} = -3GM^2/(5R_{\mathrm{cl}})$, with $R_{\mathrm{cl}} = L/2$ and $M = \rho_0 L^3$. It is important to highlight that the cloud structure becomes highly inhomogeneous and the actual value of α_{vir} at the time when a steady state of turbulence is reached can be significantly different from the simple spherical approximation given by Eq. (4.1) of an a homogeneous, gravitationally isolated cloud (Federrath & Klessen 2012). However, we refer to α_{vir} from Eq. (4.1) to simply denote the distinction between the three simulation models.

To investigate the impact of the virial parameter on the cloud evolution, we conduct three sets of simulations with $\alpha_{\mathrm{vir}} = 0.0625, 0.125$ and 0.5 by varying the initial mean gas density ρ_0 in the simulations (keeping the Mach number $\mathcal{M}$ constant). We adjust the magnetic field strength B_0 in each of the three simulation sets to keep the Alfvén Mach number $\mathcal{M}_{\mathrm{A}}$ fixed. Maintaining constant values of $\mathcal{M}_{\mathrm{A}}$ across the three models is crucial to ensure that the observed variations are independent of the magnetic fields (Mac Low et al. 1998; Krumholz & Federrath 2019; Beattie et al. 2021). We emphasise that rather than the absolute quantities like σ_v and B_0, the relative (dimensionless) quantities like $\mathcal{M}$ and $\mathcal{M}_{\mathrm{A}}$ should be given greater consideration since the fundamental physical processes at play are better reflected in such relative (dimensionless) quantities. The mass-to-flux ratio μ_{B} is different in the three models because of the adjustments in ρ_0 and B_0, but the variations are not significant enough to affect the results. Tab. 4.1 lists initial values associated with important quantities in each model.

It is to be noted that changing α_{vir} without affecting any of the other dimensionless cloud parameters is not possible as many of them are mathematically and physically related. We choose to adjust α_{vir} by changing the mean gas density, which also changes the mean thermal Jeans mass (and the number of Jeans masses) but keeps the other crucial parameters like $\mathcal{M}$ and $\mathcal{M}_{\mathrm{A}}$ fixed (see Tab. 4.1). Alternatively, one could adjust α_{vir} by changing the velocity dispersion or the cloud size. However, changing the velocity dispersion would affect the Mach number, which would have distinct consequences on the cloud evolution (see §4.4). Changing the cloud size would vary the number of Jeans masses too. Moreover, since $\alpha_{\mathrm{vir}} \propto L^{-2}$,

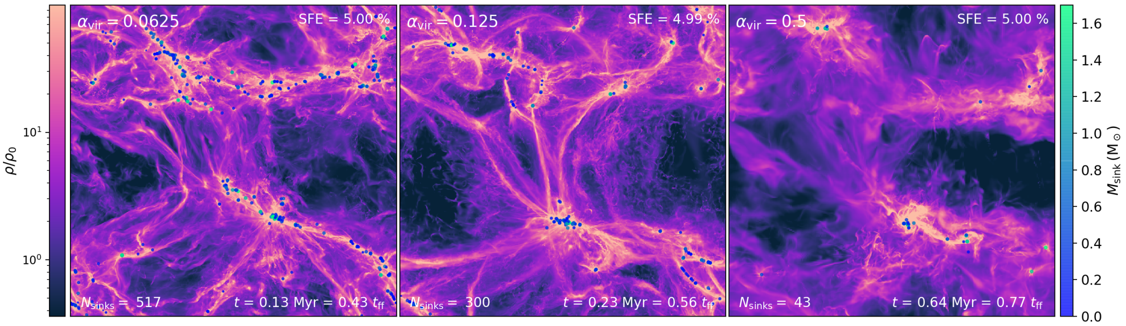

Figure 4.1: Mass-weighted gas density projection divided by the corresponding initial density for the models $\alpha_{\rm vir} = 0.0625$ (left panel), $\alpha_{\rm vir} = 0.125$ (middle panel), and $\alpha_{\rm vir} = 0.5$ (right panel) at star formation efficiency (SFE) of 5%. The circular markers represent sink particle (star+disc system) positions and the colour bar on the right corresponds to the mass of the sink particles. See §4.5 for 3D visualisation of the respective simulations.

the cloud size has to be increased to obtain lower virial parameters, which would make performing the corresponding simulations challenging due to the increase in the computational volume and therefore the computational expense.

4.3 Results

For $\alpha_{\rm vir} = 0.0625$, we carried out one simulation, which produced 517 sink particles (young stellar objects; YSOs). For $\alpha_{\rm vir} = 0.125$, we performed 2 simulations with different random seeds for the turbulence driving (Ornstein-Uhlenbeck process; see Sec. 4.2, but otherwise identical cloud properties), which generated a total of 520 sink particles. In the case of $\alpha_{\rm vir} = 0.5$, we performed 10 simulations with different turbulence driving seeds, producing a total of 449 sink particles. In each of the models, the choice of the number of simulations performed is based on the aim to achieve a similar number of sink particles or similar IMF statistics among the three models. With the target of obtaining a statistically representative sample of the IMF, 10 simulations (turbulence seeds) were needed to produce a significant number of sinks or star particles (> 400), while for $\alpha_{\rm vir} = 0.125$ and 0.0625, only 2 and 1 simulation(s), respectively, were required to produce a similar overall number of sink particles. For $\alpha_{\rm vir} = 0.125$ and 0.5, different quantities studied here are averaged (or compiled together) over the set of simulations in each of the models (2 and 10 simulations, respectively), while for $\alpha_{\rm vir} = 0.0625$ it is from the single simulation performed.

Fig. 4.1 shows the mass-weighted gas density projection for the three simulation models at SFE = 5%. For $\alpha_{\rm vir} = 0.5$ (right panel), the high-density structures are

Table 4.1: Initial conditions and important results for different simulation models.

Model (1)	$L\,[\mathrm{pc}]$ (2)	$\rho_0\,[\mathrm{g\,cm^{-3}}]$ (3)	$M_{\mathrm{cl}}\,[\mathrm{M_\odot}]$ (4)	$M_{\mathrm{cl}}/M_{\mathrm{J}}$ (5)	$\mathcal{M}$ (6)	$B_0\,[\mu\mathrm{G}]$ (7)	$\mathcal{M}_{\mathrm{A}}$ (8)	μ_{B} (9)	β (10)	N_{sims} (11)	N_{tot} (12)	$\overline{M}_{\mathrm{median}}\,[\mathrm{M_\odot}]$ (13)	$\overline{M}_{\mathrm{average}}\,[\mathrm{M_\odot}]$ (14)	$\overline{M}_{50}\,[\mathrm{M_\odot}]$ (15)
$\alpha_{\mathrm{vir}} = 0.0625$	2	5.25×10^{-20}	6200	2091.0	5	10	2.9	19.7	0.7	1	517	0.25 ± 0.02	0.50 ± 0.05	1.04 ± 0.19
$\alpha_{\mathrm{vir}} = 0.125$	2	2.62×10^{-20}	3100	737.1	5	28	2.9	13.7	0.7	2	520	0.27 ± 0.05	0.46 ± 0.08	0.93 ± 0.15
$\alpha_{\mathrm{vir}} = 0.5$	2	6.56×10^{-21}	775	92.4	5	20	2.9	6.9	0.7	10	449	0.46 ± 0.06	0.73 ± 0.08	1.38 ± 0.16

Notes. Column 1: MHD simulation models with different virial parameter α_{vir}. Column 2: size of the cloud/computational domain. Columns 3: initial mean gas density. Column 4: total mass of the cloud. Columns 5: number of Jeans masses in the cloud. Column 6: rms sonic Mach number. Column 7: initial magnetic field strength. Column 8: Alfvén Mach number. Column 9: mass-to-flux ratio. Column 10: plasma beta (thermal-to-magnetic pressure ratio). Column 11: number of simulations (random seeds for the turbulence driving) performed. Column 12: total number of sink particles formed. Column 13: median stellar mass. Column 14: mean stellar mass. Column 15: M_{50}, which is the median mass in a cumulative mass function. Quantities in Columns 13-15 are averaged over the SFE range $1 - 5\%$ (represented by overbars).

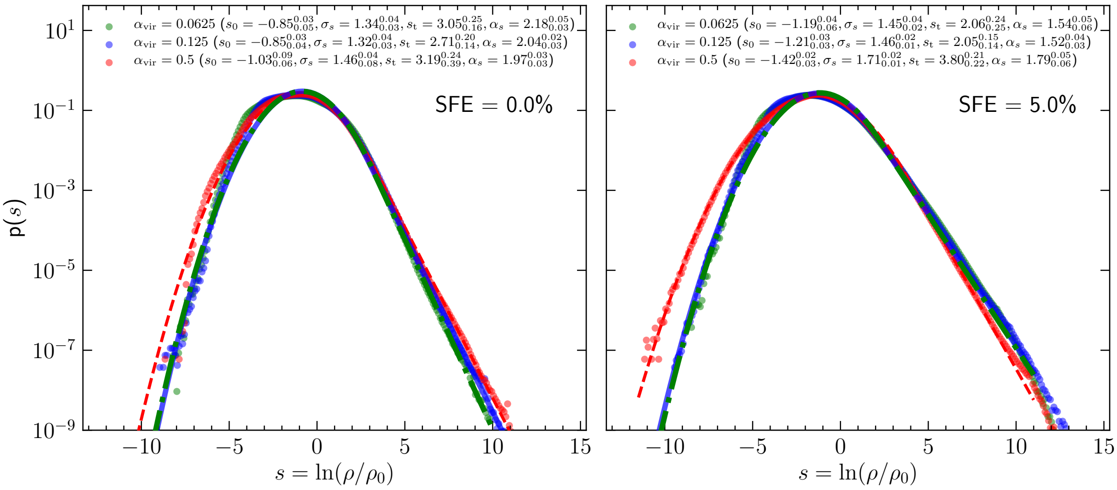

Figure 4.2: The volume-weighted gas density distribution for the three models in units of the corresponding initial density at the time the first sink particle forms (left panel) and at SFE = 5% (right panel). A log-normal+power-law curve (see Eq. 4.2) is fitted to the distributions, and the parameters of the fit, namely the peak and width of the log-normal part (s_0 and σ_s, respectively), the transition density between the log-normal and power-law parts ($s_{\rm t}$), and the slope of the power-law part (α_s), are shown in the legends.

localised and there are mainly three star-forming regions, while in the lower virial parameter cases of $\alpha_{\rm vir} = 0.0625$ (left panel) and $\alpha_{\rm vir} = 0.125$ (middle panel), the high-density regions are spread across the simulation box with a large network of star-forming regions. Since gravity is more dominant in the lower virial parameter models, it is able to amplify the anisotropies produced by turbulence more strongly, creating additional sheet-like and filamentary structures (Vázquez-Semadeni et al. 2007; Bonnell et al. 2008; Federrath 2015; Matsumoto et al. 2015; Vázquez-Semadeni et al. 2019; Hennebelle & Grudić 2024). Thus, a higher fraction of the cloud can form stars. 3D visualisations of the respective simulations are shown in §4.5.

4.3.1 Gas density probability distribution function

Previous theoretical and numerical works find that the form of the density probability distribution function (PDF) of supersonic turbulence is approximately log-normal (Vazquez-Semadeni 1994; Padoan et al. 1997a; Kritsuk et al. 2007; Federrath et al. 2008; Federrath 2013a; Hopkins 2013b; Federrath & Banerjee 2015). In the presence of gravity, the PDF develops a power-law tail in the high-density regime (Klessen 2000; Kritsuk et al. 2011; Ballesteros-Paredes et al. 2011a; Collins et al. 2012b; Federrath & Klessen 2013; Girichidis et al. 2014; Schneider et al. 2015; Myers 2015; Matsumoto et al. 2015; Mocz et al. 2017b; Padoan et al. 2017; Burkhart 2018).

With time and increasing SFE, the slope of the power-law part (in logarithmic scale) becomes shallower (Federrath & Klessen 2013), and the density at which the PDF transitions from log-normal to a power-law decreases (Burkhart 2018).

Fig. 4.2 shows the PDFs of the volume-weighted logarithmic density contrast $s = \ln(\rho/\rho_0)$ in our simulations with $\alpha_{\mathrm{vir}} = 0.0625$ (green, dash-dotted), 0.125 (blue, solid), and 0.5 (red, dashed) at the moment the first sink particle forms (left panel) and at SFE = 5% (right panel). The PDFs obtained from the simulations are plotted with circular markers and the curves denote the corresponding fits. Following the method in Khullar et al. (2021), we fit a log-normal+power-law function to the density PDFs, where the free parameters are the width of the log-normal part (σ_s) and the slope of the power-law part (α_s). The form of the fit function is given by

$$\mathrm{p}(s) = \begin{cases} \frac{N_{\mathrm{d}}}{\sqrt{2\pi\sigma_s^2}} \exp\left(-\frac{(s-s_0)^2}{2\sigma_s^2}\right) & \text{for } s < s_{\mathrm{t}}, \\ N_{\mathrm{d}} k_{\mathrm{d}} \exp\left(-s\alpha_s\right) & \text{for } s \geq s_{\mathrm{t}}. \end{cases} \tag{4.2}$$

For defining the parameters like the peak of the log-normal part (s_0), transition density (s_{t}), and the normalisation constants (N_{d} and k_{d}), we use the corresponding expressions derived in Khullar et al. (2021) based on constraints like continuity and differentiability at the transition density, mass conservation, and normalisation of the PDF to unity (see §2.2 in Khullar et al. 2021, for more details). The derived parameter values of the fitted function are shown in the legend of Fig. 4.2.

At the time the first star particle forms (SFE = 0%; left panel), the density PDF for the $\alpha_{\mathrm{vir}} = 0.5$ model has a slightly higher fraction of dense gas (high s) than those with $\alpha_{\mathrm{vir}} = 0.0625$ and $\alpha_{\mathrm{vir}} = 0.125$. The reason for the relatively lower fraction in the simulations with $\alpha_{\mathrm{vir}} = 0.0625$ and $\alpha_{\mathrm{vir}} = 0.125$ is that stars start to form much earlier in these simulations (at $t \sim 0.05-0.1$ Myr) compared to those with $\alpha_{\mathrm{vir}} = 0.5$, where the first stars form at $t \sim 0.2$ Myr. Therefore, the clouds corresponding to $\alpha_{\mathrm{vir}} = 0.0625$ and $\alpha_{\mathrm{vir}} = 0.125$ are comparatively less dynamically evolved when compared at the moment the first star forms. Conversely, at SFE = 5% (right panel), the simulations with $\alpha_{\mathrm{vir}} = 0.0625$ and $\alpha_{\mathrm{vir}} = 0.125$ have a higher fraction of high-s regions than that for $\alpha_{\mathrm{vir}} = 0.5$. This is also apparent when comparing the slope of the power-law part α_s of the density PDF between the simulation models (compare legends in Fig. 4.2). In the left panel, α_s in the model with $\alpha_{\mathrm{vir}} = 0.5$ is shallower than that of the models with $\alpha_{\mathrm{vir}} = 0.0625$ and $\alpha_{\mathrm{vir}} = 0.125$, while in the right panel, it is steeper.

Fig. 4.3 shows the dependence of α_s on SFE. It is evident that α_s remains almost constant with time (SFE) in the case of $\alpha_{\mathrm{vir}} = 0.5$, which agrees with Khullar

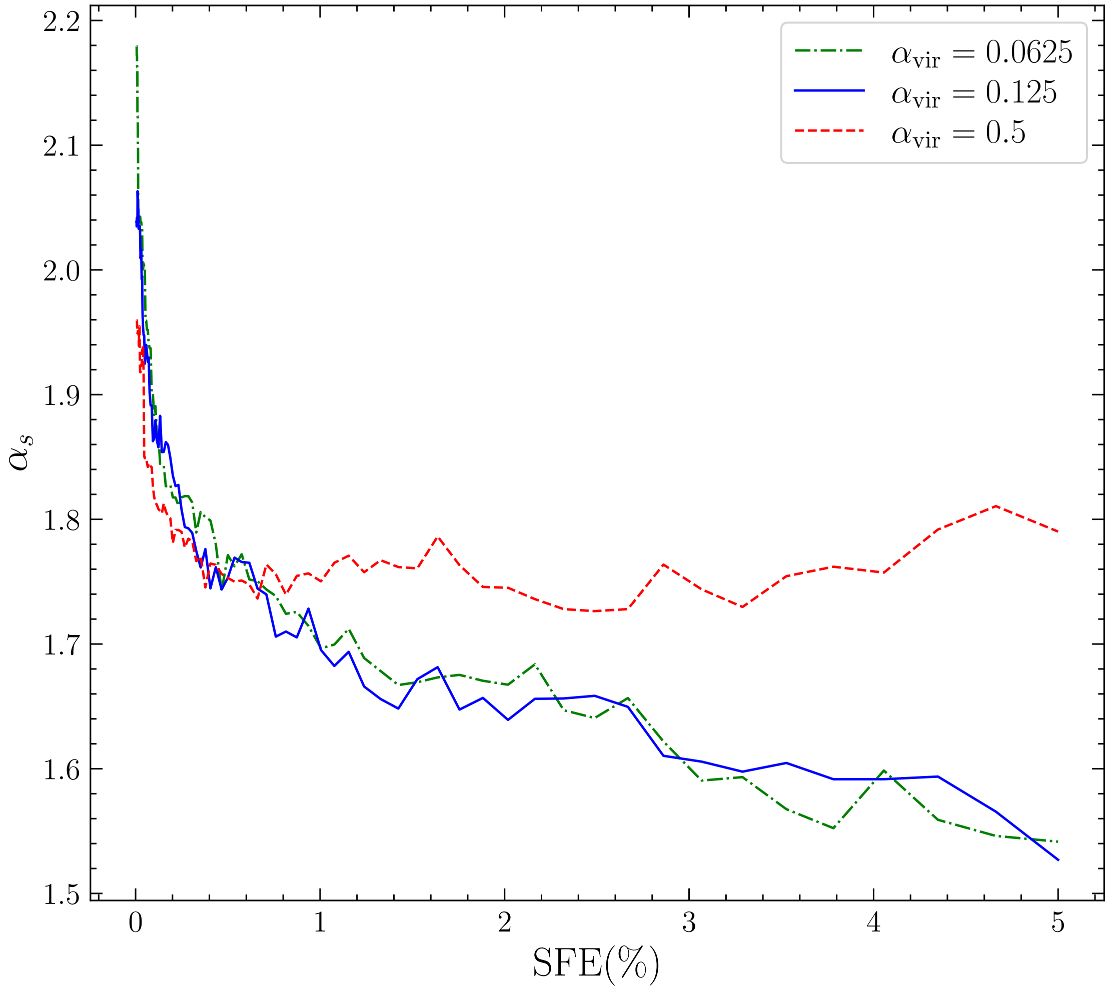

Figure 4.3: The slope of the power-law part of the density PDF as a function of SFE for $\alpha_{\rm vir} = 0.0625$ (green, dash-dotted), 0.125 (blue, solid), and 0.5 (red, dashed).

et al. (2021) who find the same for $\alpha_{\rm vir} = 0.5 - 2$ (also, see Appel et al. 2022, 2023). This is because, in the case of high virial parameters, stars primarily form in the high-density regions initially seeded by turbulence, i.e., the mass reservoir is predetermined by the initial turbulence properties. On the other hand, α_s decreases (slopes become shallower) with SFE for $\alpha_{\rm vir} = 0.0625$ and 0.125, which is because low virial parameters imply that gravity is more efficient in enhancing the dense structures in the cloud. Once gravity has had sufficient time to amplify the anisotropies and develop filamentary channels, simulations with lower virial parameters develop over-densities, and consequently form stars at a higher rate, which is discussed next.

4.3.2 Star formation rate

The star formation rate is given by $\mathrm{SFR} = M_*/\tau_{\rm c}$, where M_* is the cloud mass converted into stellar mass and $\tau_{\rm c}$ is the average time scale of the conversion process. SFR is generally referenced in its dimensionless form, i.e., in mass fraction per freefall time, given by (Krumholz & McKee 2005)

$$\begin{aligned} \mathrm{SFR_{ff}} &= \frac{\mathrm{SFR}}{M_{\rm cl}} \times t_{\mathrm{ff},\,\rho_0} \\ &= \frac{M_*}{M_{\rm cl}} \times \frac{t_{\mathrm{ff},\,\rho_0}}{\tau_{\rm c}}, \end{aligned} \tag{4.3}$$

where $M_{\rm cl}$ and $t_{\mathrm{ff},\,\rho_0}$ are the total mass of the cloud and the freefall time at the mean density ρ_0, respectively.

Fig. 4.4 shows SFE (top panel) and $\mathrm{SFR_{ff}}$ (bottom panel) as a function of time in our simulations with $\alpha_{\rm vir} = 0.0625$ (green, dash-dotted), 0.125 (blue, solid), and 0.5 (red, dashed). It is clear that, when considered at the same time, $\mathrm{SFR_{ff}}$ is higher for lower virial parameters, with the highest $\mathrm{SFR_{ff}}$ in the simulation with $\alpha_{\rm vir} = 0.0625$. The offset between the $\mathrm{SFR_{ff}}$ curves for $\alpha_{\rm vir} = 0.0625$ and $\alpha_{\rm vir} = 0.125$ is simply because the onset of star formation is earlier in $\alpha_{\rm vir} = 0.0625$ than for $\alpha_{\rm vir} = 0.125$. The lower the value of $\alpha_{\rm vir}$, the faster gravity acts in rearranging gas to form stars. However, once the star formation gets underway, the rate of change of $\mathrm{SFR_{ff}}$ is similar for $\alpha_{\rm vir} = 0.0625$ and 0.125, which becomes more evident when $\mathrm{SFR_{ff}}$ is compared at the same SFE. Fig. 4.5 shows the evolution of $\mathrm{SFR_{ff}}$ with SFE in our three simulation models. Here the $\mathrm{SFR_{ff}}$ values for $\alpha_{\rm vir} = 0.0625$ and 0.125 are similar, while $\mathrm{SFR_{ff}}$ for $\alpha_{\rm vir} = 0.5$ is lower. When $\alpha_{\rm vir}$ is sufficiently low, the process is more strongly dictated by the gravitational interactions than other mechanisms and the SFR accelerates with time. In other words, when the virial parameter is

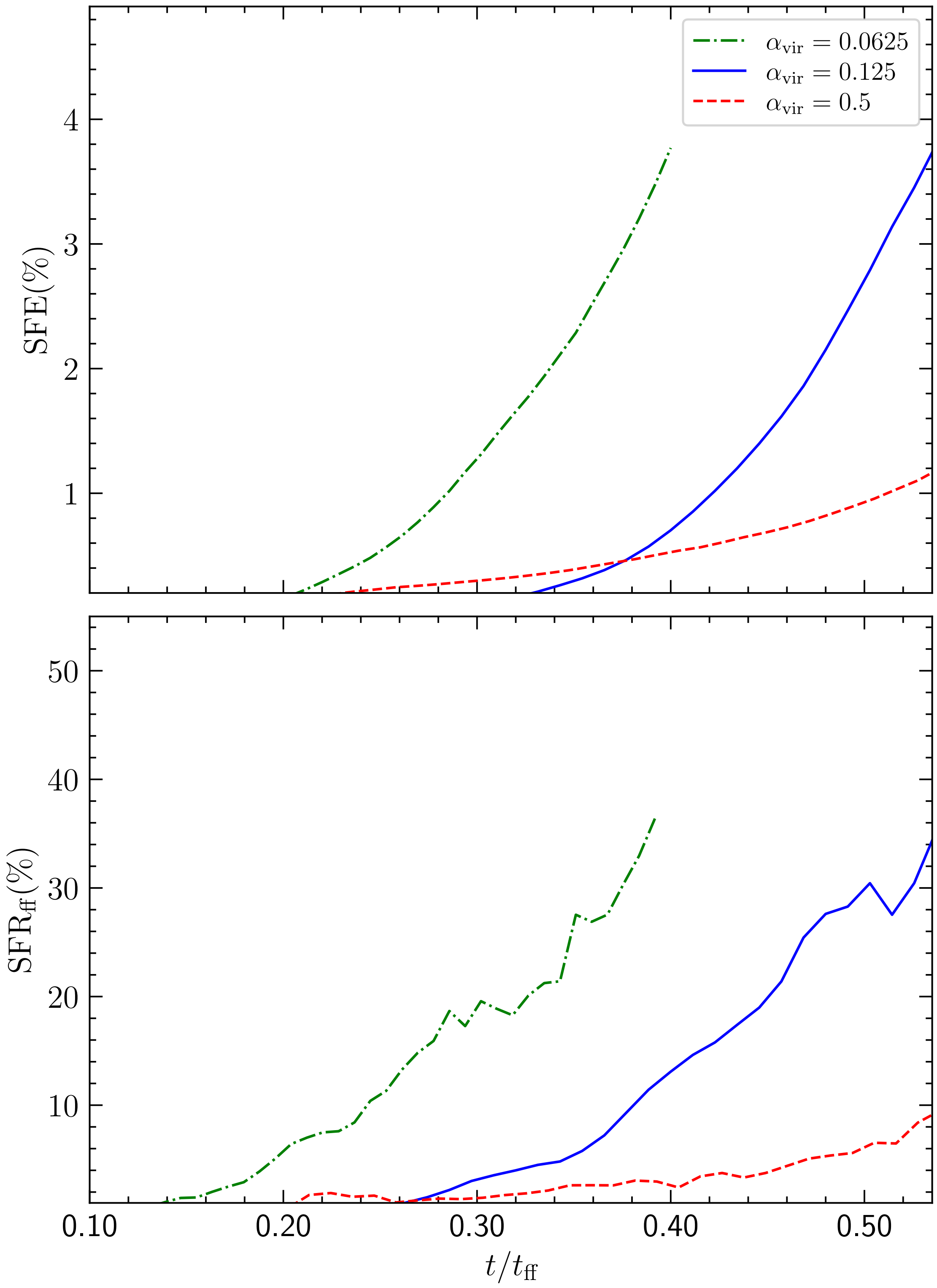

Figure 4.4: Top panel: The star formation efficiency SFE (%), as a function of time (in units of the mean freefall time) for $\alpha_{\rm vir} = 0.0625$ (green, dash-dotted), 0.125 (blue, solid), and 0.5 (red, dashed). Note that the mean freefall time is different for each of the simulation models since their mean densities are different. Bottom panel: Same as the top panel, but for the star formation rate per freefall time, $\mathrm{SFR_{ff}}$.

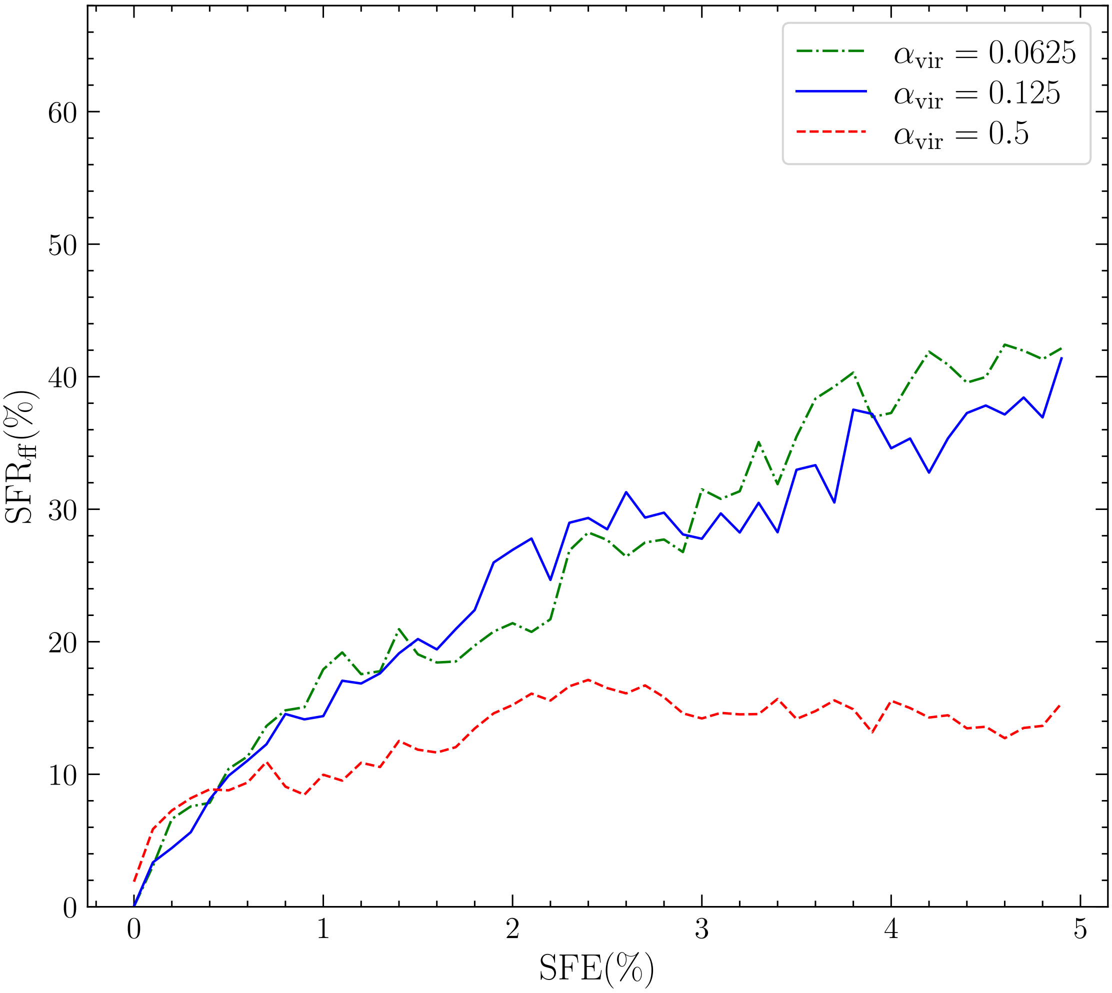

Figure 4.5: SFR$_{\rm ff}$ as a function of SFE (%) in our simulations with different $\alpha_{\rm vir}$, showing that lowering $\alpha_{\rm vir}$ leads to an increase in SFR$_{\rm ff}$, but only mildly so when $\alpha_{\rm vir} \ll 1$. This is due to a saturation of the effect of gravitational binding at very low $\alpha_{\rm vir}$.

sufficiently low, SFR is almost independent of the value of $\alpha_{\rm vir}$. Hence the rate of change of SFR is similar for $\alpha_{\rm vir} = 0.0625$ and $\alpha_{\rm vir} = 0.125$. However, in the case of $\alpha_{\rm vir} = 0.5$, the turbulent support still plays a substantial role throughout the process, and thus the acceleration in SFR is not as significant. The SFR$_{\rm ff}$ = 0.30, 0.29, and 0.14, averaged over the SFE range $1-5\%$, for $\alpha_{\rm vir} = 0.0625, 0.125$, and 0.5, respectively.

4.3.3 Initial mass function

Fig. 4.6 presents the mass distribution of sink particles (star+disc systems) obtained in the simulations with $\alpha_{\rm vir} = 0.0625$ (green histogram with dash-dotted edges), 0.0125 (blue histogram with solid edges), and 0.5 (red histogram with dashed edges).

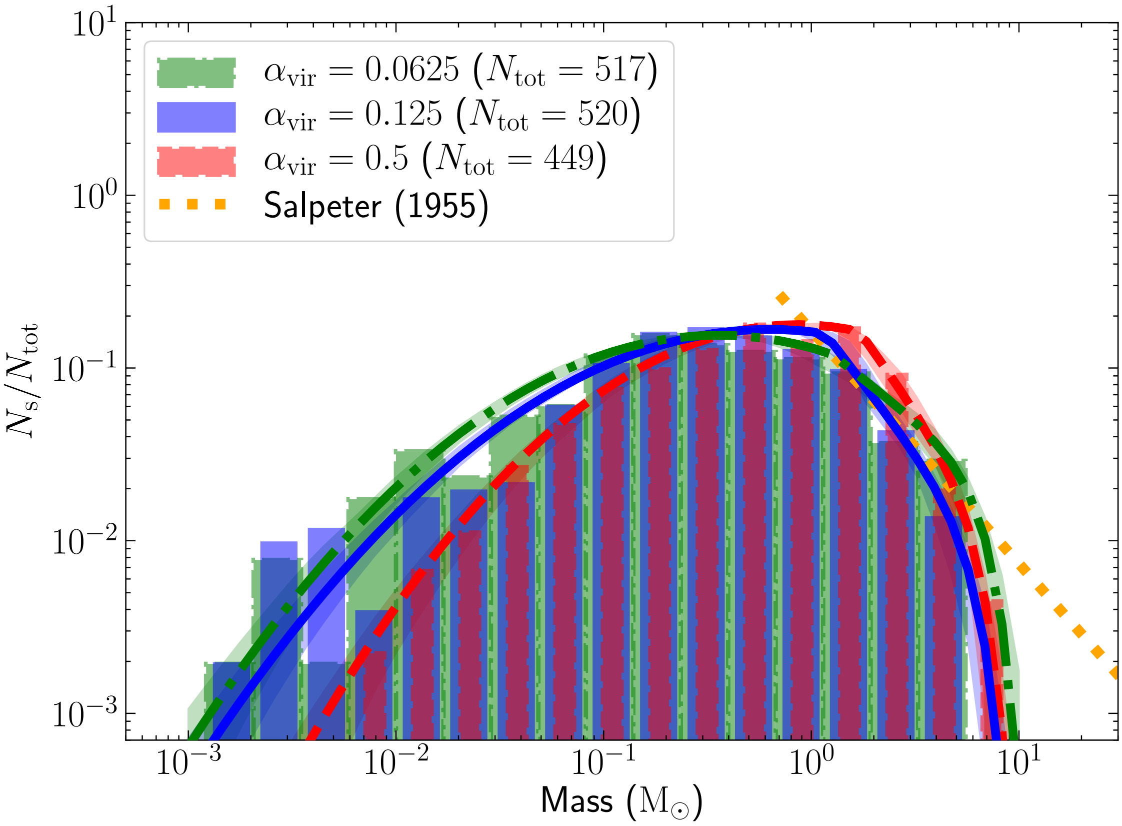

Figure 4.6: The IMF for simulations with $\alpha_{\rm vir} = 0.0625$ (green histogram with dash-dotted edges), 0.0125 (blue histogram with solid edges), and 0.5 (red histogram with dashed edges) at SFE = 5%. Each bin represents the ratio of the number of star particles in the associated mass range ($N_{\rm s}$) to the total number of star particles ($N_{\rm tot}$). The dash-dotted, solid, and dashed curves represent the modified Chabrier (2005) IMF fits using Eq. (4.4) for the simulation IMFs corresponding to the models with $\alpha_{\rm vir} = 0.0625, 0.125$, and 0.5, respectively (see §4.3.3). The parameters for the fit are derived using MCMC sampling and are listed in Tab. 4.2. The dotted line shows the Salpeter (1955) IMF.

The curves represent a modified version of the Chabrier (2005) IMF fitted to the simulation data using the Markov Chain Monte-Carlo (MCMC) sampler emcee of Foreman-Mackey et al. (2013) (see also Nam et al. 2021). The input to the sampling algorithm is the list of sink particle masses rather than the binned data, and hence the method has the advantage that the fit is not affected by the binning choice. The modified version is similar to the standard Chabrier (2005) IMF form except that, to take into consideration the finite mass in our computational domain, we include an exponential term that serves as a smooth cutoff in the high-mass regime of the Chabrier (2005) IMF,

$$dN/d\log M = \begin{cases} k_1 \exp\left(-\frac{1}{2}\left(\frac{\log M - \log M_0}{\sigma}\right)^2\right) & \text{for } M < M_{\rm T}, \\ k_2\, M^{-\Gamma} \exp\left(-(M/M_{\rm cut})^p\right) & \text{for } M \geq M_{\rm T}, \end{cases} \tag{4.4}$$

where all masses are in units of $\mathrm{M}_\odot$. Here the appropriate values for the five free parameters $\theta_{\rm fit} = (\sigma, \log M_0, \log M_{\rm T}, \Gamma, \log M_{\rm cut})$ are derived using MCMC sampling based on the simulated data. σ, M_0, $M_{\rm T}$ and Γ are the standard deviation of the log-normal part, the peak mass, transition mass between the log-normal and power-law forms, and the slope of the power-law part, respectively. k_1 and k_2 are normalisation factors, defined to ensure continuity at $M_{\rm T}$. As a consequence of the exponential term in the power-law part, the IMF will be truncated at high masses. $M_{\rm cut}$ characterises the mass at which the exponential term begins to dominate and p describes how sharply the cut-off occurs around $M_{\rm cut}$. We use $p = 4$ to achieve a sufficiently sharp drop around $M_{\rm cut}$. We refer the reader to §3.2 in Mathew et al. (2023) for a more detailed description of the MCMC fitting technique used here.

The three stellar mass distributions are not substantially different, but they exhibit some distinctions. The derived values for the fit parameters corresponding to the simulated IMFs are listed in Tab. 4.2. The distributions for the lower virial parameters have a higher fraction of low-mass stars, which is expected since the large-scale turbulent support is weaker (or equivalently, gravity is comparatively more efficient), and therefore there is more fragmentation. The peak of the distributions for $\alpha_{\rm vir} = 0.0625$ and $\alpha_{\rm vir} = 0.125$ are comparable, however, the peak for $\alpha_{\rm vir} = 0.5$ is at a relatively higher mass (see Tab. 4.2). Changing the virial parameter in the simulation from $\alpha_{\rm vir} = 0.5$ to $\alpha_{\rm vir} = 0.0625$, i.e., by a factor of 8, reduces the peak mass by a factor of ~ 2.4. This shows that the IMF has a relatively weak, but systematic dependence on the cloud virial parameter. Lower $\alpha_{\rm vir}$ suggests that the overdensities are more bound and stable against disruption by shocks (Federrath & Klessen 2012; Bertelli Motta et al. 2016), and hence more low-mass overdensities can collapse to form stars.

Table 4.2: Characteristics of the sink particle mass distribution and parameter values from the MCMC fit to the distribution.

Model	Simulation		MCMC fit					
	Peak [$\mathrm{M}_\odot$]	Median [$\mathrm{M}_\odot$]	M_0 [$\mathrm{M}_\odot$]	σ	M_T [$\mathrm{M}_\odot$]	Γ	M_cut [$\mathrm{M}_\odot$]	p
(1)	(2)	(3)	(4)	(5)	(6)	(7)	(8)	(9)
$\alpha_\mathrm{vir} = 0.0625$	0.14-0.24	0.27 ± 0.02	$0.36^{+0.13}_{-0.07}$	$0.77^{+0.08}_{-0.06}$	$1.25^{+2.35}_{-0.53}$	$0.90^{+0.60}_{-0.30}$	$7.10^{+1.30}_{-1.20}$	4
$\alpha_\mathrm{vir} = 0.125$	0.24-0.40	0.33 ± 0.02	$0.63^{+0.19}_{-0.15}$	$0.81^{+0.06}_{-0.06}$	$1.17^{+0.44}_{-0.28}$	$1.60^{+0.70}_{-0.40}$	$6.30^{+1.30}_{-1.10}$	4
$\alpha_\mathrm{vir} = 0.5$	0.40-0.67	0.54 ± 0.04	$0.86^{+0.29}_{-0.20}$	$0.71^{+0.07}_{-0.06}$	$1.70^{+0.84}_{-0.33}$	$1.70^{+0.90}_{-0.40}$	$6.50^{+1.20}_{-0.90}$	4

Notes. Column 1: MHD simulation models with different virial parameter α_vir. Column 2: peak in the sink mass distribution (see Fig. 4.6). Columns 3: median of the mass distribution. Columns 4-9: 50th percentile of the IMF parameters derived from the MCMC fit to the distribution, with the uncertainty bracketed by the 16th and 84th percentiles. All quantities presented here represent the measurement at SFE = 5%.

The slopes Γ of the fit at the high-mass end for $\alpha_{\rm vir} = 0.0625, 0.125$, and 0.5 are $0.90^{+0.60}_{-0.30}, 1.60^{+0.70}_{-0.40}$, and $1.70^{+0.90}_{-0.40}$, respectively (note that the Salpeter slope would be $\Gamma = 1.35$ in this definition of Γ). The slope for $\alpha_{\rm vir} = 0.0625$ is shallower than that of the other $\alpha_{\rm vir}$ values. However, since the high-mass range is narrow in our simulations, the error bars on the Γ estimates are large and therefore it is difficult to make conclusive remarks on the dependence of the high-mass regime of the IMF on the cloud virial parameter just based on Γ.

The median masses of the IMFs at SFE = 5% for $\alpha_{\rm vir} = 0.0625, 0.125$, and 0.5 are $\sim 0.26\,{\rm M}_\odot, 0.32\,{\rm M}_\odot$, and $0.53\,{\rm M}_\odot$, respectively. The average masses at SFE = 5% are $\sim 0.59\,{\rm M}_\odot, 0.60\,{\rm M}_\odot$, and $0.86\,{\rm M}_\odot$, respectively. We also evaluate M_{50}, which is, as outlined in Krumholz et al. (2012b), the median mass in a cumulative mass distribution, i.e., M_{50} is the value below which 50% of the total stellar mass is found. We find $M_{50} \sim 1.32\,{\rm M}_\odot, 1.17\,{\rm M}_\odot$, and $1.56\,{\rm M}_\odot$ at SFE = 5% for $\alpha_{\rm vir} = 0.0625, 0.125$, and 0.5, respectively. Fig. 4.7 shows the evolution of the median mass (top panel), the average mass (middle panel), and M_{50} (bottom panel) with SFE in the three $\alpha_{\rm vir}$ models. The median mass remains relatively constant from SFE ~ 1 for the three models, while the average mass increases moderately with SFE. The increase in the average mass reflects the development of the high-mass end of the IMF with time. The median, mean and M_{50} masses averaged over the SFE range $1-5\%$ for $\alpha_{\rm vir} = 0.0625, 0.125$, and 0.5 are listed in Tab. 4.1.

4.3.4 Comparison with observational IMF

Figure 4.8 depicts the comparison between our simulation IMFs and the observational IMF models. We compare our data with the system IMFs (unresolved close binaries) rather than the individual-star IMF since the accretion discs in our simulations are not fully resolved. All the observational models broadly agree with each other, though there are slight variations in the low-mass regime. While Parravano et al. (2011) propose a higher fraction of very low-mass stars or brown dwarfs than the Chabrier (2005) IMF, Da Rio et al. (2012) and Damian et al. (2021) suggest a lower fraction than Chabrier (2005). Such a difference also exists between the IMFs for our three simulation models, where the simulation corresponding to $\alpha_{\rm vir} = 0.0625$ has the highest fraction of very low-mass objects and the simulations with $\alpha_{\rm vir} = 0.5$ have the lowest fraction.

For comparisons between observations and simulations, it is also beneficial to measure the ratio between the number of stars in different mass ranges, which is more robust than deriving quantities such as the peak mass or the power-law slope. Observations find that the ratio of the number of sub-stellar objects ($M \leq 0.08\,{\rm M}_\odot$)

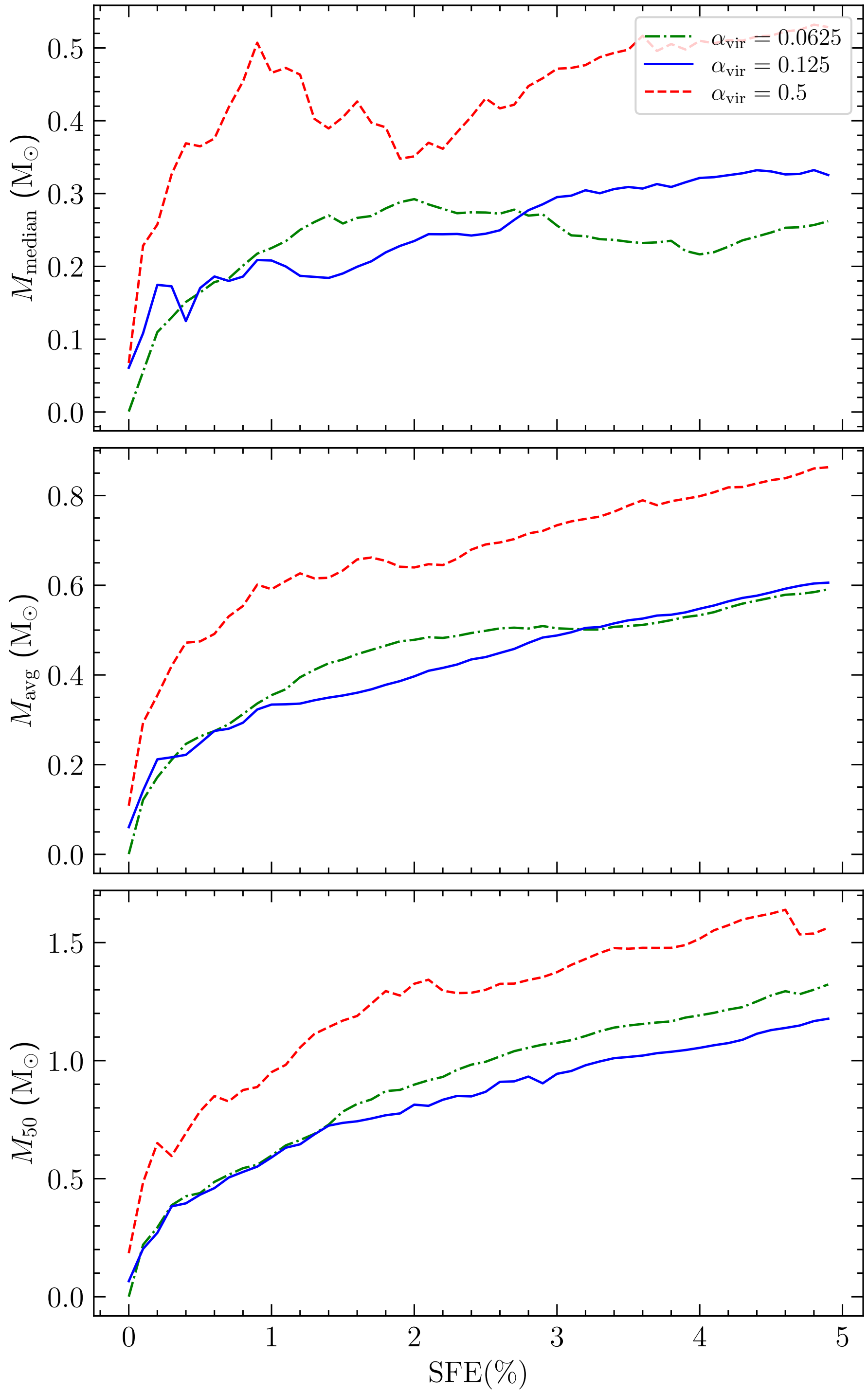

Figure 4.7: Top panel: The median stellar mass as a function of SFE (%) for $\alpha_{\rm vir} = 0.0625$ (green, dash-dotted), 0.125 (blue, solid), and 0.5 (red, dashed). Middle panel: same as top panel, but for the average stellar mass. Bottom panel: same as top panel, but for M_{50}, which is the median mass in a cumulative mass function.

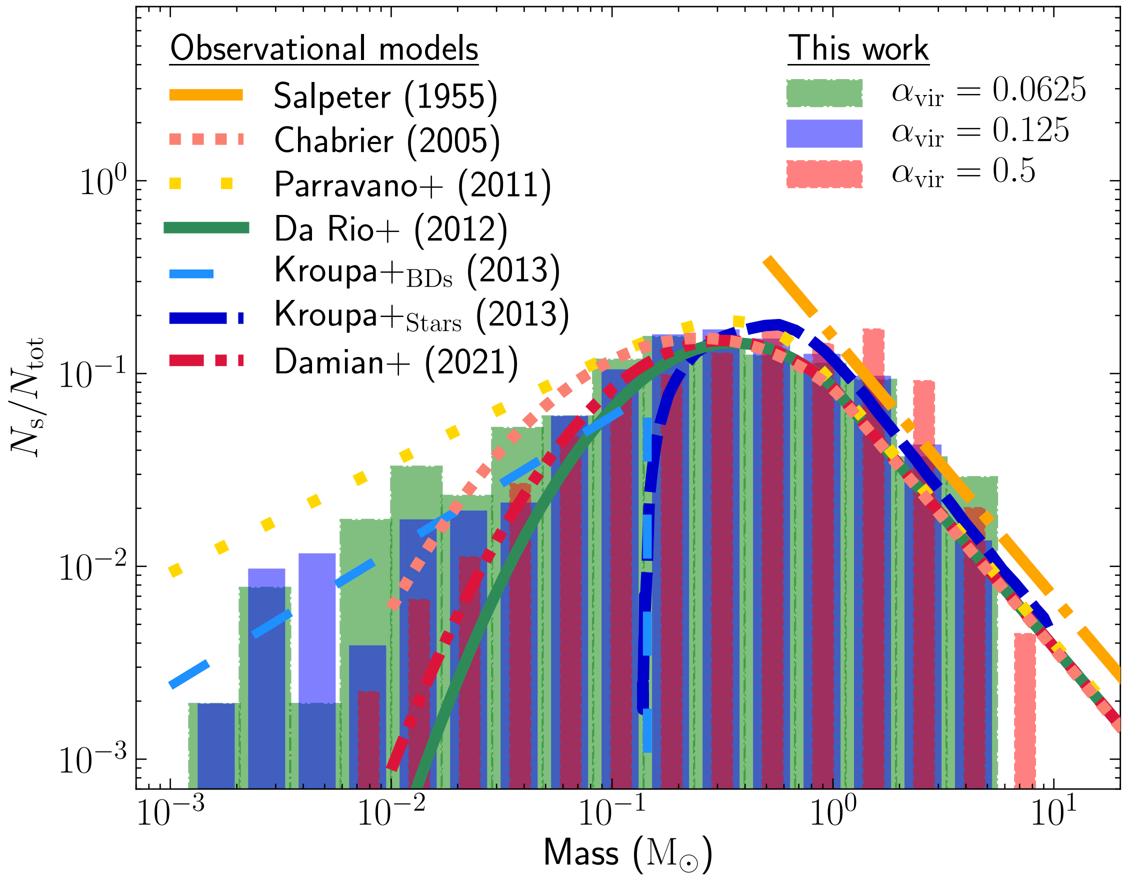

Figure 4.8: Comparison of our simulation IMFs at SFE = 5% with the different IMF models based on observational surveys. The plotted curves are the system IMF models by Salpeter (1955) (dash-dotted), Chabrier (2005) (short-dotted), Parravano et al. (2011) (long-dotted), Da Rio et al. (2012) (solid), Kroupa et al. (2013) for brown dwarfs (long-dashed) and stars (short-dashed), and Damian et al. (2021) (dash-dot-dotted).

to that with stellar masses ($0.15 < M \leq 1.0\,\mathrm{M}_{\odot}$) is ~ 0.2, i.e., one brown dwarf (sub-stellar) is formed per every five late-type (sub-solar) stars on average (Andersen et al. 2006, 2008; Thies & Kroupa 2007; Parravano et al. 2011; Kroupa et al. 2013). The corresponding ratios for the simulation models with $\alpha_{\mathrm{vir}} = 0.0625, 0.125$, and 0.5 are $0.41, 0.25$, and 0.19, respectively. The ratio for $\alpha_{\mathrm{vir}} = 0.5$ agrees with the typical value from observations, while that for $\alpha_{\mathrm{vir}} = 0.0625$ is higher by a factor of ~ 2.

4.3.5 Multiplicity

The multiplicity statistics is closely linked to the IMF and is a critical probe to test star formation theories. We identify multiple systems in our simulations based on the procedure employed in Bate (2009a), which we briefly summarise. In the list of stars (single objects) obtained from the simulations, we search for the closest gravitationally bound pair. The corresponding two stars are removed from the list and replaced by a binary object with the mass, centre-of-mass position and centre-of-mass velocity of the removed bound pair. In the new list, we again find the closest bound pair. In the scenario where the pair consists of a single and a binary object, the pair is substituted by a triple object. The above algorithm is repeated until no new bound pairs can be found in the list or the only possible option is a quintuple. We rule out pairings that result in a quintuple or systems of higher order since such high-order multiple systems tend to be dynamically unstable and are likely to decay to lower-order systems as the cloud evolves. This procedure is the same as the one used in Mathew & Federrath (2021) and Mathew et al. (2023).

With the list of singles, binaries, triples and quadruples derived from the above technique, we calculate the multiplicity fraction in different mass ranges. The multiplicity fraction (mf) in a mass range is the ratio of the number of multiple systems to the total number of systems whose primary star falls within the specified mass range, i.e.,

$$mf = \frac{B + T + Q}{S + B + T + Q}, \tag{4.5}$$

where S, B, T, and Q represent the number of singles, binaries, triples, and quadruples, respectively.

We show mf as a function of the primary mass for the three simulation models in Fig. 4.9. We see that mf increases with primary mass, which is consistent with the established understanding (Bate 2012; Krumholz et al. 2012b; Duchêne & Kraus 2013; Cunningham et al. 2018; Sharda et al. 2020; Offner et al. 2023). It is evident that, at sub-solar masses, mf for $\alpha_{\mathrm{vir}} = 0.0625$ and $\alpha_{\mathrm{vir}} = 0.125$ in each of the

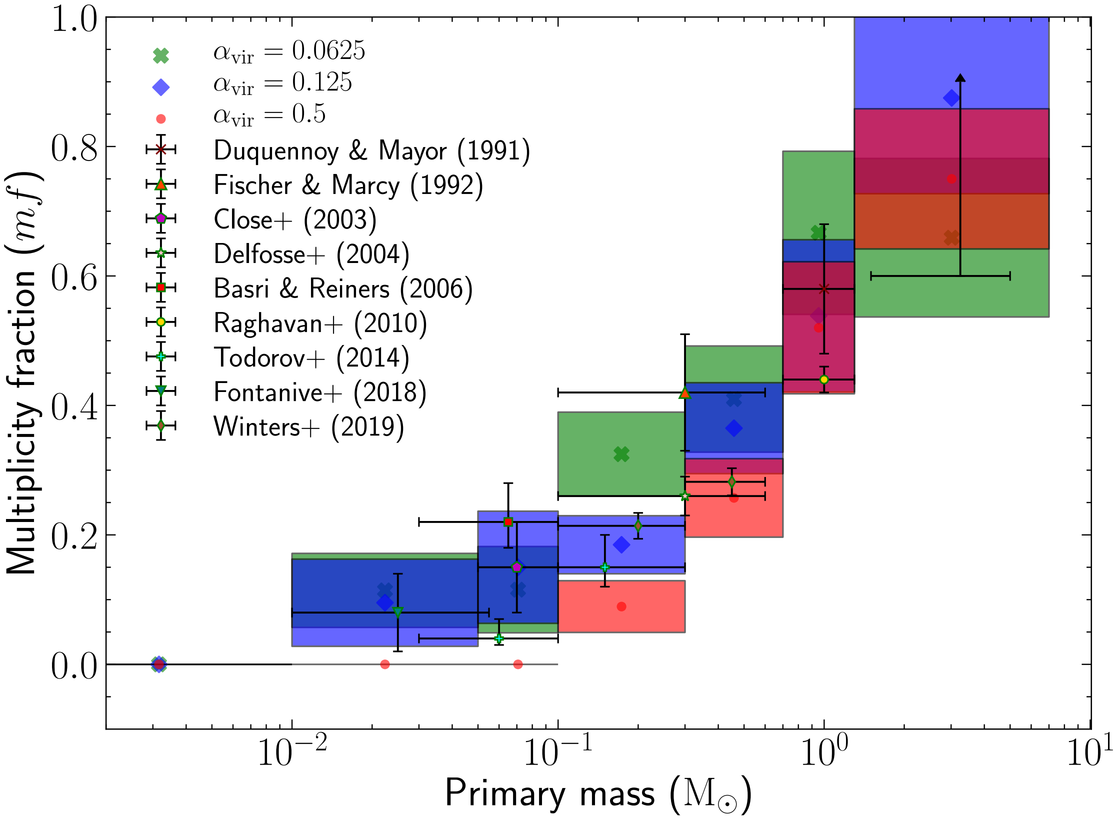

Figure 4.9: Multiplicity fraction (mf) computed via Eq. (4.5) in different primary mass intervals for the simulation models with $\alpha_{\rm vir} = 0.0625$ (green crossed markers and boxes), $\alpha_{\rm vir} = 0.125$ (blue diamond markers and boxes) and $\alpha_{\rm vir} = 0.5$ (red circular markers and boxes). The markers represent the mf in the mass range denoted by the width of the box enclosing the marker. The height of the box represents the error margin in the mf obtained. The multiplicity fractions measured in different observations are depicted by the centre of the crosses, with the horizontal and vertical components representing the mass interval considered in the survey and the uncertainties, respectively. The observational data are (from low to high primary mass), from Fontanive et al. (2018), Todorov et al. (2014), Basri & Reiners (2006), Close et al. (2003), Todorov et al. (2014), Winters et al. (2019) (not corrected for undetected companions), Delfosse et al. (2004), Fischer & Marcy (1992), Raghavan et al. (2010) and Duquennoy & Mayor (1991). The mf for high-mass stars is not well understood. The lower limit of mf in the mass range of 1.5–5 $\mathrm{M}_\odot$ is $\sim$ 0.5–0.6 (Chini et al. 2012; Duchêne & Kraus 2013). Massive stars are considered to have $mf \sim 1$ (Mason et al. 2009; Sana & Evans 2011; Sana et al. 2017; Lee et al. 2020).

mass intervals are higher than that for $\alpha_{\rm vir} = 0.5$. The multiplicity fraction over the sub-solar range (primary mass $< 1\,\mathrm{M}_\odot$) for $\alpha_{\rm vir} = 0.0625, 0.125$, and 0.5 are $\sim 0.27, 0.22$, and 0.14, respectively. The higher mf in lower $\alpha_{\rm vir}$ cases might be because the local region in which the binaries form will be more bound and gas-rich in the case of low virial parameters. Therefore, the binaries are better shielded from dynamical interactions that result in binary decay (Rozner & Perets 2024a). At super-solar masses, the derived mf values are similar and $\gtrsim 0.6$ for the three cases. High-mass binaries generally form in the most gas-rich regions within the cloud, which is why they can accrete gas rapidly. Hence, the high-mass binaries are relatively shielded from interactions even in the highest virial parameter case of $\alpha_{\rm vir} = 0.5$. We note that, to confirm our interpretation of the higher mf in lower $\alpha_{\rm vir}$ cases, a comprehensive quantitative study is required, measuring the local virial parameter in cluster regions and analysing the evolution of binary orbits, which is beyond the scope of this work. Finally, we find that the fraction of singles across the full mass range is ~ 0.65, irrespective of $\alpha_{\rm vir}$. Previous numerical and observational works also yield similar values for the fraction of single stars (Lada 2006; Rohde et al. 2021; Mathew & Federrath 2021).

4.4 Discussion

4.4.1 Comparison with previous numerical works

In our study, the mean thermal Jeans mass $M_{\rm J}$ and the number of Jeans masses for the three simulations models are different since the initial mean density varies between them. Bate & Bonnell (2005) find that the IMF is linearly dependent on the mean thermal Jeans mass in their simulations. However, Bate (2009b) establish that the inclusion of radiative feedback removes the dependence on the thermal Jeans mass, finding that the IMFs are indistinguishable for simulations with mean Jeans masses of $1\,\mathrm{M}_\odot$ and $1/3\,\mathrm{M}_\odot$ (see also Krumholz et al. 2011). In our study, the mean Jeans mass in the simulations with $\alpha_{\rm vir} = 0.0625$ and $\alpha_{\rm vir} = 0.125$ also varies by a factor of ~ 3. However, contrary to our case, $\alpha_{\rm vir}$ is similar for the two simulation sets with different $M_{\rm J}$ in Bate (2009b) as a result of using a different combination of cloud size and $\mathcal{M}$ in each of their two sets. Therefore, a direct comparison between the two studies cannot be made.

Lee & Hennebelle (2018a) performed a similar numerical experiment to Bate (2009b) by changing the gas density (and hence the thermal Jeans mass) while keeping $\alpha_{\rm vir}$ fixed, by adjusting the cloud size and $\mathcal{M}$. They find that the IMF is relatively flat in the $0.1-1\,\mathrm{M}_\odot$ range at low densities, while at higher densities, the distribution starts to become more peaked, producing a power-law distribution with $\Gamma \sim 3/4$ at masses greater than a few $0.1\,\mathrm{M}_{\odot}$. However, stellar radiative heating was absent in their simulations, and therefore the influence of varying densities or thermal Jeans masses might be overestimated (Bate 2009b; Krumholz et al. 2011; Guszejnov et al. 2016; Federrath et al. 2017b; Mathew & Federrath 2020; Hennebelle et al. 2020a).

Ballesteros-Paredes et al. (2015) and Bertelli Motta et al. (2016) investigated the effect of the turbulent Mach number and found that the form of the IMF remains the same irrespective of $\mathcal{M}$ in their simulations. This contradicts the analytical theories of the CMF or the IMF, which predict that the characteristic mass decreases with an increase in the Mach number (Padoan & Nordlund 2002; Hennebelle & Chabrier 2008; Hopkins 2012). According to these theories, a higher Mach number results in stronger shocks, leading to greater density contrasts and higher fragmentation. The observed trends in Ballesteros-Paredes et al. (2015) and Bertelli Motta et al. (2016) arise because raising the Mach number through the increase of the velocity dispersion also increases the cloud virial parameter, as $\alpha_{\mathrm{vir}} \propto \sigma_{\mathrm{v}}^2$. Higher virial parameters imply that over-densities are less susceptible to collapse, with only the sufficiently massive ones eventually collapsing (Bertelli Motta et al. 2016). On the other hand, Lee & Hennebelle (2018a) observe slight variations in the IMF on changing the Mach number in their simulations by a factor of 5. Here again, the Mach number is varied by adjusting the velocity dispersion, which alters the virial parameter.

Guszejnov et al. (2022b) find that a higher virial parameter results in a lower star formation rate, which agrees with our results. They find that variations in the virial parameter of the cloud do not significantly affect the form of the IMF, while in our study we see a weak dependence of the IMF on α_{vir}. However, Guszejnov et al. (2022b) also vary the virial parameter by adjusting the velocity dispersion, which in turn affects $\mathcal{M}$. Since a higher Mach number is expected to enhance the formation of low-mass over-densities and a higher virial parameter is expected to suppress them, the net impact on the IMF is expected to be minimal as seen in the simulations of Ballesteros-Paredes et al. (2015), Bertelli Motta et al. (2016), and Lee & Hennebelle (2018a). At very high Mach number (or very high σ_{v}), the effect of the virial parameter (increased kinetic support) can dominate over the effect of the Mach number (density-enhancement via stronger shocks) and quench star formation altogether since $\alpha_{\mathrm{vir}} \propto \sigma_{\mathrm{v}}^2$, while $\mathcal{M} \propto \sigma_{\mathrm{v}}$. However, the details of the dependence are non-linear and depend on the region of parameter space considered (Federrath & Klessen 2012).

The numerical experiments carried out here are distinct from the numerical approaches discussed above. While the above works concentrate on the influence of the mean thermal Jeans mass (keeping the virial parameter constant) or the Mach number (keeping the mean thermal Jeans mass constant), i.e., in a sense the impact of the mean density or the velocity dispersion, we focus on the effect of the virial parameter, but keep the Mach number fixed. The mean density and hence the mean thermal Jeans mass varies between our simulation models, which could have some effect on the initial fragmentation in the cloud. However, since the turbulence in our simulations is supersonic ($\mathcal{M} = 5$), the kinetic energy dominates over the thermal energy and hence will govern most of the fragmentation in the early stages. Further, once the stars start to form, the protostellar heating increases the local temperature and Jeans mass in the star-forming cores on sub-parsec scales (Bate 2009b; Krumholz et al. 2011; Guszejnov et al. 2016; Federrath et al. 2017b; Mathew & Federrath 2020; Hennebelle et al. 2020a). Thus, the IMF variations that we observe between the three simulation models may be determined more by the variation in $\alpha_{\rm vir}$ than by variations in the mean thermal Jeans mass.

Haugbølle et al. (2018b) carried out a numerical experiment similar to our analysis, where they changed the virial parameter by varying the mean density, but keeping $\mathcal{M}$ fixed. They find that lowering $\alpha_{\rm vir}$ shifts the peak of the IMF to lower masses, which aligns with our findings. However, Haugbølle et al. (2018b) focus on a regime with $\alpha_{\rm vir} \sim 0.2 - 2$, while we concentrate on a lower $\alpha_{\rm vir}$ regime ($0.06 - 0.5$). Haugbølle et al. (2018b) study the $\alpha_{\rm vir}$ range where either the gravitational and turbulent energies are comparable ($\alpha_{\rm vir} \sim 0.5$) or turbulence dominates ($\alpha_{\rm vir} \gtrsim 1$), while we study the $\alpha_{\rm vir}$ range where either the gravitational and turbulent energies are comparable ($\alpha_{\rm vir} \sim 0.5$) or gravity dominates ($\alpha_{\rm vir} \lesssim 0.1$). Thus, the present work is complementary to the works of Bate & Bonnell (2005), Bate (2009b), Ballesteros-Paredes et al. (2015), Bertelli Motta et al. (2016), Lee & Hennebelle (2018a), Haugbølle et al. (2018b), and Guszejnov et al. (2022b). Ultimately, star formation may depend on a combination of all of the dimensionless parameters (e.g., $\mathcal{M}$, $\alpha_{\rm vir}$, b, $\mu_{\rm B}$, and $\mathcal{M}_{\rm A}$), and future work is needed to quantify the effects of each of these parameters on the SFR and IMF.

4.4.2 Outlier IMFs

The high gas density and large velocity dispersion measured in massive, elliptical early-type galaxies (ETGs) have been suggested as candidates for explaining their bottom-heavy nature (Chabrier et al. 2014; Dib 2022). However, evaluation of the virial parameter in these regions is crucial to obtain conclusive results since understanding the respective $\alpha_{\rm vir}$ regime is important to comprehend the net effect of turbulence. Large velocity dispersion or very high $\alpha_{\rm vir}$ can quench star formation because the large-scale support by turbulence dominates over its ability to enhance fragmentation on small scales (Federrath & Klessen 2012; Chabrier et al. 2014; Brucy et al. 2024). Another possible candidate that can partly contribute to the bottom-heavy nature is the mode of turbulence driving in such regions. Since ETGs are considered to be formed in a starburst event associated with galaxy mergers, the turbulence driving is likely dominated by compressive modes (Federrath et al. 2008; Renaud et al. 2009), which can enhance the formation of low-mass stars (Chabrier et al. 2014; Mathew et al. 2023). Further, our results suggest that the high virial parameters ($\alpha_{\mathrm{vir}} > 1$) measured in the Central Molecular Zone (CMZ) (Myers et al. 2022) contribute in part to the low SFR and top-heavy IMFs (Figer et al. 1999; Kim et al. 2006; Lu et al. 2013; Hosek et al. 2019) observed in the embedded clouds, with the prevalence of solenoidal driving (Federrath et al. 2016; Rani et al. 2022b) being another factor (see also Klessen et al. 2007; Haugbølle et al. 2018b; Mathew et al. 2023). We note that, given the non-linear IMF dependence found in our study, to understand the extent of the contribution of the virial parameter to the top-heavy nature of the IMF observed in the CMZ, regimes where $\alpha_{\mathrm{vir}} > 1$ have to be considered, which are not directly explored in this study.

4.4.3 Origin of the IMF peak

The weak dependence of the IMF on the cloud properties like the virial parameter and mode of turbulence driving (Padoan & Nordlund 2002; Hennebelle & Chabrier 2008; Schmidt et al. 2010; Hopkins 2012; Mathew et al. 2023) may account for why the region around the IMF peak is broad or resembles a plateau (see also Kroupa et al. 2024). When the net effect of the combination of cloud properties favours extensive fragmentation, the peak shifts to lower masses, and when the combination tends to suppress fragmentation, the peak shifts to higher masses. Nonetheless, it still needs to be addressed why the broad peak or plateau exists in the sub-solar or more specifically in the M-dwarf range. Some preferred candidates are the feedback mechanisms that emerge from the stars themselves, such as radiative heating and protostellar outflows, which have been found to be effective in self-regulation (Li & Nakamura 2006; Bate 2009b; Wang et al. 2010; Krumholz et al. 2011; Federrath et al. 2014; Frank et al. 2014; Guszejnov et al. 2016; Offner & Chaban 2017; Federrath et al. 2017b; Mathew & Federrath 2020; Hennebelle et al. 2020a; Mathew & Federrath 2021; Guszejnov et al. 2021; Lebreuilly et al. 2024), or generally, the thermodynamics in the immediate vicinity of stars (Li et al. 2003; Larson 2005; Jappsen et al. 2005; Elmegreen et al. 2008; Hennebelle et al. 2019; Colman & Teyssier 2020; Grudić & Hopkins 2023).

4.5 Conclusions

We conduct a series of star cluster formation simulations to investigate the impact of the cloud virial parameter α_{vir} on the formation process. The simulations incorporate gravity, magnetic fields, turbulence, protostellar radiative heating and mechanical feedback in the form of jets/outflows. We have three sets of simulations corresponding to $\alpha_{\mathrm{vir}} = 0.0625, 0.125$ and $\alpha_{\mathrm{vir}} = 0.5$. We observe that the number of stars formed increases with decreasing α_{vir}. In the case of high virial parameters, the formation of large-scale structures that host star clusters is primarily a consequence of turbulent shocks. By lowering the virial parameter, the relative influence of gravity in the large-scale structure building process increases. Gravity is able to enhance the anisotropies in the cloud and promote the formation of additional large-scale filaments, which eventually fragment to form stars (Vázquez-Semadeni et al. 2007; Bonnell et al. 2008; Mac Low 2013; Vázquez-Semadeni et al. 2019; Hennebelle & Grudić 2024).

We find that reducing the virial parameter from $\alpha_{\mathrm{vir}} = 0.5$ to $\alpha_{\mathrm{vir}} = 0.125$ increases the star formation rate per freefall time $\mathrm{SFR_{ff}}$ by a factor of ~ 2. Reducing the virial parmeter further to $\alpha_{\mathrm{vir}} = 0.0625$ does not result in an additional increase in $\mathrm{SFR_{ff}}$, showing that α_{vir} has a non-linear effect on $\mathrm{SFR_{ff}}$ (see Fig. 4.5). Similar $\mathrm{SFR_{ff}}$ in simulations with $\alpha_{\mathrm{vir}} = 0.0625$ and $\alpha_{\mathrm{vir}} = 0.125$ imply that, at $\alpha_{\mathrm{vir}} \sim 0.1$, gravity has transformed most of the anisotropies or over-densities in the turbulent cloud into stars, i.e., the maximum possible efficiency of star formation at the given Mach number of $\mathcal{M} = 5$ is reached. Thus, lowering α_{vir} further would not affect $\mathrm{SFR_{ff}}$ significantly. Nevertheless, the time at which star formation starts varies between the three models. The first stars form the latest in the simulations with $\alpha_{\mathrm{vir}} = 0.5$ and the earliest in the simulation with $\alpha_{\mathrm{vir}} = 0.0625$ (see Fig. 4.4).

Previous numerical studies of how the initial turbulence influences the IMF are primarily centred on the aspect of the velocity dispersion, with most of the studies finding that the IMF is nearly insensitive to the velocity dispersion or Mach number (see §4.4.1). However, analysing the effect of turbulence on the basis of the velocity dispersion alone is inadequate since changes in σ_{v} change both α_{vir} and $\mathcal{M}$ at the same time, each of which has a unique influence on the cloud dynamics, structure, SFR, and IMF. Since in our simulations, we keep the velocity dispersion and therefore $\mathcal{M}$ fixed, our analysis is principally focused on the effect of changes in the virial parameter. Thus, our work complements previous studies on the influence of turbulence.

We find that the IMF has a weak dependence on the cloud virial parameter. On varying $\alpha_{\rm vir}$ in the simulations from $\alpha_{\rm vir} \sim 0.5$ to $\alpha_{\rm vir} \lesssim 0.1$, the peak mass of the IMF and the median mass decreases by ~ 2. We also find that the multiplicity fraction, mf, is higher for the lower cloud virial parameter cases, particularly in the sub-solar range. mf in the sub-solar primary mass range for simulations with $\alpha_{\rm vir} = 0.0625$ and 0.125 are higher than that for $\alpha_{\rm vir} = 0.5$ by a factor ~ 2 (see Fig. 4.9). Such a difference is important given that this is the mass range where the peak of the IMF is expected. Nevertheless, all three models reproduce the trend of increasing multiplicity fraction with mass and the mf estimates in individual mass intervals broadly agree with the values derived in observational surveys.

We highlight that the non-linear dependence of the SFR and IMF on $\alpha_{\rm vir}$ needs to be considered (see Fig. 4.5 and Fig. 4.7). If $\alpha_{\rm vir}$ is investigated solely within a limited range of either very low or high values, its impact on the SFR and IMF will appear to be negligible, simply because either gravity or turbulence dominates over the other. To reach conclusive results, the effect of the virial parameter should be examined across a broad range of $\alpha_{\rm vir}$ values.

Acknowledgements

We thank the anonymous referee for their quick and constructive review of the work. We would like to thank Blakesley Burkhart, Patrick Hennebelle, Noé Brucy, and Mark Krumholz for discussions regarding SFR theory. S.S.M. would like to acknowledge the useful discussions during ‘The Physics of Star Formation’ winter school held in February 2024 at Les Houches, France. C.F. acknowledges funding provided by the Australian Research Council (Discovery Project DP230102280), and the Australia-Germany Joint Research Cooperation Scheme (UA-DAAD). We further acknowledge high-performance computing resources provided by the Leibniz Rechenzentrum and the Gauss Centre for Supercomputing (grants pr32lo, pr48pi and GCS Large-scale project 10391), the Australian National Computational Infrastructure (grant ek9) and the Pawsey Supercomputing Centre (project pawsey0810) in the framework of the National Computational Merit Allocation Scheme and the ANU Merit Allocation Scheme. The simulation software FLASH was in part developed by the DOE-supported Flash Center for Computational Science at the University of Chicago and the University of Rochester. This work makes use of the yt-project (Turk et al. 2011) and colormaps in the CMasher package (van der Velden 2020).

Appendix A: 3D visualisation of the simulations

Fig. 4.10, Fig. 4.11, and Fig. 4.12 present 3D visualisations of the simulations shown in Fig. 4.1. Movies for these visualisations can be seen at https://sajaymathew.github.io/visualisations.html.

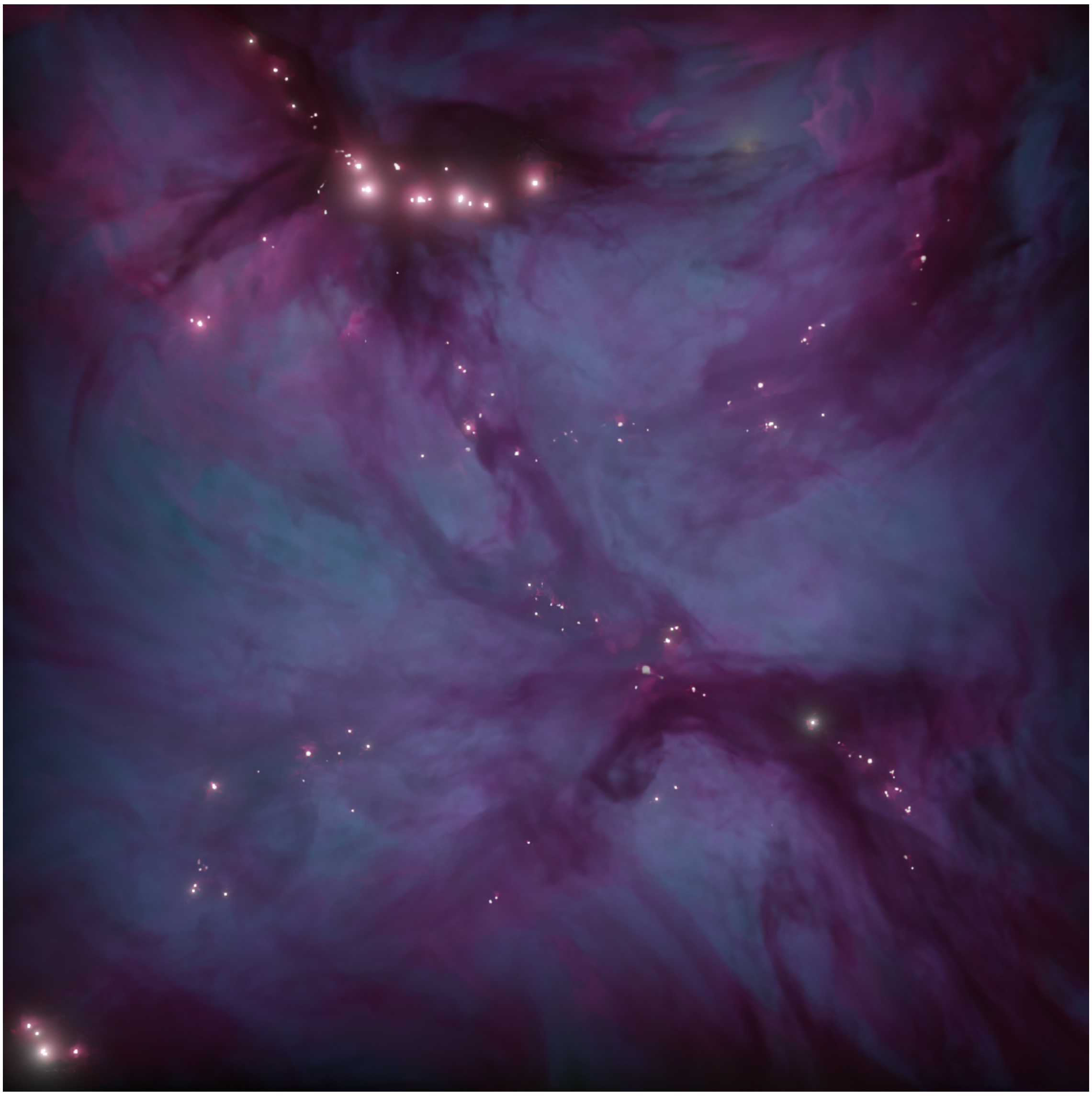

Figure 4.10: 3D visualisation of the simulation with $\alpha_{\mathrm{vir}} = 0.0625$ at SFE = 5%. The visualisation here presents the same simulation (same turbulence seed) as in the left panel of Fig. 4.1. Movies of the above visualisation can be seen at https://sajaymathew.github.io/visualisations.html.

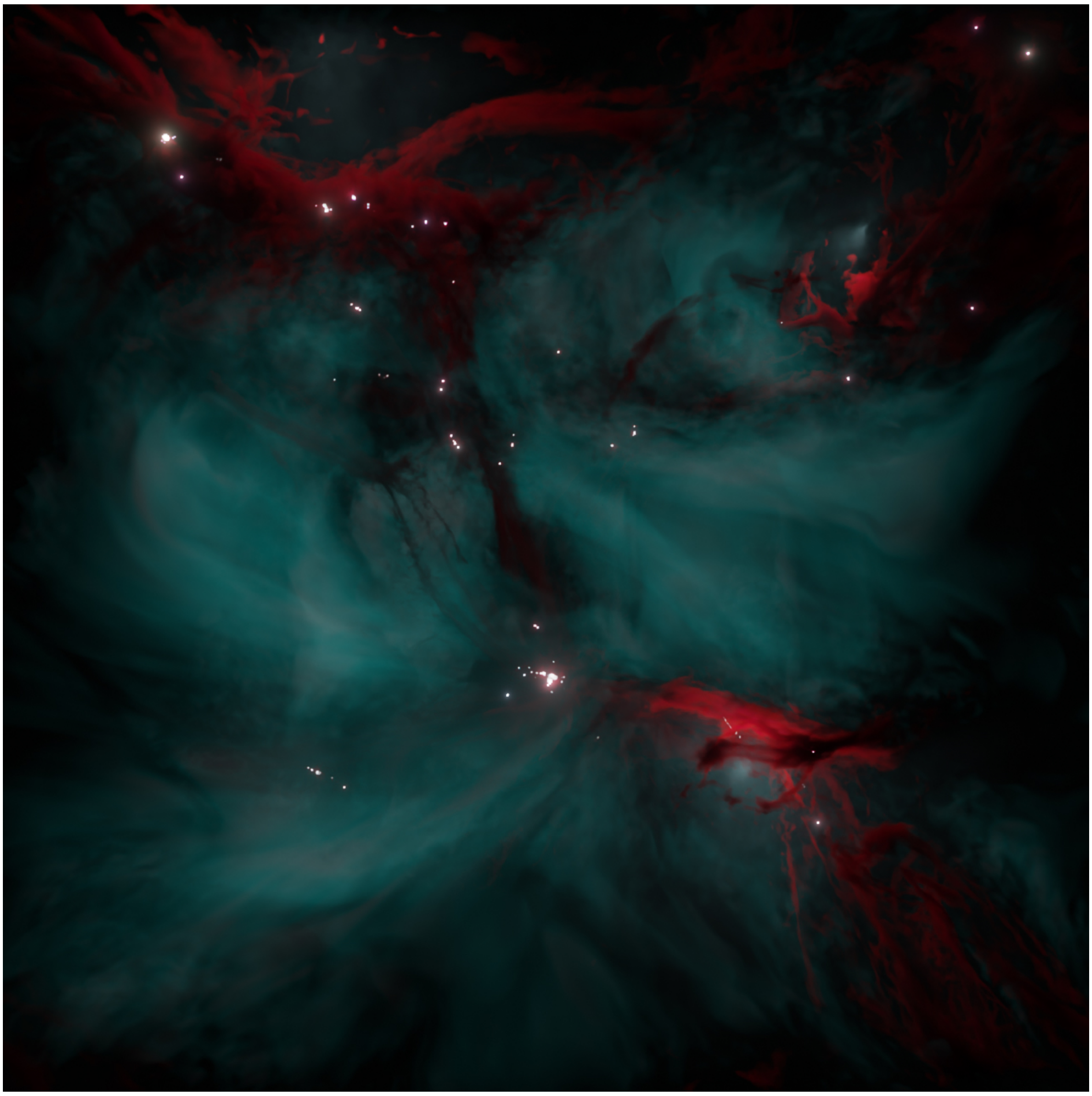

Figure 4.11: 3D visualisation of the simulation with $\alpha_{\rm vir} = 0.125$ at SFE = 5%. The visualisation depicts the same simulation as in the middle panel of Fig. 4.1.

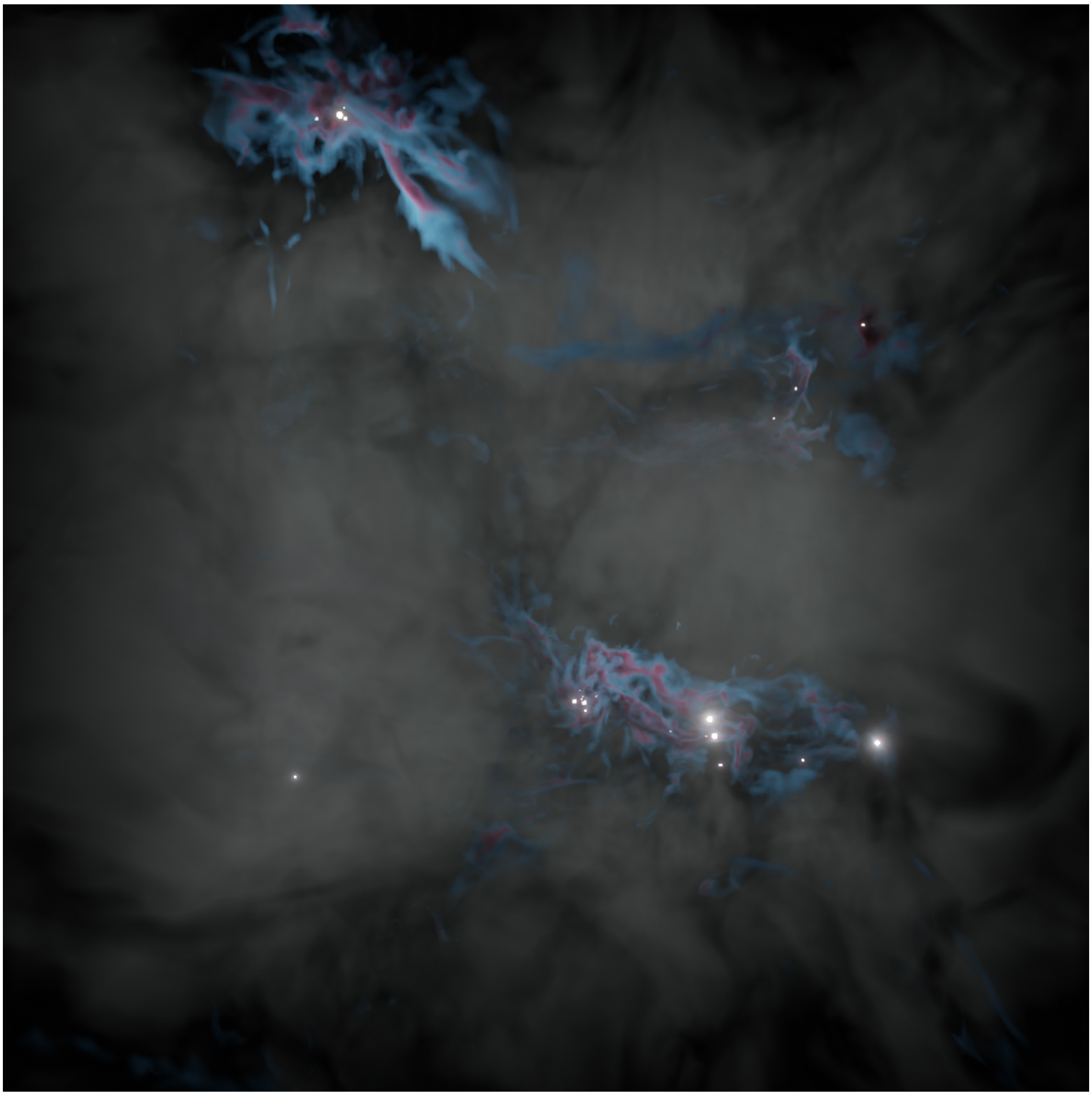

Figure 4.12: 3D visualisation of the simulation with $\alpha_{\rm vir} = 0.5$ at SFE = 5%. The visualisation shows the same simulation as in the right panel of Fig. 4.1.

Chapter 5

Wide-binary eccentricity distribution in young star clusters: dependence on the binary separation and mass

Context and Contribution

This chapter has been previously published as 'Wide-binary eccentricity distribution in young star clusters: dependence on the binary separation and mass', by Sajay Sunny Mathew, Siyao Xu, Christoph Federrath, Yue Hu, Amit Seta, 2024, MNRAS, 532, 2374. The research is presented here as it appears in the original publication, except for a few minor typographical changes. I have carried out the simulations described in this paper, and post-processed the data for further investigation. I have written the majority of the paper, with inputs and suggestions from the 4 co-authors.

Abstract

We study the wide-binary eccentricity (e) distribution in young star clusters and the role of turbulence in setting the form of the e distribution using magnetohydrodynamical (MHD) simulations of star cluster formation. The simulations incorporate gravity, turbulence, magnetic fields, protostellar heating, and jets/outflows. We find that (1) simulations that employ purely compressive turbulence driving produce binaries with a superthermal e distribution ($\alpha > 1$ in $p(e) \propto e^{\alpha}$), while simulations with purely solenoidal driving or natural mixture of driving modes produce subthermal/thermal distributions ($\alpha \leq 1$), (2) the e distribution over the full range of binary separations in our simulations is set at the early stages of the star cluster for-

mation process, (3) while binaries (separation of $r_{\rm pair} \leq 1000\,{\rm AU}$) have subthermal to thermal e distributions ($\alpha \sim 0.8$), wide binaries ($r_{\rm pair} > 1000\,{\rm AU}$) have a superthermal distribution ($\alpha \sim 1.8$), and (4) low-mass binary systems (system masses of $M_{\rm sys} \leq 0.8\,{\rm M}_{\odot}$) have a highly superthermal distribution ($\alpha \sim 2.4$), whereas high-mass systems ($M_{\rm sys} > 0.8\,{\rm M}_{\odot}$) exhibit a subthermal/thermal distribution ($\alpha \sim 0.8$). The binary eccentricity distribution is often modelled as a thermal distribution. However, our results suggest that the e distribution depends on the range of separation of the sampled binaries, which agrees with the findings from recent *Gaia* observations. We conclude that the dependence of the e distribution on the binary separation and mass is linked to the binary formation mechanism governed by the turbulent properties of the parent cloud.

5.1 Introduction

The prevalent existence of binary stars places them at the forefront of many fundamental astrophysical problems (e.g., Bahcall et al. 1985; Monroy-Rodríguez & Allen 2014; Peñarrubia et al. 2016; Liu et al. 2019; Andrews et al. 2022; Tauris & van den Heuvel 2023; Offner et al. 2023; Chen et al. 2024). As a key parameter of binary orbital dynamics, the eccentricity e is often modelled to follow a thermal[1] eccentricity distribution $p(e) = dN/de = 2e$ (Jeans 1919). Recent *Gaia* observations with high-quality parallaxes and proper motions (Gaia Collaboration et al. 2023) have significantly expanded the sample of binaries (El-Badry et al. 2021), including wide binaries with semimajor axes $a \gtrsim 10^3$ AU (El-Badry & Rix 2018; Hwang et al. 2022a), which enables detailed statistical studies on their eccentricity distribution. The *Gaia* observations indicate a non-universal eccentricity distribution among binary stars in the solar neighbourhood, with a transition from a uniform distribution at separations $\sim 10^2$ AU to a superthermal[1] distribution at separations greater than 10^3 AU (Hwang et al. 2022a). This shift challenges our traditional understanding of binary eccentricity distributions which are usually modelled as a thermal distribution. The superthermal eccentricity distribution of wide binaries cannot be accounted for by their evolution in the Galaxy under the effects of Galactic tides and encounters with passing stars (Modak & Hamilton 2023; Hamilton & Modak 2023). Hamilton & Modak (2023) suggest that the observed superthermal distribution is more likely a result of an even more superthermal initial distribution at the time of their formation.

The formation mechanisms and statistical properties of binaries, such as eccentricity, in the regime of $a \lesssim 100\,{\rm AU}$, have been extensively studied with hydrodynamic and magnetohydrodynamic simulations in the literature (e.g., Ostriker 1999; Bate 2000; Offner et al. 2010; Ryu et al. 2017; Lee et al. 2019; Rozner et al. 2023; Kuruwita & Haugbølle 2023). For instance, Bate (2014) find that the e distribution is almost uniform in their star cluster formation simulations consisting of a large population of M-dwarfs and later type stars (see also Guszejnov et al. 2023). The median binary separation calculated in the simulations of Bate (2014) is $\sim 20\,\text{AU}$, which agrees with the peak of the separation distribution obtained for M-dwarf systems in observational surveys (Janson et al. 2012; Winters et al. 2019). At similar binary separation ranges, observations also find a uniform eccentricity distribution (Tokovinin & Kiyaeva 2016; Hwang et al. 2022a). With the new finding that the e distribution has a strong dependence on the binary separation (Tokovinin 2020; Hwang et al. 2022a), which in turn, is dependent on the binary mass (Raghavan et al. 2010; Janson et al. 2012; Winters et al. 2019) and the evolutionary state (Tobin et al. 2016, 2022; Kuruwita & Haugbølle 2023) (see Fig. 5.4), it remains to be extensively studied what mechanisms play dominant roles in the origin of binary eccentricity on different mass and separation scales. In particular, the formation mechanisms and statistical properties of wide binaries with $a \gg 100\,\text{AU}$ need further numerical investigation.

Recent *Gaia* observations have new evidence of the important role of turbulence in star and binary formation. Studies by Ha et al. (2021, 2022) have observationally demonstrated that young stars born in turbulent interstellar medium inherit turbulent velocities from their parent cloud. They found that the relative velocities of pairs of young stars are well coupled with the turbulent velocities of the surrounding gas, exhibiting a power-law dependence on their separations across scales within $1 - 100$ pc. Xu et al. (2023) propose that wide binaries naturally form in turbulent molecular clouds, with the scaling relation between the initial relative velocities and initial separations of binary stars regulated by turbulence. They found this initial condition governed by turbulence naturally results in a superthermal distribution of eccentricities at birth. Using star cluster formation simulations, in this paper, we study the eccentricity distribution of binary star systems and their dependence on the turbulent properties of the parent cloud.

The ubiquitous magnetohydrodynamics (MHD) turbulence in the interstellar medium (e.g., Armstrong et al. 1995; Chepurnov & Lazarian 2010; Planck Col-

---

[1] A thermal e distribution, $p(e) = 2e$, is proposed to arise when a group of binaries undergo sufficient dynamical interactions with exchange of energy such that the group approximately approaches a state of energy equipartition and follows Boltzmann distribution (Jeans 1919; Ambartsumian 1937; Kroupa 2008; Geller et al. 2019). $p(e)$ is referred to as a superthermal distribution when $p(e) \propto e^{\alpha}$ with $\alpha > 1$ and as subthermal where $p(e) \propto e^{\alpha}$ with $\alpha < 1$. The distribution is uniform when $\alpha \sim 0$ (Hwang et al. 2022a; Modak & Hamilton 2023).

laboration et al. 2016b; Hu et al. 2019; Ha et al. 2022) plays an essential role in star and binary formation (e.g., Federrath & Klessen 2012; Krumholz et al. 2012b; Farias et al. 2024). In this study, we use MHD turbulence simulations of star cluster formation (Mathew & Federrath 2021; Mathew et al. 2023) to analyse the eccentricity distribution of binaries within $\sim 1\,\mathrm{Myr}$ of their formation. The simulations incorporate gravity, turbulence, magnetic fields, protostellar radiative heating, and jets/outflows. Including all the above physical mechanisms is essential since each of these mechanisms has a significant effect on the star cluster formation process. Turbulence dictates the gas density distribution of the cloud and hence regulates fragmentation (Vazquez-Semadeni 1994; Padoan et al. 1997a; Padoan & Nordlund 2002; Kritsuk et al. 2007; Kowal et al. 2007; Hennebelle & Chabrier 2008; Federrath et al. 2008; Hennebelle & Chabrier 2009; Hopkins 2012, 2013a; Federrath 2013a; Federrath & Banerjee 2015; Mocz & Burkhart 2018; Xu et al. 2019; Abe et al. 2021; Seta & Federrath 2022). The bipolar outflows impact the protostellar mass through the removal of accreting material from protostars (Li & Nakamura 2006; Federrath et al. 2014; Frank et al. 2014; Mathew & Federrath 2021; Guszejnov et al. 2021; Lebreuilly et al. 2024), and rearrange the gas around these stars, which in turn influences the formation of new stars in their vicinity (Wang et al. 2010; Federrath et al. 2014). Magnetic fields and protostellar heating provide additional pressure support and suppress fragmentation into multiple systems (e.g., Krumholz et al. 2011; Federrath et al. 2017b; Krumholz & Federrath 2019; Xu et al. 2019; Mathew & Federrath 2020; Hennebelle et al. 2020b). Further, star-forming clouds can have turbulent magnetic fields (e.g., Hull et al. 2017; King et al. 2018; Hu et al. 2019; Hu & Lazarian 2023; Liu et al. 2024) and the fraction of energy in the turbulent component can have important consequences for binary formation (Gerrard et al. 2019).

Our primary goal is to numerically probe the possible origin of the observed non-universal $p(e)$ of binaries with $a \gtrsim 100$ AU and its dependence on binary separation, system mass, and mass ratio. Previous numerical works focused on the role played by dynamical interaction and gas friction/gas accretion in the formation of closer binaries ($a < 100\,\mathrm{AU}$) (e.g., Ostriker 1999; Bate 2000; Ryu et al. 2017; Lee et al. 2019; Rozner et al. 2023). Since the importance of these two formation mechanisms in the regime of close binaries has been already extensively studied in the literature (e.g., Bate 2009a, 2012, 2019), we focus on the third new mechanism of scale-dependent turbulent velocities of gas inherited by wide binaries ($\gg 100\,\mathrm{AU}$), which has not been studied with numerical simulations before. We will test the analytical predictions by Xu et al. (2023) regarding the formation of wide binary stars in turbulent environments and the origin of their superthermal $p(e)$. Specifically, we will also for the first time investigate the role of turbulence with different driving conditions in shaping $p(e)$. The paper is organized as follows. In Section 5.2, we detail the simulation data utilised in our study and describe the methodology for calculating the orbital eccentricity of binary systems. In Section 5.3, we perform statistical analysis on $p(e)$ and its dependence on turbulence driving mechanism, binary separation, system mass, and mass ratio. In Section 5.4, we delve into the implications of our findings. Section 5.5 presents the limitations of this study, and in Section 5.6, we summarise the key results.

5.2 Methodology

To study the properties of young binary stars, we use the star cluster formation simulations from Mathew & Federrath (2021) and Mathew et al. (2023). These simulations are carried out in a 3D computational domain of $2 \times 2 \times 2\,\mathrm{pc}^3$ dimensions with triply periodic boundaries. An adaptive mesh refinement (AMR) grid structure is used and the maximum effective resolution is 4096^3 cells with a minimum cell size of approximately 100 AU. The star cluster formation is modelled by solving the MHD equations with gravity using a modified version of the FLASH (version 4) code (Fryxell et al. 2000; Dubey et al. 2008).

The simulations incorporate a vast array of physical mechanisms including gravity, magnetic fields, turbulence, and protostellar feedback in the form of radiative heating and mechanical outflows. Sink particles are used to model protostellar objects. Whenever a spherical region of radius $r_{\mathrm{sink}} = 250\,\mathrm{AU}$ centered on a cell satisfies the criterion for gravitational collapse (Federrath et al. 2010c), the gas within the region is replaced by a sink particle (see discussion on limitations in §5.5). The position, linear momentum, and angular momentum of the sink particle are determined by the respective quantities of the enclosed gas within the spherical volume of radius r_{sink} (which is set to be the accretion radius of the sink particle). Sub-grid models are used for modelling the protostellar heating (Mathew & Federrath 2020) and outflow feedback (Federrath et al. 2014; Mathew & Federrath 2021). We encourage the reader to refer to Mathew & Federrath (2021) and Mathew et al. (2023) for more detailed description of the simulation model used here.

5.2.1 Turbulence driving

We drive turbulence within the gas in the computational domain by introducing a forcing term in the momentum equation of MHD. The forcing (acceleration) field is modelled using a stochastic Ornstein-Uhlenbeck (OU) process (Eswaran & Pope

1988), which enables us to drive turbulence continuously, with the field varying smoothly in space and time. The turbulence driving module injects kinetic energy on the largest scales, which naturally cascades down to smaller scales, producing a velocity power spectrum $\sim k^{-2}$ or equivalently a velocity dispersion – size relation of $\sigma_v \propto \ell^{1/2}$ (Larson 1981; Ossenkopf & Mac Low 2002; Heyer & Brunt 2004; Roman-Duval et al. 2011; Federrath 2013a; Federrath et al. 2021). Our forcing approach allows us to control the fraction of compressive-to-solenoidal modes by performing a Helmholtz decomposition. When the total power in the forcing is contributed by compressive modes, we obtain a purely compressive driving (curl-free), and when the total power is associated with solenoidal modes, we get a purely solenoidal turbulence driving (divergence-free). When no decomposition is carried out, a natural mixture of driving modes emerges (see Federrath et al. 2008, 2010b, for more details on the turbulence driving method adopted here). A public version of the turbulence driving module is available (Federrath et al. 2022).

5.2.2 Initial conditions

The gas density in the computational domain is initially uniform with $\rho_0 = 6.56 \times 10^{-21}\,\mathrm{g\,cm^{-3}}$. Since the size of the box $L = 2\,\mathrm{pc}$, the total cloud mass $M_{\mathrm{cl}} = \rho_0 \times L^3 \approx 775\,\mathrm{M}_\odot$, yielding a mean free-fall time of $t_{\mathrm{ff}} \approx 0.82\,\mathrm{Myr}$. Once the turbulence driving module (Federrath et al. 2010b, 2022) is turned on, over-densities in the form of clumps and filaments are created due to the stirring of the gas and the presence of turbulent shocks. The magnetic field, which is uniform initially with $B = 10^{-5}\,\mathrm{G}$ along the z-axis of the computational domain, is modified as a result of the twisting, mixing and compression (Cho & Lazarian 2002), and elongation of magnetic field lines by the turbulent motions (Seta & Federrath 2021), generating a field structure similar to that observed in real molecular clouds (Federrath 2016).

The turbulence driving is first performed without self-gravity for two turbulent crossing times, $2t_{\mathrm{turb}} = L/(\mathcal{M} c_{\mathrm{s}}) = 2\,\mathrm{Myr}$ (Federrath et al. 2010b), where $\mathcal{M}$ is the steady state sonic Mach number and $c_{\mathrm{s}} = 0.2\,\mathrm{km/s}$ is the isothermal sound speed for solar metallicity, molecular gas at 10 K. The velocity dispersion on the turbulence driving scale is set as $\sigma_v = c_{\mathrm{s}}\,\mathcal{M} = 1.0\,\mathrm{km\,s^{-1}}$ such that $\mathcal{M} = 5$ and Alfvén Mach number $\mathcal{M}_{\mathrm{A}} = 2.9$. The initial virial parameter is $\alpha_{\mathrm{vir}} = 2E_{\mathrm{kin}}/E_{\mathrm{grav}} = 0.5$, which is in the range of observed values (Falgarone et al. 1992; Kauffmann et al. 2013; Hernandez & Tan 2015). A steady state of turbulence will be reached as the simulation reaches two turbulent crossing times (Federrath et al. 2010b; Price & Federrath 2010a), which is when self-gravity is turned on ($t = 0$). The turbulence driving is maintained during the further evolution. The simulation is then allowed to evolve until a star formation efficiency (SFE) of 5% is reached, i.e., when 5% of the total cloud mass has formed stars. During this evolution phase, the high-density regions (analogous to dense cores) produced by the turbulent shocks become gravitationally unstable and form star clusters (see Mathew & Federrath 2021; Mathew et al. 2023, for further description of the numerical setup).

5.2.3 Multiplicity identification algorithm

To identify the binary pairs in the simulations, we follow the iterative technique used in Bate (2009a). In each iteration, we find the closest bound pair in the list of sink particles. This pair is replaced in the list by a binary object with a mass that is equal to the sum of the respective pair. The position and velocity of the binary object are given by the centre-of-mass position and velocity of the pair, respectively. In the next iteration, using the new list, we again search for the closest bound pair and replace them with an object of higher order, i.e., if the pair consists of two single objects, they are replaced by a binary object or if the pair comprises of a single object and binary object, they are replaced by a triple. The process of finding and replacing the closest bound pair is iterated until none of the objects in the set are bound anymore or the only possible combination is a quintuple. Systems of order higher than quadruples are rejected since high-order systems are highly unstable and they can easily decay dynamically. The output of the above algorithm is a list of multiple systems, i.e., a list consisting of singles, binaries, triples, and quadruples. From this list, we can calculate different multiplicity properties of the systems such as the eccentricity and semi-major axis (Offner et al. 2023). This method is already used in Mathew & Federrath (2021) and Mathew et al. (2023) to determine multiplicity properties. The eccentricity e of the binary orbit is given by,

$$e = \sqrt{1 + \frac{2\varepsilon h^2}{G^2\left(M_1 + M_2\right)^2}}. \tag{5.1}$$

Here ε, h, and G are the specific energy (kinetic+gravitational), specific angular momentum, and the gravitational constant, respectively. M_1 and M_2 correspond to the mass of the two binary components. Using Eq. 5.1, we calculate the eccentricity associated with the binaries in our simulations and analyse the eccentricity distribution and its dependence on the turbulent driving mechanism, binary separation, mass and mass ratio, which is presented next.

5.3 Results

To study the binary statistics, we utilise a total of 28 simulations of star cluster formation that form 1362 sink particles (stellar objects) overall. The sink particles themselves represent star+disc systems. However, for clarity, we will refer to sink particles as stars here although they might represent an under-resolved binary since disc fragmentation is not fully resolved (see discussion on limitations in §5.5).

Using the method described in §5.2.3, we categorise the stars formed in each of the simulations into multiple systems. The simulations have the same numerical setup and initial conditions as described in §5.2.2, except that they are characterised by different modes of turbulence driving. In the suite of simulations used here, there are 7 simulations (forming a total of 468 stars) with a purely compressive mode of turbulence driving (curl-free driving), 11 simulations (forming 445 stars) with purely solenoidal turbulence driving mode (divergence-free), and 10 simulations (forming 449 stars) with a natural mixture (equal power in compressive and solenoidal modes). In each of the three sets, all simulations have the same setup but have different turbulence realisations (random seed to generate numerical turbulence). For example, a different turbulence realisation is used in each of the 7 simulations with purely compressive driving, providing a statistically robust sample of stars. The number of stars formed depends on the type of turbulence driving (Mathew et al. 2023). Therefore, in order to obtain a similar number of stars (i.e., similar statistics) from each of the three simulation models, the number of simulations performed for each of the models is different. For example, the model with purely compressive turbulence driving produces the highest number of stars in a single simulation, and hence requires the least number of simulations to reach a total of ~ 450 stars.

5.3.1 Effect of the mode of turbulence driving

The mode of turbulence driving has a significant influence on the density distribution of a gas cloud and in turn on the stellar properties like the star formation rate (Federrath et al. 2008, 2010b; Padoan & Nordlund 2011; Hennebelle & Chabrier 2011) and the initial mass function (IMF) (Schmidt et al. 2010; Lomax et al. 2015; Mathew et al. 2023). To determine which mode of turbulence driving dominates the driving in a cloud, the turbulence driving parameter b can be estimated. b is the constant of proportionality in the relation between the standard deviation of gas density and Mach number, $\sigma_{\rho/\rho_0} = b\mathcal{M}$ (see Federrath et al. 2008, 2010b, for a detailed description of b). Purely compressive driving has $b \sim 1$ and purely solenoidal driving has $b \sim 1/3$ (Federrath et al. 2008). The b value of real clouds is between

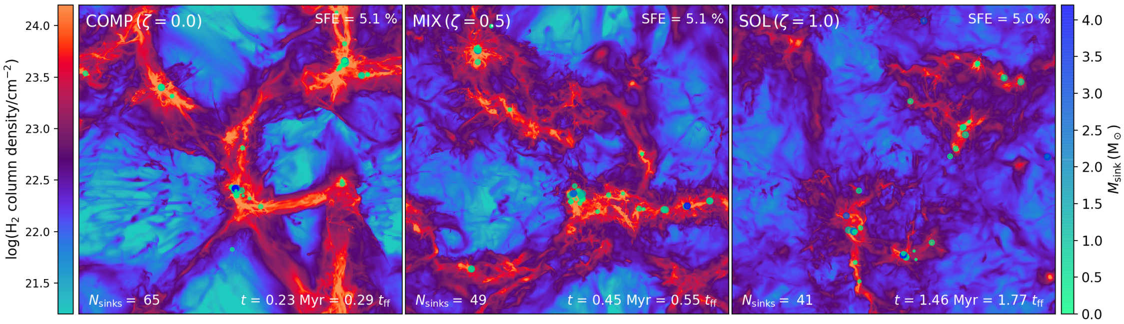

Figure 5.1: Column density maps (mass-weighted) of the purely compressive driving (COMP; left panel), mixed driving (MIX; middle panel), and solenoidal driving (SOL; right panel) simulations, at a star formation efficiency (SFE) of 5%. The circular markers correspond to the sink particle (star+disc system) positions, and the colour bar on the right represents the mass of the sink particles. The size of the markers is also scaled by the mass of the sink particles.

1/3 and 1 (Federrath et al. 2016; Menon et al. 2021; Sharda et al. 2022; Dhawalikar et al. 2022; Gerrard et al. 2023), where a value of $b \sim 0.4$ represents a natural mixture of the two driving modes (Federrath et al. 2008, 2010b). Fig. 5.1 presents the density structure in three simulations that have the same numerical setup and turbulence realisation but have different turbulence driving modes – from left to right: purely compressive (COMP), natural mixture (MIX) and purely solenoidal (SOL). The simulations are compared at a star formation efficiency SFE = 5% (i.e., the ratio of stellar mass to initial cloud mass). The morphology of the star-forming regions in the three simulation models are different and the number of stars formed also varies between them, as discussed in detail in Mathew et al. (2023). Here we primarily focus on the eccentricities of the binary stars.

Fig. 5.2 compares the eccentricity distributions between the three simulation models. The histograms are normalised such that the total area under the histogram is unity. In each of the eccentricity distributions, only the binary pairs that contain the primary star (highest mass star) in the corresponding multiple system are included. For example, in a triple system where a binary subsystem (secondary+tertiary) orbits a primary, only the bound pair that involves the primary is included in the distributions (the secondary+tertiary subsystem is excluded). With such a selection criterion, the COMP model yields a total of 140 pairs, the SOL model gives 132 pairs, and the MIX model yields 117 pairs. The power-law fits to the eccentricity distributions ($p(e) \propto e^{\alpha}$) are obtained by Monte-Carlo sampling where the red solid line represents the 50th percentile and the shaded region is bracketed by the 16th and 84th. The dashed line corresponds to a thermal distribution with $p(e) = 2e$. The mean

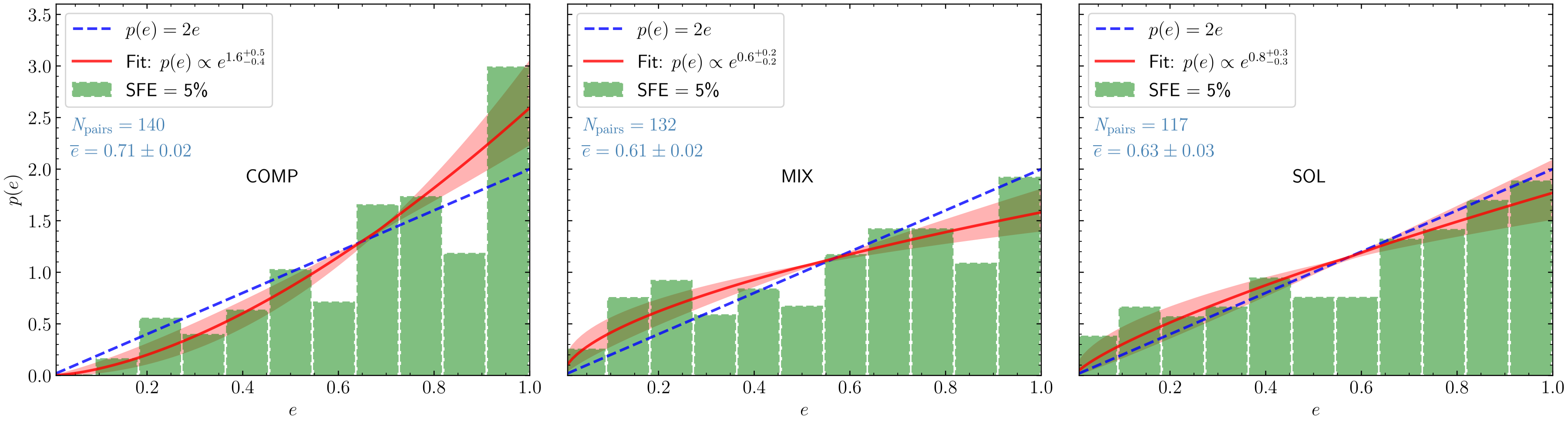

Figure 5.2: Eccentricity distribution of the bound pairs at SFE = 5% for each of the three simulation models (from left to right: COMP, MIX, SOL). The solid curves represent power-law fits ($p(e) \propto e^{\alpha}$) to the distributions, and the dashed curves correspond to a thermal eccentricity distribution $p(e) \propto e^1$. The mean eccentricity is also indicated in the legends, which is higher for the COMP case than for MIX and SOL cases, which have similar values. The COMP case shows superthermal ($\alpha > 1$) eccentricity distribution whereas the MIX and SOL cases show subthermal to thermal ($\alpha \leq 1$) distributions. This demonstrates that the eccentricity distribution of binary stars depends on the turbulent driving mode of the parent cloud in which they are formed.

eccentricities for the COMP, MIX, and SOL models are $\overline{e} = 0.71 \pm 0.02, 0.61 \pm 0.02,$ and 0.63 ± 0.03, respectively (see Tab. 5.1). The e distribution of the COMP model is superthermal ($\alpha \sim 1.6$) while the e distributions for the MIX and SOL models are in the subthermal-thermal range ($\alpha \sim 0.6$ and $\alpha \sim 0.8$, respectively), and are similar to each other (α values are within the 1-sigma variations of each other). We performed Kolmogorov–Smirnov (K–S) tests to quantify the differences between the distributions. The p-values obtained when comparing the distributions for COMP and MIX is 0.034, and that for COMP and SOL is 0.11. These p-values suggest that $p(e)$ for COMP is likely different from that of MIX or SOL. The p-value of 0.59 obtained from comparing MIX and SOL implies that the e distributions for MIX and SOL are likely similar. This is expected because the turbulence driving parameter b for MIX and SOL is similar (0.4 and 0.3, respectively), i.e., MIX and SOL yield statistically very similar distributions. The variations caused by randomness are likely comparable to that caused by the small change in b between MIX and SOL. Overall, it can be inferred that the e distribution has a considerable dependence on the turbulence driving mode (SOL or MIX on one hand vs. COMP on the other). When compressive turbulence driving dominates, the e distribution tends to be superthermal, while for solenoidal or mixed driving, it corresponds to a subthermal/thermal distribution.

The effect of the turbulent properties of the cloud on the eccentricity statistics will be investigated further in a follow-up work. Here we will mainly focus on the effects of the binary parameters including the binary separation and mass. For the purpose of increasing our sample size, from here on, all analyses will be carried out by compiling together data from the three simulation models, i.e, using the binary pairs from the COMP, MIX, and SOL simulations, yielding a total of 389 binaries. We justify this choice of adding all the models together, in the next paragraph.

The data compilation we obtain will be analogous to binary data obtained from star-forming clouds in the Milky Way since the initial conditions employed in the simulations are typical of low-mass star-forming regions in the Milky Way. Similar to the different modes of turbulence driving obtained in the simulations ($b \sim 1$, $b \sim 0.4$, and $b \sim 0.3$), the extent to which a particular driving mode dominates varies between the clouds in the Milky Way (i.e., a range of b values can be associated with the clouds). The binaries in the solar neighbourhood collected by observational surveys possibly originate from clouds with different turbulence properties. Since these surveys generally do not distinguish the binary systems based on the initial turbulence environment, combining our simulation models is reasonable. Combining all the simulations also ensures that we have more statistics than the individual

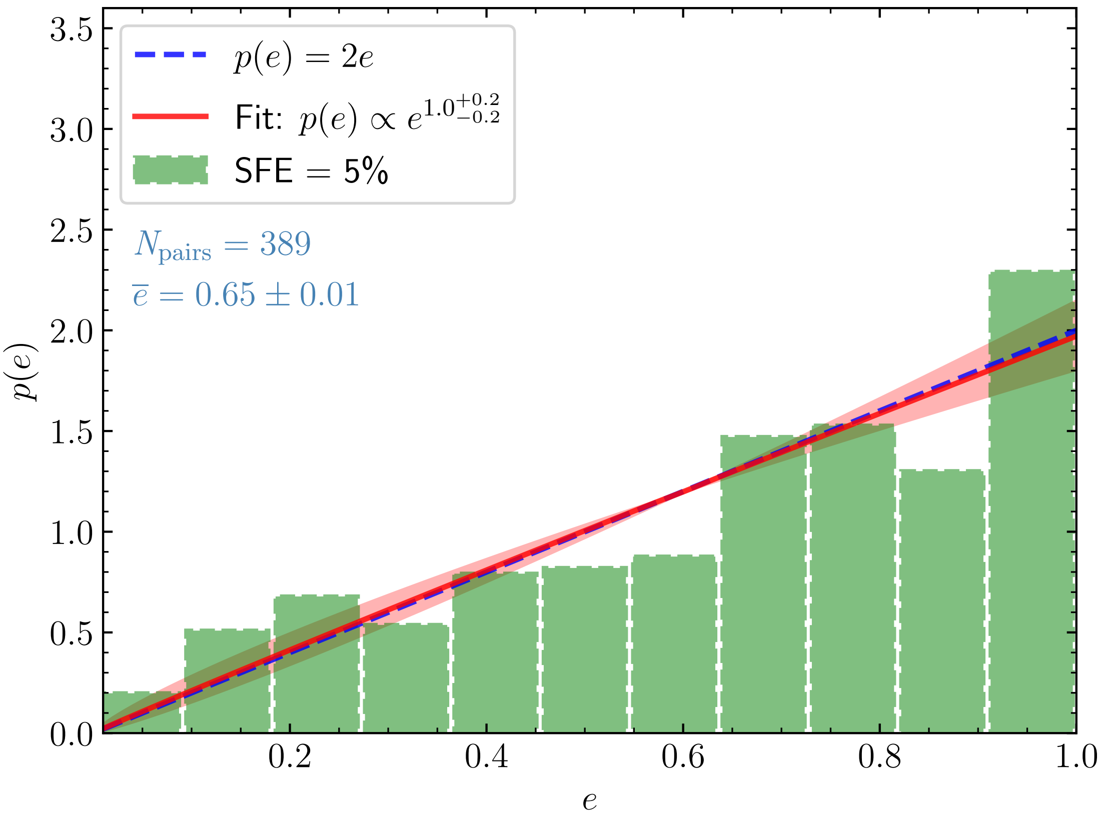

Figure 5.3: Eccentricity distribution at SFE = 5% for the three simulation models compiled together. We see that the power-law fit (solid) agrees with a thermal distribution (dashed).

cases.

Fig. 5.3 presents the measured $p(e)$ when the data from the three simulation models are considered as a whole (i.e., plotting the data in the three panels of Fig. 5.2 together). The resulting collection provides 389 binary pairs. The mean eccentricity is $\bar{e} = 0.65 \pm 0.01$, denoting the presence of a relatively high fraction of highly eccentric orbits. It is evident from the figure that the fit to the distribution compares well with a thermal distribution of $p(e) = 2e$. The thermal distribution here is simply a result of combining superthermal (COMP) and subthermal/thermal (MIX, SOL) distributions together. Fig. 5.2 clearly shows that the physics of the turbulence gives rise to different distributions. This suggests that observations might be encouraged to look for non-thermal distributions, which might have been the results of different turbulence in different environments. The distribution corresponds to the simulation time at which SFE = 5%. Since the star formation rate differs greatly between the three simulation models, the time at which the SFE = 5% is reached varies between the simulations here. However, as compared to the field stars, the stars here are still very young, with even the oldest stars having a lifetime (time between star formation and end of simulation) of < 1 Myr. We examined the $p(e)$ at SFE $= 2$, 3, 5%, combining the different simulation models together. The value of α measured for the three groups can be found in Tab. 5.1. The p-value returned while comparing the e distribution corresponding to SFE $= 2\%$ and 3% is 0.23. Comparisons between $p(e)$ at SFE $= 2\%$ and SFE $= 5\%$, and $p(e)$ at SFE $= 3\%$ and SFE $= 5\%$ gives p-values of 0.69 and 0.93, respectively. The distributions are similar and approximately thermal for all SFE, i.e., at different points in time and star formation efficiency, implying that the overall form of the e distribution is decided at the early stages of the cluster formation process.

Observational studies of the eccentricity in binaries generally find mean eccentricity values of < 0.5 (Duquennoy & Mayor 1991; Abt 2006; Raghavan et al. 2010), which is comparatively lower than the value calculated from our simulations ($\bar{e} \sim 0.65$). However, the sample of binaries used in these studies have orbital periods of less than a few 10^5 days, i.e., a semi-major axis of $<\sim 100$ AU. Recently, it has been shown that the e distribution is dependent on the separation between pairs or the semi-major axis (e.g., Tokovinin 2020; Hwang et al. 2022a). Hence, the mean estimation will be sensitive to the selection scheme in the survey, i.e., whether the sample has a higher population of wide or close pairs. The binary pairs in our simulations represent a sample with a wide range of semi-major axes, varying from around 10 AU to 10^5 AU, although we are underestimating the number of close binaries. Bate (2014) find a mean eccentricity of 0.33 ± 0.02 with a standard deviation of 0.28 in their simulations, which have comparatively much higher maximum spatial resolution (see also Bate 2009a, 2012, 2019; Guszejnov et al. 2023). The mean eccentricity in Bate (2014) is almost a factor of 2 less than our estimate, because a major fraction of their binary population has separations of around $10 - 20$ AU, while most of the binaries from this work have separations of > 200 AU. The binary statistics, including the eccentricity, are significantly different for different separation or semi-major axis ranges, which is discussed next.

Semi-major axis distribution

Fig. 5.4 shows the binary semi-major axis formed in the three simulation models combined together, in comparison with the a distributions collected from the radiation hydrodynamical simulations of Bate (2012) (dash-dotted histogram in Fig. 5.4) and some observational surveys (Raghavan et al. 2010; Winters et al. 2019; Tobin et al. 2022). The peak of the distribution occurs at around 200 AU, although there exists a considerable number of pairs at separations greater than 1000 AU. The

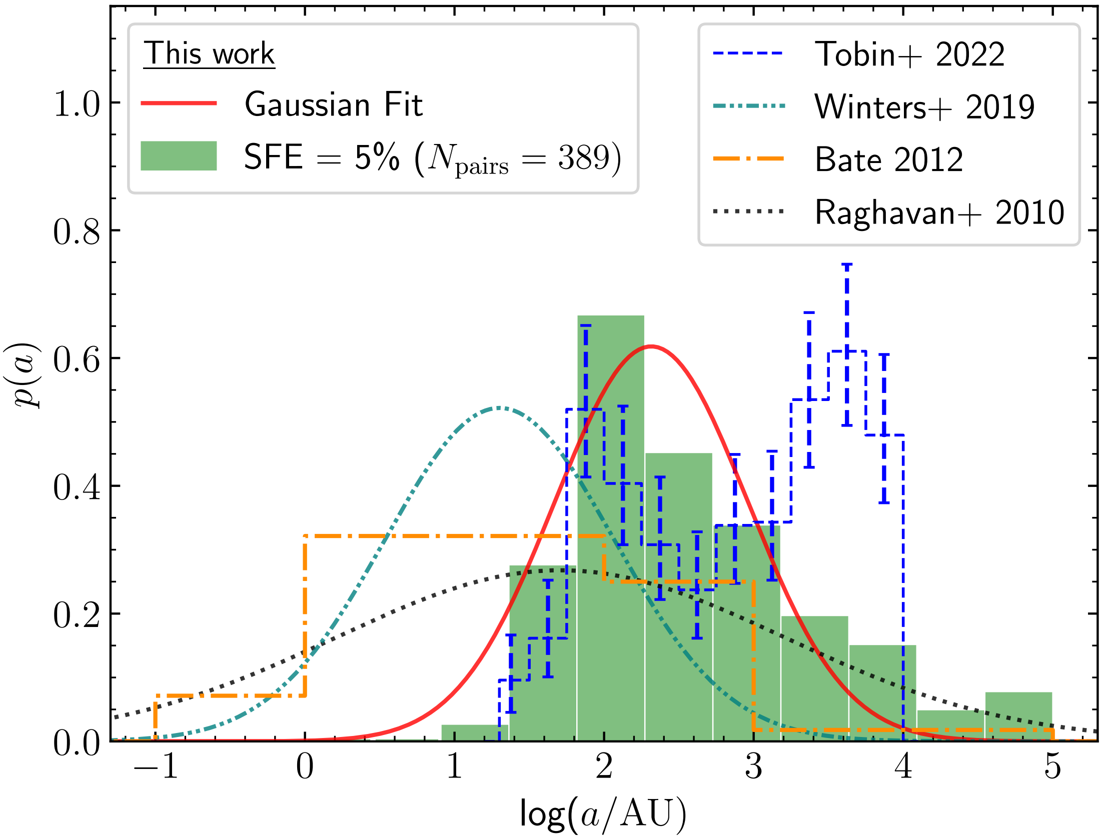

Figure 5.4: The distribution of the semi-major axis a of the bound pairs from our simulations (histogram with solid edges). The solid line corresponds to a Gaussian fit with a peak at $a = 206\,\mathrm{AU}$ and a standard deviation $\sigma_{\log(a/\mathrm{AU})} = 0.98$. The dash-dotted histogram (adapted from Bate 2012) represents the a distribution (including the pairs in binary, triple, and quadruple systems) in the radiation hydrodynamical simulations of Bate (2012). The dotted curve represents $p(a)$ for solar-type binaries obtained by Raghavan et al. (2010). The dash-double-dotted curve represents $p(a)$ for M-dwarf systems derived in the survey by Winters et al. (2019). The dashed histogram (adapted from Tobin et al. 2022) corresponds to the bimodal a distribution obtained for a binary sample in the Orion and Perseus molecular clouds combined together (~ 400 protostars), consisting mainly of Class 0 and Class I objects.

number of closer pairs (< 100 AU) is only a lower limit since fragmentation on small scales (at $<\sim$ 200 AU) is not resolved (see §5.5 for more details). The criterion for sink particle formation in our simulations does not allow new sink particles to form within the accretion radius of an existing sink particle (250 AU). Therefore, in our simulations, the pairs at separations less than 250 AU are probably the ones that formed at larger separations which later migrated to closer separations due to dynamical interactions (Reipurth & Clarke 2001; Bate et al. 2002b; Goodwin & Kroupa 2005; Offner et al. 2010). Although new sink particles cannot form within the accretion radius of an existing sink particle (in that case the gas is accreted onto the existing sink particle), there is no resolution-dependent restriction on how close two sink particles can come together as the trajectory of sink particles are decided by Lagrangian dynamics, i.e., the gravitational interaction between each other and with the gas. However, the gravitational potential is softened at distances of around 100 AU to prevent artificial collision between sink particles (see §5.5).

Raghavan et al. (2010) find that, in the solar neighbourhood, the distribution of projected separation of binaries with solar-type primaries is Gaussian (on a logarithmic scale) with a peak at 50 AU (see dotted curve in Fig. 5.4) (see also Duquennoy & Mayor 1991; Mathieu 1994). For M-dwarf primaries in the solar neighbourhood, the distribution is Gaussian as well, but with a slightly lower peak of 20 AU (Janson et al. 2012; Winters et al. 2019). The standard deviation of the distribution in Winters et al. (2019) is $\sigma_{\log(a/\mathrm{AU})} \approx 1.16$ (see dash-double-dotted curve in Fig. 5.4). The separation distribution of pre-main sequence (PMS) stars is found to be different from the distribution of the field stars with median separations estimated at a few hundred AU (Mathieu 1994; Duchêne et al. 2004; Connelley et al. 2008; Chen et al. 2013; Tobin et al. 2016).

The VANDAM survey (Tobin et al. 2016) looked at a sample of 94 protostars consisting of Class 0 and Class I objects within Perseus (Enoch et al. 2009) and obtained a bimodal separation distribution with a peak at $\sim$ 75 AU and another peak at $\sim$ 1000 AU. Tobin et al. (2022) find that the separation distribution is still bimodal with a peak at $\sim$ 100 AU and a second peak at $\sim$ 1000 AU after combining the samples from the Perseus (Enoch et al. 2009; Tobin et al. 2016) and Orion molecular clouds (Fischer et al. 2010; Stutz et al. 2013; Furlan et al. 2016), although the minimum projected separation that can be measured is $\sim$ 20 AU (see dashed histogram in Fig. 5.4). Tobin et al. (2022) suggest that the bimodal behaviour is mainly driven by the Class 0 protostars since the peak at $\sim$ 1000 AU becomes insignificant for Class I and more evolved protostars (see also Kuruwita & Haugbølle 2023). The age of the stars in our simulations lie in the range $10^3 - 10^5$ yr which resembles the Class 0 and Class I lifetimes of approximately 10^4–10^5 yr and a few 10^5yr, respectively (Froebrich et al. 2006; Dunham et al. 2014). Therefore, the separation distribution in our simulations is more relatable to the distribution for young star-forming regions than that for field stars. However, the comparison of the position of the peak in the distribution with the observationally derived peaks should be done with caution because of the inherent limitations in the numerical resolution. This paper is focused on the relative differences in the binary statistics, particularly the variation in the eccentricity distribution for different separation and mass ranges, i.e., the relative change in the value of α.

5.3.2 Dependence on the binary separation

The top row in Fig. 5.5 depicts the difference in $p(e)$ (at SFE = 5%) between binary pairs with a separation of $r_{\rm pair} \leq 1000\,\rm AU$ (close binaries) and those with $r_{\rm pair} > 1000\,\rm AU$ (wide binaries). We see that wide binaries have a higher fraction of highly eccentric orbits. The mean eccentricities for the close and wide binaries are $\overline{e} = 0.63 \pm 0.02$ and $\overline{e} = 0.73 \pm 0.02$, respectively. It is clear from the fits that the distribution is in the subthermal to thermal range for close binaries ($\alpha \sim 0.8$) and superthermal ($\alpha \sim 1.8$) for wide binaries, which is consistent with the observational findings by Tokovinin (2020) and Hwang et al. (2022a). The p-value derived from the K-S test on the distributions is 0.013, which means that the distributions are most probably different. Xu et al. (2023) propose that the superthermal nature of wide binaries is an outcome of star formation in the turbulent interstellar medium, where the scaling relations between the velocity differences and the initial separation of stars is regulated by turbulence. Their analytical derivation for $p(e)$ (see Eq. 12 in Xu et al. 2023) agrees comparatively well with our e distribution for wide binaries (see top-right and bottom-right panels in Fig. 5.5).

The bottom row presents the e distribution when the distinction is based not on the separation but on the semi-major axis a. The p-value obtained from the K-S test is 10^{-3}, which means that we can reject the hypothesis that the distributions are derived from the same underlying distribution. We see that the trend is similar to that in the top row with $\overline{e} = 0.61 \pm 0.02$ and $\alpha \sim 0.6$ for pairs with $a \leq 1000\,\rm AU$ and $\overline{e} = 0.74 \pm 0.02$ and $\alpha \sim 1.9$ for binaries with $a > 1000\,\rm AU$. It is possible that in a highly eccentric binary that has a large semi-major axis, the secondary (lower-mass star) may be close to the periastron (closest point) when the separation is measured and hence the separation between the components may be small at that instant of time, i.e., large a but small $r_{\rm pair}$. However, since the velocity is low close to the apastron (furthest point) and high close to the periastron, at any time instance, it

Table 5.1: Summary of eccentricity distribution results for different cases.

Driving (1)	SFE (2)	Range of $r_{\rm pair}$ (3)	Range of $M_{\rm sys}$ (4)	Range of q (5)	$N_{\rm pairs}$ (6)	$\overline{e}$ (7)	α (8)
COMP	5%	FULL	FULL	FULL	140	0.71 ± 0.02	$1.6^{+0.5}_{-0.4}$
MIX	5%	FULL	FULL	FULL	132	0.61 ± 0.02	$0.6^{+0.2}_{-0.2}$
SOL	5%	FULL	FULL	FULL	117	0.63 ± 0.03	$0.8^{+0.3}_{-0.3}$
ALL	5%	FULL	FULL	FULL	389	0.65 ± 0.01	$1.0^{+0.2}_{-0.2}$
ALL	2%	FULL	FULL	FULL	249	0.63 ± 0.02	$0.8^{+0.2}_{-0.2}$
ALL	3%	FULL	FULL	FULL	316	0.66 ± 0.01	$1.0^{+0.2}_{-0.2}$
ALL	5%	$\leq 1000\,{\rm AU}$	FULL	FULL	304	0.63 ± 0.02	$0.8^{+0.2}_{-0.1}$
ALL	5%	$> 1000\,{\rm AU}$	FULL	FULL	85	0.73 ± 0.02	$1.8^{+0.6}_{-0.4}$
ALL	5%	$1.5 \leq \log(r_{\rm pair}/{\rm AU}) < 2.5$	FULL	FULL	217	0.62 ± 0.02	$0.7^{+0.2}_{-0.2}$
ALL	5%	$2.5 \leq \log(r_{\rm pair}/{\rm AU}) < 3.5$	FULL	FULL	133	0.67 ± 0.02	$1.2^{+0.5}_{-0.3}$
ALL	5%	$3.5 \leq \log(r_{\rm pair}/{\rm AU}) < 4.5$	FULL	FULL	32	0.76 ± 0.03	$2.5^{+1.5}_{-0.7}$
ALL	5%	FULL	$\leq 0.8\,{\rm M}_\odot$	FULL	77	0.70 ± 0.03	$2.4^{+1.3}_{-0.9}$
ALL	5%	FULL	$> 0.8\,{\rm M}_\odot$	FULL	312	0.64 ± 0.01	$0.8^{+0.1}_{-0.1}$
ALL	5%	FULL	FULL	≤ 0.5	203	0.65 ± 0.02	$1.0^{+0.3}_{-0.2}$
ALL	5%	FULL	FULL	> 0.5	186	0.65 ± 0.02	$1.0^{+0.3}_{-0.2}$
ALL	5%	$\leq 500\,{\rm AU}$	FULL	≤ 0.5	117	0.64 ± 0.02	$0.9^{+0.4}_{-0.3}$
ALL	5%	$\leq 500\,{\rm AU}$	FULL	> 0.5	141	0.61 ± 0.02	$0.6^{+0.2}_{-0.2}$
ALL	5%	$> 500\,{\rm AU}$	FULL	≤ 0.5	86	0.67 ± 0.03	$1.1^{+0.3}_{-0.3}$
ALL	5%	$> 500\,{\rm AU}$	FULL	> 0.5	45	0.75 ± 0.03	$2.7^{+1.5}_{-1.0}$

Notes. Column 1: MHD simulation model from which binaries are obtained ('ALL' means data from all simulation models are included, i.e., COMP, MIX, and SOL combined). Column 2: star formation efficiency (SFE) at which the calculations are made. Columns 3–5: selected range of separation ($r_{\rm pair}$), system mass ($M_{\rm sys}$), and mass ratio (q), with 'FULL' denoting the full range. Column 6: number of binaries that satisfy the constraints in Columns 1–5. Columns 7 and 8: mean eccentricity ($\overline{e}$) and power-law exponent (α) in the eccentricity distribution, determined by fitting $p(e) \propto e^{\alpha}$.

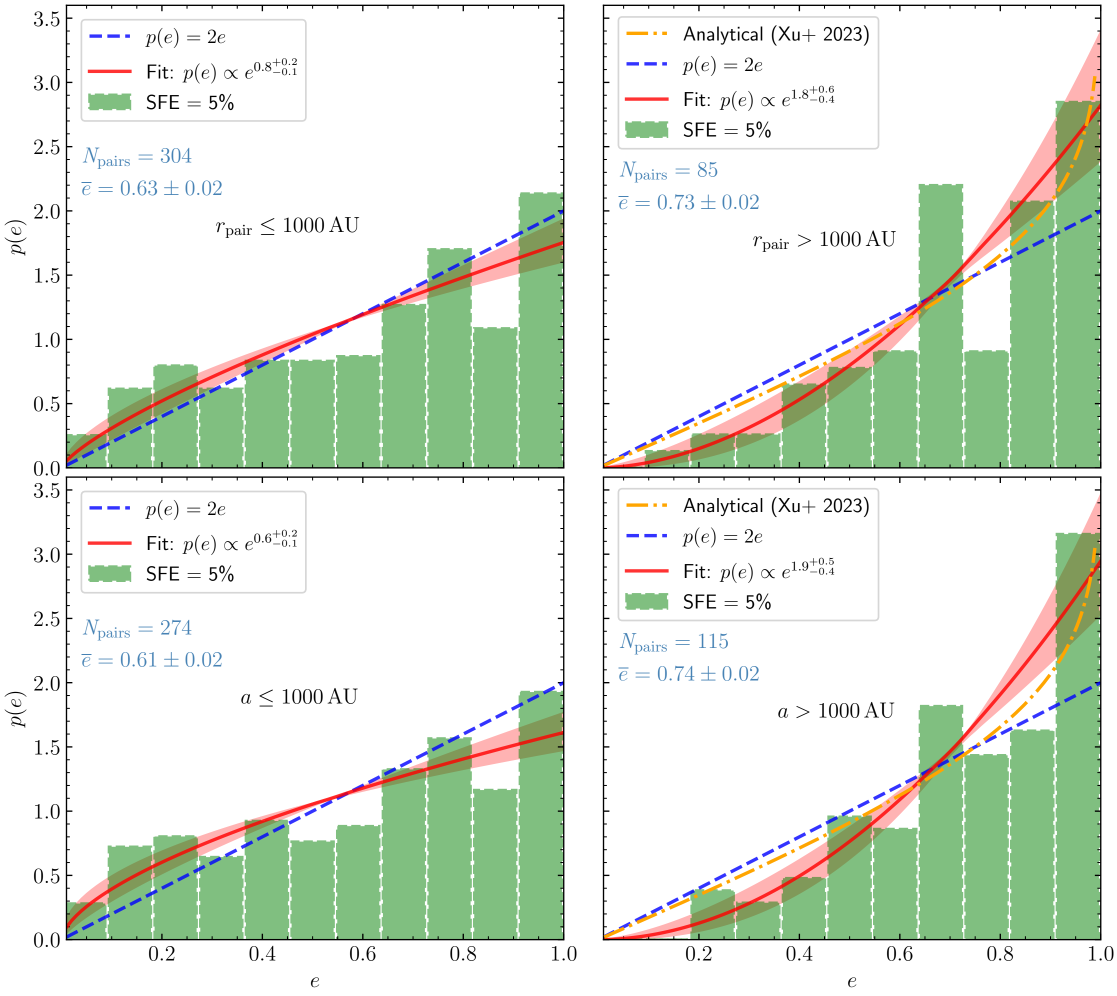

Figure 5.5: Top: The e distribution at SFE = 5% where the separation between the bound pairs is $r_{\rm pair} \leq 1000$ AU (left) and $r_{\rm pair} > 1000$ AU (right). Bottom: The e distribution at SFE = 5% where the semi-major axis of the bound pairs is $a \leq 1000$ AU (left) and $a > 1000$ AU (right). For the small separations, the distribution is sub-thermal, while the distribution is super-thermal for the large separations. This is consistent with observational findings by Tokovinin (2020) and Hwang et al. (2022a). The dash-dotted line represents the analytically derived $p(e)$ for wide binaries by Xu et al. (2023).
]]>

is more probable for the components to be at large separations in the case of wide pairs (large a). Hence the corresponding distributions in the top and bottom rows are statistically similar, i.e., the separation and semi-major axis are analogous when analysing the e distribution (see also Dupuy & Liu 2011; Hwang et al. 2022b).

The mean eccentricity is found to be increasing on increasing the separation range by an order of magnitude with $\bar{e} = 0.62 \pm 0.02$ in the range $1.5 \leq \log(r_{\rm pair}/{\rm AU}) < 2.5$, $\bar{e} = 0.67 \pm 0.02$ in the range $2.5 \leq \log(r_{\rm pair}/{\rm AU}) < 3.5$, and $\bar{e} = 0.76 \pm 0.03$ in the range $3.5 \leq \log(r_{\rm pair}/{\rm AU}) < 4.5$. The distributions also transition from subthermal ($\alpha \sim 0.7$) in $1.5 \leq \log(r_{\rm pair}/{\rm AU}) < 2.5$ to a thermal distribution ($\alpha \sim 1.2$) in $2.5 \leq \log(r_{\rm pair}/{\rm AU}) < 3.5$, and then to a superthermal distribution ($\alpha \sim 2.5$) in $3.5 \leq \log(r_{\rm pair}/{\rm AU}) < 4.5$ (see Tab. 5.1). This shows that the type of distribution can be different even when the separation ranges of interest differ by just an order of magnitude.

Tokovinin (2020) finds that the e distribution at $200 - 1000$ AU separations is nearly thermal and at < 200 AU, the distribution has a clear shortage of highly eccentric pairs. They find that, at $> 10^3$ AU separations, the distribution is slightly superthermal. Hwang et al. (2022a) find that the $p(e)$ is uniform at ~ 100 AU, thermal at $\sim 10^{2.5} - 10^3$ AU and superthermal at $> 10^3$ AU. Our findings are consistent with these observations.

We remind the reader that the actual lower error limits in the mean calculations and α estimates might be even lower. This is because we are probably underestimating the number of low eccentricities due to the inherent numerical limitations (see §5.5). The underestimation is not taken into account while calculating error limits because an extensive resolution study is needed to quantify the extent of underestimation, which would require a separate study altogether. The underestimation becomes particularly significant for close binaries, e.g., in the above discussed binary range $1.5 < \log(r_{\rm pair}/{\rm AU}) < 2.5$.

Fig. 5.6 compares the value of α obtained in the three separation ranges ($1.5 \leq \log(r_{\rm pair}/{\rm AU}) < 2.5$, $2.5 \leq \log(r_{\rm pair}/{\rm AU}) < 3.5$, and $3.5 \leq \log(r_{\rm pair}/{\rm AU}) < 4.5$) with the measurements of α as a function of the binary separation by Hwang et al. (2022a) using the *Gaia* data. The α estimates in the ranges $1.5 \leq \log(r_{\rm pair}/{\rm AU}) < 2.5$ and $2.5 \leq \log(r_{\rm pair}/{\rm AU}) < 3.5$ agree well with the measurements of Hwang et al. (2022a). However, our simulations produce a higher value of α in the range $3.5 \leq \log(r_{\rm pair}/{\rm AU}) < 4.5$ as compared to that for the wide binaries with separations of $> 10^{3.5}$ AU in Hwang et al. (2022a). The excess of highly eccentric orbits is most likely because the stars in our simulations represent a very young cluster as compared to the ones probed by the *Gaia* observations. The value of α for the wide binaries

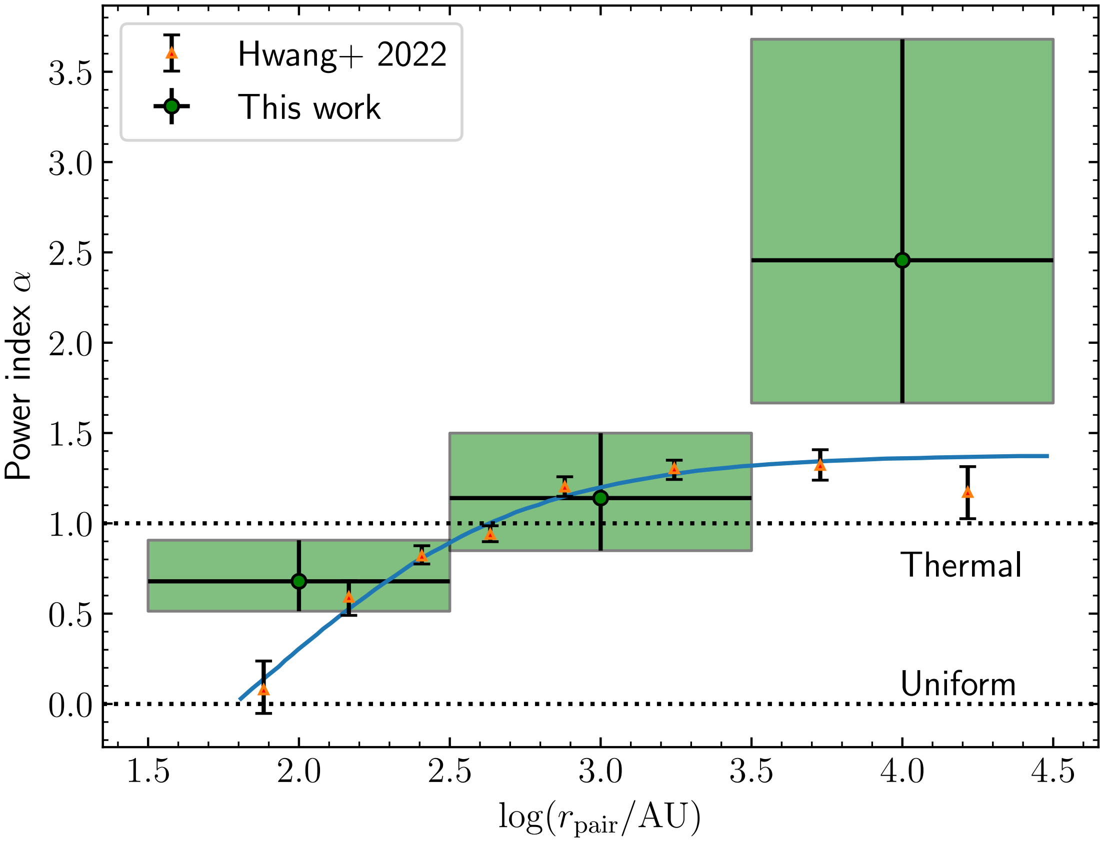

Figure 5.6: The power-law index α of the e distribution at SFE = 5% as a function of the separation. The circular markers within the rectangular boxes represent the 50th percentile estimate of α in our simulations in the separation range denoted by the width of the boxes. The height of the boxes represents the 16th to 84th percentile range of α. The triangular markers correspond to the α values measured in Hwang et al. (2022a) at different binary separations, and the solid curve represents the fit to their data points.

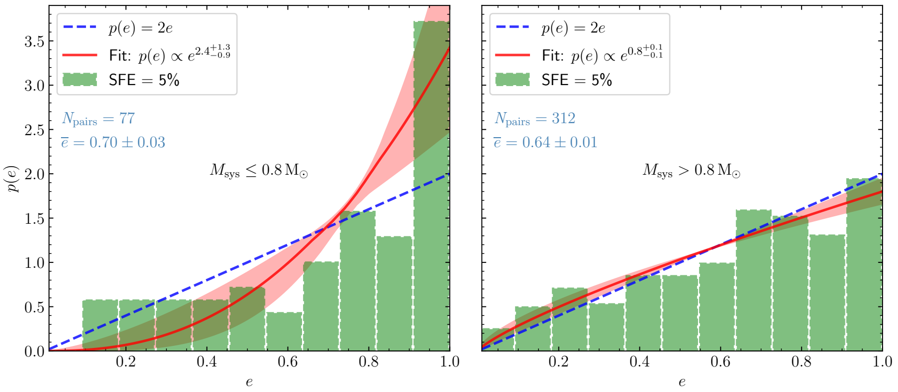

Figure 5.7: The e distribution at SFE $= 5\%$ for binaries with system masses $M_{\mathrm{sys}} \leq 0.8\,\mathrm{M}_{\odot}$, i.e., binaries with mainly M-dwarfs and later type stars (left) and $M_{\mathrm{sys}} > 0.8\,\mathrm{M}_{\odot}$, i.e., binaries with mainly solar and earlier type stars (right). The low-mass systems ($M_{\mathrm{sys}} \leq 0.8\,\mathrm{M}_{\odot}$) have highly superthermal e distribution while the relatively higher-mass systems have subthermal/thermal distribution.

is likely to be reduced with further evolution in the Galactic field as a result of physical processes like dynamical scatterings between binaries and passing stars and molecular clouds (Modak & Hamilton 2023; Hamilton & Modak 2023).

5.3.3 Dependence on the binary mass and mass ratio

Fig. 5.7 shows $p(e)$ for low-mass binary systems ($M_{\mathrm{sys}} \leq 0.8\,\mathrm{M}_{\odot}$, left panel) and high-mass systems ($M_{\mathrm{sys}} > 0.8\,\mathrm{M}_{\odot}$, right panel), where $M_{\mathrm{sys}} = M_1 + M_2$. A large fraction of the low-mass binaries have highly eccentric orbits ($e > 0.9$) with $\bar{e} = 0.70 \pm 0.03$. The p-value obtained from the K-S test on the distributions is 0.022, and therefore we can say that the two distributions are different with 98% confidence. Further, the low-mass systems have a highly superthermal distribution ($\alpha \sim 2.4$) while the distribution for the high-mass systems is almost thermal ($\alpha \sim 0.8$, $\bar{e} = 0.64 \pm 0.01$), i.e., $p(e)$ is dependent on the total mass of the binary. This suggests that the form of the e distribution obtained in observations would vary depending on the mass range of binaries selected in the survey (see also Dupuy & Liu 2011).

We compared $p(e)$ for binaries with a mass ratio ($q = M_2/M_1$, where $M_2 < M_1$) of $q \leq 0.5$ and those with $q > 0.5$ and find that the distributions for both groups are similar (p-value $= 0.96$) and represent thermal distributions, suggesting that the form of the e distribution is generally independent of the q value (see Tab. 5.1). However, when looked at on different separation scales, the q value does seem to influence $p(e)$. The top row in Fig. 5.8 compares the $p(e)$ for binaries with $q \leq 0.5$ (left panel) and $q > 0.5$ (right panel) in the separation range $r_{\mathrm{pair}} \leq 500\,\mathrm{AU}$. The distribution is thermal ($\alpha \sim 0.9$, $\bar{e} = 0.64 \pm 0.02$) in the former and subthermal

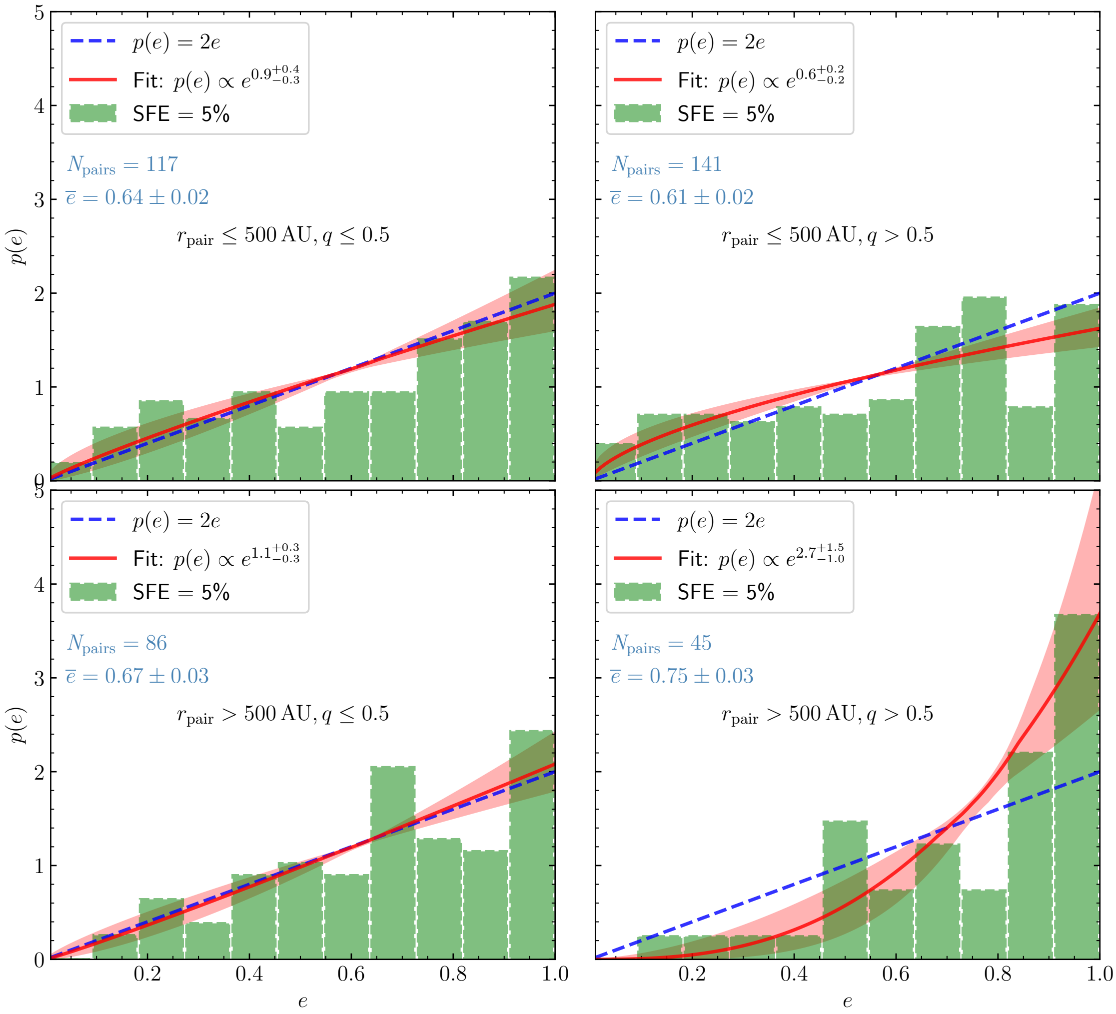

Figure 5.8: Top: The e distribution at SFE = 5% for binary systems with $r_{\rm pair} \leq 500$ AU and q value given by $q \leq 0.5$ (left) and $q > 0.5$ (right). Bottom: The e distribution at SFE = 5% for binaries with $r_{\rm pair} > 500$ AU and q value given by $q \leq 0.5$ (left) and $q > 0.5$ (right).

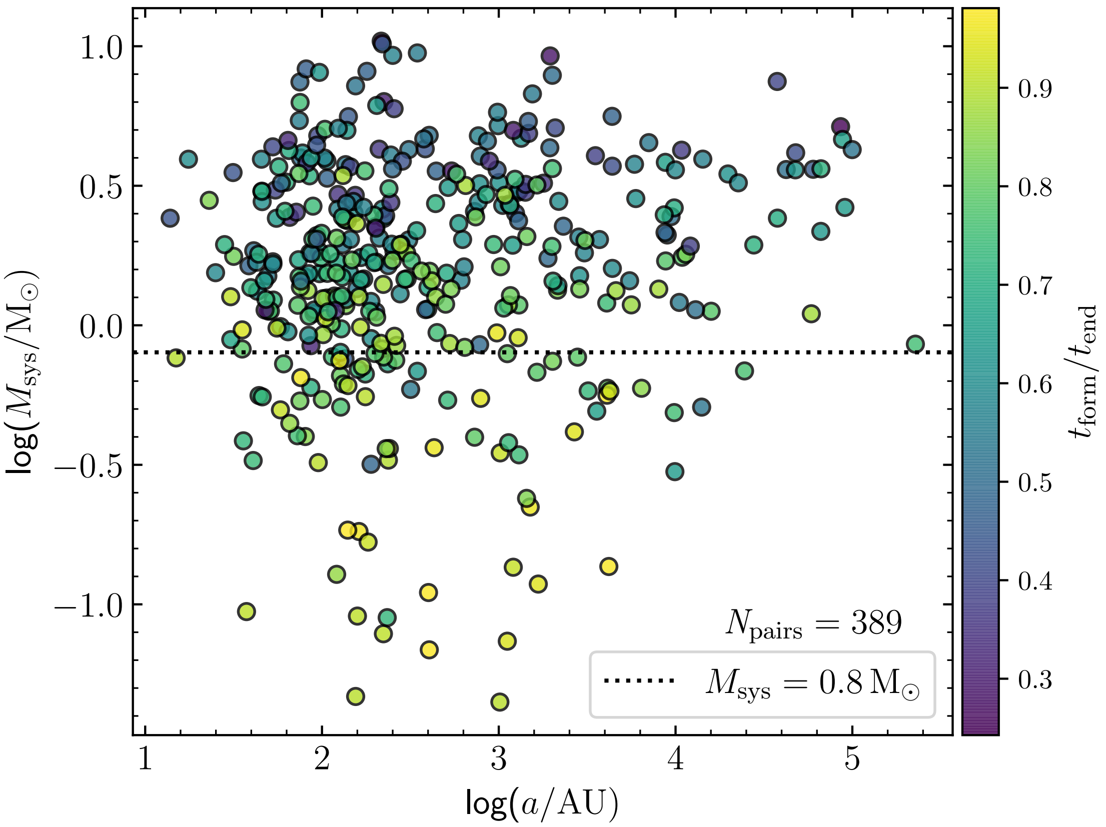

Figure 5.9: System mass ($M_{\rm sys}$) vs. semi-major axis (a) at SFE = 5%. The dashed line represents $M_{\rm sys} = 0.8\,{\rm M}_\odot$. The marker colour is scaled to the time of formation of the binary ($t_{\rm form}$) in units of the simulation end time ($t_{\rm end}$).

in the latter ($\alpha \sim 0.6$, $\bar{e} = 0.61 \pm 0.02$). However, a K-S test returns a p-value of 0.39, which means it is possible that the distributions are similar. The opposite trend can be seen in the bottom panel, where the same comparison is made, but for binaries with $r_{\rm pair} > 500\,{\rm AU}$. For $q \leq 0.5$ (left panel), we have a thermal distribution ($\alpha \sim 1.1$, $\bar{e} = 0.67 \pm 0.03$), while for $q > 0.5$ (right panel), the distribution is highly superthermal ($\alpha \sim 2.7$, $\bar{e} = 0.75 \pm 0.03$). The p-value obtained from the K-S test is 0.097, i.e., we can say with 90% confidence that the distributions are different. The features seen in Fig. 5.8 suggest again that the properties related to the eccentricity distribution are dependent on the separation range. The superthermal distribution obtained for the wide binaries with high mass ratios agrees with the observational finding in Hwang et al. (2022b).

Fig. 5.9 shows a scatter plot of the system mass $M_{\rm sys}$ as a function of the semi-major axis, a. The markers are colour-coded based on the time of formation (in units of the total simulation time) of the primary star in the pair. It is clear that the pairs with high system masses form in the early stages of cluster formation. These pairs also fall under a wide range of semi-major axis values ranging from around 10 AU to a few 10^5 AU. The low-mass systems on the other hand form towards the last stages of the cluster formation and they lie mostly in the $100 - 1000$ AU range. This, along with the finding that low-mass systems have an e distribution that is different to that of high-mass systems (see Fig. 5.7), suggests that different mechanisms may be responsible for binary formation on different mass scales, which is discussed next.

5.4 Discussion

5.4.1 Eccentricity distribution and binary formation mechanism

In the following, we discuss several binary formation mechanisms, ranging from large-scale (cloud) to small-scale (disc) fragmentation.

Fragmentation on cloud scales (fragmentation by turbulence-induced density fluctuations)

Star formation is typically initiated by the turbulent shocks prevalent in molecular clouds. These shocks induce overdensities in the gas cloud, which, when they become gravitationally unstable, lead to the birth of stars (Robertson & Goldreich 2018; Mocz & Burkhart 2018). When a pair of stars (originating from two individually collapsing overdensities) are gravitationally bound at birth, they form as a binary. Due to the log-normal distribution of gas density in turbulent environments (e.g., Vazquez-Semadeni 1994; Padoan et al. 1997a; Kowal et al. 2007; Kritsuk et al. 2007; Federrath et al. 2008; Federrath 2013a; Hopkins 2013b; Federrath & Banerjee 2015; Kuffmeier et al. 2019; Seta & Federrath 2022), these overdensities vary significantly in size and mass. This variation gives rise to diverse stellar formations, including binary systems with different separations and system masses. Since the overdensities are produced by supersonic turbulent shocks, the binaries formed by pairing-up of individually collapsing overdensities will generally have separations comparable to the supersonic and transonic scales, i.e., $\gtrsim 0.1$ pc (Federrath et al. 2021).

Different mechanisms for the formation of wide binaries have been proposed in the literature (e.g., Kouwenhoven et al. 2010; Moeckel & Clarke 2011; Reipurth & Mikkola 2012; Peñarrubia et al. 2016; Tokovinin 2017; Livernois et al. 2023; Rozner & Perets 2023; Rozner et al. 2023). Xu et al. (2023) clearly addressed the role of turbulence and analytically derived that wide binaries ($\sim 0.01 - 1$ pc) formed from turbulence-induced density fluctuations have superthermal e distributions by considering that the initial velocity difference and separation of the binary components follow the turbulent gas velocity scaling. The superthermal $p(e)$ obtained for the high r_{pair} binaries in our simulations confirms their theoretical prediction (see Fig. 5.5). We also find that the form of the e distribution obtained for the simulations that employ purely compressive turbulence driving is different from that of the simulations with purely solenoidal driving or a natural mixture of turbulence driving modes. This indicates that the turbulent properties of the parent cloud play a critical role in the binary eccentricity statistics.

Fragmentation on core scales (fragmentation induced by turbulence, rotation, gravity, and outflows)

As the formation of the star cluster proceeds, some of the overdensities fragment further (analogous to core fragmentation) due to the interplay between the inherent turbulence, rotation, and gravity (e.g., Larson 1972; Inutsuka & Miyama 1992; Padoan & Nordlund 2002; Hennebelle & Chabrier 2008, 2009; Offner et al. 2010; Hopkins 2012; Bate 2012; Guszejnov & Hopkins 2015; Offner et al. 2023). In addition, protostellar outflow feedback promotes fragmentation by driving core-scale turbulence (Federrath et al. 2014; Mathew & Federrath 2021; Guszejnov et al. 2021; Hu et al. 2022). The fragmentation on core scales would produce binaries with separations in the range of $\sim 10^3$ AU to 0.1 pc (Offner et al. 2023). On smaller scales, the turbulence transitions from transonic to subsonic (Federrath et al. 2021), where gravity, thermal effects, magnetic fields, and rotation begin to dominate over turbulence. The formation of systems with very low masses and with close separations ($\lesssim 500$ AU) at the time of their formation by turbulent fragmentation is relatively uncommon, as it is difficult to generate sufficiently strong overdensities through turbulent shocks on core scales, as those scales are intrinsically trans- to subsonic, at best very midly supersonic (Elmegreen & Elmegreen 1978; Lubow & Pringle 1993; Clarke 1999; Bonnell et al. 2008; Offner et al. 2023).

The low-mass systems formed in the present simulations, which represent a relatively small population, have highly superthermal e distributions (see Fig. 5.7). These systems are found to have formed during the late stages of the cluster formation and have separations predominantly in the range $100 - 1000$ AU (see Fig. 5.9). These characteristics are unlike those of higher-mass systems, which form relatively early (likely via turbulence-induced density fluctuations in shocks; see above), and span wider separations of up to a few 10^5 AU (see Fig. 5.9). The variation in the characteristics of $p(e)$ can be explained by the significant changes in the environment in which the binaries form, at early vs. late stages or on large vs. small scales. As stars continue to form in the shocked regions of gas, the local density increases and the local virial parameter decreases (more unstable gas) in cluster-forming regions due to the concentration of gas there. At late stages, the increase in the density and the increased influence of gravity allow the small collapsing overdensities to develop substructures with low Jeans length and low Jeans mass (Bonnell et al. 2008). The binaries that form by the gravitational fragmentation in these collapsing overdensities typically posses lower system masses and shorter separations compared to their counterparts that formed earlier through turbulent fragmentation. Numerical works (Bonnell et al. 2008; Mathew & Federrath 2021), including the simulations presented here (see Fig. 10 in Mathew & Federrath 2021), have shown the existence of a negative correlation between the velocity at the time of formation and the final stellar mass, i.e., the low-mass (late-forming) stars have relatively high velocities as compared to the high-mass (early-forming) stars. This agrees with the argument that the low-mass stars that form in the late stages fragment out of the infalling gas (Bonnell et al. 2008). Such a negative correlation was also obtained in the recent observations of Wei et al. (2023) (see Fig. 10 & 11 in Wei et al. 2023). The superthermal nature of the binaries formed from gravitational fragmentation is possibly due to the preferential stretching of the binary orbit by the gravitational pull in the direction of the nearby sub-cluster. However, a detailed study would be required to test this scenario.

Fragmentation on disc scales

Fragmentation in extended discs (Bate et al. 2002a; Goodwin & Whitworth 2007; Stamatellos et al. 2007, 2011; Rogers & Wadsley 2012; Thies et al. 2015) is likely to happen in our simulations. However, disc fragmentation on typical scales of $\lesssim 200\,\mathrm{AU}$ (see reviews by Kratter & Lodato 2016; Lee et al. 2020, and the references therein) does not occur here, as these scales are not sufficiently resolved in our simulations (see §5.5). We expect disc fragmentation (e.g., Adams et al. 1989; Shu et al. 1990; Bonnell & Bate 1994; Stamatellos & Whitworth 2009; Stamatellos et al. 2011; Kratter & Lodato 2016) to be an important binary formation mechanism (see also Hennebelle et al. 2019) on these scales, favouring a uniform e distribution (Raghavan et al. 2010; Duchêne & Kraus 2013; Moe & Di Stefano 2017; Hwang et al. 2022a; Ceppi et al. 2024), where very close binaries become circularised due to tidal effects. Thus, with higher numerical resolution, the α value in the short separation ranges is expected to be somewhat lower than suggested based on our current simulation results. However, since these simulations incorporate a large array of physical mechanisms and we carry out multiple such simulations to produce statistically significant data, achieving higher resolutions is not feasible at the moment, due to the associated computational cost, but remains a high priority for future work.

Dynamical interactions and gas friction/gas accretion

Stars generally form in highly clustered environments (Lada & Lada 2003), and therefore dynamical interactions are a natural outcome of the star formation process. A considerable number of binaries undergo dynamical decay due to interactions with the gas or with other systems and migrate to closer separations in ~ 100 kyr (Reipurth & Clarke 2001; Bate et al. 2002b; Goodwin & Kroupa 2005; Offner et al. 2016; Lee et al. 2019). This explains why our simulations have a significant number of binaries with separations in the range $\sim 10-200\,\mathrm{AU}$, even though fragmentation on these scales is not resolved in our simulations. A recent study by Kuruwita & Haugbølle (2023) finds that core fragmentation and dynamical capture can produce a considerable number of low-mass close binaries (with disc-scale separations) via efficient in-spiral. During the migration, the eccentricity can change to a different value due to the dynamic nature of the orbital decay. For instance, the hydrodynamic drag forces cause eccentric orbits to become more circular (Szölgyén et al. 2022). Similarly, initially close binaries can be widened due to interactions with other multiple systems and some of the initially wide binaries can even become unbound, since they are generally more weakly bound than close binaries.

5.4.2 Future prospects

An initial thermal eccentricity distribution (Jeans 1919) is frequently adopted in theoretical and numerical modelling of binary populations and star clusters (Kroupa 1995; Dabringhausen et al. 2021). However, adhering to a purely thermal eccentricity distribution can lead to inaccuracies in predicting the evolution of binary populations and their merger rates (Geller et al. 2019). Our study provides physically justified and numerically tested initial eccentricity distributions of wide binaries for future studies. These distributions account for the complexities and variations introduced by different MHD turbulence properties in the surrounding medium. The superthermal eccentricity distribution of wide outer binaries in triple stellar systems also has important implications for the formation channel of black hole binary mergers (Su et al. 2024). Su et al. (2024) find that the outer eccentricity distribution can remain significantly superthermal for modestly hierarchical black hole triples.

The turbulence in our current simulations is weakly magnetized with $\mathcal{M}_\mathrm{A} \approx 3$. Observations suggest variations of $\mathcal{M}_\mathrm{A}$ values in different molecular clouds (Hu et al. 2019). Earlier studies show that strong magnetic fields can play an important role in the formation of binaries, especially for the formation of massive close binaries (e.g., Lund & Bonnell 2018; Harada et al. 2021). We will investigate the effect of magnetic fields on shaping the eccentricity distributions of binaries in our future work.

5.5 Limitations

5.5.1 Numerical resolution

Due to the limitations in the numerical grid resolution, the accretion discs are not fully resolved in our simulations. Further, to prevent artificial fragmentation due to resolution limitations, the sink particle formation criteria (Federrath et al. 2010c) in our simulations does not allow the formation of a new sink particle within the accretion radius of an existing one (250 AU). Hence, the presence of close binaries ($\lesssim 200\,\mathrm{AU}$) in our simulations cannot be directly linked to fragmentation on those scales, e.g., disc fragmentation. These binaries are the ones that formed at relatively large separations initially and then decayed to small separations (Reipurth & Clarke 2001; Bate et al. 2002b; Goodwin & Kroupa 2005; Offner et al. 2010).

The resulting effect of the resolution limitation is that, although stars can form in extended discs in our simulations (Bate et al. 2002a; Goodwin & Whitworth 2007; Stamatellos et al. 2007, 2011; Rogers & Wadsley 2012; Thies et al. 2015), binary formation due to fragmentation on typical disc scales ($\sim 100\,\mathrm{AU}$), particularly the formation of spectroscopic binaries (period of a few days), is underestimated. Spectroscopic binaries are found to have eccentricities close to zero (Abt 2006) as a result of the tidal circularisation (Zahn 1977; Tassoul & Tassoul 1992). Hence the fraction of pairs with low eccentricities is underestimated in our simulations.

5.5.2 Gravitational softening

When the separation between two star particles becomes very small, the gravitational acceleration becomes exceptionally high. As the distance approaches zero, the acceleration will go to infinity and the simulation timestep will tend to zero, which will stall the simulation. To overcome such a problem and also because the sink particle accretion radius is limited to the gas resolution, gravitational softening is introduced for distances shorter than a given softening radius (here equal to the sink particle accretion radius of 250 AU). We utilise the version of spline softening (Price & Monaghan 2007) used in Federrath et al. (2010c) to soften the gravitational interaction. The interaction is unaffected at distances greater than the softening radius, while at shorter distances, the acceleration smoothly approaches zero. Such a softening scheme may result in some of the orbits having artificial eccentricities if the binary spends time at separations shorter than the softening radius. The underestimation in the acceleration will be around a factor of 2 at a distance of half of the softening radius (see Fig. 1 in Federrath et al. 2010c).

The limitations in numerical resolution and the application of gravitational softening imply that the actual values of α are affected. However, the main objective of this study is to understand the relative change in α, for example, when considering binaries in different separation and mass ranges. Therefore, at least the relative inferences from this paper still hold.

5.6 Conclusions

We use the star cluster formation simulations of Mathew & Federrath (2021) and Mathew et al. (2023) to investigate binary statistics, particularly the eccentricity distribution and its dependence on the binary separation, mass, and mass ratio. The simulations employ gravity, turbulence, magnetic fields, and protostellar feedback in the form of radiative heating and jets/outflows, and therefore include most of the main relevant physical ingredients for star and binary formation. The dataset comprises a total of 28 simulations, which together produce 1362 stars, of which 389 are binaries, allowing us to make statistically conclusive remarks. We find that

(1) the eccentricity distribution $p(e)$ is dependent on the mode of turbulence driving (see Fig. 5.2). The simulations with purely compressive driving produce e distributions with the form $p(e) \propto e^{\alpha}$ with $\alpha > 1$, while simulations with purely solenoidal and a natural mixture of driving modes have $\alpha < 1$. Kolmogorov–Smirnov tests performed on the three simulation sets suggest that (with $\gtrsim 90\%$ confidence), the e distribution obtained from the purely compressive driving simulations is different from that of simulations with purely solenoidal or a natural mixture of driving modes. This suggests that the turbulent properties of the cloud could play a significant role in shaping the e distribution. We conclude that this is because the turbulence regulates the cloud dynamics including the density and velocity statistics of the gas from which the binaries emerge, and therefore influences their orbital parameters as well.

(2) $p(e)$ is thermal ($\alpha \sim 1$) when data from all the simulations are compiled together (see Fig. 5.3). Recent observational surveys also find that the e distribution is thermal for broad separation ranges comparable to that in our simulations ($10-10^5$ AU).

It is likely that these surveys include binary stars that formed in different turbulent conditions and environments, including different turbulence driving modes. It is also worth noting that the binary systems included in the surveys generally have undergone significant dynamical evolution in comparison to the young systems in our simulations, which tends to drive the eccentricity distribution towards thermal (e.g., Hamilton & Modak 2023).

(3) $p(e)$ is similar with $\alpha \sim 1$ at different points in time in our simulations where the cluster formation process is followed up to around 1 Myr (see Tab. 5.1). This shows that the overall form of the e distribution is imprinted in the early stages of the formation process, and small-scale dynamical interactions (within a cluster) do not significantly influence the α value.

(4) $p(e)$ is dependent on the binary separation or the semi-major axis, where wide binaries ($r_{\mathrm{pair}} > 1000\,\mathrm{AU}$ or $a > 1000\,\mathrm{AU}$) have superthermal distributions with $\alpha \sim 2$ as compared to binaries with $r_{\mathrm{pair}} \leq 1000\,\mathrm{AU}$ or $a \leq 1000\,\mathrm{AU}$, which have subthermal distributions with $\alpha < 1$ (see Fig. 5.5). K-S tests suggest that the hypothesis that the two distributions are the same can be ruled out. The value of α transitions from subthermal to thermal, to superthermal, with increasing binary separation (see Tab. 5.1), which concurs with the recent observational findings of e.g., Tokovinin (2020), Hwang et al. (2022a) from *Gaia* (see Fig. 5.6). We also find that the birth eccentricity distribution of wide binaries is more superthermal than the observed one in the Galactic field.

(5) $p(e)$ also depends on the system mass of the binary with low-mass systems ($M_{\mathrm{sys}} \leq 0.8\,M_{\odot}$) producing highly superthermal distributions ($\alpha \sim 2.4$), and higher-mass systems ($M_{\mathrm{sys}} > 0.8\,M_{\odot}$) producing subthermal to thermal e distributions ($\alpha \sim 0.8$) (see Fig. 5.7). Based on a K-S test, we can say with 98% confidence that the two distributions are different.

(6) $p(e)$ is independent of the binary mass ratio (q) when looked at in the whole separation range (see Tab. 5.1). However, for relatively close binaries (here $r_{\mathrm{pair}} \leq 500\,\mathrm{AU}$), the distribution is thermal ($\alpha \sim 0.9$) when $q \leq 0.5$ and subthermal ($\alpha \sim 0.6$) when $q > 0.5$ (see Fig. 5.8). However, a K-S test suggests that there is a 40% chance that the two distributions are similar. In the separation range $r_{\mathrm{pair}} > 500\,\mathrm{AU}$, the distribution is thermal ($\alpha \sim 1.1$) when $q \leq 0.5$ and highly superthermal ($\alpha \sim 2.7$) when $q > 0.5$, i.e., an opposite trend in the change of α as compared to that for close binaries ($r_{\mathrm{pair}} \leq 500\,\mathrm{AU}$). We find that the above distributions are different with 90% confidence based on a K-S test. Our finding is consistent with the observational finding on the highly superthermal eccentricity distribution of equal-mass wide binaries (Hwang et al. 2022b).

Our study suggests that the often adopted thermal eccentricity distribution (Jeans 1919) may not always be valid or appropriate, and properties of the cloud in which stars are formed have a direct influence on the form of the eccentricity distribution (see Tab. 5.1). The dependence of the eccentricity distribution on the binary separation and mass indicates that different mechanisms are responsible for binary formation on different scales (see also Bate 2009a, 2012, 2014, 2019; Guszejnov et al. 2023). Our results suggest that wide binaries ($r_{\rm pair} \gtrsim 1000\,$AU) predominantly result from turbulence-induced density fluctuations (Xu et al. 2023) and turbulent fragmentation in cores (Padoan & Nordlund 2002; Krumholz & McKee 2005; Hennebelle & Chabrier 2008, 2009; Offner et al. 2010; Hopkins 2012; Bate 2012; Guszejnov & Hopkins 2015; Kuffmeier et al. 2019; Offner et al. 2023). Our findings are consistent with the theoretical predictions of Xu et al. (2023) that the superthermal nature of the eccentricity distribution of wide binaries is an outcome of the turbulent characteristics of the cloud in which they are born. In the intermediate separation range ($100 < r_{\rm pair}\,({\rm AU}) < 1000$), turbulent fragmentation, gravitational fragmentation (Bonnell et al. (2008); see also Lee & Hennebelle (2018a)) and fragmentation in extended discs (Bate et al. 2002a; Goodwin & Whitworth 2007; Stamatellos et al. 2007, 2011; Rogers & Wadsley 2012; Thies et al. 2015) may have a greater influence on the eccentricity distribution.

It is to be noted that, due to the highly dynamic nature of the star formation process, close binaries can form from initially wider binaries. The decrease of their separations can be caused by e.g., gas dynamical friction (Ostriker 1999; Lee et al. 2019; Rozner et al. 2023; Rozner & Perets 2024b), gas accretion (Bate 2000), and dynamical interactions in unstable multiple systems (Reipurth & Clarke 2001; Bate et al. 2002b; Goodwin & Kroupa 2005; Offner et al. 2010). Similarly, dynamical interactions can also widen the binary orbit (Hwang et al. 2022b). On scales less than a few hundred AU, disc fragmentation (e.g., Adams et al. 1989; Shu et al. 1990; Bonnell & Bate 1994; Stamatellos & Whitworth 2009; Stamatellos et al. 2011; Kratter & Lodato 2016) may be a dominant mechanism leading to a uniform eccentricity distribution (Raghavan et al. 2010; Duchêne & Kraus 2013; Moe & Di Stefano 2017; Hwang et al. 2022a; Ceppi et al. 2024). However, disc fragmentation is not resolved in our simulations and hence on those scales, only binaries that formed from turbulent fragmentation, which then dynamically decay to short separations exist.

We conclude that the properties of binaries, in particular their eccentricity, separation, total mass, and mass ratio, depend on the turbulence properties of the parent cloud from which they form. The statistical studies of binaries in young clusters provide valuable constraints on binary formation mechanisms and physically justified initial conditions for binary population synthesis.

Acknowledgements

We thank the anonymous referees for their valuable remarks which improved the quality of the paper. C.F. acknowledges funding provided by the Australian Research Council (Future Fellowship FT180100495), and the Australia-Germany Joint Research Cooperation Scheme (UA-DAAD). We further acknowledge high-performance computing resources provided by the Leibniz Rechenzentrum and the Gauss Centre for Supercomputing (grants pr32lo, pr48pi and GCS Large-scale project 10391), the Australian National Computational Infrastructure (grant ek9) and the Pawsey Supercomputing Centre (project pawsey0810) in the framework of the National Computational Merit Allocation Scheme and the ANU Merit Allocation Scheme. The simulation software, `FLASH`, was in part developed by the Flash Centre for Computational Science at the University of Chicago and the Department of Physics and Astronomy at the University of Rochester. S.X. acknowledges support from grant NSF PHY-2309135 to the Kavli Institute for Theoretical Physics (KITP), the Aspen Center for Physics, which is supported by National Science Foundation grant PHY-2210452, Durand fund, a grant from the Simons Foundation (1161654, Troyer), and NASA ATP award 80NSSC24K0896. S.X. also acknowledges the inspiring discussion with the participants of the program on "Turbulence in Astrophysical Environments" at KITP. This work makes use of the yt-project (Turk et al. 2011) and colormaps in the CMasher package (van der Velden 2020).

Chapter 6

Conclusions

6.1 Summary

Understanding star formation is one of the fundamental frontiers in astrophysics. A core topic of study in star formation research is the origin of stellar masses or the initial mass function. Obtaining a complete picture of the IMF is critical since it dictates how the star cluster evolves and interacts with the surrounding environment. In this thesis, we conducted an extensive analysis of the origin of the IMF through magnetohydrodynamical simulations of star cluster formation with an AMR grid framework. The simulations incorporate gravity, magnetic fields, turbulence, protostellar outflows and radiative heating, representing the central ingredients of star formation. Our work shows that the turbulent properties of the cloud, the stellar processes (feedback), and dynamics (ejection of stars) are all important in the star cluster formation process and for determining the IMF. The summary of this thesis is as follows:

6.1.1 Effect of jets and outflows

Young stars lose a considerable amount of accreting mass through jets/outflows and the mechanical feedback excites turbulent motions within the cloud by sweeping around the gas surrounding the progenitor star. The outflow feedback plays a vital role in self-regulating star formation (Li & Nakamura 2006; Wang et al. 2010; Federrath et al. 2014; Frank et al. 2014; Offner & Chaban 2017; Mathew & Federrath 2021; Guszejnov et al. 2021; Lebreuilly et al. 2024). We incorporated jets and outflows into star cluster formation simulations and investigated how they affect the dynamical properties such as the SFR and IMF. In this work, we also carried out a comprehensive comparison of our simulations with observations and theory, not only in terms of the IMF, but also related to multiplicity properties and angular momentum of stars. This work is published in peer-reviewed journal (Mathew & Federrath 2021). The main results associated with this study are:

- Protostellar jets and outflows influence the cloud dynamics significantly through the momentum injection and lowers the star formation rate by a factor of ~ 2. The reduction in SFR is due to the mass loss associated with the ejection of the accreting material and the interruption of the gas inflow to the protostars.

- The outflow feedback is pivotal in setting the characteristic mass scale of the IMF by regulating the fragmentation of the cloud and bringing the peak mass in line with the observed range. The inclusion of jets and outflows in the star cluster formation simulations increases fragmentation and shifts the IMF to lower masses by a factor of ~ 2, without altering the overall form of the IMF.

- The theoretical models of the IMF based on gravo-turbulent fragmentation reproduce the shape of our simulation IMF reasonably well, although they underestimate the number of the very-low mass stars in our simulations. This is because the models do not take into account the stellar dynamics. Stellar interactions resulting in dynamical ejections play a crucial role in determining the shape of the IMF.

6.1.2 Influence of the turbulence driving mode

Turbulence in the ISM is a varying mixture of compressive and solenoidal driving modes. Numerical works (e.g., Federrath & Klessen 2012) find that the SFR associated with a purely compressive turbulence driving (curl-free) is higher by an order of magnitude than that for a purely solenoidal driving (divergence-free). Given that high-SFR galaxies have IMF slopes shallower than that for low-SFR galaxies (Gunawardhana et al. 2011) and the turbulence driving mode is one of the most prominent contributors to SFR variations among clouds (Federrath & Klessen 2012), a relationship between the IMF shape and the turbulence driving mode is highly likely. We carried out simulations that employ a purely compressive turbulence driving and compared them with simulations that employ a purely solenoidal driving. Through this comparison, we revealed that the mode of turbulence plays a key role in shaping the IMF. This work is published in peer-reviewed journal (Mathew et al. 2023). The main conclusions and discussion points are:

- A purely compressive driving results in a higher fraction of low-mass stars as compared to a purely solenoidal driving. This is consistent with the predictions of the gravo-turbulent models (Padoan & Nordlund 2002; Hennebelle & Chabrier 2008; Hopkins 2012).

- The IMF peak in the solenoidally driven case is higher by a factor of ~ 1.5.

While this shows that the IMF is sensitive to the mode of turbulence driving, such a variation may not be detected by observations due to the current limitations in restricting the measurements to narrow error margins.

- The top-heavy nature (higher-fraction of high-mass stars as compared to standard IMF models) of the IMFs in the central molecular zone (CMZ) can be partly accounted for by the dominance of solenoidal driving measured in these environments.

6.1.3 Impact of the cloud virial parameter

The cloud virial parameter α_{vir}, which is twice the ratio of turbulent kinetic to gravitational energy, can provide important insights into the interplay between gravity and turbulence. We performed a suite of star cluster formation simulations with three different values of α_{vir}. Our work finds that the IMF exhibits a crucial dependence on the cloud virial parameter. Since cloud-to-cloud variations in the virial parameter can be more than an order of magnitude, our study reaffirms that the notion of a true universal IMF is not an accurate representation. This work is published in peer-reviewed journal (Mathew et al. 2025). The main results are:

- In lower virial parameter conditions, gravity is more efficient in enhancing the formation of sheet-like and filamentary structures that eventually become unstable, leading to more fragmentation.
- Both SFR and IMF exhibit a weak dependence on the cloud virial parameter, where a shift in α_{vir} from 0.5 to $\lesssim 0.1$ increases the SFR by a factor of ~ 2, and lowers the IMF peak by a similar factor.
- The dependence of SFR and IMF on α_{vir} is non-linear, implying that a wide range of α_{vir} has to be explored to arrive at a holistic view of the impact of the cloud virial parameter.

6.1.4 Binary properties

The IMF of star clusters is closely linked to their binary properties. Utilising the simulations from our parameter study, we were able to investigate the multiplicity properties in different environments. We compared the binary statistics in our simulations such as the multiplicity fraction, binary separation distribution, and binary mass ratio with observations and showed that the observed trends are reproduced in our simulations, indicating an overall consistency between theory and observations (Chapter 2, 3, and 4). In chapter 5, we carried out an extensive analysis of the binary orbital eccentricity, e. We studied the role of turbulence in setting the binary eccentricities and investigated how the dependence of the eccentricity distribution on the binary separation and mass relates to our understanding of the fragmentation scenarios on different scales. Since our simulations do not resolve fragmentation on disc scales (except in cases of extended discs), our sample of binaries underestimates the short-separation binaries, particularly the spectroscopic binaries. Due to this limitation, our study is focused on the relative changes in the binary properties for different conditions, rather than the actual values. The work associated with Chapter 5 is published in peer-reviewed journal (Mathew et al. 2024).

The main results are:

- The multiplicity fraction mf is an increasing function of the primary mass in our simulations, which is complementary to the observational findings. mf is influenced by the turbulent properties of the cloud, where more compressive turbulence driving or lower virial parameter results in a higher mf, particularly in the sub-solar range.
- In clouds where compressive modes of turbulence driving dominate, the mean orbital eccentricity of binaries is higher as compared to that when the solenoidal driving modes dominate.
- The eccentricity distribution of wide binaries (separations greater than 1000 AU) is superthermal ($p(e) \propto e^{\alpha}$, where $\alpha > 1$) while that for shorter binaries is subthermal to thermal ($p(e) \propto e^{\alpha}$, where $\alpha \lesssim 1$). This result aligns well with the current observational findings and will provide crucial insights into the mechanism(s) of binary formation on different scales.

6.2 Future Prospects

6.2.1 Expanding the parameter study

Impact of the Mach number of turbulence

It is common in the literature to associate the role of turbulence with the velocity dispersion in the cloud, where high-velocity dispersions are typically regarded as an indicator of turbulent support. However, the overall effect of the turbulent velocity dispersion in the cloud is controlled by the relative dominance of the cloud parameters like the virial parameter and the Mach number (Federrath & Klessen 2012), and therefore it is crucial to understand their individual effects. In this thesis, we numerically demonstrated that a higher virial parameter decreases fragmentation because of the increased kinetic support by the turbulence. In our study focused on the virial parameter, we kept the Mach number fixed, to isolate its effect. A fitting

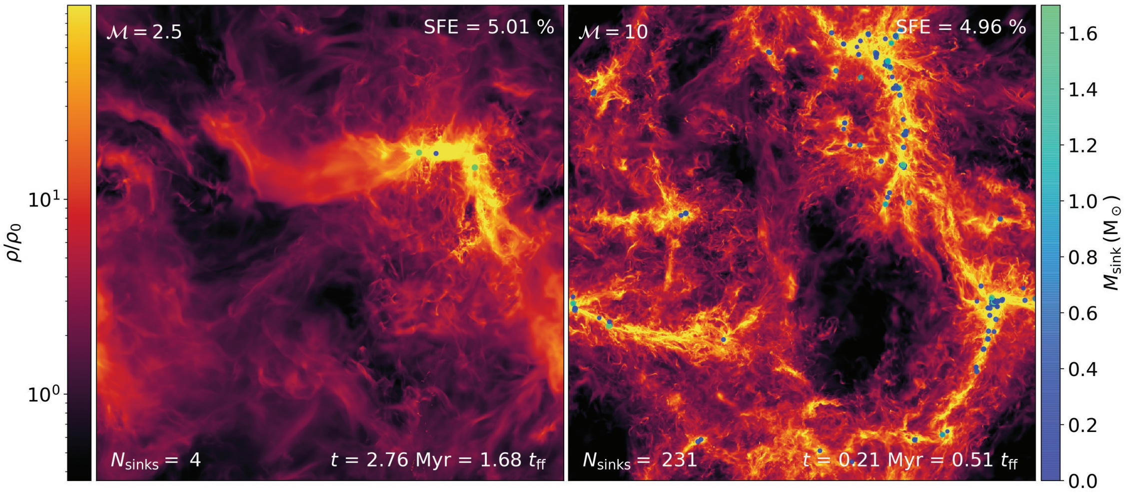

Figure 6.1: Gas density maps of simulations with rms Mach number $\mathcal{M} = 2.5$ (left) and $\mathcal{M} = 10$ (right) for the same seed in the random number generator for the turbulence driving.

continuation to this work would be to analyse the influence of the Mach number, keeping the virial parameter fixed. Such a follow-up study would help to disentangle the effects of $\alpha_{\rm vir}$ and $\mathcal{M}$, enabling us to draw robust conclusions on the role of turbulence. The preparations for this study are underway and the preliminary results reveal that the Mach number has significant consequences on the cloud evolution and fragmentation. Fig. 6.1 shows a comparison between the density projections of simulations with rms Mach number values of $\mathcal{M} = 2.5$ (left panel) and $\mathcal{M} = 10$ (right panel). It is clear that the simulation with $\mathcal{M} = 10$ has a higher fraction of large-scale structures as a result of the increased turbulent shock strength. The degree of fragmentation within the cloud is higher for $\mathcal{M} = 10$ as compared to $\mathcal{M} = 2.5$, pointing to a potential influence of Mach number on the shape of the IMF, which I aim to study in the future.

Effect of the Alfvén Mach number

The influence of magnetic fields is a research avenue we have not yet explored in detail and is therefore a natural extension of this thesis. The extent of the role of magnetic fields is still ambiguous, particularly in the presence of turbulence and protostellar heating (Krumholz & Federrath 2019). Since our simulation setup includes all three components simultaneously, we will be able to contextualise the relative effectiveness of magnetic support over the kinetic and thermal support in controlling the efficiency of star formation and shaping the IMF. A notable focus would be the contribution of the Alfvén Mach number $\mathcal{M}_{\rm A}$ towards the origin of the IMF, which is a largely unexplored topic. With $\mathcal{M}_{\mathrm{A}}$ being a measure of the relative dominance of magnetic fields and turbulence, the knowledge gained from this thesis on the characteristics of turbulence will provide valuable insights for this study. $\mathcal{M}_{\mathrm{A}}$ affects the morphology of the magnetic field, its scaling with density, and the direction of gravitational collapse (Hennebelle & Inutsuka 2019; Krumholz & Federrath 2019; Pattle et al. 2023). Therefore, a thorough study on the effect of $\mathcal{M}_{\mathrm{A}}$ is critical to fully capture the role of magnetic fields in shaping the IMF. Recent observational works are increasingly proficient in extracting the 3D structure and properties of magnetic fields by combining data from Zeeman splitting, dust polarization, and Faraday rotation measurements (Crutcher 2012; Planck Collaboration et al. 2016a; Friberg et al. 2016; Tahani et al. 2018). Thus, expanding our research to include $\mathcal{M}_{\mathrm{A}}$ in our parameter study is well-timed, and will provide a solid framework for comparisons with observations.

6.2.2 Observational comparisons and outlier IMFs

Having explored the effect of the main turbulence-related properties such as the turbulence driving mode b and virial parameter α_{vir}, the proposed studies on the Mach number $\mathcal{M}$ and Alfvén Mach number $\mathcal{M}_{\mathrm{A}}$ will complete a comprehensive analysis on the interplay between gravity, turbulence, and magnetic fields, which are the principal components of the physics of star formation. The associated simulation collection will be one of the largest databases for studying star cluster formation, yielding crucial insights towards the origin of the IMF.

Our simulations with diverse initial conditions would be ideal for comparison with observations. Such a study is in progress where we attempt to connect our simulation results and insights with the observed correlation of the IMF with different cloud properties, for instance, the IMF-SFR relationship derived from the Galaxy and Mass Assembly survey (Gunawardhana et al. 2011; Hopkins 2018). A parallel focus of this study would be on developing new schemes for observation-theory IMF comparisons that are more robust than the peak or the power-law slope. Our parameter study can also be used to reinforce the observational evidences of outlier IMFs in the Taurus molecular cloud (Luhman et al. 2009; Bastian et al. 2010) and the Galactic centre (Figer et al. 1999; Kim et al. 2006; Lu et al. 2013; Hosek et al. 2019). In future surveys, quantifying the turbulence properties, which this thesis found to have important consequences on the IMF, will unveil new approaches to explaining the outlier IMFs in these regions. Our simulations can serve as a benchmark for future observational works aimed at exploring variations in the IMF and SFR, e.g., using JWST (Harikane et al. 2023; Yasui et al. 2024) and the SAMI Galaxy survey

(Croom et al. 2012; Medling et al. 2018).

6.2.3 An environment-dependent IMF model

A promising area of further research is modelling an environment-dependent IMF based on the results from the parameter study in this thesis. Our work conclusively demonstrated that the characteristics of the IMF are dependent on the properties of the cloud in which the star cluster forms, which is consistent with the principles of the current gravo-turbulent IMF models (Padoan & Nordlund 2002; Hennebelle & Chabrier 2008; Hopkins 2012). Further, we found that the Bate & Bonnell (2005) model (BB05 hereafter) based on competitive accretion and dynamical ejections is well-matched with our simulation IMF, highlighting the significance of stellar dynamics (see Fig. 2.8). However, BB05 is a semi-analytical model that reproduces the IMF based on stellar properties such as the average accretion rate and timescale of dynamical ejections, which need to be derived from the simulation output. Therefore, while the BB05 reproduces our simulation IMF better than the gravo-turbulent models, BB05 lacks the ability to predict the IMF from gas properties alone.

These aspects provide opportunities for developing a detailed IMF model that combines the concepts of gravo-turbulent fragmentation with stellar properties and dynamics, applying the insights from our parameter study on the IMF. This will involve modelling the input parameters in the BB05 IMF model, i.e, stellar properties (such as the accretion rate and accretion time-period) from the cloud properties (such as the mode of turbulence driving, cloud virial parameter, and Mach number), which can be built into the framework of gravo-turbulent theories on the SFR and IMF. Such a model would be capable of not only accurately reproducing the IMF shape like BB05, but will also embody the predictive power of the gravo-turbulent models, allowing to fully capture IMF variations in star-forming regions with different environmental conditions. Since the IMF determines the fraction of high-mass stars, and therefore the total energy output from feedback processes in clusters, a physically motivated IMF model will have vast applications in galaxy formation and evolution studies.

6.2.4 Application to large-scale simulations

Large-scale simulations of the ISM generally assume a universal IMF to calculate the luminosity-to-mass ratio and supernova rates in their unresolved star clusters. Our ongoing research shows that non-typical/outlier IMFs can emerge when multiple cloud properties act in tandem to either suppress or enhance fragmentation

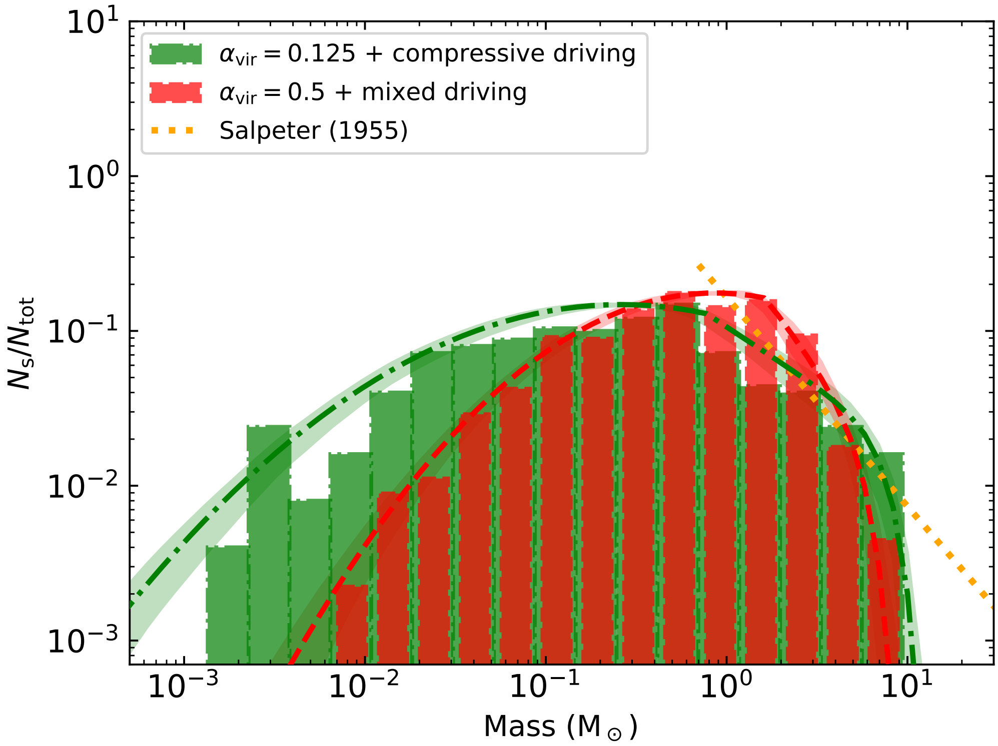

Figure 6.2: Comparison of the IMF for simulations with $\alpha_{\rm vir} = 0.125$ + compressive driving (dash-dotted histogram and curve) with simulations having $\alpha_{\rm vir} = 0.5$ + natural mixture of driving (dashed histogram and curve). The comparison shows that varying the virial parameter $\alpha_{\rm vir}$ and the mode of turbulence driving simultaneously in star cluster formation simulations can significantly affect the shape of the IMF, including the high-mass slope. This shows that non-typical IMFs are expected in such environments and therefore adopting a universal IMF for galaxy-scale simulations is not an appropriate general approach.

(see Fig. 6.2). Considering such outlier IMFs in ISM simulations can substantially redefine the total momentum and energy output from stellar clusters, affecting the galaxy evolution. Moreover, simulations in the cosmological context typically assume a constant SFR or model the SFR based exclusively on the associated density within collapsing structures, overlooking environmental conditions. However, the SFR can vary over an order of magnitude depending on the turbulence driving mode (Federrath & Klessen 2012; Mathew et al. 2023). Furthermore, in this thesis, we showed that the SFR has a non-linear dependence on the cloud virial parameter.

The wealth of data and insights from our parameter study can help enhance the subgrid physics in large-scale galaxy evolution simulations by incorporating the effects of the environmental conditions on the IMF and SFR. This thesis involved conducting cloud-collapse simulations at the scale of 2 pc. The current simulations of ISM patch, isolated dwarfs, and zoom-in cosmological simulations (e.g., Hopkins et al. 2014; Walch et al. 2015; Kim & Ostriker 2017) are ideally suited for employing our simulation results, as the spatial resolution in these ISM simulations is a few parsecs. By implementing an environment-dependent IMF in the stellar population synthesis codes employed in the ISM simulations, the luminosity-to-mass ratio and supernova rates, both of which are primary drivers of galaxy evolution, can be better constrained. With the capabilities of the JWST to explore galaxies at high redshifts—environments significantly different from the Milky Way—there is a growing need to move away from assuming a universal IMF.

Bibliography

Abe D., Inoue T., Inutsuka S.-i., Matsumoto T., 2021, ApJ, 916, 83

Abt H. A., 2006, ApJ, 651, 1151

Achikanath Chirakkara R., Federrath C., Trivedi P., Banerjee R., 2021, Phys. Rev. Lett., 126, 091103

Adams F. C., Ruden S. P., Shu F. H., 1989, ApJ, 347, 959

Allen P. R., Koerner D. W., Reid I. N., Trilling D. E., 2005, ApJ, 625, 385

Alves J., Lombardi M., Lada C. J., 2007, A&A, 462, L17

Ambartsumian V. A., 1937, Azh, 14, 207

Andersen M., Meyer M. R., Oppenheimer B., Dougados C., Carpenter J., 2006, AJ, 132, 2296

Andersen M., Meyer M. R., Greissl J., Aversa A., 2008, ApJl, 683, L183

Andersen M., Zinnecker H., Moneti A., McCaughrean M. J., Brandl B., Brandner W., Meylan G., Hunter D., 2009, ApJ, 707, 1347

André P., et al., 2010, A&A, 518, L102

André P., Di Francesco J., Ward-Thompson D., Inutsuka S. I., Pudritz R. E., Pineda J. E., 2014, in Beuther H., Klessen R. S., Dullemond C. P., Henning T., eds, Protostars and Planets VI. p. 27 (`arXiv:1312.6232`), doi:10.2458/azu˙uapress˙9780816531240-ch002

Andrews J. J., Taggart K., Foley R., 2022, arXiv e-prints, p. arXiv:2207.00680

Appel S. M., Burkhart B., Semenov V. A., Federrath C., Rosen A. L., 2022, ApJ, 927, 75

Appel S. M., Burkhart B., Semenov V. A., Federrath C., Rosen A. L., Tan J. C., 2023, ApJ, 954, 93

Armstrong J. W., Rickett B. J., Spangler S. R., 1995, ApJ, 443, 209

Arzoumanian D., et al., 2011, A&A, 529, L6

Bacciotti F., Ray T. P., Mundt R., Eislöffel J., Solf J., 2002, ApJ, 576, 222

Bacciotti F., Whelan E. T., Alcalá J. M., Nisini B., Podio L., Randich S., Stelzer B., Cupani G., 2011, ApJl, 737, L26

Bahcall J. N., Hut P., Tremaine S., 1985, ApJ, 290, 15

Ballesteros-Paredes J., Klessen R. S., Mac Low M. M., Vazquez-Semadeni E., 2007, in Reipurth B., Jewitt D., Keil K., eds, Protostars and Planets V. p. 63 (`arXiv:astro-ph/0603357`), doi:10.48550/arXiv.astro-ph/0603357

Ballesteros-Paredes J., Hartmann L. W., Vázquez-Semadeni E., Heitsch F., Zamora-Avilés M. A., 2011a, MNRAS, 411, 65

Ballesteros-Paredes J., Vázquez-Semadeni E., Gazol A., Hartmann L. W., Heitsch F., Colín P., 2011b, MNRAS, 416, 1436

Ballesteros-Paredes J., Hartmann L. W., Pérez-Goytia N., Kuznetsova A., 2015, MNRAS, 452, 566

Banerjee R., Pudritz R. E., 2006, ApJ, 641, 949

Baraffe I., Chabrier G., Allard F., Hauschildt P. H., 1998, A&A, 337, 403

Basri G., Reiners A., 2006, AJ, 132, 663

Bastian N., Covey K. R., Meyer M. R., 2010, ARA&A, 48, 339

Basu S., Jones C. E., 2004, MNRAS, 347, L47

Basu S., Gil M., Auddy S., 2015, MNRAS, 449, 2413

Bate M. R., 2000, MNRAS, 314, 33

Bate M. R., 2009a, MNRAS, 392, 590

Bate M. R., 2009b, MNRAS, 392, 1363

Bate M. R., 2009c, MNRAS, 397, 232

Bate M. R., 2012, MNRAS, 419, 3115

Bate M. R., 2014, MNRAS, 442, 285

Bate M. R., 2019, MNRAS, 484, 2341

Bate M. R., 2023, MNRAS, 519, 688

Bate M. R., Bonnell I. A., 2005, MNRAS, 356, 1201

Bate M. R., Bonnell I. A., Price N. M., 1995, MNRAS, 277, 362

Bate M. R., Bonnell I. A., Bromm V., 2002a, MNRAS, 332, L65

Bate M. R., Bonnell I. A., Bromm V., 2002b, MNRAS, 336, 705

Bate M. R., Bonnell I. A., Bromm V., 2003, MNRAS, 339, 577

Beattie J. R., Federrath C., 2020, MNRAS, 492, 668

Beattie J. R., Mocz P., Federrath C., Klessen R. S., 2021, MNRAS, 504, 4354

Belloche A., 2013, in Hennebelle P., Charbonnel C., eds, EAS Publications Series Vol. 62, EAS Publications Series. pp 25–66 (`arXiv:1305.0627`), doi:10.1051/eas/1362002

Berger M. J., Colella P., 1989, Journal of Computational Physics, 82, 64

Bertelli Motta C., Clark P. C., Glover S. C. O., Klessen R. S., Pasquali A., 2016, MNRAS, 462, 4171

Bertoldi F., 1989, ApJ, 346, 735

Bisbas T. G., Wünsch R., Whitworth A. P., Hubber D. A., Walch S., 2011, ApJ, 736, 142

Blandford R. D., Payne D. G., 1982, MNRAS, 199, 883

Blitz L., 1993, in Levy E. H., Lunine J. I., eds, Protostars and Planets III. p. 125

Bochanski J. J., Hawley S. L., Covey K. R., West A. A., Reid I. N., Golimowski D. A., Ivezić Ž., 2010, AJ, 139, 2679

Bodenheimer P., 1978, ApJ, 224, 488

Bodenheimer P., 1995, ARA&A, 33, 199

Boffin H. M. J., Watkins S. J., Bhattal A. S., Francis N., Whitworth A. P., 1998, MNRAS, 300, 1189

Bond J. R., Cole S., Efstathiou G., Kaiser N., 1991, ApJ, 379, 440

Bondi H., 1952, MNRAS, 112, 195

Bonnell I. A., Bate M. R., 1994, MNRAS, 269, L45

Bonnell I. A., Bate M. R., 2006, MNRAS, 370, 488

Bonnell I. A., Bate M. R., Clarke C. J., Pringle J. E., 1997, MNRAS, 285, 201

Bonnell I. A., Bate M. R., Clarke C. J., Pringle J. E., 2001a, MNRAS, 323, 785

Bonnell I. A., Clarke C. J., Bate M. R., Pringle J. E., 2001b, MNRAS, 324, 573

Bonnell I. A., Bate M. R., Vine S. G., 2003, MNRAS, 343, 413

Bonnell I. A., Clarke C. J., Bate M. R., 2006, ApJ, 368, 1296

Bonnell I. A., Clark P., Bate M. R., 2008, MNRAS, 389, 1556

Boss A. P., 1999, ApJ, 520, 744

Bracco A., et al., 2017, A&A, 604, A52

Brandenburg A., Subramanian K., 2005, Phys. Rep., 417, 1

Brandl B., et al., 1996, ApJ, 466, 254

Briceño C., Luhman K. L., Hartmann L., Stauffer J. R., Kirkpatrick J. D., 2002, ApJ, 580, 317

Brucy N., Hennebelle P., Colman T., Klessen R. S., Le Yhuelic C., 2024, arXiv e-prints, p. arXiv:2404.17374

Brunt C. M., 2010, A&A, 513, A67

Buntemeyer L., Banerjee R., Peters T., Klassen M., Pudritz R. E., 2016, NewA, 43, 49

Burkert A., Bodenheimer P., 2000, ApJ, 543, 822

Burkhart B., 2018, ApJ, 863, 118

Burkhart B., Falceta-Gonçalves D., Kowal G., Lazarian A., 2009, ApJ, 693, 250

Burkhart B., Collins D. C., Lazarian A., 2015, ApJ, 808, 48

Cabrit S., Codella C., Gueth F., Nisini B., Gusdorf A., Dougados C., Bacciotti F., 2007, A&A, 468, L29

Calamida A., et al., 2015, ApJ, 810, 8

Cappellari M., et al., 2012, Nature, 484, 485

Caselli P., Benson P. J., Myers P. C., Tafalla M., 2002, ApJ, 572, 238

Cenarro A. J., Gorgas J., Vazdekis A., Cardiel N., Peletier R. F., 2003, MNRAS, 339, L12

Ceppi S., Cuello N., Lodato G., Longarini C., Price D. J., Elsender D., Bate M. R., 2024, A&A, 682, A104

Chabrier G., 2001, ApJ, 554, 1274

Chabrier G., 2002, ApJ, 567, 304

Chabrier G., 2003, PASP, 115, 763

Chabrier G., 2005, in Corbelli E., Palla F., Zinnecker H., eds, Astrophysics and Space Science Library Vol. 327, The Initial Mass Function 50 Years Later. p. 41 (`arXiv:astro-ph/0409465`), doi:10.1007/978-1-4020-3407-7˙5

Chabrier G., Dumond P., 2024, ApJ, 966, 48

Chabrier G., Hennebelle P., Charlot S., 2014, ApJ, 796, 75

Chen X., et al., 2013, ApJ, 768, 110

Chen X., Liu Z., Han Z., 2024, Progress in Particle and Nuclear Physics, 134, 104083

Chepurnov A., Lazarian A., 2010, ApJ, 710, 853

Chini R., Hoffmeister V. H., Nasseri A., Stahl O., Zinnecker H., 2012, MNRAS, 424, 1925

Cho J., Lazarian A., 2002, Phys. Rev. Lett., 88, 245001

Clark P. C., Klessen R. S., Bonnell I. A., 2007, MNRAS, 379, 57

Clarke C. J., 1999, MNRAS, 307, 328

Close L. M., Siegler N., Freed M., Biller B., 2003, ApJ, 587, 407

Collins D. C., Kritsuk A. G., Padoan P., Li H., Xu H., Ustyugov S. D., Norman M. L., 2012a, ApJ, 750, 13

Collins D. C., Kritsuk A. G., Padoan P., Li H., Xu H., Ustyugov S. D., Norman M. L., 2012b, ApJ, 750, 13

Colman T., Teyssier R., 2020, MNRAS, 492, 4727

Connelley M. S., Reipurth B., Tokunaga A. T., 2008, AJ, 135, 2526

Conroy C., Dutton A. A., Graves G. J., Mendel J. T., van Dokkum P. G., 2013, ApJl, 776, L26

Covey K. R., et al., 2008, AJ, 136, 1778

Croom S. M., et al., 2012, MNRAS, 421, 872

Crutcher R. M., 2012, ARA&A, 50, 29

Crutcher R. M., Wandelt B., Heiles C., Falgarone E., Troland T. H., 2010, ApJ, 725, 466

Cunningham A. J., Krumholz M. R., McKee C. F., Klein R. I., 2018, MNRAS, 476, 771

Da Rio N., Robberto M., Hillenbrand L. A., Henning T., Stassun K. G., 2012, ApJ, 748, 14

Dabringhausen J., Marks M., Kroupa P., 2021, BiPoS1: Dynamical processing of the initial binary star population, Astrophysics Source Code Library, record ascl:2109.029

Dale J. E., Bonnell I., 2011, MNRAS, 414, 321

Dale J. E., Bonnell I. A., Whitworth A. P., 2007, MNRAS, 375, 1291

Damian B., Jose J., Samal M. R., Moraux E., Das S. R., Patra S., 2021, MNRAS, 504, 2557

Delfosse X., Forveille T., Ségransan D., Beuzit J. L., Udry S., Perrier C., Mayor M., 2000, A&A, 364, 217

Delfosse X., et al., 2004, in Hilditch R. W., Hensberge H., Pavlovski K., eds, Astronomical Society of the Pacific Conference Series Vol. 318, Spectroscopically and Spatially Resolving the Components of the Close Binary Stars. pp 166–174

Dhawalikar S., Federrath C., Davidovits S., Teyssier R., Nagel S. R., Remington B. A., Collins D. C., 2022, MNRAS, 514, 1782

Dib S., 2014, MNRAS, 444, 1957

Dib S., 2022, A&A, 666, A113

Dib S., 2023, ApJ, 959, 88

Dib S., Shadmehri M., Padoan P., Maheswar G., Ojha D. K., Khajenabi F., 2010, MNRAS, 405, 401

Dib S., Schmeja S., Hony S., 2017, MNRAS, 464, 1738

Dieterich S. B., Henry T. J., Golimowski D. A., Krist J. E., Tanner A. M., 2012, AJ, 144, 64

Draine B. T., 2011, Physics of the Interstellar and Intergalactic Medium. Princeton University Press

Dubey A., et al., 2008, in Pogorelov N. V., Audit E., Zank G. P., eds, Astronomical Society of the Pacific Conference Series Vol. 385, Numerical Modeling of Space Plasma Flows. p. 145

Duchêne G., Kraus A., 2013, ARA&A, 51, 269

Duchêne G., Bouvier J., Bontemps S., André P., Motte F., 2004, A&A, 427, 651

Dunham M. M., et al., 2014, in Beuther H., Klessen R. S., Dullemond C. P., Henning T., eds, Protostars and Planets VI. p. 195 (`arXiv:1401.1809`), doi:10.2458/azu_uapress_9780816531240-ch009

Dupuy T. J., Liu M. C., 2011, ApJ, 733, 122

Duquennoy A., Mayor M., 1991, A&A, 500, 337

El-Badry K., Rix H.-W., 2018, MNRAS, 480, 4884

El-Badry K., Rix H.-W., Heintz T. M., 2021, MNRAS, 506, 2269

Elmegreen B. G., 1993a, in Levy E. H., Lunine J. I., eds, Protostars and Planets III. p. 97

Elmegreen B. G., 1993b, ApJl, 419, L29

Elmegreen B. G., 2009a, in Sheth K., Noriega-Crespo A., Ingalls J. G., Paladini R., eds, The Evolving ISM in the Milky Way and Nearby Galaxies. p. 14 (`arXiv:0803.3154`), doi:10.48550/arXiv.0803.3154

Elmegreen B. G., 2009b, in Andersen J., Nordströara m B., Bland-Hawthorn J., eds, IAU Symposium Vol. 254, The Galaxy Disk in Cosmological Context. pp 289–300 (`arXiv:0810.5406`), doi:10.1017/S1743921308027713

Elmegreen B. G., Elmegreen D. M., 1978, ApJ, 220, 1051

Elmegreen B. G., Lada C. J., 1977, ApJ, 214, 725

Elmegreen B. G., Scalo J., 2004, ARA&A, 42, 211

Elmegreen B. G., Scalo J., 2006, ApJ, 636, 149

Elmegreen B. G., Klessen R. S., Wilson C. D., 2008, ApJ, 681, 365

Enoch M. L., Evans Neal J. I., Sargent A. I., Glenn J., 2009, ApJ, 692, 973

Eswaran V., Pope S. B., 1988, Computers and Fluids, 16, 257

Evans Neal J. I., et al., 2009, ApJs, 181, 321

Falgarone E., Puget J. L., Perault M., 1992, A&A, 257, 715

Farias J. P., Offner S. S. R., Grudić M. Y., Guszejnov D., Rosen A. L., 2024, MNRAS, 527, 6732

Federrath C., 2013a, MNRAS, 436, 1245

Federrath C., 2013b, MNRAS, 436, 3167

Federrath C., 2015, MNRAS, 450, 4035

Federrath C., 2016, Journal of Plasma Physics, 82, 535820601

Federrath C., 2018, Physics Today, 71, 38

Federrath C., Banerjee S., 2015, MNRAS, 448, 3297

Federrath C., Klessen R. S., 2012, ApJ, 761, 156

Federrath C., Klessen R. S., 2013, ApJ, 763, 51

Federrath C., Klessen R. S., Schmidt W., 2008, ApJl, 688, L79

Federrath C., Klessen R. S., Schmidt W., 2009, ApJ, 692, 364

Federrath C., Duval J., Klessen R. S., Schmidt W., Low M. M. M., 2010a, Highlights of Astronomy, 15, 404

Federrath C., Roman-Duval J., Klessen R. S., Schmidt W., Mac Low M. M., 2010b, A&A, 512, A81

Federrath C., Banerjee R., Clark P. C., Klessen R. S., 2010c, ApJ, 713, 269

Federrath C., Chabrier G., Schober J., Banerjee R., Klessen R. S., Schleicher D. R. G., 2011a, Phys. Rev. Lett., 107, 114504

Federrath C., Banerjee R., Seifried D., Clark P. C., Klessen R. S., 2011b, in Alves J., Elmegreen B. G., Girart J. M., Trimble V., eds, Vol. 270, Computational Star Formation. pp 425–428 (`arXiv:1007.2504`), doi:10.1017/S1743921311000755

Federrath C., Sur S., Schleicher D. R. G., Banerjee R., Klessen R. S., 2011c, ApJ, 731, 62

Federrath C., Schrön M., Banerjee R., Klessen R. S., 2014, ApJ, 790, 128

Federrath C., et al., 2016, ApJ, 832, 143

Federrath C., et al., 2017a, in Crocker R. M., Longmore S. N., Bicknell G. V., eds, IAU Symposium Vol. 322, The Multi-Messenger Astrophysics of the Galactic Centre. pp 123–128 (`arXiv:1609.08726`), doi:10.1017/S1743921316012357

Federrath C., Krumholz M., Hopkins P. F., 2017b, in Journal of Physics Conference Series. p. 012007, doi:10.1088/1742-6596/837/1/012007

Federrath C., Klessen R. S., Iapichino L., Beattie J. R., 2021, Nature Astronomy, 5, 365

Federrath C., Roman-Duval J., Klessen R. S., Schmidt W., Mac Low M. M., 2022, TG: Turbulence Generator, Astrophysics Source Code Library, record ascl:2204.001 (ascl:2204.001)

Fendt C., Sheikhnezami S., 2013, ApJ, 774, 12

Figer D. F., Kim S. S., Morris M., Serabyn E., Rich R. M., McLean I. S., 1999, ApJ, 525, 750

Fischer D. A., Marcy G. W., 1992, ApJ, 396, 178

Fischer W. J., et al., 2010, A&A, 518, L122

Fontanive C., Biller B., Bonavita M., Allers K., 2018, MNRAS, 479, 2702

Foreman-Mackey D., Hogg D. W., Lang D., Goodman J., 2013, PASP, 125, 306

Fowler W. A., Hoyle F., 1963, Royal Greenwich Observatory Bulletins, 67, 301

Frank A., et al., 2014, in Beuther H., Klessen R. S., Dullemond C. P., Henning T., eds, Protostars and Planets VI. p. 451 (`arXiv:1402.3553`), doi:10.2458/azu˙uapress˙9780816531240-ch020

Friberg P., Bastien P., Berry D., Savini G., Graves S. F., Pattle K., 2016, in Holland W. S., Zmuidzinas J., eds, Society of Photo-Optical Instrumentation Engineers (SPIE) Conference Series Vol. 9914, Millimeter, Submillimeter, and Far-Infrared Detectors and Instrumentation for Astronomy VIII. p. 991403, doi:10.1117/12.2231943

Frisch U., 1995, Turbulence. The legacy of A.N. Kolmogorov. Cambridge University Press, doi:10.1017/CBO9781139170666

Froebrich D., Schmeja S., Smith M. D., Klessen R. S., 2006, MNRAS, 368, 435

Fryxell B., et al., 2000, ApJs, 131, 273

Furlan E., et al., 2016, ApJs, 224, 5

Gaia Collaboration et al., 2023, A&A, 674, A1

Gammie C. F., Ostriker E. C., 1996, ApJ, 466, 814

Gaudel M., et al., 2020, A&A, 637, A92

Geller A. M., Leigh N. W. C., Giersz M., Kremer K., Rasio F. A., 2019, ApJ, 872, 165

Gerrard I. A., Federrath C., Kuruwita R., 2019, MNRAS, 485, 5532

Gerrard I. A., et al., 2023, MNRAS, 526, 982

Gerrard I. A., Noon K. A., Federrath C., Di Teodoro E. M., Marchal A., McClure-Griffiths N. M., 2024, MNRAS, 530, 4317

Gillis J., Mestel L., Paris R. B., 1974, Ap&SS, 27, 167

Ginsburg A., Federrath C., Darling J., 2013, ApJ, 779, 50

Ginsburg A., et al., 2016, A&A, 586, A50

Girichidis P., Federrath C., Banerjee R., Klessen R. S., 2011, MNRAS, 413, 2741

Girichidis P., Konstandin L., Whitworth A. P., Klessen R. S., 2014, ApJ, 781, 91

Glover S. C. O., Federrath C., Mac Low M. M., Klessen R. S., 2010, MNRAS, 404, 2

Goodman A. A., Benson P. J., Fuller G. A., Myers P. C., 1993, ApJ, 406, 528

Goodwin S. P., Kroupa P., 2005, A&A, 439, 565

Goodwin S. P., Whitworth A., 2007, A&A, 466, 943

Grudić M. Y., Hopkins P. F., 2023, arXiv e-prints, p. arXiv:2308.16268

Grudić M. Y., Hopkins P. F., Faucher-Giguère C.-A., Quataert E., Murray N., Kereš D., 2018a, MNRAS, 475, 3511

Grudić M. Y., Guszejnov D., Hopkins P. F., Lamberts A., Boylan-Kolchin M., Murray N., Schmitz D., 2018b, MNRAS, 481, 688

Grudić M. Y., Hopkins P. F., Lee E. J., Murray N., Faucher-Giguère C.-A., Johnson L. C., 2019, MNRAS, 488, 1501

Grudić M. Y., Guszejnov D., Hopkins P. F., Offner S. S. R., Faucher-Giguére C.-A., 2021, MNRAS, p. arXiv:2010.11254

Grudić M. Y., Hafen Z., Rodriguez C. L., Guszejnov D., Lamberts A., Wetzel A., Boylan-Kolchin M., Faucher-Giguère C.-A., 2023, MNRAS, 519, 1366

Guieu S., Dougados C., Monin J. L., Magnier E., Martín E. L., 2006, A&A, 446, 485

Gunawardhana M. L. P., et al., 2011, MNRAS, 415, 1647

Guszejnov D., Hopkins P. F., 2015, MNRAS, 450, 4137

Guszejnov D., Krumholz M. R., Hopkins P. F., 2016, MNRAS, 458, 673

Guszejnov D., Hopkins P. F., Krumholz M. R., 2017, MNRAS, 468, 4093

Guszejnov D., Hopkins P., Grudich M., 2018a, in American Astronomical Society Meeting Abstracts #231. p. 114.03

Guszejnov D., Hopkins P. F., Grudić M. Y., Krumholz M. R., Federrath C., 2018b, MNRAS, 480, 182

Guszejnov D., Grudić M. Y., Hopkins P. F., Offner S. S. R., Faucher-Giguère C.-A., 2020, MNRAS, 496, 5072

Guszejnov D., Grudić M. Y., Hopkins P. F., Offner S. S. R., Faucher-Giguère C.-A., 2021, MNRAS, 502, 3646

Guszejnov D., Grudić M. Y., Offner S. S. R., Faucher-Giguère C.-A., Hopkins P. F., Rosen A. L., 2022a, arXiv e-prints, p. arXiv:2205.10413

Guszejnov D., Grudić M. Y., Offner S. S. R., Faucher-Giguère C.-A., Hopkins P. F., Rosen A. L., 2022b, MNRAS, 515, 4929

Guszejnov D., Raju A. N., Offner S. S. R., Grudić M. Y., Faucher-Giguère C.-A., Hopkins P. F., Rosen A. L., 2023, MNRAS, 518, 4693

Ha T., Li Y., Xu S., Kounkel M., Li H., 2021, ApJl, 907, L40

Ha T., Li Y., Kounkel M., Xu S., Li H., Zheng Y., 2022, ApJ, 934, 7

Hamilton C., Modak S., 2023, arXiv e-prints, p. arXiv:2311.04352

Hansen C. E., Klein R. I., McKee C. F., Fisher R. T., 2012, ApJ, 747, 22

Harada N., Hirano S., Machida M. N., Hosokawa T., 2021, MNRAS, 508, 3730

Harikane Y., et al., 2023, ApJS, 265, 5

Hartmann L., Calvet N., 1995, AJ, 109, 1846

Hartmann L., Hewett R., Stahler S., Mathieu R. D., 1986, ApJ, 309, 275

Haugbølle T., Padoan P., Nordlund Å., 2018b, The Astrophysical Journal, 854, 35

Haugbølle T., Padoan P., Nordlund Å., 2018a, ApJ, 854, 35

Hawley S. L., Gizis J. E., Reid I. N., 1996, AJ, 112, 2799

Hawley S. L., Gizis J. E., Reid N. I., 1997, AJ, 113, 1458

Heiderman A., Evans Neal J. I., Allen L. E., Huard T., Heyer M., 2010, ApJ, 723, 1019

Hennebelle P., Chabrier G., 2008, ApJ, 684, 395

Hennebelle P., Chabrier G., 2009, ApJ, 702, 1428

Hennebelle P., Chabrier G., 2011, ApJl, 743, L29

Hennebelle P., Chabrier G., 2013, ApJ, 770, 150

Hennebelle P., Fromang S., 2008, A&A, 477, 9

Hennebelle P., Grudić M. Y., 2024, ARA&A, 62, 63

Hennebelle P., Inutsuka S.-i., 2019, Frontiers in Astronomy and Space Sciences, 6, 5

Hennebelle P., Teyssier R., 2008, A&A, 477, 25

Hennebelle P., Banerjee R., Vázquez-Semadeni E., Klessen R. S., Audit E., 2008, A&A, 486, L43

Hennebelle P., Lee Y.-N., Chabrier G., 2019, ApJ, 883, 140

Hennebelle P., Commercon B., Lee Y.-N., Chabrier G., 2020a, arXiv e-prints, p. arXiv:2010.03539

Hennebelle P., Commerçon B., Lee Y.-N., Chabrier G., 2020b, ApJ, 904, 194

Hernandez A. K., Tan J. C., 2015, ApJ, 809, 154

Heyer M. H., Brunt C. M., 2004, ApJl, 615, L45

Heyer M., Gutermuth R., Urquhart J. S., Csengeri T., Wienen M., Leurini S., Menten K., Wyrowski F., 2016, A&A, 588, A29

Hillenbrand L. A., Carpenter J. M., 2000, ApJ, 540, 236

Hopkins A. M., 2007, in Afonso J., Ferguson H. C., Mobasher B., Norris R., eds, Astronomical Society of the Pacific Conference Series Vol. 380, Deepest Astronomical Surveys. p. 423 (`arXiv:astro-ph/0611283`), doi:10.48550/arXiv.astro-ph/0611283

Hopkins P. F., 2012, MNRAS, 423, 2037

Hopkins P. F., 2013a, MNRAS, 430, 1653

Hopkins P. F., 2013b, MNRAS, 430, 1880

Hopkins A. M., 2018, Publ. Astron. Soc. Australia, 35, 39

Hopkins A. M., Beacom J. F., 2006, ApJ, 651, 142

Hopkins P. F., Kereš D., Oñorbe J., Faucher-Giguère C.-A., Quataert E., Murray N., Bullock J. S., 2014, MNRAS, 445, 581

Hosek Matthew W. J., Lu J. R., Anderson J., Najarro F., Ghez A. M., Morris M. R., Clarkson W. I., Albers S. M., 2019, ApJ, 870, 44

Hoyle F., 1953, ApJ, 118, 513

Hoyle F., Lyttleton R. A., 1939, Proceedings of the Cambridge Philosophical Society, 35, 405

Hu Y., Lazarian A., 2023, MNRAS, 524, 4431

Hu Y., et al., 2019, Nature Astronomy, 3, 776

Hu Y., Federrath C., Xu S., Mathew S. S., 2022, MNRAS, 513, 2100

Hull C. L. H., et al., 2017, ApJ, 847, 92

Hwang H.-C., Ting Y.-S., Zakamska N. L., 2022a, MNRAS, 512, 3383

Hwang H.-C., El-Badry K., Rix H.-W., Hamilton C., Ting Y.-S., Zakamska N. L., 2022b, ApJl, 933, L32

Inutsuka S.-i., 2001, ApJl, 559, L149

Inutsuka S.-I., Miyama S. M., 1992, ApJ, 388, 392

Janson M., et al., 2012, ApJ, 754, 44

Jappsen A. K., Klessen R. S., 2004, A&A, 423, 1

Jappsen A. K., Klessen R. S., Larson R. B., Li Y., Mac Low M. M., 2005, A&A, 435, 611

Jeans J. H., 1919, MNRAS, 79, 408

Jeffries R. D., 2012, in Reylé C., Charbonnel C., Schultheis M., eds, EAS Publications Series Vol. 57, EAS Publications Series. pp 45–89 (`arXiv:1205.2966`), doi:10.1051/eas/1257002

Johnstone D., Wilson C. D., Moriarty-Schieven G., Joncas G., Smith G., Gregersen E., Fich M., 2000, ApJ, 545, 327

Jones B. F., Walker M. F., 1988, AJ, 95, 1755

Kainulainen J., Federrath C., Henning T., 2013, A&A, 553, L8

Kauffmann J., Pillai T., Goldsmith P. F., 2013, ApJ, 779, 185

Kennicutt Robert C. J., 1998, in Gilmore G., Howell D., eds, Astronomical Society of the Pacific Conference Series Vol. 142, The Stellar Initial Mass Function (38th Herstmonceux Conference). p. 1

Khullar S., Krumholz M. R., Federrath C., Cunningham A. J., 2019, MNRAS, 488, 1407

Khullar S., Federrath C., Krumholz M. R., Matzner C. D., 2021, MNRAS, 507, 4335

Kim C.-G., Ostriker E. C., 2017, ApJ, 846, 133

Kim S. S., Figer D. F., Kudritzki R. P., Najarro F., 2006, ApJl, 653, L113

Kim J.-G., Kim W.-T., Ostriker E. C., 2018, ApJ, 859, 68

Kim D., Lu J. R., Konopacky Q., Chu L., Toller E., Anderson J., Theissen C. A., Morris M. R., 2019, AJ, 157, 109

King P. K., Fissel L. M., Chen C.-Y., Li Z.-Y., 2018, MNRAS, 474, 5122

Kitsionas S., et al., 2009, A&A, 508, 541

Klessen R. S., 2000, ApJ, 535, 869

Klessen R. S., Heitsch F., Mac Low M.-M., 2000, ApJ, 535, 887

Klessen R. S., Ballesteros-Paredes J., Vázquez-Semadeni E., Durán-Rojas C., 2005, ApJ, 620, 786

Klessen R. S., Spaans M., Jappsen A.-K., 2007, MNRAS, 374, L29

Konopacky Q. M., Ghez A. M., Rice E. L., Duchêne G., 2007, ApJ, 663, 394

Könyves V., et al., 2015, A&A, 584, A91

Kouwenhoven M. B. N., Goodwin S. P., Parker R. J., Davies M. B., Malmberg D., Kroupa P., 2010, MNRAS, 404, 1835

Kowal G., Lazarian A., Beresnyak A., 2007, ApJ, 658, 423

Kratter K., Lodato G., 2016, ARA&A, 54, 271

Kraus A. L., Hillenbrand L. A., 2007, ApJ, 662, 413

Kritsuk A. G., Norman M. L., Padoan P., Wagner R., 2007, ApJ, 665, 416

Kritsuk A. G., Norman M. L., Wagner R., 2011, ApJl, 727, L20

Kroupa P., 1995, MNRAS, 277, 1491

Kroupa P., 2001, MNRAS, 322, 231

Kroupa P., 2002, Science, 295, 82

Kroupa P., 2008, in Aarseth S. J., Tout C. A., Mardling R. A., eds, , Vol. 760, The Cambridge N-Body Lectures. p. 181, doi:10.1007/978-1-4020-8431-7˙8

Kroupa P., Weidner C., 2003, ApJ, 598, 1076

Kroupa P., Tout C. A., Gilmore G., 1993, MNRAS, 262, 545

Kroupa P., Weidner C., Pflamm-Altenburg J., Thies I., Dabringhausen J., Marks M., Maschberger T., 2013, The Stellar and Sub-Stellar Initial Mass Function of Simple and Composite Populations. Planets, Stars and Stellar Systems. Volume 5: Galactic Structure and Stellar Populations, p. 115, doi:10.1007/978-94-007-5612-0˙4

Kroupa P., Gjergo E., Jerabkova T., Yan Z., 2024, arXiv e-prints, p. arXiv:2410.07311

Krumholz M. R., 2011, in Telles E., Dupke R., Lazzaro D., eds, American Institute of Physics Conference Series Vol. 1386, XV Special Courses at the National Observatory of Rio de Janeiro. AIP, pp 9–57 (`arXiv:1101.5172`), doi:10.1063/1.3636038

Krumholz M. R., 2014, Phys. Rep., 539, 49

Krumholz M. R., Federrath C., 2019, Frontiers in Astronomy and Space Sciences, 6, 7

Krumholz M. R., Matzner C. D., 2009, ApJ, 703, 1352

Krumholz M. R., McKee C. F., 2005, ApJ, 630, 250

Krumholz M. R., Tan J. C., 2007, ApJ, 654, 304

Krumholz M. R., Thompson T. A., 2012, ApJ, 760, 155

Krumholz M. R., McKee C. F., Klein R. I., 2004, ApJ, 611, 399

Krumholz M. R., Klein R. I., McKee C. F., 2005, in Cesaroni R., Felli M., Churchwell E., Walmsley M., eds, IAU Symposium Vol. 227, Massive Star Birth: A Crossroads of Astrophysics. pp 231–236 (`arXiv:astro-ph/0510432`), doi:10.1017/S1743921305004588

Krumholz M. R., McKee C. F., Tumlinson J., 2009, ApJ, 699, 850

Krumholz M. R., Klein R. I., McKee C. F., 2011, ApJ, 740, 74

Krumholz M. R., Dekel A., McKee C. F., 2012a, ApJ, 745, 69

Krumholz M. R., Klein R. I., McKee C. F., 2012b, ApJ, 754, 71

Krumholz M. R., et al., 2014, in Beuther H., Klessen R. S., Dullemond C. P., Henning T., eds, Protostars and Planets VI. p. 243 (`arXiv:1401.2473`), doi:10.2458/azu˙uapress˙9780816531240-ch011

Kuffmeier M., Calcutt H., Kristensen L. E., 2019, A&A, 628, A112

Kuhn M. A., Hillenbrand L. A., Sills A., Feigelson E. D., Getman K. V., 2019, ApJ, 870, 32

Kuiper R., Yorke H. W., Turner N. J., 2015, The Astrophysical Journal, 800, 86

Kuruwita R. L., Haugbølle T., 2023, A&A, 674, A196

Lada C. J., 2006, ApJl, 640, L63

Lada C. J., Lada E. A., 2003, ARA&A, 41, 57

Lada C. J., Lombardi M., Roman-Zuniga C., Forbrich J., Alves J. F., 2013, ApJ, 778, 133

Larson R. B., 1969, MNRAS, 145, 271

Larson R. B., 1972, MNRAS, 156, 437

Larson R. B., 1973a, Fundamentals Cosmic Phys., 1, 1

Larson R. B., 1973b, MNRAS, 161, 133

Larson R. B., 1981, MNRAS, 194, 809

Larson R. B., 1985, MNRAS, 214, 379

Larson R. B., 2005, MNRAS, 359, 211

Lebreuilly U., Hennebelle P., Maury A., González M., Traficante A., Klessen R., Testi L., Molinari S., 2024, A&A, 683, A13

Lee Y.-N., Hennebelle P., 2018a, A&A, 611, A88

Lee Y.-N., Hennebelle P., 2018b, A&A, 611, A89

Lee E. J., Miville-Deschênes M.-A., Murray N. W., 2016, ApJ, 833, 229

Lee A. T., Offner S. S. R., Kratter K. M., Smullen R. A., Li P. S., 2019, ApJ, 887, 232

Lee Y.-N., Offner S. S. R., Hennebelle P., André P., Zinnecker H., Ballesteros-Paredes J., Inutsuka S.-i., Kruijssen J. M. D., 2020, Space Sci. Rev, 216, 70

Lequeux J., 2005, The Interstellar Medium. Springer, doi:10.1007/b137959

Li Z.-Y., Nakamura F., 2006, ApJl, 640, L187

Li Y., Klessen R. S., Mac Low M.-M., 2003, ApJ, 592, 975

Li Z.-Y., Wang P., Abel T., Nakamura F., 2010, The Astrophysical Journal, 720, L26

Li J., Liu C., Zhang Z.-Y., Tian H., Fu X., Li J., Yan Z.-Q., 2023, Nature, 613, 460

Liptai D., Price D. J., Wurster J., Bate M. R., 2017, MNRAS, 465, 105

Liu B., Lai D., Wang Y.-H., 2019, ApJ, 881, 41

Liu M., Hu Y., Lazarian A., 2024, MNRAS, 530, 1066

Livernois A. R., Vesperini E., Pavlík V., 2023, MNRAS, 521, 4395

Lomax O., Whitworth A. P., Hubber D. A., 2015, MNRAS, 449, 662

Lu J. R., Do T., Ghez A. M., Morris M. R., Yelda S., Matthews K., 2013, ApJ, 764, 155

Lubow S. H., Pringle J. E., 1993, MNRAS, 263, 701

Luhman K. L., 2004, Apj, 617, 1216

Luhman K. L., 2012, ARA&A, 50, 65

Luhman K. L., Rieke G. H., Young E. T., Cotera A. S., Chen H., Rieke M. J., Schneider G., Thompson R. I., 2000, ApJ, 540, 1016

Luhman K. L., Mamajek E. E., Allen P. R., Cruz K. L., 2009, ApJ, 703, 399

Lund K., Bonnell I. A., 2018, MNRAS, 479, 2235

Mac Low M.-M., 1999, ApJ, 524, 169

Mac Low M.-M., 2013, in Wong T., Ott J., eds, IAU Symposium Vol. 292, Molecular Gas, Dust, and Star Formation in Galaxies. pp 3–15 (`arXiv:1210.7723`), doi:10.1017/S1743921313000161

Mac Low M.-M., Klessen R. S., 2004, Reviews of Modern Physics, 76, 125

Mac Low M.-M., Klessen R. S., Burkert A., Smith M. D., 1998, Phys. Rev. Lett., 80, 2754

MacNeice P., Olson K. M., Mobarry C., de Fainchtein R., Packer C., 2000, Computer Physics Communications, 126, 330

Maciel W. J., Rocha-Pinto H. J., 1998, MNRAS, 299, 889

Marcus A. H., 1968, The Astronomical Journal Supplement, 73, 24

Marsh K. A., et al., 2016, MNRAS, 459, 342

Maschberger T., Bonnell I. A., Clarke C. J., Moraux E., 2014, MNRAS, 439, 234

Mason B. D., Hartkopf W. I., Gies D. R., Henry T. J., Helsel J. W., 2009, AJ, 137, 3358

Massey P., Parker J. W., Garmany C. D., 1989, AJ, 98, 1305

Masunaga H., Inutsuka S.-i., 2000, ApJ, 531, 350

Masunaga H., Miyama S. M., Inutsuka S.-i., 1998, ApJ, 495, 346

Mathew S. S., Federrath C., 2020, MNRAS, 496, 5201

Mathew S. S., Federrath C., 2021, MNRAS, 507, 2448

Mathew S. S., Federrath C., Seta A., 2023, MNRAS, 518, 5190

Mathew S. S., Xu S., Federrath C., Hu Y., Seta A., 2024, MNRAS, 532, 2374

Mathew S. S., Federrath C., Seta A., 2025, MNRAS, 536, 1932

Mathieu R. D., 1994, ARA&A, 32, 465

Matsumoto T., Dobashi K., Shimoikura T., 2015, ApJ, 801, 77

Matzner C. D., 2002, ApJ, 566, 302

Matzner C. D., McKee C. F., 2000, ApJ, 545, 364

McCrady N., Graham J. R., Vacca W. D., 2005, ApJ, 621, 278

McKee C. F., Ostriker E. C., 2007, ARA&A, 45, 565

McKee C. F., Zweibel E. G., Goodman A. A., Heiles C., 1993, in Levy E. H., Lunine J. I., eds, Protostars and Planets III. p. 327

Medling A. M., et al., 2018, MNRAS, 475, 5194

Menon S. H., Federrath C., Klaassen P., Kuiper R., Reiter M., 2021, MNRAS, 500, 1721

Menon S. H., Federrath C., Krumholz M. R., Kuiper R., Wibking B. D., Jung M., 2022, MNRAS, 512, 401

Menon S. H., Federrath C., Krumholz M. R., 2023, MNRAS, 521, 5160

Menon S. H., Lancaster L., Burkhart B., Somerville R. S., Dekel A., Krumholz M. R., 2024, ApJl, 967, L28

Meyer M. R., Adams F. C., Hillenbrand L. A., Carpenter J. M., Larson R. B., 2000, in Mannings V., Boss A. P., Russell S. S., eds, Protostars and Planets IV. p. 121 (`arXiv:astro-ph/9902198`)

Miller G. E., Scalo J. M., 1979, ApJs, 41, 513

Mocz P., Burkhart B., 2018, MNRAS, 480, 3916

Mocz P., Burkhart B., Hernquist L., McKee C. F., Springel V., 2017a, ApJ, 838, 40

Mocz P., Burkhart B., Hernquist L., McKee C. F., Springel V., 2017b, ApJ, 838, 40

Modak S., Hamilton C., 2023, MNRAS, 524, 3102

Moe M., Di Stefano R., 2017, ApJs, 230, 15

Moeckel N., Clarke C. J., 2011, MNRAS, 415, 1179

Molina F. Z., Glover S. C. O., Federrath C., Klessen R. S., 2012, MNRAS, 423, 2680

Monroy-Rodríguez M. A., Allen C., 2014, ApJ, 790, 159

Mor R., Robin A. C., Figueras F., Lemasle B., 2017, A&A, 599, A17

Motte F., Andre P., Neri R., 1998, A&A, 336, 150

Mouschovias T. C., 1995, in Ferrara A., McKee C. F., Heiles C., Shapiro P. R., eds, Astronomical Society of the Pacific Conference Series Vol. 80, The Physics of the Interstellar Medium and Intergalactic Medium. p. 184

Mouschovias T. C., Ciolek G. E., 1999, in Lada C. J., Kylafis N. D., eds, NATO Advanced Study Institute (ASI) Series C Vol. 540, The Origin of Stars and Planetary Systems. p. 305

Mouschovias T. C., Paleologou E. V., 1979, ApJ, 230, 204

Mouschovias T. C., Paleologou E. V., 1980, ApJ, 237, 877

Muench A. A., Lada E. A., Lada C. J., Alves J., 2002, ApJ, 573, 366

Murray N., 2011, ApJ, 729, 133

Myers P. C., 1983, ApJ, 270, 105

Myers P. C., 2008, ApJ, 687, 340

Myers P. C., 2011, ApJ, 743, 98

Myers P. C., 2015, ApJ, 806, 226

Myers A. T., Klein R. I., Krumholz M. R., McKee C. F., 2014, MNRAS, 439, 3420

Myers P. C., Hatchfield H. P., Battersby C., 2022, ApJ, 929, 34

Nakamura F., Li Z.-Y., 2011, ApJ, 740, 36

Nam D. G., Federrath C., Krumholz M. R., 2021, MNRAS, 503, 1138

Nolan C. A., Federrath C., Sutherland R. S., 2015, MNRAS, 451, 1380

Nutter D., Ward-Thompson D., 2007, MNRAS, 374, 1413

Ochsendorf B. B., Meixner M., Roman-Duval J., Rahman M., Evans Neal J. I., 2017, ApJ, 841, 109

Offner S. S. R., Arce H. G., 2014, ApJ, 784, 61

Offner S. S. R., Chaban J., 2017, ApJ, 847, 104

Offner S. S. R., Klein R. I., McKee C. F., Krumholz M. R., 2009, ApJ, 703, 131

Offner S. S. R., Kratter K. M., Matzner C. D., Krumholz M. R., Klein R. I., 2010, ApJ, 725, 1485

Offner S. S. R., Clark P. C., Hennebelle P., Bastian N., Bate M. R., Hopkins P. F., Moraux E., Whitworth A. P., 2014, in Beuther H., Klessen R. S., Dullemond C. P., Henning T., eds, Protostars and Planets VI. p. 53 (`arXiv:1312.5326`), doi:10.2458/azu˙uapress˙9780816531240-ch003

Offner S. S. R., Dunham M. M., Lee K. I., Arce H. G., Fielding D. B., 2016, ApJl, 827, L11

Offner S. S. R., Moe M., Kratter K. M., Sadavoy S. I., Jensen E. L. N., Tobin J. J., 2022, arXiv e-prints, p. arXiv:2203.10066

Offner S. S. R., Moe M., Kratter K. M., Sadavoy S. I., Jensen E. L. N., Tobin J. J., 2023, in Inutsuka S., Aikawa Y., Muto T., Tomida K., Tamura M., eds, Astronomical Society of the Pacific Conference Series Vol. 534, Protostars and Planets VII. p. 275 (`arXiv:2203.10066`), doi:10.48550/arXiv.2203.10066

Ohashi N., Hayashi M., Ho P. T. P., Momose M., Tamura M., Hirano N., Sargent A. I., 1997, ApJ, 488, 317

Ossenkopf V., Mac Low M. M., 2002, A&A, 390, 307

Ostriker E. C., 1999, ApJ, 513, 252

Ostriker E. C., Stone J. M., Gammie C. F., 2001, ApJ, 546, 980

Ouyed R., Pudritz R. E., 1997, ApJ, 482, 712

Padoan P., 1995, MNRAS, 277, 377

Padoan P., Nordlund Å., 2002, ApJ, 576, 870

Padoan P., Nordlund Å., 2004, ApJ, 617, 559

Padoan P., Nordlund Å., 2011, ApJ, 730, 40

Padoan P., Nordlund A., Jones B. J. T., 1997a, MNRAS, 288, 145

Padoan P., Jones B. J. T., Nordlund Å. P., 1997b, ApJ, 474, 730

Padoan P., Juvela M., Goodman A. A., Nordlund Å., 2001, ApJ, 553, 227

Padoan P., Federrath C., Chabrier G., Evans N. J. I., Johnstone D., Jørgensen J. K., McKee C. F., Nordlund Å., 2014, in Beuther H., Klessen R. S., Dullemond C. P., Henning T., eds, Protostars and Planets VI. p. 77 (`arXiv:1312.5365`), doi:10.2458/azu˙uapress˙9780816531240-ch004

Padoan P., Pan L., Haugbølle T., Nordlund Å., 2016, ApJ, 822, 11

Padoan P., Haugbølle T., Nordlund Å., Frimann S., 2017, ApJ, 840, 48

Padoan P., Pan L., Juvela M., Haugbølle T., Nordlund Å., 2020, ApJ, 900, 82

Palmeirim P., et al., 2013, A&A, 550, A38

Papaloizou J. C. B., Lin D. N. C., 1995, ARA&A, 33, 505

Paresce F., De Marchi G., 2000, ApJ, 534, 870

Parravano A., McKee C. F., Hollenbach D. J., 2011, ApJ, 726, 27

Pascucci I., Wolf S., Steinacker J., Dullemond C. P., Henning T., Niccolini G., Woitke P., Lopez B., 2004, A&A, 417, 793

Passot T., Vázquez-Semadeni E., 1998, Phys. Rev. E, 58, 4501

Patience J., Ghez A. M., Reid I. N., Matthews K., 2002, AJ, 123, 1570

Pattle K., Fissel L., Tahani M., Liu T., Ntormousi E., 2023, in Inutsuka S., Aikawa Y., Muto T., Tomida K., Tamura M., eds, Astronomical Society of the Pacific Conference Series Vol. 534, Protostars and Planets VII. p. 193 (`arXiv:2203.11179`), doi:10.48550/arXiv.2203.11179

Peñarrubia J., Ludlow A. D., Chanamé J., Walker M. G., 2016, MNRAS, 461, L72

Pinfield D. J., et al., 2008, MNRAS, 390, 304

Planck Collaboration et al., 2016a, A&A, 586, A136

Planck Collaboration et al., 2016b, A&A, 586, A138

Polzin A., Kravtsov A. V., Semenov V. A., Gnedin N. Y., 2024, arXiv e-prints, p. arXiv:2407.11125

Porter D. H., Pouquet A., Woodward P. R., 1992, Phys. Rev. Lett., 68, 3156

Press W. H., Schechter P., 1974, ApJ, 187, 425

Price D. J., Bate M. R., 2009, MNRAS, 398, 33

Price D. J., Federrath C., 2010a, MNRAS, 406, 1659

Price D. J., Federrath C., 2010b, MNRAS, 406, 1659

Price D. J., Monaghan J. J., 2007, MNRAS, 374, 1347

Price D. J., Bate M. R., Dobbs C. L., 2008, Magnetic fields in star formation: from galaxies to stars (`arXiv:0804.4647`)

Price D. J., Federrath C., Brunt C. M., 2011, ApJl, 727, L21

Pudritz R. E., Ouyed R., Fendt C., Brandenburg A., 2007, in Reipurth B., Jewitt D., Keil K., eds, Protostars and Planets V. p. 277 (`arXiv:astro-ph/0603592`)

Raghavan D., et al., 2010, ApJs, 190, 1

Rana N. C., Basu S., 1992, A&A, 265, 499

Rani R., Moore T. J. T., Eden D. J., Rigby A. J., 2022a, arXiv e-prints, p. arXiv:2206.13442

Rani R., Moore T. J. T., Eden D. J., Rigby A. J., 2022b, MNRAS, 515, 271

Reid I. N., Gizis J. E., 1997, AJ, 113, 2246

Reid I. N., Hawley S. L., Gizis J. E., 1995, AJ, 110, 1838

Reid I. N., et al., 1999, ApJ, 521, 613

Reid I. N., Gizis J. E., Hawley S. L., 2002, AJ, 124, 2721

Reipurth B., Clarke C., 2001, AJ, 122, 432

Reipurth B., Mikkola S., 2012, Nature, 492, 221

Renaud F., Boily C. M., Naab T., Theis C., 2009, ApJ, 706, 67

Richer J. S., Shepherd D. S., Cabrit S., Bachiller R., Churchwell E., 2000, in Mannings V., Boss A. P., Russell S. S., eds, Protostars and Planets IV. p. 867 (`arXiv:astro-ph/9904097`)

Ricker P. M., 2008, ApJs, 176, 293

Robertson B., Goldreich P., 2018, ApJ, 854, 88

Rogers P. D., Wadsley J., 2012, MNRAS, 423, 1896

Rohde P. F., Walch S., Clarke S. D., Seifried D., Whitworth A. P., Klepitko A., 2021, MNRAS, 500, 3594

Roman-Duval J., Federrath C., Brunt C., Heyer M., Jackson J., Klessen R. S., 2011, ApJ, 740, 120

Rozner M., Perets H. B., 2023, ApJ, 955, 134

Rozner M., Perets H. B., 2024a, ApJ, 968, 80

Rozner M., Perets H. B., 2024b, ApJ, 968, 80

Rozner M., Generozov A., Perets H. B., 2023, MNRAS, 521, 866

Ryu T., Leigh N. W. C., Perna R., 2017, MNRAS, 467, 4447

Sabbi E., et al., 2008, AJ, 135, 173

Sales L. V., Marinacci F., Springel V., Petkova M., 2014, MNRAS, 439, 2990–3006

Salim D. M., Federrath C., Kewley L. J., 2015, ApJl, 806, L36

Salpeter E. E., 1955, ApJ, 121, 161

Sana H., Evans C. J., 2011, in Neiner C., Wade G., Meynet G., Peters G., eds, IAU Symposium Vol. 272, Active OB Stars: Structure, Evolution, Mass Loss, and Critical Limits. pp 474–485 (`arXiv:1009.4197`), doi:10.1017/S1743921311011124

Sana H., Ramírez-Tannus M. C., de Koter A., Kaper L., Tramper F., Bik A., 2017, A&A, 599, L9

Scalo J. M., 1986, Fundamentals Cosmic Phys., 11, 1

Schmidt W., Hillebrandt W., Niemeyer J. C., 2006, Computers and Fluids, 35, 353

Schmidt W., Federrath C., Hupp M., Kern S., Niemeyer J. C., 2009, A&A, 494, 127

Schmidt W., Kern S. A. W., Federrath C., Klessen R. S., 2010, A&A, 516, A25

Schneider S., Elmegreen B. G., 1979, ApJS, 41, 87

Schneider N., et al., 2013, A&A, 551, C1

Schneider N., et al., 2015, MNRAS, 453, L41

Schneider F. R. N., et al., 2018a, Science, 359, 69

Schneider F. R. N., et al., 2018b, A&A, 618, A73

Schober J., Schleicher D., Federrath C., Glover S., Klessen R. S., Banerjee R., 2012, ApJ, 754, 99

Schober J., Schleicher D. R. G., Klessen R. S., 2013, A&A, 560, A87

Seifried D., Pudritz R. E., Banerjee R., Duffin D., Klessen R. S., 2012, MNRAS, 422, 347

Seta A., Federrath C., 2020, MNRAS, 499, 2076

Seta A., Federrath C., 2021, Physical Review Fluids, 6, 103701

Seta A., Federrath C., 2022, MNRAS, 514, 957

Seta A., Bushby P. J., Shukurov A., Wood T. S., 2020, Physical Review Fluids, 5, 043702

Sharda P., Krumholz M. R., 2022, MNRAS, 509, 1959

Sharda P., Federrath C., Krumholz M. R., 2020, MNRAS, 497, 336

Sharda P., et al., 2022, MNRAS, 509, 2180

Shen S., Wadsley J., Hayfield T., Ellens N., 2010, MNRAS, 401, 727

Shu F. H., Adams F. C., Lizano S., 1987, ARA&A, 25, 23

Shu F. H., Lizano S., Ruden S. P., Najita J., 1988, ApJl, 328, L19

Shu F. H., Tremaine S., Adams F. C., Ruden S. P., 1990, ApJ, 358, 495

Silk J., 1978, in Gehrels T., Matthews M. S., eds, IAU Colloq. 52: Protostars and Planets. p. 172

Simon M., 1992, in McAlister H. A., Hartkopf W. I., eds, Astronomical Society of the Pacific Conference Series Vol. 32, IAU Colloq. 135: Complementary Approaches to Double and Multiple Star Research. p. 41

Sirianni M., Nota A., De Marchi G., Leitherer C., Clampin M., 2002, ApJ, 579, 275

Slesnick C. L., Hillenbrand L. A., Carpenter J. M., 2004, ApJ, 610, 1045

Smith L. J., Gallagher J. S., 2001, MNRAS, 326, 1027

Smith R. J., Clark P. C., Bonnell I. A., 2008, MNRAS, 391, 1091

Smith R. J., Clark P. C., Bonnell I. A., 2009, Monthly Notices of the Royal Astronomical Society, 396, 830–841

Spitzer L., 1978, Physical processes in the interstellar medium. Wiley-Interscience Publication, New York: Wiley, 1978, doi:10.1002/9783527617722

Stamatellos D., Whitworth A. P., 2009, MNRAS, 392, 413

Stamatellos D., Hubber D. A., Whitworth A. P., 2007, MNRAS, 382, L30

Stamatellos D., Whitworth A. P., Hubber D. A., 2011, ApJ, 730, 32

Stanke T., Smith M. D., Gredel R., Khanzadyan T., 2006, A&A, 447, 609

Stone J. M., Ostriker E. C., Gammie C. F., 1998, ApJl, 508, L99

Stutz A. M., et al., 2013, ApJ, 767, 36

Su Y., Liu B., Xu S., 2024, arXiv e-prints, p. arXiv:2405.12270

Subramanian K., 1998, MNRAS, 294, 718

Sur S., Schleicher D. R. G., Banerjee R., Federrath C., Klessen R. S., 2010, ApJ, 721, L134

Szölgyén Á., MacLeod M., Loeb A., 2022, MNRAS, 513, 5465

Tahani M., Plume R., Brown J. C., Kainulainen J., 2018, A&A, 614, A100

Tanvir T. S., Krumholz M. R., 2024, MNRAS, 527, 7306

Tassis K., Mouschovias T. C., 2004, ApJ, 616, 283

Tassoul J.-L., Tassoul M., 1992, ApJ, 395, 259

Tauris T. M., van den Heuvel E. P. J., 2023, Physics of Binary Star Evolution. From Stars to X-ray Binaries and Gravitational Wave Sources, doi:10.48550/arXiv.2305.09388.

Testi L., Sargent A. I., 1998, ApJl, 508, L91

Theissen C. A., Konopacky Q. M., Lu J. R., Kim D., Zhang S. Y., Hsu C.-C., Chu L., Wei L., 2021, arXiv e-prints, p. arXiv:2105.05871

Thielemann F. K., Nomoto K., Hashimoto M., 1993, in Prantzos N., Vangioni-Flam E., Casse M., eds, Origin and Evolution of the Elements. pp 297–309

Thies I., Kroupa P., 2007, ApJ, 671, 767

Thies I., Kroupa P., Goodwin S. P., Stamatellos D., Whitworth A. P., 2010, ApJ, 717, 577

Thies I., Pflamm-Altenburg J., Kroupa P., Marks M., 2015, ApJ, 800, 72

Tobin J. J., Hartmann L., Furesz G., Mateo M., Megeath S. T., 2009, ApJ, 697, 1103

Tobin J. J., et al., 2016, ApJ, 818, 73

Tobin J. J., et al., 2022, ApJ, 925, 39

Todorov K. O., Luhman K. L., Konopacky Q. M., McLeod K. K., Apai D., Ghez A. M., Pascucci I., Robberto M., 2014, ApJ, 788, 40

Tokovinin A., 2011, AJ, 141, 52

Tokovinin A., 2017, MNRAS, 468, 3461

Tokovinin A., 2020, MNRAS, 496, 987

Tokovinin A., Kiyaeva O., 2016, MNRAS, 456, 2070

Tomisaka K., 1998, ApJ, 502, L163

Treu T., Auger M. W., Koopmans L. V. E., Gavazzi R., Marshall P. J., Bolton A. S., 2010, ApJ, 709, 1195

Tritsis A., Panopoulou G. V., Mouschovias T. C., Tassis K., Pavlidou V., 2015, MNRAS, 451, 4384

Truelove J. K., Klein R. I., McKee C. F., Holliman John H. I., Howell L. H., Greenough J. A., 1997, ApJl, 489, L179

Turk M. J., Smith B. D., Oishi J. S., Skory S., Skillman S. W., Abel T., Norman M. L., 2011, The Astrophysical Journal Supplement Series, 192, 9

Vazquez-Semadeni E., 1994, ApJ, 423, 681

Vázquez-Semadeni E., Gómez G. C., Jappsen A. K., Ballesteros-Paredes J., González R. F., Klessen R. S., 2007, ApJ, 657, 870

Vázquez-Semadeni E., González-Samaniego A., Colín P., 2017, MNRAS, 467, 1313

Vázquez-Semadeni E., Palau A., Ballesteros-Paredes J., Gómez G. C., Zamora-Avilés M., 2019, MNRAS, 490, 3061

Veltchev T., Nedialkov P., Borisov G., 2004, A&A, 426, 495

Vutisalchavakul N., Evans Neal J. I., Heyer M., 2016, ApJ, 831, 73

Waagan K., Federrath C., Klingenberg C., 2011, Journal of Computational Physics, 230, 3331

Walch S. K., Whitworth A. P., Bisbas T., Wünsch R., Hubber D., 2012, MNRAS, 427, 625

Walch S., et al., 2015, MNRAS, 454, 238

Wang P., Li Z.-Y., Abel T., Nakamura F., 2010, ApJ, 709, 27

Ward-Duong K., et al., 2015, MNRAS, 449, 2618

Watkins S. J., Bhattal A. S., Boffin H. M. J., Francis N., Whitworth A. P., 1998, MNRAS, 300, 1214

Wei L., Theissen C. A., Konopacky Q. M., Lu J. R., Hsu C.-C., Kim D., 2023, arXiv e-prints, p. arXiv:2312.04751

Weights D. J., Lucas P. W., Roche P. F., Pinfield D. J., Riddick F., 2009, MNRAS, 392, 817

Weisz D. R., et al., 2013, ApJ, 762, 123

Weisz D. R., et al., 2015, ApJ, 806, 198

Whitworth A., 1979, MNRAS, 186, 59

Winters J. G., et al., 2019, AJ, 157, 216

Woitas J., Ray T. P., Bacciotti F., Davis C. J., Eislöffel J., 2002, ApJ, 580, 336

Wolfire M. G., Hollenbach D., McKee C. F., Tielens A. G. G. M., Bakes E. L. O., 1995, ApJ, 443, 152

Wurster J., Li Z.-Y., 2018, Frontiers in Astronomy and Space Sciences, 5, 39

Wyse R. F. G., 1998, in Gilmore G., Howell D., eds, Astronomical Society of the Pacific Conference Series Vol. 142, The Stellar Initial Mass Function (38th Herstmonceux Conference). p. 89

Wyse R. F. G., Gilmore G., 1992, AJ, 104, 144

Xu S., Ji S., Lazarian A., 2019, ApJ, 878, 157

Xu S., Hwang H.-C., Hamilton C., Lai D., 2023, ApJl, 949, L28

Yan Z., Li J., Kroupa P., Jerabkova T., Gjergo E., Zhang Z.-Y., 2024, ApJ, 969, 95

Yasui C., Izumi N., Saito M., Lau R. M., Kobayashi N., Ressler M. E., 2024, ApJ, 975, 152

Yen H.-W., Koch P. M., Takakuwa S., Ho P. T. P., Ohashi N., Tang Y.-W., 2015a, ApJ, 799, 193

Yen H.-W., Takakuwa S., Koch P. M., Aso Y., Koyamatsu S., Krasnopolsky R., Ohashi N., 2015b, ApJ, 812, 129

Yorke H. W., Sonnhalter C., 2002, ApJ, 569, 846

Yorke H. W., Bodenheimer P., Laughlin G., 1993, ApJ, 411, 274

Zahn J. P., 1977, A&A, 57, 383

Zinnecker H., 1982, Annals of the New York Academy of Sciences, 395, 226

Zinnecker H., 1984, MNRAS, 210, 43

Zuckerman B., Evans N. J. I., 1974, ApJ, 192, L149

van Dokkum P. G., Conroy C., 2010, Nature, 468, 940

van der Velden E., 2020, The Journal of Open Source Software, 5, 2004